

Polymeric Nanocarriers for the Visualisation and Quantification of Molecular Release

Zur Erlangung des akademischen Grades eines

DOKTORS DER NATURWISSENSCHAFTEN

(Dr. rer. nat.)

der KIT-Fakultät für Chemie und Biowissenschaften

des Karlsruher Instituts für Technologie (KIT)

genehmigte
DISSERTATION
von

M. Sc. Matthias Eing

aus

Karlsruhe, Deutschland

KIT Dekan: Prof. Dr. Reinhard Fischer
Referent: Prof. Dr. Christopher Barner-Kowollik, Dr. James P. Blinco
Korreferent: Prof. Dr. Ute Schepers
Tag der mündlichen Prüfung: 14.12.2018

Die vorliegende Arbeit wurde von März 2015 bis Oktober 2018 im Rahmen einer Cotutelle Vereinbarung zwischen KIT und QUT unter Anleitung von Prof. Dr. Christopher Barner-Kowollik am Karlsruher Institut für Technologie (KIT) - Universitätsbereich und unter Anleitung von Dr. James P. Blinco und Associate Prof. Kathryn E. Fairfull-Smith an der Queensland University of Technology (QUT) angefertigt.

Erklärung

Hiermit erkläre ich, dass die vorliegende Arbeit im Rahmen der Betreuung durch Prof. Dr. Christopher Barner-Kowollik (KIT), Associate Prof. Dr. Kathryn E. Fairfull-Smith (QUT) und Dr. James P. Blinco (QUT) selbstständig von mir verfasst wurde und keine anderen als die angegebenen Quellen und Hilfsmittel verwendet wurden. Die wörtlich oder inhaltlich übernommenen Stellen wurden als solche kenntlich gemacht. Die Regeln zur Sicherung guter wissenschaftlicher Praxis des Karlsruher Instituts für Technologie (KIT) wurden beachtet und die Abgabe und Archivierung der Primärdaten gemäß Abs. A (6) der Regeln zur Sicherung guter wissenschaftlicher Praxis des KIT beim Institut ist gesichert. Die elektronische Version der Arbeit stimmt mit der schriftlichen überein. Die Arbeit wurde im Rahmen der bestehenden Cotutelle-Vereinbarung zwischen dem KIT und der QUT gemeinschaftlich durchgeführt und ist ebenfalls an der ausländischen Universität als Bestandteil einer Prüfungs- oder Qualifikationsleistung zur Erlangung des dortigen Doktorgrades (Doctor of Philosophy, PhD) vorgelegt. Des Weiteren erkläre ich, dass ich keine vorausgegangenen Promotionsversuche unternommen habe und mich derzeit nur in dem oben genannten laufenden Cotutelle-Promotionsverfahren befinde.

Ort, Datum, Unterschrift

Abstract

Macromolecular assemblies for the delivery of chemotherapeutics pose a widely established tool in the field of cancer therapies. With a broad variety of biocompatible strategies to immobilise and release anti-tumour therapeutics readily available, quantification of both delivery and molecular release needs deeper investigation. This thesis focusses on the synthesis and investigation of such macromolecular transporter systems. With pH- and light-triggered release, two avenues of fluorescence-based reporting were explored. The central feature of the reporting systems presented in this thesis was the exploitation of nitroxides as quenchers, to establish a wavelength-independent architecture.

The first part of the works presented herein focuses on the design and synthesis of a polymethacrylate-based transporter assembly for the quantification of pH-triggered release. It encompassed the utilisation of nitroxides as quenchers in combination hydrolytically labile hydrazone-anchoring moieties on defined, PEGylated methacrylates. Two approaches were explored. The first approach focussed on the immobilisation of fluorophore and nitroxide on the same repeating unit of a statistical RAFT copolymer of glycidyl methacrylate and triethylene glycol methacrylate (TEGMA). In the second approach, nitroxide precursors in the form of 2,2,6,6-tetramethyl-4-piperidyl methacrylate (TMPMA), hydrazide precursors in the form of *tert*-butoxycarbonyl-hydrazido methacrylate (bHMA), and TEGMA were statistically copolymerised *via* RAFT. The second approach could successfully yield nitroxide-loaded polymers with free hydrazides for the conjugation of doxorubicin (Dox). The fluorescence-based monitoring of pH-triggered release of Dox was successfully demonstrated for the synthesised architecture. The assembly was subsequently tested in 2D and 3D cell culture in an effort to both evaluate biological activity and investigate the effect of polymeric assemblies on spheroidal 3D cell culture models. In the course of the biological investigations, a refined approach for the computer-assisted evaluation of confocal microscopy images was established. The method allowed the evaluation of drug-penetration into tumour-spheroids. The expansion of the nanocarrier towards immobilisation of both fluorophore and nitroxide on one repeating unit *via* adoption of Ugi-reaction based ligation chemistry was explored. Additionally the possibility of extending the reporter system by a second, red-shifted fluorophore was investigated.

In the second section of this thesis, a release system, photo-responsive to visible light was established. A successful immobilisation of pyreneacyl sulfide as a photolytically cleavable fluorophore and linker moiety, and amino-TEMPO as a nitroxide quencher could be demonstrated. The system was based on a statistical RAFT copolymer of methyl methacrylate and formylphenyl methacrylate as anchor units. The assembly was coupled in a multicomponent chemistry approach by Ugi-reaction protocols.

The third and last section explored the applicability of findings from the first two projects for the creation of an optoacoustic-imaging agent. An end group functionalised RAFT poly-TMPMA was successfully synthesised and examined for its fluorescent properties.

In summary, two powerful tools for the visualisation and quantification of molecular release from polymeric carrier platforms are presented. Additionally, bioapplicability of one of the assemblies is demonstrated.

Zusammenfassung

Makromolekulare Konstrukte zur Verabreichung von Chemotherapeutika stellen ein weitläufig etabliertes Konzept im Feld der Krebstherapie dar. Mit einem reichen Angebot verfügbarer Strategien zu gerichtetem Transport von anti-Tumor Therapeutika bedarf es nach wie vor eingehender Untersuchung und Quantifizierung von korrekter Lokalisierung und Freisetzung von derartigen makromolekularen Transportern. Die vorliegende Arbeit legt den Fokus auf die Synthese und Evaluierung solcher Systeme. Mit pH-gesteuerten und lichtabhängigen Ansätzen wurden zwei Herangehensweisen zur fluoreszenzbasierten Detektion von Wirkstofffreisetzung eingehend untersucht. Fokus der hier demonstrierten Systeme lag auf der Ausnutzung fluoreszenzlöschender Eigenschaften von Nitroxiden, um ein wellenlängenunabhängiges System zu etablieren.

Der erste Abschnitt der vorliegenden Arbeit setzt sich mit dem Entwurf und der synthetischen Umsetzung eines Polymethacrylat-basierten Transportkonstrukts zur Quantifizierung von pH-abhängiger Freisetzung auseinander. Eine geeignete Herangehensweise an die Kombination von Nitroxiden und hydrolytisch spaltbaren Hydrazonen, gebunden an PEGylierte Methacrylate ist eingehend beschrieben. Zwei Architekturen wurden untersucht. Eine Strategie basierte auf der Verankerung von Hydrazon und Nitroxid an derselben Glycidylgruppe eines RAFT Copolymers aus Glycidylmethacrylat und Triethylenglycolmethacrylat (TEGMA). Die andere Strategie legte eine statistische RAFT-Copolymerisation von 2,2,6,6-Tetramethyl-4-Piperidylmethacrylat (TMPMA), Hydrazidvorläufern in Form von *tert*-butoxycarbonyl-hydrazido Methacrylat (bHMA), und TEGMA zugrunde. Mithilfe letzterer Strategie konnten erfolgreich Polymere mit TEMPO-Seitenketten und freien Hydraziden zur Beladung mit Doxorubicin (Dox) synthetisiert werden. Der fluoreszenzbasierte Nachweis pH-kontrollierter Freisetzung konnte erfolgreich gezeigt werden. Des Weiteren wurde das Konstrukt erfolgreich in zwei- und dreidimensionaler Zellkultur auf Aktivität in biologischen Systemen untersucht. Im Zuge der biologischen Untersuchungen wurde ein Ansatz zur computergestützten Auswertung von konfokalen Fluoreszenzmikroskopieaufnahmen erstellt. Die vorgestellte Methode erlaubte nicht nur Quantifizierung der Wirkstoffaufnahme, sondern auch eine Abschätzung der Eindringtiefe fluoreszenter Konstrukte in Tumorsphäroide. Eine Erweiterung der Transporterplattform im Hinblick auf die Coimmobilisierung von Nitroxid und Wirkstoff an derselben Seitenkette eines Polymers einerseits,

und die Einbindung eines rotverschobenen zweiten Fluorophors andererseits, wurde basierend auf der Ugi-Reaktion ebenfalls unternommen.

Der zweite Abschnitt dieser Arbeit stellt ein Freisetzungssystem, basierend auf der Nutzung eines Lichtstimulus aus dem sichtbaren Spektrum, vor. Die erfolgreiche Immobilisierung von Pyrenacylsulfid als photolytisch spaltbarer Gruppe und Modellfluorophor in einem, und Amino-TEMPO als fluoreszenzlöschendem Nitroxid konnte erfolgreich gezeigt werden. Das System nutzt ein RAFT-basiertes Copolymer von Methylmethacrylat und Formylphenylmethacrylat zur Bereitstellung einer carbonylfunktionalen Polymerplattform. Das Gesamtkonstrukt wurde in einem eleganten Multikomponentenschritt nach Ugi zusammengefügt.

Der dritte und letzte Abschnitt untersucht die Anwendbarkeit der Erkenntnisse aus den ersten beiden Teilen zur Konstruktion eines neuartigen Farbstoffs für optoakustische Bildgebung. Ein mit Cyanin-5 endgruppenfunktionalisiertes RAFT poly-TMPMA Konstrukt wurde erfolgreich synthetisiert und im Hinblick auf seine fluoreszenten Eigenschaften untersucht.

Zusammenfassend stellt diese Thesis zwei vielversprechende Werkzeuge zur Visualisierung und Quantifizierung molekularer Freisetzung von polymerbasierten Transporterkonstrukten vor. Darüber hinaus wurde eine Anwendbarkeit in biologischen Systemen erfolgreich demonstriert.

Publications Arising from this Thesis

- [1] - M. Eing, B. Olshausen, K. E. Fairfull-Smith, U. Schepers, C. Barner-Kowollik and J. P. Blinco, *Polym. Chem.*, 2018, **9**, 499–505.
- [2] - M. Eing, B. Tuten, J. P. Blinco and C. Barner-Kowollik, *Chem. Eur. J.*, 2018, 1–5.

Table of Contents

Erklärung.....	III
Abstract.....	I
Zusammenfassung.....	III
Publications Arising from this Thesis.....	V
Table of Contents.....	VII
List of Abbreviations.....	XI
1 Introduction.....	1
1.1 Motivation and aim of the Thesis.....	1
2 Theoretical Background.....	5
2.1 Polymer Chemistry.....	6
2.1.1 Radical Polymerisation.....	7
2.1.2 Reversible Deactivation Radical Polymerisation (RDRP) Techniques.....	9
2.1.3 Reversible Addition Fragmentation Polymerisation (RAFT).....	11
2.1.4 Characterisation.....	15
2.2 Photochemistry.....	18
2.2.1 Overview.....	19
2.2.2 Photoenols.....	22
2.2.3 Photo-cleavable Arylacyl sulfides.....	24
2.3 Nitroxides.....	26
2.3.1 Profluorescent Nitroxides.....	28
2.3.2 Nitroxides in Biology.....	29
2.4 Solid Tumours.....	32
2.4.1 Physiological Properties – the EPR effect.....	32
2.4.2 Release and Reporting Strategies.....	35
2.4.3 Tumour Modelling in Spheroids.....	37
2.5 Multicomponent Reactions.....	42
3 A Polymeric Nanocarrier for the Visualisation of pH-Triggered Release.....	45
3.1 Motivation and Strategy.....	46
3.2 Preliminary Small Molecule Studies.....	51
3.2.1 Nitroxide and Fluorescence quantification.....	51
3.2.2 A Small-Molecule Proof-of-Concept.....	52
3.3 Polymeric Approach - Single Anchor.....	55
3.4 Polymeric Approach - Distributed Anchors.....	66

3.4.1	Proof of Concept	68
3.4.2	A pH-Sensitive Nanodrug for Self-Reporting Controlled Release.....	74
3.5	Biological Testing	83
3.5.1	2D Experiments	84
3.5.2	3D-Experiments	88
3.5.3	Development of a Method for the Investigation of Penetration-Depth	97
3.6	Incorporation of a Secondary Fluorescent Tracker	100
3.7	An MCR Approach to Macromolecular Reporters	103
4	Visible-Light Activation of Self-Reporting Molecular Release.....	107
4.1	Motivation and Strategy	107
4.2	Small Molecule Studies.....	110
4.3	An MCR based Reporter for Photorelease from Polymeric Nanocarriers	112
5	Investigation of a Proof-of-Concept Dye for MSOT applications	123
5.1	Motivation and Strategy	123
5.2	Synthesis and Evaluation	124
6	Concluding Remarks and Outlook	129
7	Experimental.....	133
7.1	Instrumentation and materials	133
7.2	General Procedures	134
7.3	Methods pH – Responsive Nanocarrier	135
7.3.1	Monomer syntheses	135
7.3.2	Small Molecule Studies	137
7.3.3	Single Anchor SAP-System.....	141
7.3.4	Statistical PC-System.....	143
7.3.5	Statistical SSPC System.....	146
7.3.6	Biological Testing.....	150
7.3.7	Automated Evaluation of Microscopy images.....	155
7.3.8	DLPC-System	157
7.3.9	ULC-System	158
7.4	Methods light-responsive nanocarrier.....	160
7.5	Methods MSOT contrast agent	162
8	Appendix	165
8.1	pH-Sensitive Release Systems	165
8.1.1	Monomers	165
8.1.2	Small Molecules.....	168
8.1.3	SAP system	177
8.1.4	PC system.....	178

8.1.5	SSPC system	179
8.1.6	DLPC System.....	185
8.1.7	ULC-system	186
8.1.8	2D Bio-Testing.....	187
8.1.9	3D Bio-Testing.....	188
8.1.10	Appendix Bio-Evaluation	194
8.2	Appendix light responsive release system	202
8.3	Appendix MSOT dye	209
9	Lists	211
	List of References.....	211
	List of Figures	229
	List of Schemes	241
	List of Tables.....	247
	Acknowledgements	249

List of Abbreviations

ACN	acetonitrile
AIBN	2,2'-azobis(2-methylpropionitrile)
AM	acrylamide
AN	acrylonitrile
ATR	attenuated total reflectance
ATRP	atom transfer radical polymerisation
a.u.	arbitrary units
bHMA	boc-hydrazido methacrylamides
CPDB	2-cyano-2-propyl benzodithioate
CTA	chain transfer agent
CuAAC	copper catalysed azide alkyne click
DA	Diels-Alder
DIV	days <i>in vitro</i>
DMF	N,N-dimethylformamide
DMSO	dimethyl sulfoxide
DMAP	dimethylamino pyridine
DOSY	diffusion-ordered NMR spectroscopy
Dox	doxorubicin
Dox·HCl	doxorubicin hydrochloride salt
DPBS	Dulbecco's phosphate buffered saline
EA	ethyl acetate
ECM	extracellular matrix
EDC·HCl	N'-ethylcarbodiimide hydrochloride

EPR	enhanced permeation and retention effect
ESI	electrospray ionisation
eq	equivalents
ESR	electron spin resonance spectroscopy, electron paramagnetic resonance spectroscopy
FGM	fibroblast growth medium
FLSM	fluorescence laser scanning microscopy
FPMA	formyl-phenyl methacrylate
FRP	free radical polymerisation
FTIR	fourier-transform infrared spectroscopy
GMA	glycidyl methacrylate
GPC	gel permeation chromatography
HCl	Hydrogen chloride
HDA	hetero Diels-Alder
HOMO	highest occupied molecular orbital
HPMAM	N-(2-hydroxypropyl) methacrylamides
IC	internal conversion
i.e.	that is (<i>id est</i>)
ISC	inter system crossing
IR	infrared
LED	light emitting diode
LUMO	lowest unoccupied molecular orbital
MA	methyl acrylate
MAA	methacrylamide
MACl	methacryloyl chloride
MCR	multicomponent reaction

MSOT	multispectral optoacoustic tomography
NMP	nitroxide mediated polymerisation
NMR	nuclear magnetic resonance
NO	nitric oxide
NVC	N-vinyl caprolactam
NVP	N-vinylpyrrolidone
p.a.	yearly (<i>per annum</i>)
PAS	pyreneacyl sulfide
PBS	phosphate buffered saline
PE	photoenol, 2-methoxy-6-methylbenzaldehyde
PEG	polyethylene glycol
ppm	parts per million
PPM	polymer post modification
PPTTC	2-cyanoisopropyl-pentyl trithiocarbonate
RAFT	reversible addition fragmentation chain transfer
RDRP	reversible activation deactivation polymerisation
RI	refractive index
ROI	region of interest
ROS	reactive oxygen species
SEC	size exclusion chromatography
SOMO	singly occupied molecular orbital
SPAAC	strain promoted alkyne azide click
St	styrene
TEA	triethylamine
TFA	trifluoroacetic acid
THF	tetrahydrofuran

List of Abbreviations

TMPMA	2,2,6,6-Tetramethyl-4-piperidyl methacrylate
TEMPO	(2,2,6,6-Tetramethyl-4-piperin-1-yl)-oxyl
TEMPOL	4-hydroxy-(2,2,6,6-Tetramethyl-4-piperin-1-yl)-oxyl
TEMPOMA	(2,2,6,6-Tetramethyl-4-piperin-1-yl)-oxyl methacrylate
UV	ultraviolet
VAc	vinyl acetate

1

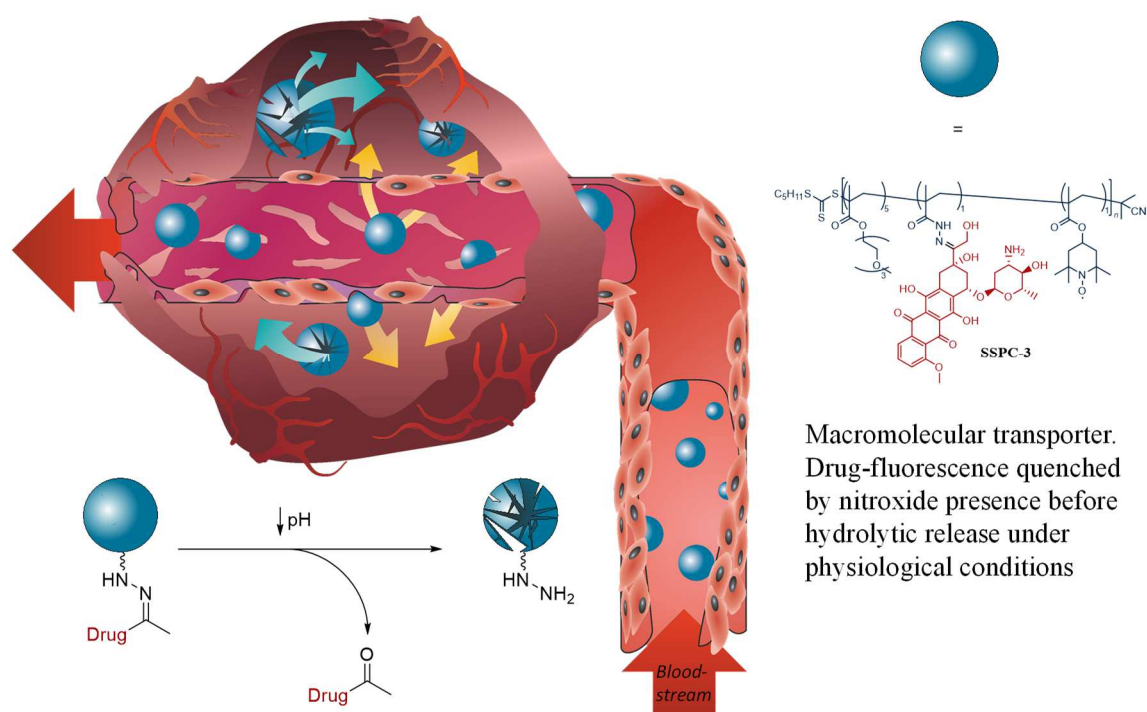
Introduction

Improvement of life-quality has always been one of the main driving factors for scientists all over the world. The shape of modern society is deeply rooted in scientific history, which sports a long record of great successes, aiding all aspects of daily life. Perhaps most critically, the alleviation of debilitating diseases has enabled society to move forward in a fashion, unthinkable under purely ‘nature-given’ circumstances. In our time, one of the most severe factors negatively affecting human health and wellbeing is the prevalence of cancer in all populations and demographics. Being responsible for a total of 8.8 million deaths, an overall rate of about 15%, and an estimated economic impact of US\$1.16 trillion p.a., it is without a doubt one of the main challenges the world is facing in today’s day and age.^[1]

1.1 MOTIVATION AND AIM OF THE THESIS

The motivation of the works presented herein is to encompass a prodrug that allows the combined delivery, release, and *in vivo* monitoring of fluorescent chemotherapeutics. The goal was to focus on establishing a novel architectural building block for polymeric drug delivery platforms. A major issue in chemotherapy is the potentially undirected nature of the employed drugs on one hand, and possible emergence of drug resistance and an ensuing decrease in efficacy on the other hand. The general approach to overcome both those hurdles is the incorporation of the compound in question into drug conjugates capable of either targeting the tumour or avoiding uptake into healthy tissue. A macroscopic way to approach cancer-tissue specificity is targeting tumour-specific physiological factors. One of the most commonly exploited phenomena in the field is the enhanced permeation and

retention effect (EPR),^[2] depicted in **Scheme 1.1**, which was one of the main targets for the works presented in this thesis. As an effect of elevated rates of proliferation in cancerous tissue, metabolic rates increase, causing an elevated demand for nutrients in the tumour. In order to compensate for this deficiency, solid tumours exhibit a tendency to develop increased levels of vascularisation. Such abnormal vasculature frequently exhibit defective or fenestrated vascular walls. In comparison to healthy blood vessels, these ‘leaks’ allow the nearly unhindered escape of macromolecular assemblies into the surrounding tissue. The generation of macromolecular drug nanocarriers can thus be employed to deliver drug molecules specifically to such cancerous tissue, where the assemblies can extravasate the bloodstream into the interstitial space and extracellular matrix (ECM) of a tumour.



Scheme 1.1: Basic structure and mode of action of a model drug, capable of self reporting of targeted molecular release. The macromolecular nature allows exploitation of the EPR effect, wherein transporters can permeate defective blood vessels in a tumour. Decreased pH in the tumour tissue facilitates the hydrolytic cleavage of hydrazones, binding Doxorubicin, a common chemotherapeutic to a nitroxide bearing carrier polymer. Nitroxides enable fluorescent readout of release and potentially increase permeation and uptake.

Enhanced retention is achieved through another widely prevalent deficiency of tumour tissue. Where healthy tissue is drained by lymphatic pathways, tumour tissue lacks lymphatic drainage and exhibits a heavily decreased turnover in extracellular fluids. As a direct result, drug-conjugates experience an increased dwell-time at their site of action, providing a larger temporal window for drug-release or cellular uptake.

The effectiveness of a delivery agent is not only defined by its ability to reach the targeted tissue. After transport, an efficient release of the drug and subsequent uptake *via* the correct pathway is just as crucial as delivery itself. Most measurements thereof are usually carried out in off-line experiments, such as biopsies and analysis of extracted tissue. Precise quantification of such release events can therefore be extremely complex. Efforts to achieve real-time readouts are hampered by the physical nature of an investigated organism. The human physiology is extremely sensitive to external influences. As the interaction between an organism and an external stimulus can be highly unpredictable, the range of accessible investigative methods is oftentimes highly limited. Tissue, blood and interstitial fluids are laden with compounds absorbing short-wavelength light to such an extent that exposure over an extended timeframe leads to irreversible damage. As most fluorescent methods require the application of UV-range light sources, all of these become impractical as soon as an assembly is transferred from the laboratory into a living organism. The emergence of visible-light and infrared-active dyes has opened up a vast range of possibilities. Through the incorporation of a quencher molecule into a transporter assembly, release of such molecules can be visualised. As classic fluorophore/quencher-pairs usually follow a classical FRET mechanism, they are generally wavelength dependent and thus require elaborate synthetic strategies.^[3] Alternatively, gold-nanoparticles have been explored as quencher systems in the past, providing quenching capabilities *via* the evanescent field in their surface's plasmon resonance.^[4] A comparatively unexplored field is the application of nitroxides as quencher moieties. Organic free radicals in nitroxides have shown excellent quenching capability independent of wavelengths and excitation energies. Even though their quenching capabilities have been shown to exhibit a certain level of orientation-dependence, their ability to silence fluorescent signals through space are outstanding. The project goal of the works presented herein was the investigation of accessibility and applicability of systems utilizing nitroxide-silenced fluorescent as a release-quantifier. The general underlying concept was the co-immobilisation of a nitroxide-based quencher and a fluorophore or fluorescent drug on a polymer. The latter was linked *via* chemistries allowing for controlled cleavage and release upon specific triggers such as light irradiation or pH-change.

Chapter 2 will give a brief introduction into the theoretical background and state of the art of the investigated systems, as well as a short overview and cancer and established

therapies. An introduction on the employed polymerisation techniques, as well as the underlying concept of profluorescent nitroxides is presented. Furthermore an introduction on photochemical ligation- and release techniques is given. Biological applications for the envisioned systems are discussed and the utilised cell culture models are introduced.

The focus of this thesis, the successful establishment of a pH-responsive system for the delivery and quantifiable release of doxorubicin (Dox) from a polymeric system, is described in **Chapter 3**. Two architectures based on statistically copolymerised RAFT-polymethacrylates were explored, out of which one could achieve the envisioned goal. The polymeric construct could successfully be employed to visualise controlled release of Dox *via* fluorescence readout. Synthesis, analysis and the evaluation of release experiments are discussed in detail. Furthermore, investigations in three-dimensional tumour models are described. The presented assembly exhibited increased uptake into both two- and three-dimensional cell cultures, demonstrating the *in vivo* applicability of the construct as a transporter system.

Chapter 4 transfers the release system to a light-responsive assembly. Pyreneacyl sulfide was employed as both fluorophore and linker, labile and irradiation in the blue spectrum. Architecturally, fluorophore and quencher nitroxide were co-immobilised on a polymethacrylate backbone in a multicomponent reaction to achieve maximum quenching efficiency. Fluorescence recovery upon blue-light irradiation could successfully be followed in real-time. Synthesis, characterisation and release experiments are discussed in detail.

Lastly, the potential of polymeric nitroxides as universal quenchers for signal enhancement in optoacoustic imaging is outlined in **Chapter 5**. A nitroxide-functionalised methacrylate was end group-modified with a cyanine dye, fluorescent in the red spectrum. The construct showed a decrease in fluorescence in accordance with the anticipated trend. Synthesis, characterisation and initial results from fluorescence investigations are discussed in detail.

2

Theoretical Background

The following chapter will provide background information relevant to the topics presented in the current thesis. Methods employed for the defined synthesis of polymeric platforms for molecular release are described in **Section 2.1**. Additionally, a brief overview of methods employed for the characterisation of polymeric constructs has been included. Light-driven techniques were utilised in the course of this thesis to carry out both ligation- and release reactions. To elucidate them, an introduction to the underlying processes in photochemistry will be presented in **Section 2.2**. A summary of the photo-ligation processes exploited to allow end group protection of polymers for analytical purposes is given. The overview further gives insight on photo-cleavage systems employed to facilitate light-responsive molecular release. The reporting systems presented herein are centred on the utilisation of fluorescent nitroxides – fluorophores quenched by the presence of a nitroxide’s stable radical. Their physical and chemical properties as well as analytical methods for complex polymer constructs are described in **Section 2.3**. In addition, a short summary of established and further possible bio-applications is given. The reporting systems presented herein were designed with medical applications in mind, aimed at the elucidation of release events at the tumour site. Thus, the field of cancer research and therapy is discussed, with special attention to targeted therapeutics. An introduction to traditional and modern tumour model systems, as well as analytical methods for their investigation is provided in **Section 2.4**. Lastly, multicomponent reactions employed for the ligation of polymers and reporter-systems are discussed in **Section 2.5**.

2.1 POLYMER CHEMISTRY

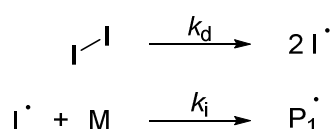
Natural polymers pose the basis for all complex life as it is known to date. They are present in every chemical and physical aspect thereof: Starting with nucleic acids, which encode the ‘blueprint’ for every living organism, spanning polypeptides and proteins as the molecular tools in nature and finally manifesting in macroscopic structures made from cellulose or chitin. The exploitation of natural polymers by humanity dates back to the very beginnings of recorded history in 1600 BC, when our early ancestors had reportedly been using natural rubbers for toys, art or ties.^[5] Aside from the obvious use of woods and weeds for structural elements, polymer coatings and finishes made from cured oils, wax or shellac date back as far as 1000 BC. They were used for their wide applicability and variety of shapes, and are still found in modern-day carpentry and artistry.^[5] The history of modern synthetic polymers begins in the early 19th century. In 1839 Eduard Simon discovered polystyrene, followed by a line of discoveries (vulcanised rubber, celluloid, PCV, polyethylene, Bakelite, cellophane), which laid the ground for soft matter materials science.^[6] For almost a century, polymers had mostly been discussed as crystalline structures, until 1922, when Hermann Staudinger published his theories on polystyrene.^[7] He had shown that polymers like polystyrene were long, linear macromolecules, effectively revolutionizing the field of polymer chemistry and changing the science community’s view on it. Staudinger’s findings set off a revolution in the development of different polymer types and polymerisation techniques. In just under a century, polymers have become of vital importance to all facets of modern society. Spanning everything from food containers, lacquers and finishes, structural elements in cars and buildings, medical implants and drug-assemblies, or nanoscale applications in electronics manufacturing, they make up one of the most important classes of compounds in the modern world. The following sections shall provide a general background on the synthesis and characterisation of the polymers employed in this thesis.

2.1.1 Radical Polymerisation

Free radical polymerisation (FRP) is one of the most important techniques for the commercial production of polymers. Outstanding compatibility with a wide range of monomers, solvents and applicability in a range of production processes make it an accessible and well-scaling tool. The mechanism of FRP chain reaction proceeds in four major steps, occurring in parallel over the course of a polymerisation:

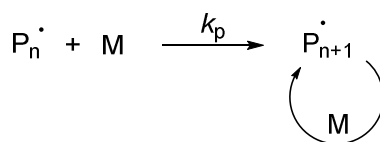
- (I) Initiation
- (II) Propagation
- (III) Termination
- (IV) Chain Transfer

The first step of FRP is the initiation.



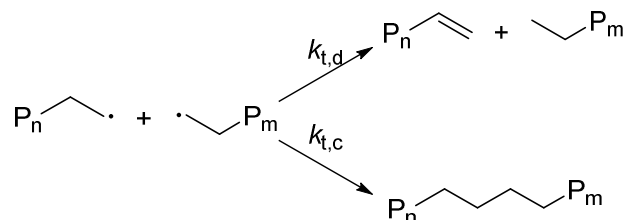
Scheme 2.1: FRP initiation steps. First, a radical initiator undergoes homolysis, forming two radicals in the process. Addition of an initiator radical to a monomer starts a radical-bearing, growing polymer chain.

Initiation proceeds *via* two steps as shown in **Scheme 2.1**. Firstly, an initiator is split into two radical-bearing molecules by heat, light or redox processes.^[8] The initiator fragment adds to the double bond of a monomer, forming a radical-bearing, now growing chain. Chain growth occurs during propagation, by the sequential addition of monomers as shown in **Scheme 2.2**. Propagation rates are dependent on monomer choice and solvent. Steric bulk as well as stabilizing electronic effects have significant influence on the propagation rate.^[8]



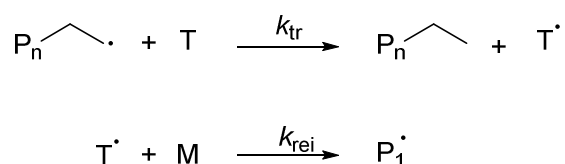
Scheme 2.2: Propagation of a growing chain by the sequential addition of monomers. The rate of addition is determined by the propagation constant k_p .

Chain elongation can be stopped by two types of events – termination and chain transfer. Termination occurs when two propagating chains meet, resulting in either recombination or disproportionation products.



Scheme 2.3: Termination by either disproportionation, or recombination of two polymer chains. Abstraction of a hydrogen atom from one chain leaves a saturated chain and a macromonomer. The recombination of two growing chains yields a single chain of higher molecular weight.

Disproportionation as shown in **Scheme 2.3** takes place, when a hydrogen atom is abstracted from one chain and added to the other chain. Effectively, this leads to one terminated, ‘dead’ chain, and a macromonomer, which can subsequently take part in polymerisation, leading to branched polymers.^[8] Termination by recombination occurs when two growing chains form a new bond, yielding a single chain of higher molecular weight. Disproportionation is heavily influenced by monomer- and solvent choice. Sterically hindered monomers such as methacrylates have been reported to promote termination *via* disproportionation.^[9]



Scheme 2.4: Chain transfer in FRP. Propagation is terminated by chain transfer to a transfer agent, which in turn is capable of reinitiation a new growing chain. The rate of transfer is governed by the rate coefficient k_{tr} , the rate of reinitiation is expressed by k_{rei} .

Another way to terminate propagation is chain transfer to a so-called a transfer agent. Chain transfer agents (CTA) can be introduced to a reaction either as contaminants or purposely as means to influence chain length. The transfer agent caps the chain by transfer of one fragment and initiates another new chain. For low conversions, the average chain length can be described by the Mayo equation:

$$\frac{1}{DP_n} = (1 + \delta) \frac{k_t R_p}{k_p^2 [M]^2} + C_M + C_T \frac{[T]}{[M]}$$

With δ giving the fraction of termination events resulting in disproportionation, C_M and C_T representing the ratios of transfer to monomer or transfer agent respectively, $[M]$ and $[T]$ the concentrations of monomer and transfer agent, and R_p expressing the rate of polymerisation. For many polymerisations, a stationary level of initiator radicals can be assumed, allowing an expression of R_p as:

$$R_p = k_p[M][R\cdot]$$

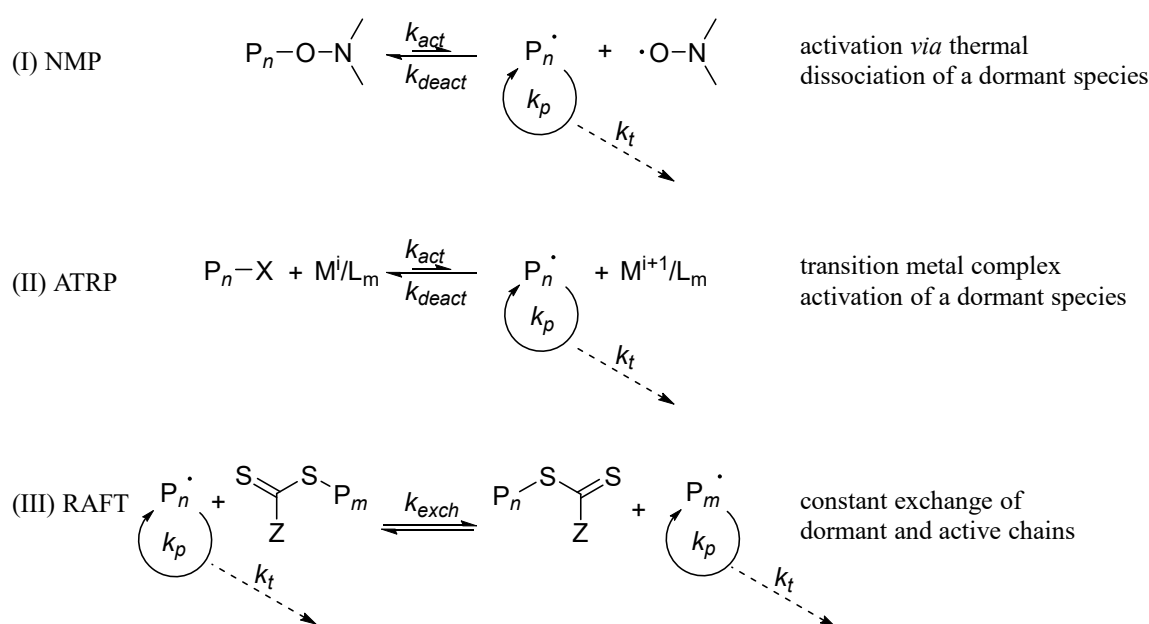
where k_p is the rate of propagation, $[M]$ is the monomer concentration and $[R\cdot]$ is the concentration of initiator-derived radicals. It is the nature of FRP to lead to highly disperse polymers of poor end group fidelity and architectural definition. This reduces its applicability for the construction of highly defined polymers. A range of techniques based on chain transfer reactions have been developed to provide control over molecular weight and dispersity. Commonly described as controlled radical polymerisation (CRP), reversible deactivation radical polymerisation (RDRP) or living polymerisation, they employ reversible chain transfer reactions to suppress uncontrolled termination- and transfer events.

2.1.2 Reversible Deactivation Radical Polymerisation (RDRP) Techniques

Polymeric constructs offer great potential for diagnostic or therapeutic applications, yet a number of factors need to be controlled for this. Many chemically diverse molecules can be immobilised in a highly controlled fashion on a polymer backbone. When constructed with high precision, polymers thereby enable control over the organisation of therapeutic formulations with respect to both stoichiometry and spatial arrangement. A high level of control over chain length, dispersity and molecular composition is of critical relevance to enable synergistic effects between different compounds in a therapeutic application: in high dilutions, diffusion would separate the compounds in question, effectively annihilating their combined effects.^[10] Especially when considering sensitive biological systems, defined physical attributes of the constructs are of crucial importance. Polymer size and shape takes influence on critical attributes as solubility and behaviour in solution at different temperatures. Tissue compatibility depends greatly on particle size and thus needs to be custom tailored towards the application. In order to be able to access useful features of polymers, control over size and shape is thus indispensable. In order to generate defined polymeric backbones from a radical polymerisation, one critical issue with radical polymerisation has to be addressed first. Conventional free radical polymerisation offers very little control over polymer size and thus sample dispersity. One of the methods to gain

such control is the utilisation of – in IUPAC terms - living or reversible deactivation radical polymerisation (RDRP).^[11,12]

The most commonly employed methods to control radical polymerisations are nitroxide mediated polymerisation (NMP),^[8,13] atom transfer radical polymerisation (ATRP),^[14,15] and reversible addition fragmentation polymerisation (RAFT).^[16–18] The underlying concept in all cases is a low concentration of active species bearing a radical which could terminate *via* recombination.^[19] All three methods increase control over molecular weight and dispersity by reducing the termination events to a minimum.



Scheme 2.5: Commonly used techniques for RDRP. (I) NMP employs nitroxides, which scavenge growing chain macro-radicals. Polymerisation is reactivated by thermal dissociation. (II) In ATRP a leaving group, typically a halogen is transferred from the dormant chain to a metal complex. (III) RAFT relies on an equilibrium of dormant chains, bound to the CTA. The radical concentration stays constant, yet termination events are suppressed by chain transfer to the CTA. Figure adapted from [19] with permission from ACS.

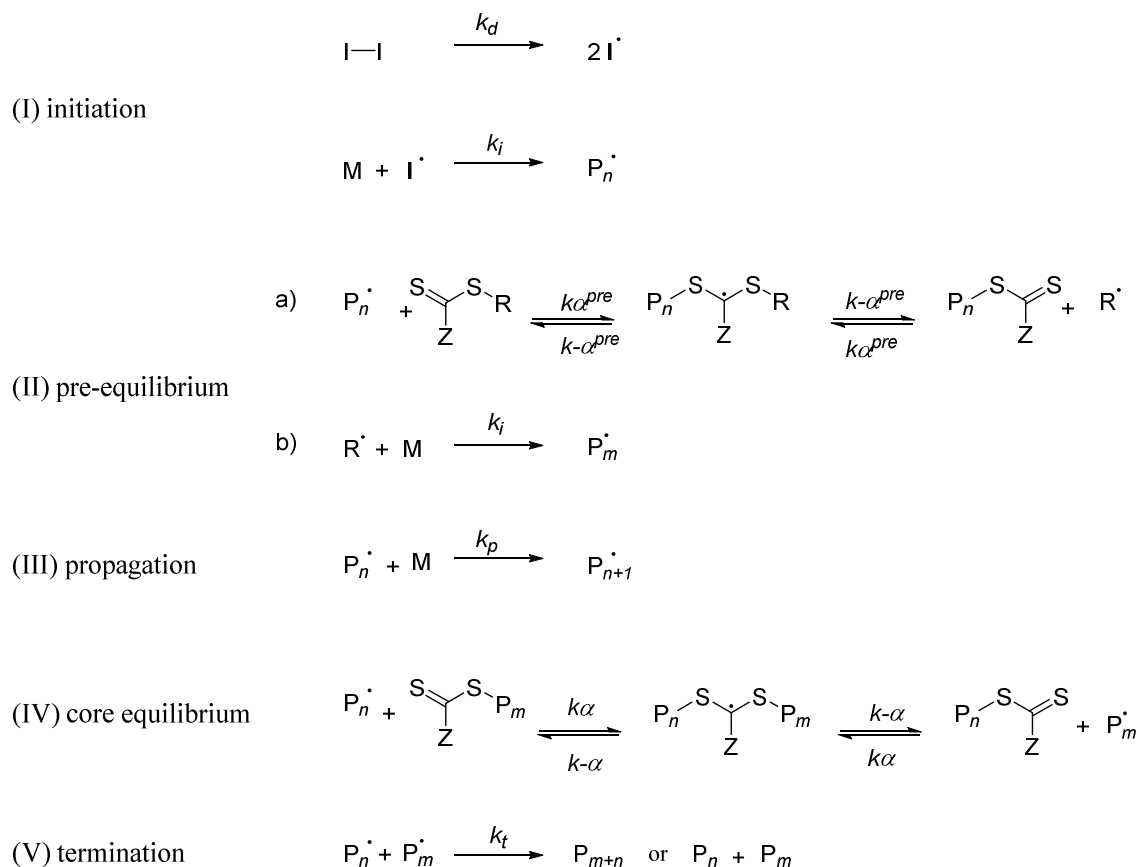
As shown in **Scheme 2.5**, the difference between the three techniques lies in their deactivated (dormant) species and their reactivation. In all approaches, the active, growing chain is covalently trapped in an equilibrium reaction. In the case of NMP and ATRP, the dormant species no longer bear radicals and need to be activated by thermal dissociation (NMP) or halogen-transfer to a metal catalyst. In contrast to ATRP or NMP, the radical concentration never changes in the RAFT process. Growing chains are rapidly transferred to the RAFT agent, resulting in an intermediate species, which still bears a radical, yet does

not add to another monomer. The intermediate expels either its R-group, which in turn initiates a new chain, or an already bound chain, which subsequently continues chain elongation until it is trapped by another (macro-)RAFT agent. Transfer agents can be exchanged: A commonly employed technique is the trapping of a growing macro-RAFT agent with a nitroxide, forming an NMP-compatible macro-transfer agent.^[19]

2.1.3 Reversible Addition Fragmentation Polymerisation (RAFT)

Transfer reactions as reactions for controlling polymerisations have been known to polymer chemists since the 1980s. Initially employing vinyl ethers and allyl sulfides addition-fragmentation reactions, they laid the ground for polymerisations with living characteristics, yet suffered from irreversibility.^[20–22] Reversible addition-fragmentation control over polymerisations using thiocarbonylthio compounds was demonstrated in 1998, rapidly gaining relevance under the term RAFT^[23] or the less widely used MADIX process, where xanthates were employed as transfer agents.^[24] The RAFT process grants access to a range of key features, typically inaccessible by classical FRP methods: (i) Molecular weights can precisely be fine-tuned by the ratio of monomer/transfer agent and the target conversion. (ii) Polymerisations proceed at the same rate as conventional radical polymerisation. (iii) A drastic suppression of chain-breaking events achieves low dispersity (\mathcal{D}). The resulting polymers (iv) exhibit high levels of end group fidelity and (v) can further be employed as macro-transfer-agents. In the RAFT process, the number of termination events are drastically reduced, as they are outweighed by the addition of the RAFT agent to the propagating chain. ($k_a \gg k_t$). The lifetime of a living chain is increased from seconds to hours.^[25] Contrary to ATRP or NMP the radical concentration is kept at a steady level.^[26] In practical applications, dithioesters, trithiocarbonates, dithiocarbamates and xanthates are commonly employed to facilitate this.^[17,27,28]

2. Theoretical Background



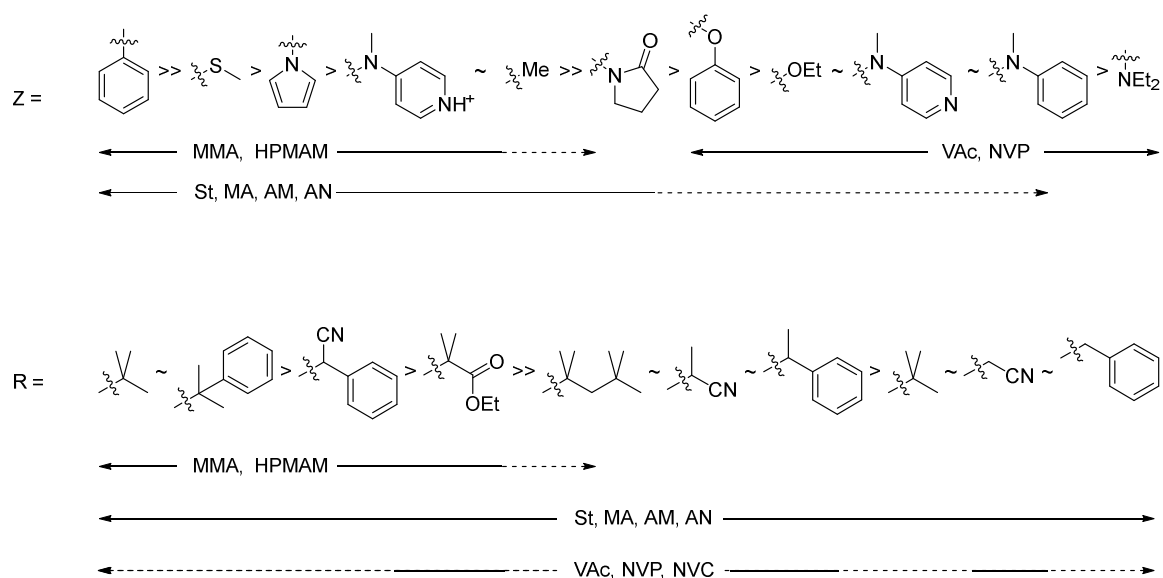
Scheme 2.6: General RAFT mechanism. (I) Initiator decomposition, generating two radicals and initiation by addition of the initiator radical to a monomer M to form a macro-radical P_n^\bullet . (II) Pre-equilibrium, in which a) initiated macro-radical add to the RAFT agent's C=S bond, forming an intermediate species and b) the R-group is released to initiate another chain P_m^\bullet . (III) Propagation occurs, while the unbound macro-radical is elongated by more monomer units, forming a growing chain. (IV) Core-equilibrium, the controlling step in RAFT polymerisation, where growing chains add to the RAFT agent and dormant chains are released to continue propagation. (V) Termination by general FRP mechanisms.^[19]

The RAFT mechanism is depicted in **Scheme 2.6**. The initiation step proceeds in an FRP-like manner. The initiating radical covalently adds to the thiocarbonyl group of the RAFT agent, forming a semi-stable intermediate. The intermediate releases the R-group, forming a radical R^\bullet , which in turn reinitiates another chain. During polymerisation, equal chain growth is ensured by a constant equilibrium of addition and fragmentation of the intermediate species, slowly growing the chain after release of the radical and trapping it again on a RAFT agent. Termination events happen in analogy to FRP, yet in a strongly decreased fashion, as the rate of transfer to the CTA greatly outweighs the rate of termination ($k_{\alpha} \gg k_t$). Thus, RAFT ideally follows a linear evolution of molecular weight with monomer consumption. Perfect control over molecular weight and dispersity requires high

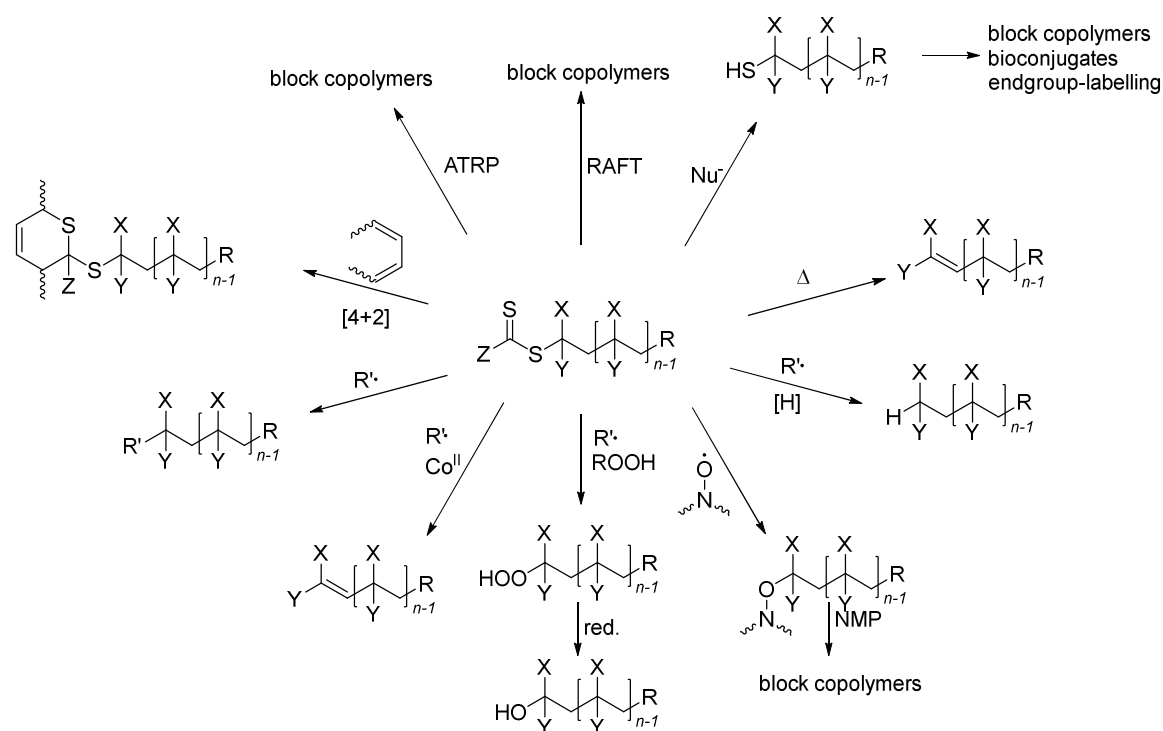
addition rates to the RAFT agent's C=S bond.^[17] The molecular weight in RAFT can be fine-tuned by the ratio of RAFT-agent and monomer, ideally following the simplified formula,^[29]

$$M_n^{theo} = \frac{X \cdot [M]_0 \cdot M_{monomer}}{[RAFT]_0} + M_{RAFT}$$

where X is conversion, $[M]_0$ and $[RAFT]_0$ are starting concentrations and $M_{monomer}$ and M_{RAFT} are the individual molecular weights of monomer and RAFT agent.^[25] The formula does not account for termination events, yet suffices to estimate satisfying starting conditions for actual experiments. In certain cases, such as when polymerising methacrylates, an initial jump in molecular weight can be observed. This so-called hybrid effect can be minimised by careful RAFT agent design.^[27] The Z-group plays a central role in regulating formation and lifetime of the intermediate species. As a key requirement in RAFT agent design, the Z-group should be chosen in a manner, where the intermediate is rapidly formed. At the same time, it needs to be sufficiently unstable to still release the propagating chain at a sufficient rate to still allow chain growth. A selection of Z- and R-groups is shown in **Scheme 2.7**, outlining their compatibility with different monomers



Scheme 2.7: Overview of Z- and R-groups and their compatibility with various monomers. Plain lines indicate good control, dashed lines indicate limited control. Z-groups: Addition- and fragmentation rates decrease from left to right. R-groups: Transfer coefficients and fragmentation rates decrease from left to right. Monomers: methyl methacrylate (MMA), N-(2-hydroxypropyl)methacrylamides (HPMAM), vinyl acetate (VAc), N-vinylpyrrolidone (NVP), N-vinyl caprolactam (NVC), styrene (St), methyl acrylate (MA), acrylamide (AM), acrylonitrile (AN).



Scheme 2.8: Possible end group modifications on the Z side. Clockwise from top left: Block-copolymerisation *via* RAFT or ATRP, nucleophilic cleavage and subsequent conjugation with enes or thiols, Thermolysis to generate alkene-terminated polymers, radically induced reduction, addition-fragmentation with a nitroxide to generate an NMP macro-CTA, radical induced oxidation with either peroxides or a cobalt-catalyst, addition-fragmentation coupling, end group-capping *via* HDA. Figure adapted from [19] with permission from ACS.

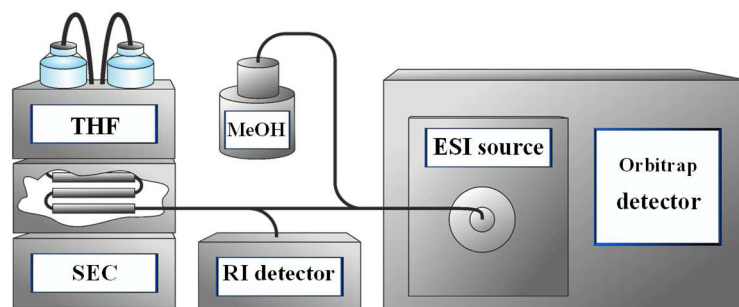
End group modifications on RAFT polymers are possible either *via* modification of a RAFT-agent's R-group, as well as *via* removal or post-polymerisation-modification of the end group.^[19] As shown in **Scheme 2.8**, the Z-group can readily be modified in (photo-) HDA reactions (refer to **Section 2.2.2**) or exchanged for ATRP or NMP chain transfer agents. Removal of the end group can provide thiols (aminolysis), hydroxyls (radical initiator aided cleavage and peroxide workup), alkenes (thermolysis), alkanes (radical induced reduction) or trapping products *via* addition-fragmentation coupling. Modifications on the initiator-side of the chain (R-group) can be introduced *via* utilisation of alkyne-, acid-, azide-, or furan-bearing R-groups among others.^[30] Sophisticated RAFT agent designs or side-chain modifications with RAFT agents on readily polymerised constructs have been demonstrated to access to a wide range of more complex architectures such as comb-, star-, or bottlebrush polymers, as well as cross-linked supramolecular structures, such as micelles or vesicles.

While offering a useful toolkit, RAFT polymerisation is also associated with some disadvantages. RAFT agents are inherently labile towards basic conditions and nucleophiles.^[27,31] Especially when dealing with long polymerisation times, high temperatures, or UV-light, experimental conditions have to be fine-tuned to circumvent degradation of the RAFT agent.^[31] Additionally, still being a radical polymerisation, RAFT is susceptible towards contaminants which can interfere with the radical process such as metals, thiols, or oxygen. Thiol-containing monomers can still be employed in the form of disulfides, and thorough preparation of solvents and reaction mixtures can avoid most of these pitfalls.^[32]

2.1.4 Characterisation

The characterisation of polymers can differ greatly from that of small molecules in a range of aspects. Traditional spectroscopic techniques rely on a certain level of isotropy and homogeneity of the analysed sample. For polymers, this is not always given, as the diffusion and rotation of individual groups is limited by their attachment to a comparatively slow-diffusing backbone. Spectrometric methods such as mass spectrometry are impaired by two additional possible issues: The molecular weight of polymers quickly outgrows the range in which typical mass spectrometers can measure samples. Sample dispersity poses another challenge in analysis. Since individual chains can differ greatly in their size, composition and the resulting chemical properties, any measurement only returns results for an analyte mixture, never for a pure fraction. To conquer these challenges, solutions to first tackle polymers by their physical parameters have been developed.

Firstly, the macroscopic nature of polymers allows for their characterisation by physical parameters. A rather simple qualifier for the nature of a molecule is its physical size or radius of gyration, when viewed as a tumbling molecule in solution. The method most commonly employed to gain insight into this feature of a polymer is gel permeation chromatography (GPC), a type of size exclusion chromatography (SEC). As the name implies, the method separates a polymer analyte by size. The dissolved polymer sample is run through a gel bed of swollen, porous resin beads. As smaller chains can enter smaller pores, they have to traverse a longer distance as they pass through a column, filled with size exclusion resin. Longer chains elute first, while shorter chains elute at higher elution times and volumes.^[8] SEC can be exploited for resolving convoluted mass spectra. Hyphenation of an injection-based MS method like ESI-MS allows for the size-dependent separation of a polymer sample prior to injection.^[33]



Scheme 2.9: SEC-ESI-MS setup for the analysis of THF-soluble polymers. The sample is separated by size on a GPC system. The resulting stream of size-resolved polymers is split into an RI- and MS detector. The RI detector enables monitoring of eluted polymer molecular weight. Prior to injection into the ESI source, the polymer flow is mixed with methanol to facilitate ionisation. Detection *via* Orbitrap detector yields highly resolved spectra.^[33]

A system like the one shown in **Scheme 2.9**, allows for the preparative deconvolution of complex sample mixtures, where molecules of different molecular weight would occupy the same portion of a spectrum in different charge states. Additionally, absolute molecular weights can be determined, by directly accessing m/z values of each elution slice.^[33] The result of an SEC-hyphenated online-measurement in comparison to a directly injected sample is shown in **Figure 2.1**.

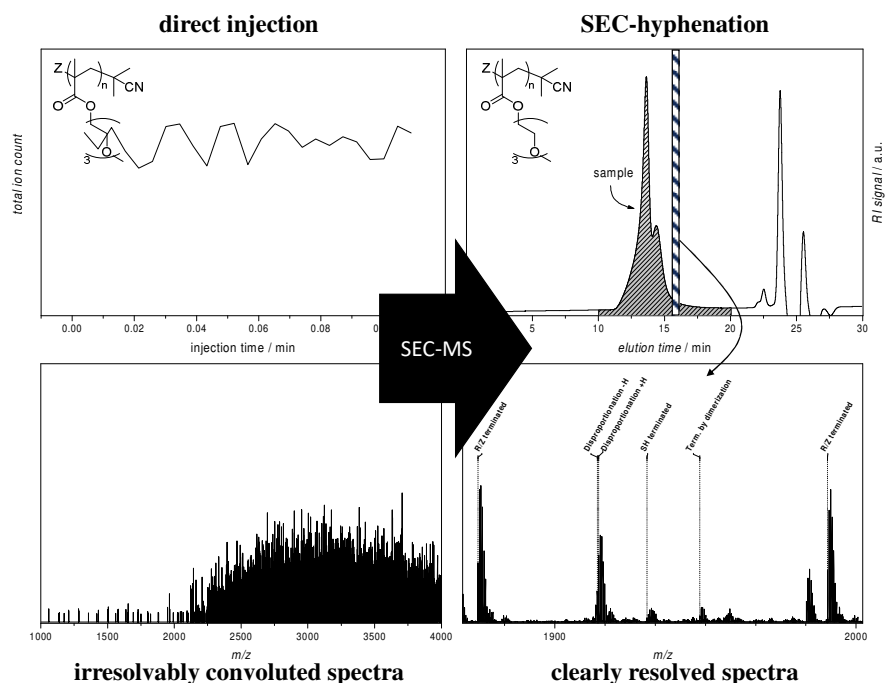


Figure 2.1: Effect of SEC-MS hyphenation. Shown are the same RAFT poly-TEGMA samples in direct injection and SEC-ESI-MS. SEC-hyphenation effectively allows for the measurement of a near-monodisperse slice of the analyte. This enables the identification of singled out isotopic patterns for each species of macromolecule present in the mixture.

As clearly visible from the exemplary spectrum in **Figure 2.1**, SEC-MS can be a powerful tool in turning cluttered, highly complex and inaccessible spectra into clear, interpretable datasets. Issues can still surface when different species in a sample possess a molecular composition of highly similar m/z as shown in **Figure 2.2**. Complications like these can either be resolved *via* elaborate analytical algorithms for evaluation or additional chromatographic methods like LC on silica or reverse-phase columns.^[34]

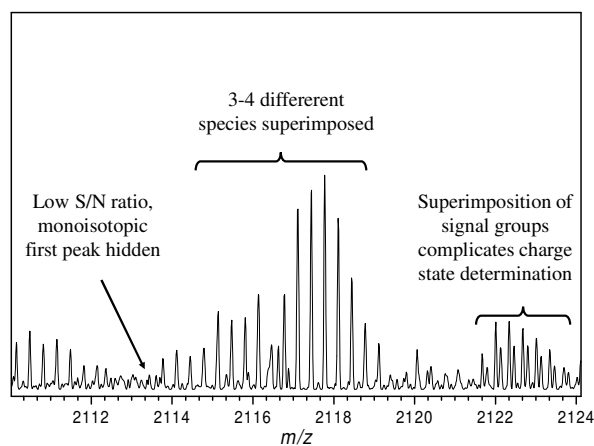


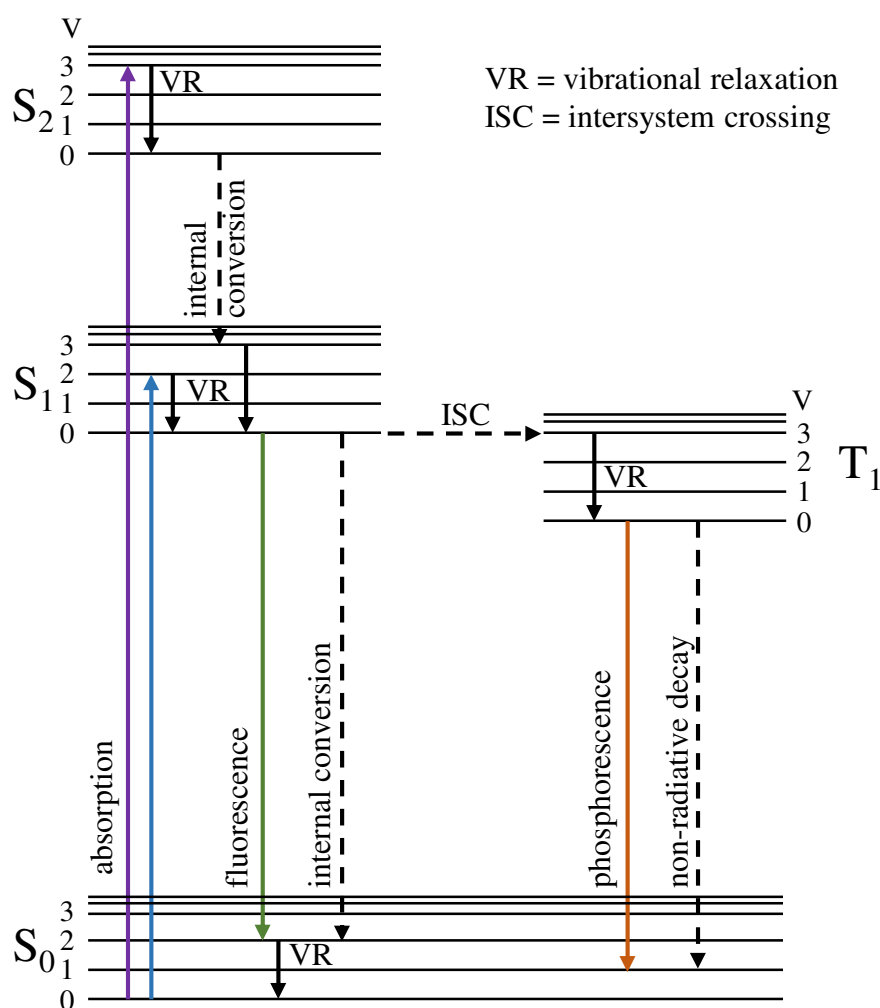
Figure 2.2: Example of a complicated copolymer SEC-ESI-MS spectrum. Overlapping signals from different chain compositions can inherently overcomplicate spectra.

2.2 PHOTOCHEMISTRY

With a constant hike in energy prices and a rising awareness for waste prevention, harnessing sunlight as a ubiquitous and near-limitless resource - as both an energy source and a reactive handle - has become more and more appealing to recent developments. Inspiration for applications of light-driven reactions can be drawn from several processes in nature. Retinal, the central compound responsible for vision undergoes an isomerisation upon irradiation, essentially converting radiation into small amounts of kinetic energy.^[35] Larger amounts of energy are converted in photosynthetic plants and bacteria. In photosynthesis, sunlight from the red and blue spectrum is harvested in large systems of chlorophylls, xanthophylls and carotenes.^[36] Here, the energy is transferred into organometallic complexes *via* electron transfer processes, and employed to split water into molecular oxygen and protons. The energy is carried in electron transfer processes, which are driving reactive cascades, storing their energy in triphosphates. These photosystems are comprised of multiple, highly defined and extremely complex protein subunits, ensuring outstanding levels of control and efficiency of catalysis.^[37] Mimicking processes like these has not yet been accomplished, but efforts are continuously being made to establish reactive toolkits driven by light. Photochemical approaches have been utilised in this thesis for both controlled ligation and release. This section will give a brief introduction on photochemical processes and introduce the photochemistries of certain enols- and acyl sulfides.

2.2.1 Overview

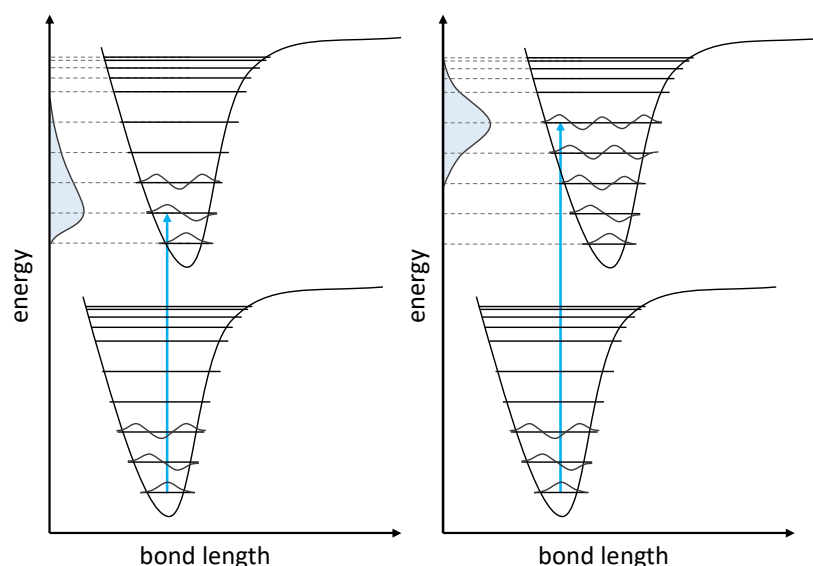
Photochemical processes rely upon the interaction of electronic systems within a molecule with incident photons. Upon absorption of a photon, a molecule can undergo various electronic transitions.



Scheme 2.10: Jablonski diagram of single-photon processes in a single molecule. Upon absorption of a photon, the molecule is excited from its ground singlet state S_0 into a vibrational ($V = 1, 2, \dots$) state of a higher singlet state. As transitions from one state to another can only occur from the individual ground state $V = 0$, higher vibrational states relax under loss of vibrational energy. From the ground state, the excited system can undergo either internal conversion (non-radiative), fluorescence (radiative), or intersystem crossing into a triplet state, from where it will either deactivate radiatively in phosphorescence or non-radiatively in a chemical reaction or another ISC.^[38]

In general, an electronic system can be described in quantised ground states. These states are characterised energy level and total spin. As shown in **Scheme 2.10**, a range of processes occurs following excitation of a molecule by a photon. Usually, molecules are

present in their ground singlet state, S_0 . Every singlet state additionally exhibits a number of quantised vibrational states. Upon absorption of a photon, an electron of the absorbing molecule transitions to an excited singlet state. Transitions between states are described by the Franck-Condon principle.^[39] Transitions can only occur from the lowest vibronic level. Vibronic levels reached in the excited state are determined by the overlap of the wave function integrals in the ground- and the target-state. The principle also provides an explanation for the shape of both absorption- and fluorescence spectra. The width of an absorption- or fluorescence-band is determined by the probability and range of vibronic levels accessible to the transition. Transitions that are more probable lead to higher intensities as shown in **Scheme 2.11**.



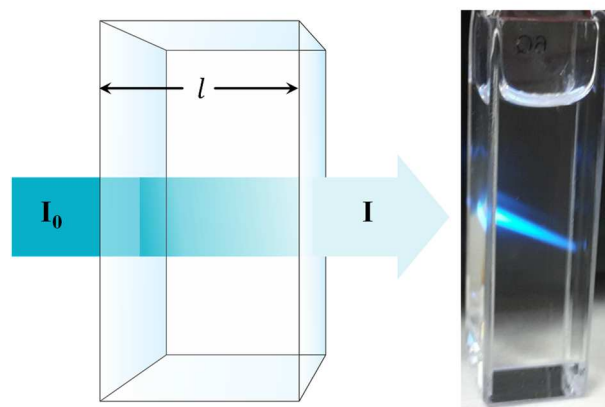
Scheme 2.11: General concept of the Franck-Condon principle. Each parabola corresponds to the Lennard-Jones potential of a ground state and an excited state. Transitions generally occur from the ground state. Probability of transition is determined by the overlap of the wave-functions of ground- and excited state. Width of the absorption bands in UV/Vis spectroscopy (indicated in blue) is determined by the probability of transitions to different states. Figure adapted from [39] with permission from the IOP.

Excited singlet states can deactivate in two different avenues. The first, fluorescence, is a radiative transition. A photon of lower energy than the incident photon is emitted as the system deactivates to a vibrationally excited level of the ground state. Alternatively, a molecule can undergo internal conversion (IC), dissipating energy as vibrational energy. If an excited state does not deactivate in either fluorescent or IC transitions, it can undergo

¹ Published under the Creative Commons License (CC-BY-3.0).

intersystem crossing (ISC). Per definition, ISC is an isoenergetic transition from one electronic state to another, where the resulting electronic state has a different multiplicity from the initial state.^[40] Similar to excitation, the resulting state is determined by wave function-integral overlap. The transition usually results in a vibrationally excited level of an energetically lower triplet state, which then deactivates to the lowest vibrational level. From there, it can either undergo radiative relaxation to S_0 in phosphorescence or deactivate through non-radiative decay. Since triplet states are long-lived and can be transferred between molecules, they are of special interest for photochemical applications. Such energy transfer allows the exploitation of a sensitizer molecule with high ISC-efficiency to access triplet states in molecules, with low ISC-efficiency.^[41] As ISC inverts the transitioning electron's spin, the transition is quantum-mechanistically forbidden and as such is typically favoured either by collision with another molecule,^[42] the presence of paramagnetic species,^[43,44] or spin-orbit coupling with heavy atoms.^[45,46]

The total of all absorption processes at a given wavelength can be macroscopically described by Beer-Lambert's law.



$$A = -\log\left(\frac{I}{I_0}\right) = \varepsilon * c * l$$

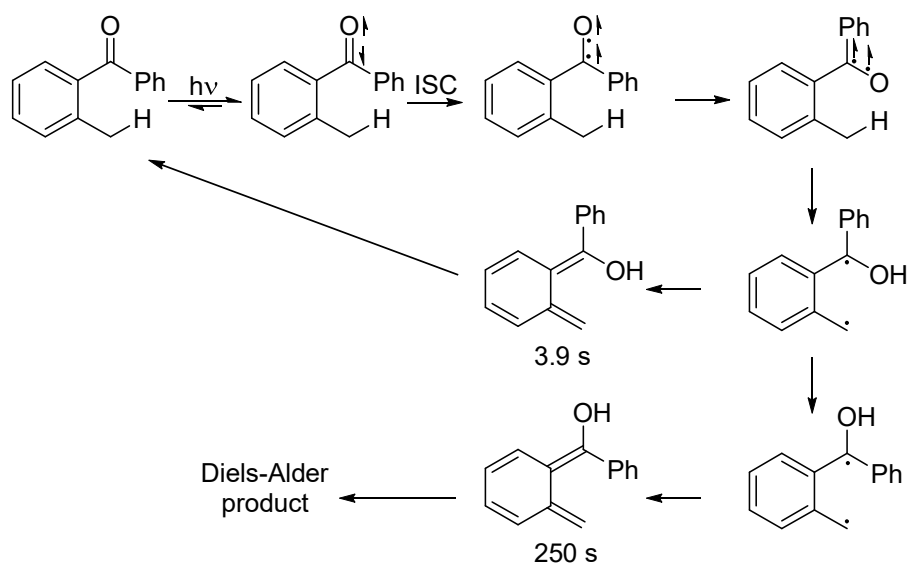
Scheme 2.12: Left: Schematic representation of the linear decrease in intensity of the incident light. Right: A solution of acetylpyrene in ACN, fluorescing in the light of a 385 nm laser beam, visualizing the decrease in intensity as light traverses the solution.

The formula in **Scheme 2.12** describes the correlation of absorbance and path length and concentration of a compound in solution. A is the absorbance, the negative decadic logarithm of transmission, described by the ratio of transmitted light (I) over incident light (I_0), ε is the molar extinction coefficient at a given wavelength, c is the molar concentration of

the analyte solution and l is the measured layer thickness. Beer-Lambert's law holds validity for analytes, where refraction is negligible and no intermolecular effects take place. A compound's ability to absorb light of a given wavelength can thus be described by ϵ , effectively enabling the comparison of two compounds by their extinction coefficients.

2.2.2 Photoenols

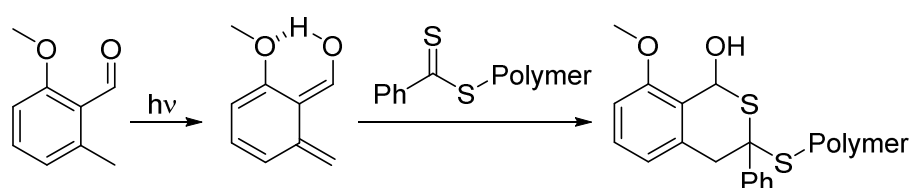
One of the photochemical approaches utilised herein is the transient generation of dienes for hetero Diels-Alder (HDA) reactions. The utilisation of light to induce the formation of a DA-active diene is a powerful tool. It allows for the exploitation of highly reactive dienes while being able to store the unreactive precursor for a long time. Additionally, it enables access to DA-chemistry in cases where one of the reaction partners is susceptible to heat, avoiding degradation or interference with thermally driven chemistry routes. Pure photochemical DA-reactions do not exist, as they would violate orbital symmetry and thus be in disagreement with the Woodward-Hoffmann rules.^[47]



Scheme 2.13: Mechanism of photoenolisation. Upon irradiation, the molecule gets excited into its S_1 from where it can cross into a triplet state. After a first rotation, a proton abstraction from the methyl group occurs, upon which the molecule can undergo either enolisation or another rotation, also followed by enolisation. The rotation step inherently leads to two different E/Z-isomers, out of which the E-isomer is longer-lived and DA-reactive.

One of the photochemistries exploited in the current work was the HDA-reaction of photo-generated dienes with the thiocarbonyl portion of RAFT end groups. The photochemical step is commonly called photoenolisation and is mechanistically demonstrated in **Scheme 2.13**. The isomerisation reaction is triggered by irradiation and a subsequent

$n \rightarrow \pi^*$ transition, which undergoes ISC to a triplet-state. Following a rotation of the carbonyl group, H-abstraction generates a biradical species, which subsequently undergoes either another rotation or a π -rearrangement, forming an E- and a Z-enol species. The Z-enol typically relaxes back to the ground state, undergoing a sigmatropic rearrangement in the process. The E-enol, being sterically favoured and highly stable with a lifetime of minutes, can subsequently react in a thermally driven DA-reaction. The rotational transitions can be exploited by trapping the unreactive Z-form *via* two-photon-absorption at 700 nm.^[48] This grants access to reaction control for applications such as sub-diffraction lithography.

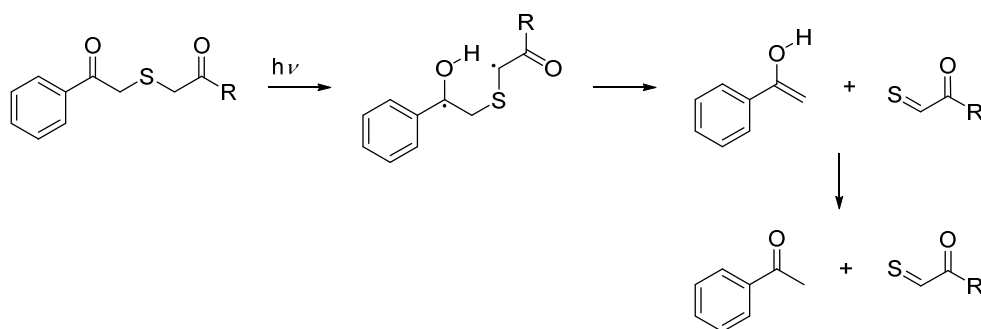


Scheme 2.14: Photoenol reaction employed for the protection of dithiobenzoate end groups. Stabilisation of the E-enol form *via* H-bonding to the methoxy-oxygen increases quantum yield of the reaction. The photo-activated diene readily reacts with thiocarbonyls in an HDA reaction.

The photoenol employed herein bears a methoxy group adjacent to the enolising carbonyl. The presence of the methoxy-oxygen enables the formation of transient hydrogen-bonds between the E-enol's hydroxyl and the methoxy-oxygen. The formation of a hydrogen-bond as shown in **Scheme 2.14** stabilises the E-conformation and greatly increases quantum yields of the reaction. The *o*-methoxy group can be utilised for further modification, turning PE into useful building block for a range of ligation chemistries. PE has successfully been employed as a reactive handle in applications such as step-growth-polymerisation in combination with RAFT macromonomers,^[49] sequence-defined polymerisation,^[50] and generation of block-copolymers.^[51] Recently, red-shifting of the photoenol has been achieved by the incorporation of sulphur as a linking group.^[52] The work presented in this thesis utilised the photoenol-group as a protecting agent for RAFT end groups to prevent nucleophilic degradation.

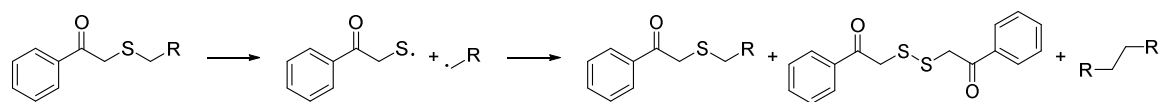
2.2.3 Photo-cleavable Arylacyl sulfides

Arylacyl sulfides provide a useful handle for both release and ligation chemistries. They have been demonstrated to efficiently form highly reactive thioaldehydes and acetophenone upon irradiation. The traditional general structure based on a phenacyl-group as the chromophore is shown in **Scheme 2.15**. Upon irradiation, phenacyl sulfide undergoes a Norrish-II-cleavage. The mechanism of the reaction is shown in **Scheme 2.15**.



Scheme 2.15: Norrish-II cleavage of phenacyl sulfide. Upon irradiation, a 1,4-biradical is formed *via* abstraction of the γ -hydrogen. Upon dissociation of the biradical, an enol and a thioaldehyde are formed. The enol rapidly tautomerises back to the keto-form.

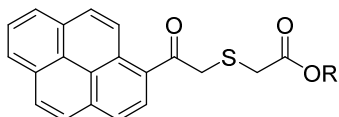
Upon irradiation, the arylketone performs an abstraction of the hydrogen producing a 1,4-biradical. The radical intermediate subsequently fragments into a thioaldehyde and an enol. The latter quickly undergoes a tautomeric shift back to the arylketone. The thioaldehyde provides a highly reactive handle for ligation reactions and readily reacts with amines and hydroxylamines to form imines and oximes, with thiols to disulfide, or with dienes to form an HDA adduct.^[53] The high reactivity of photochemically formed thioaldehydes has been exploited in the functionalisation of cellulose substrates, microspheres, 3D-microscaffolds, or RAFT block copolymers with multiple reactivities.^[54-57]



Scheme 2.16: Mechanism of β -cleavage of phenacyl sulfide in cases where no γ -hydrogen is available for abstraction.

In cases where no γ -hydrogen is available, phenacyl sulfide undergoes β -cleavage, forming two radical species, which can recombine in various ways (refer to **Scheme 2.16**). Expansion of the aromatic system has enabled access to arylaclylsulfides cleavable in the visible spectrum. Pyreneaclyl sulfide can be cleaved under biologically benign irradiation

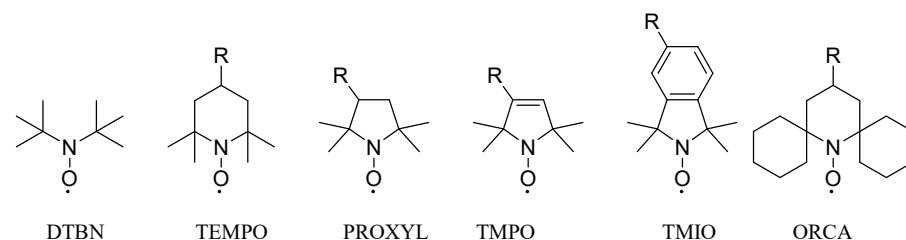
with blue light from readily available LEDs.^[53] Additionally, the pyrene chromophore retains its fluorescent attributes, even when employed as a light-harvesting group for ISC-dependent transformations.^[58] It was thus utilised as a fluorescent sensor for molecular release in the work presented in this thesis. The reactivity towards dienes was exploited to allow scavenging of the thioaldehyde as a side-product.



Scheme 2.17: Pyreneacyl sulfide, employed for polymer modification and visualisation of release in this thesis.

2.3 NITROXIDES

The term nitroxide describes a group of stable aminoxyl radicals of the general structure $R_2N-O\cdot$ (**Scheme 2.18**). Their radical structure makes them unique in the organic field. For one, the unpaired electron equips them with unparalleled reversible-redox activity.^[140] Being able to either accept or donate the unpaired electron, nitroxides can be employed in a wide range of catalytic applications as oxidative and reductive catalysts, or as chain transfer agents in radical polymerisations (refer to **Section 2.1.1**). The unpaired electron's spin also gives nitroxides unique paramagnetic properties, which can be readily detected in magnetic resonance spectroscopy (*electron spin resonance spectroscopy*, ESR), making them a useful tool in biological labelling and imaging applications.^[114,141,142]



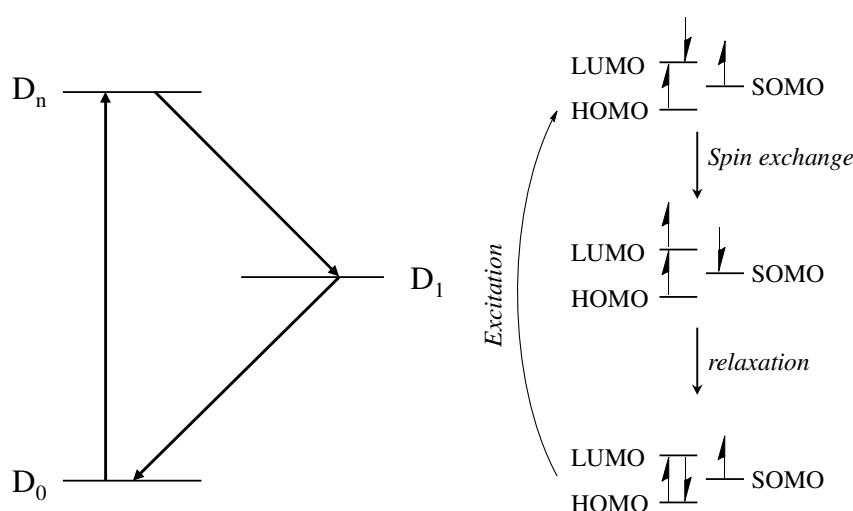
Scheme 2.18: Different types of nitroxides, typically encountered in technical or biomedical applications.

In ESR, nitroxides can readily be identified by their characteristic spectral shape. Paramagnetic resonance is subject to coupling between the electron and adjacent nuclear spins by the rule $2MI+1$. The coupling describes hyperfine coupling, which contrary to methods like NMR does not follow the signal shape rule of Pascal's triangle. Coupling between nuclear spins and the electron spin span a similar distance as NMR, with ranges of approximately two bonds in saturated, and three to five bonds in aromatic systems. In the case of nitroxides discussed, no aromatic systems are present and the radical centre is situated in proximity of only a single ^{14}N nucleus.^[143,144] The nitroxide's electron interacts with the ^{14}N -nucleus (spin $I = 1$) yielding the characteristic triplet shape in the ESR spectrum.^[143,144] The paramagnetic nature also becomes relevant in the case of NMR. When measuring NMR, the presence of paramagnetic species leads to severe spectral distortion. Effects of nitroxide proximity become readily visible by 'jagged' line shapes, and increasing radical concentrations lead to line broadening, which eventually reaches an extent, where precise determination of spectral width of a signal becomes unfeasible.^[145] NMR spectroscopic investigation of nitroxide-bearing compounds by itself is therefore not a re-

liable method on their own. In cases, where NMR spectroscopy of the compounds in question is undertaken, methods to reduce or eliminate the influence of nitroxide-borne radicals have been successfully demonstrated in the literature. One way is *in situ* reduction by ascorbic acid,^[146] pentafluorophenyl hydrazine,^[147] ⁶⁰Co-catalysed radiolysis of deuterated solvents,^[145] or Pd/C.^[148] The obvious issue with these approaches are that (i) the compound in question needs to be compatible with reducing agents, without suffering chemical alteration and (ii) the reducing agents need to be present during measurement, in order to avoid reoxidation of the nitroxide. If reducing agents like ascorbic acid are employed, they will be visible in ¹H-NMR-spectroscopy, significantly affecting the value obtained spectra, especially when employed in excess to the actual analyte. A general issue in the applicability of nitroxides is their susceptibility to light.^[92] Acyclic nitroxides are generally prone to undergo alpha-cleavage of the C-N bond.^[149] Stability has been proven to increase, if the nitroxide is either part of a rotationally locked system such as an indoline ring,^[149] or by increase of steric bulk in close proximity to the radical center.^[114,141,150] Shielding the free radical by means of sterical bulk has additionally been shown to enhance radical lifetime and reduce reduction rates in reductive environments such as biological systems.^[141,150]

2.3.1 Profluorescent Nitroxides

A feature of special interest for the works presented in this thesis, is their ability to interact with excited states in fluorophores.^[147] Nitroxides have been shown to efficiently quench excited singlet,^[151,152] triplet,^[153,154] or excimeric states both *via* intra- and intermolecular interactions on several occasions. Although the exact mechanism is still discussed in the literature, routes by which this process takes place have been proposed: (i) through electron-exchange between the excited system and the paramagnetic electron or (ii) an overlap between LUMO and SOMO orbitals and an resulting spin exchange interaction.^[155]



Scheme 2.19: Quenching mechanism *via* fluorophore-nitroxide-interaction. Nitroxide and fluorophore spins for a doublet state. After excitation spin, exchange between the now occupied fluorophore's HOMO and the nitroxide's SOMO can occur. Scheme adapted from [146,155].

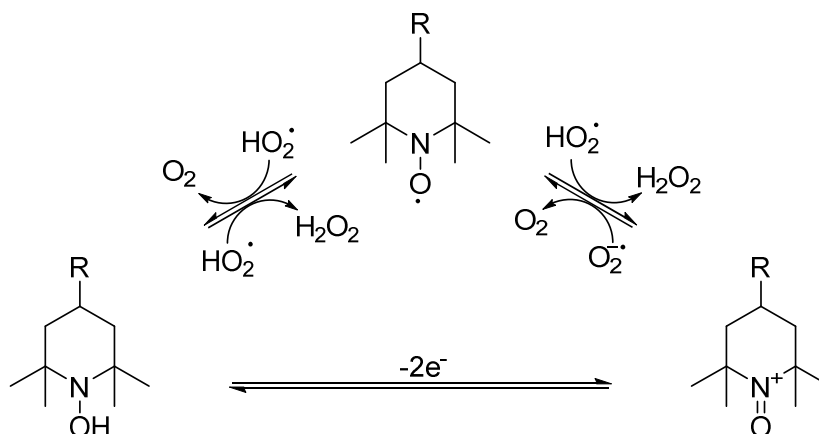
Interaction between the unpaired spin of the nitroxide and a fluorophore can be described as a doublet state as shown in **Scheme 2.19**. If the fluorophore reaches an excited state, spin exchange between the excited orbital and the radical can effectively force the excited system into a triplet state. From there, either *via* repeated interaction with the nitroxide or another collision even with a surrounding molecule, non-radiative relaxation *via* internal conversion can occur. Thereby fluorescence is effectively quenched through enhancement of an ISC-like process. Quenching efficiency in this case is dependent on two factors. Firstly, nitroxides directly incorporated into the fluorescent molecule's chromophore empirically yield the highest levels of quenching,^[58,156] which can be interpreted by

a direct intercalation of the unpaired electron's SOMO and the fluorophore's HOMO/LUMO orbitals.^[155] Additionally, the orientation of fluorophore and nitroxide are of major importance in the case of intramolecular quenching. Previous investigations have demonstrated orders of magnitude in increased quenching efficiency, in cases where the fluorophore and radical orbitals are coplanar.^[147,156] Quenching through space in collisional processes has also been demonstrated in a number of works.^[157,158] Profluorescent nitroxides have been employed in a range of sensing and reporting applications,^[114,141,147,159] making them an ideal handle for the construction of a profluorescent release reporting system.

2.3.2 Nitroxides in Biology

In biomedical applications, nitroxides are being discussed as stable agents to influence nitric oxide (NO) signalling. NO, being an extremely small and near-ubiquitous molecule, exhibits an unpaired, oxygen-centred electron, making it highly reactive towards other free-radical molecules and metal complexes such as the Fe²⁺ complex in haemoglobin.^[160] In biological systems, NO plays a crucial role in a variety of signalling pathways.^[161] NO is one of the focal responsible compounds in maintaining vascular integrity, influencing or inhibiting platelet aggregation,^[162] proliferation of vascular smooth-musculature,^[163] and endothelial adhesion of leukocytes.^[70] In addition to functions such as vasodilatory regulation, NO is one of the key signalling molecules in inflammation and inflammatory response.^[164] Playing an anti-inflammatory role under normal physiological conditions, overproduction in abnormal situations turns it into a pro-inflammatory mediator. Its simple structure and involvement in these signalling pathways has led to it being discussed as either a diagnostic or therapeutic handle in a broad range of applications, spanning (but not limited to) pulmonary diseases such as asthma, glaucoma,^[165] and tissue repair.^[160]

Usually applied in the form of pyrrolidine-, pyrroline-, isoindoline- or piperidine-derivatives, the NO-analogue nature of nitroxides is characteristically tied to a catalytic one-electron redox cycle, unlike "traditional" antioxidants, which are consumed over time.^[166] Reduction results in their conversion to hydroxylamines, oxidation yields the corresponding oxoammonium salts. Both reactions are reversible, with the hydroxylamine form still being active as an antioxidant, readily reforming the nitroxide species upon oxidation as shown in **Scheme 2.20**.^[82]

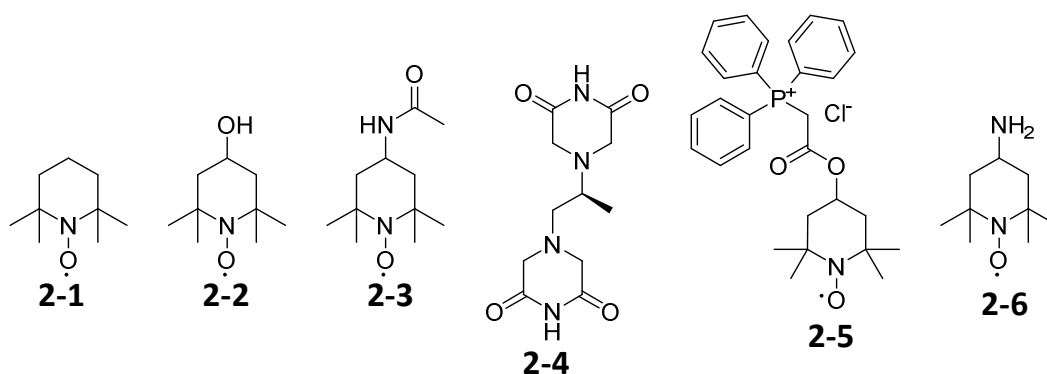


Scheme 2.20: Redox cycle of nitroxides in biological system. Reactive oxygen species are readily oxidised or reduced, giving nitroxides a superoxide dismutase (SOD)-like function.^[82]

In cancers, nitroxides have been employed to various ends. Aside from imaging applications, accessing their paramagnetic properties in MRI,^[141] signalling capabilities as NO-mimetics have been exploited to influence tumour growth,^[166] drug resistance,^[166] and delivery-routes,^[2,83] either by directly influencing inflammation levels,^[65] or the vascular environment.^[92] Furthermore, nitroxides find application in mediating oxidative stress in cancer therapy in order to reduce side effects of radiation- or chemotherapy.^[63,65] For an application targeting the EPR effect, nitroxide NO analoga could prove useful, as vascular dilation and resulting local hypertension is a common issue in many EPR-targeted applications.^[10] TEMPOL is highly biocompatible and tolerant to physiological conditions. Studies in rodent models have shown tolerances of doses up to ten-fold higher than the maximum doses required to be effective in any of the pathways discussed above.^[92,167,168]

In the context of being used as part of an assembly for drug delivery, the interaction of nitroxides and anthracycline chemotherapeutics are of special interest to the work presented in this thesis. Synergistic effects between anthracycline-derived anti-tumour drugs such as Dox, and nitroxides and their precursors have been demonstrated in the literature. Dox, a common anticancer drug, exhibits high levels of toxicity against healthy tissue, especially heart, kidney and liver.^[64,169,170] Cellular damage is caused by the generation of a semiquinone radical derivative of Dox, which interacts either directly with DNA, or with oxygen species in the surrounding solution. The latter generates a superoxide anion radical, which is converted to hydrogen peroxide by superoxide dismutase. Hydrogen peroxide subsequently takes part in a Fenton reaction, yielding hydroxyl radicals.^[166] Hydroxyl radicals induce oxidative damage to lipids, proteins and DNA. Especially cells with low antioxidant

reserves such as cardiomyocytes possess little resistance against this effect, effectively making cardiomyopathy one of the most common side-effects in Dox-based chemotherapy,^[171] Buffering the oxidative stress by combining Dox admission with nitroxides or nitroxide-precursors such as dexrazoxane has been shown to decrease cardio-, nephro- and hepatotoxic effects of the drug.^[115,163,170] A selection of discussed nitroxide and nitroxide-precursor agents is given in **Scheme 2.21**.



Scheme 2.21: Nitroxides and -precursors employed in combination with Dox. Compounds 2-1 - 2-5 have been shown to drastically decrease damage to healthy tissue, while 2-6 has been shown to increase oxidative damage as a pro-oxidant. 2-1 TEMPO, 2-2 TEMPOL, 2-3 Tempace, 2-4 dexrazoxane, 2-5 Mito-TEMPOL, 2-6 Tempamine.^[166]

Mediation of oxidative stress at the tumour site is also of significance. One of the main regulating factors in inflammatory response, NF- κ B (*nuclear factor kappa-light-chain-enhancer of activated B cells*), is also responsible for the regulation of cell proliferation and the prevention of apoptosis.^[166] An increase in oxidative stress, caused by the presence of ROS-generating drugs such as Dox, leads to the upregulation of NF- κ B, resulting in an increase in tumour proliferation. Scavenging those ROS by the incorporation of TEMPOL into micellar Dox-delivery agents has shown to increase efficacy, while decreasing oxidative damage to healthy tissue at the same time.^[115]

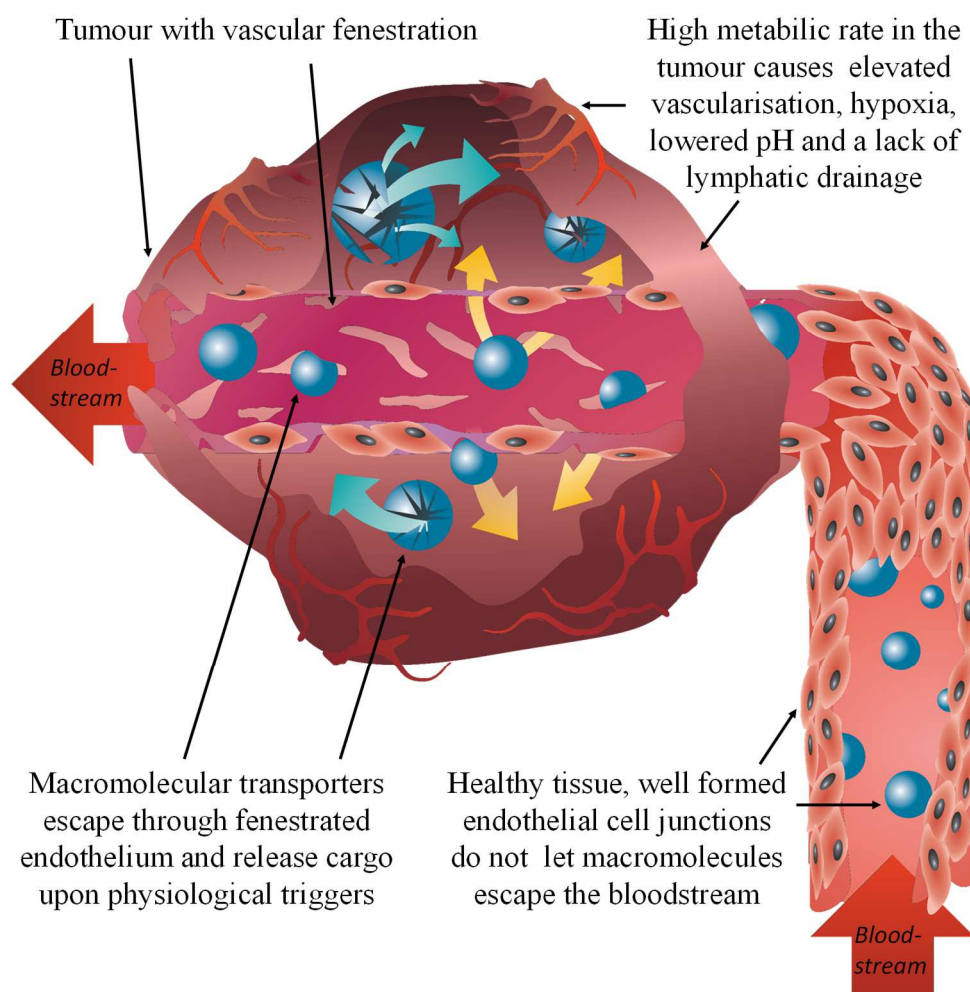
2.4 SOLID TUMOURS

The severity and persistence of cancer itself is rooted in the nature of the disease. Firstly, the term merely describes a vast range of symptoms and diseases, mostly caused by a diverse variety of genetic mutations. The superficial, physical nature of the disease already demonstrates the difficulty in classification and treatment. Forms can vary from solid, slowly growing, strongly localised tumours, oftentimes forming over years or decades, undetected and in benign ways, to fast-spreading, lethal forms, affecting remote organs at the same time. On the molecular level, finding common denominators and techniques for treatment becomes even more complex. While some tumours can be readily addressed through their genetic and ensuing molecular make-up, others elude all efforts to find a way to address them specifically. With the latter, the inherent dilemma of cancer therapy becomes readily apparent: Whilst causing harm to the organism through their altered metabolism, tumour-cells are still almost identical to healthy cells in the body. Therefore, a tumour agent, harmful or toxic to tumour tissue, is going to exhibit debilitating effects to healthy tissue in a very similar manner. As a direct result, cancer therapy is oftentimes faced with an even greater challenge than just killing the tumour – shielding the patient from the detrimental effects of the therapeutics and techniques employed.

2.4.1 Physiological Properties – the EPR effect

In order to tailor therapy to the respective type of tumour, a variety of techniques has been developed. Solid tumours can often be removed by surgery, yet this requires the tumour to be of clearly defined size and shape. In addition, the imminent risk of injury and infection, as well as long term risk of metastases in different and new tumour sites has to be ruled out for surgical approaches to suffice.^[59] Radiotherapy with ionizing radiation, phototherapy with intravenously applied singlet oxygen photosensitisers^[60,61] or photoactive nanoparticles^[62] and light irradiation decrease the therapeutic level of invasiveness. Regardless, they are either oftentimes burdened with high levels of secondary damage (radiotherapy)^[63] or hindered by inaccessibility of the tissue (photodynamic therapy).^[61] The novel assemblies presented in this thesis were aimed at possible applications in targeted chemotherapy.

Chemotherapy, usually administered intravenously is burdened with side effects such as organ damage, stem cell damage or secondary carcinogenicity.^[63–66] In order to overcome the issue of specificity, two major fields of targeting exist. Active targeting covers conjugated antibodies,^[67,68] targeting specific cellular structures such as membrane proteins overexpressed in tumour cells,^[68–70] signalling peptides or recognition sequences,^[71,72] guiding conjugates to specific organs or subcellular structures. Passive targeting can be achieved *via* an increase in circulation times and exploitation of the enhanced permeation and retention effect (EPR).^[73,74]



Scheme 2.22: Enhanced permeation and retention in a tumour is caused by physiological conditions in the tumour. Elevated proliferation rates of cancer cells elevate the demand for oxygen and nutrients. As a result, vascularisation with angiogenic blood vessels, bearing defective endothelia (fenestrations) is elevated, allowing extravasation of blood-borne macromolecular assemblies into the tissue. A lack of lymphatic drainage effects a decrease in clearance from the tissue, allowing longer dwell times of macromolecules in the tumour and thus effectively increasing the timeframe to either enter the cells or release cargo.

In short, the EPR effect as shown in **Scheme 2.22** is governed by two major physiological phenomena, abnormal vascularisation and lymphatic drainage. A significant upregulation of vascular endothelial growth factor (VEGF) in tumour tissue has been identified as the main cause for angiogenesis and elevated vascularisation.^[75,76] Being one of the most commonly encountered phenomena, it has been detected as soon as tumour sites reach diameters of 0.2-1 mm.^[10,77] The vessels formed in the course of this exhibit defective endothelial cells of irregular alignment, lack of smooth muscle and innervation as well impaired angiotensin-II receptors.^[10,78,79] As an immediate consequence of this, tight junctions between endothelial cells exhibit imperfections, allowing molecules of over 40 kDa to extravasate the bloodstream into the tumour.^[80] The molecular weight of 40 kDa marks a critical value for effective targeting, as it additionally increases circulation duration by a decrease in renal clearance.^[80] The second phenomenon – retention in the tumour – is caused by insufficient lymphatic drainage. In healthy tissue, the lymphatic system is responsible for clearing compounds from the interstitial space and regulating intercellular pressure. In rapidly growing, disordered tumour tissue, lymphatic structures do not form correctly and macromolecular or lipid-based drugs are retained in the interstitial space for a longer timeframe.^[81,82]

While posing a promising handle by which to tackle cancer therapy, a number of factors need to be considered when trying to utilise EPR for targeting and delivery.^[83] While being a feasible approach in many cases, it is yet subject to adverse effects and cannot be considered a universal treatment. Heterogeneous supply and distribution in the tumour, owed to chaotic organisation of blood vessels and resulting variations in blood pressure make homogenous application of drug conjugates a difficult task.^[84,85] The lack of lymphatic drainage, while helping with retention, can also lead to increased interstitial pressure, resulting in a decrease of blood-to-tissue diffusion.^[86] Especially in rapidly expanding tumours, growth can induce pressure and vascular constriction, inhibiting blood flow and thus drug-distribution.^[87] Lastly, tumour tissue tends to exhibit excessive production of ECM material up to signs of fibrosis as a result of elevated rates of formation and proliferation of cancer-associated fibroblasts (CAFs).^[88]

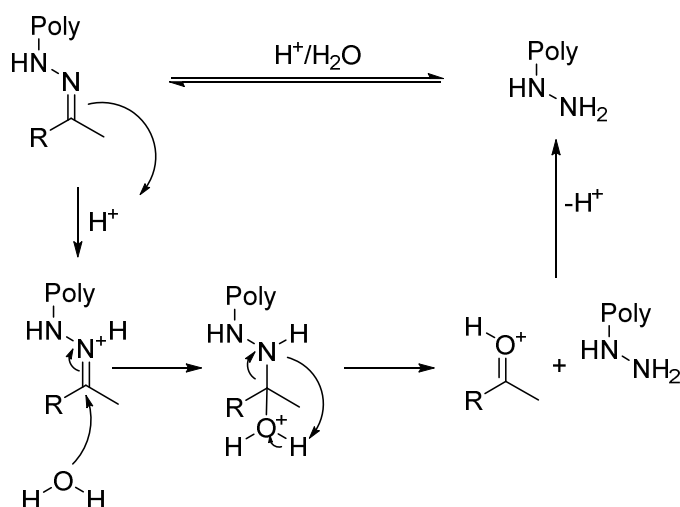
In the literature, techniques by which to overcome these factors have successfully been demonstrated. While being highly dependent of overall physiological factors in the patient's health, a wide range of tools can be applied in order to gain greater benefits from

EPR. The administration vasoconstrictors has been shown to yield elevated levels of tumour permeation, by inducing hypertension in patients.^[84,89] Overall blood pressure can be induced in this way, allowing to counter possible overpressure in tumorous tissue, as blood vessels tend to lose their ability to respond to external vasoconstrictors.^[90] For obvious reasons this technique is only suitable for patients not already affected by hypertension and therefore not applicable in every demographic. As an alternative to vasoconstriction, vasodilation and the application of vascular extravasion agents can greatly enhance vascular permeation into the tissue. The local application of botulinum neurotoxin A has shown promising results, by inhibiting neurogenic contractions of the tumour vasculature, enhancing blood supply and tissue permeation.^[91] NO-mimics and -precursors such as nitroxides and their secondary amine analogues have been shown to act as vasodilating agents, which upon application trigger an elevation of blood supply to the tumour, resulting in elevated drug circulation and EPR in the tissue.^[85,92] Kinin, an extravasion-mediator in inflammation and inflammatory tissues, or nitroxides can enhance uptake into the tissue by upregulating NO-synthase in the tissue, resulting in vasodilation and enhanced permeability of the tumour.^[85,92] As the approach towards a novel building block presented herein incorporates nitroxides as part of the envisioned reporter system, the latter is eventually going to become of central interest in delivery effectiveness.

2.4.2 Release and Reporting Strategies

After successful delivery to the tumour site, controlled release is a crucial step. A variety of strategies have been described to date and shall be discussed in brief. Most established techniques from the literature build on different factors in the tissue. Caging of a drug in a macromolecular assembly can in general be achieved by two avenues. On the one hand, the dispersion of a drug in liposomes,^[68,93,94] hydrogels,^[95–97] capsids,^[98] or hollow spheres^[99–101] allows for high drug loading. Two of the most commonly encountered examples for a drug like this are DOXIL® and Myocet®, liposomal formulations for the delivery of Dox, reducing cardiotoxicity and off-site effects.^[102,103] Additionally such assemblies enable the co-delivery of multiple agents, i.e. the combination of a chemotherapeutic and a mediator for oxidative stress.^[94,104,105] Release strategies for systems like this comprise physiological triggers such as pH,^[106,107] redox response,^[108] membrane fusion,^[109] as well as enzymatic erosion,^[95] or external stimuli such as light,^[110] or oscillating magnetic fields^[111] to fragment magnetic nanoparticular assemblies

A more defined strategy to construct macromolecular drug-carriers is the direct conjugation of a chemotherapeutic to a polymer backbone. These linkages are typically responsive to physiological triggers such as pH,^[93,112,113] or redox-processes,^[114–116] The process targeted in the current thesis was the pH-triggered release from linear polymer backbones. The strategy successfully established herein entailed the hydrolytic cleavage of hydrazones. Hydrazones have been known to drug release strategies for decades and are an established tool in drug release systems, both *in vivo* and *in vitro*.^[117] The linkage is known for facile synthesis routes as soon as hydrazides are successfully incorporated into the carrier backbone.^[118]



Scheme 2.23: Mechanism of hydrazone cleavage. The bond is formed in an equilibrium reaction. If water is withdrawn from the reaction, stable hydrazone bonds are formed. In the presence of excess water, the bond is near-quantitatively cleaved.

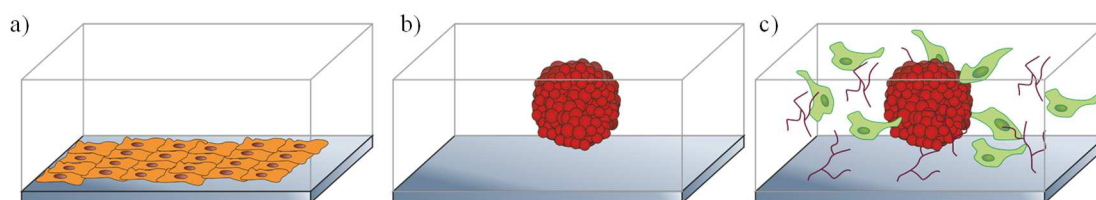
The mechanism of hydrazone-triggered release is shown in **Scheme 2.23**. Hydrazones form from hydrazine and carbonyls in the presence of weak acids. When performing the reaction in organic solvents and in the presence of a drying agent, stable hydrazones are formed. The bond can readily be hydrolysed at close to pH = 5. In aqueous solvents and sufficient volumes, release occurs rapidly and quantitatively.^[117]

2.4.3 Tumour Modelling in Spheroids

Traditionally, drug design follows a standardised path: As soon as a drug or drug assembly is sufficiently characterised, compounds are tested in cell culture. Usually, a range of cell lines is chosen for this process, ideally mimicking the targeted tissue, as well as other tissue types the drug will be expected to come into contact with, such as heart, liver, or kidney in the case of intravenous application. These initial tests are to ensure a maximum level of compatibility between the exposed tissue and the compound in question.^[119] An issue with this approach is that an actual organism will react in ways far more complex than a single type of cells, grown in a two-dimensional manner. Another issue manifests in the basic geometry of 2D cell cultures: As incubation with compounds in solution is carried out in a volume significantly larger than that of a two-dimensional layer of cells, concentration effects cannot be extrapolated to actual three-dimensional tissue. Real tissue additionally communicates stress to its surrounding - in certain cases even remote - tissues, causing inflammatory response, altered cellular uptake, or highly detrimental effects such as chaotic immune response or apoptosis.^[120,121] None of these effects can be extrapolated from simple 2D models of only a single cell type. In order to obtain a more lifelike image of what a drug will effect in a patient's body, compounds are transferred into the mammalian model. Initially utilizing rodent models, later animals with a closer genetic relation to humans, such as pigs or primates, are performed to evaluate the effect of a compound on a living mammal.^[122] Animal testing in this manner has recently come under heavy criticism, due to a number of issues.^[123,124] Test subjects traditionally have to be sacrificed as soon the tests have been carried out, posing a serious ethical question. Especially in tests, which will not directly lead to the development of an actually applied drug, their rationale has to be critically evaluated.^[124,125] In many cases, animal models have proven to be significantly less representative than initially intended. The reasons for this are vast and oftentimes unpredictable: different organisms respond differently to either pathogens,^[126,127] or treatments,^[128] with variations frequently even occurring inside the same species.^[129] A way to alleviate this recurring problem is the construction of more lifelike tissue- or even organ models.

The emergence of 3D cell culture for compound testing potentially marks a new era in preclinical trials, as it fills the gap between basic 2D *in vitro* experiments and full organisms. With the emergence of 3D cell culture in solution or hydrogels, and 3D-printed tissue scaffolds, a number of avenues to access more informative culture-testing have become

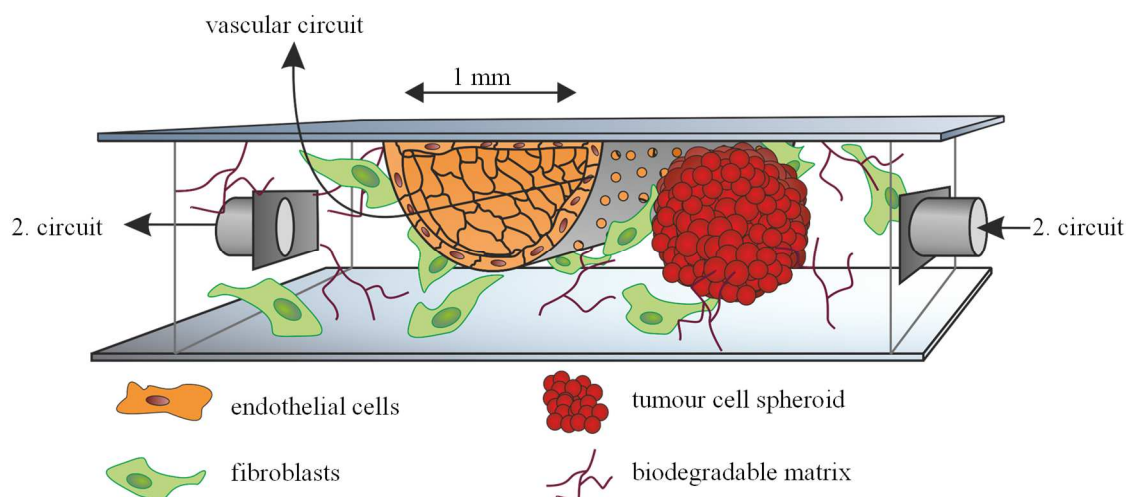
available.^[121,130,131] The 3D cell culture employed in the current thesis revolved around spheroids (**Scheme 2.24**). Generation and handling of spheroids can be carried out in a number of ways, in general following protocols quite similar to those for traditional 2D cell culture.^[132,133] For the spheroids used herein, cells are grown in complex media, passaged according to their ideal lifecycle and re-cultured on an agarose coated surface.^[130] The resulting, spheroidal cell clusters range from a few connected cells to large assemblies of multiple millimetres in diameter.^[134] Even though comparatively small in size, the spheroids exhibit key characteristics of tumour tissue, which cannot easily be reproduced in a two dimensional culture. Bordered by few layers of rapidly proliferating, active cells, the inner regions of a spheroid resemble under-vascularised inner regions of a tumour. With growing distance to the surrounding media, the supply in oxygen and nutrients grows scarce. As a result, many of the cells start switching over to anaerobic metabolic pathways, slowing their overall metabolism and ultimately entering apoptosis.^[130,135,136] This has a direct result on the molecular composition of extracellular matrix of the inner areas. Hypoxic conditions effect a decrease in pH, apoptotic cell degradation results in an increase in oxidative stress and inflammatory signalling. All of these phenomena lead to the formation of a necrotic core of very little metabolic and mitotic activity, akin to the inner areas of a tumour.^[106,135]



Scheme 2.24: : Schematic representations of 2D and 3D cell culture systems: a) 2D cell culture, a monolayer of cells grown on a flat surface, b) free floating spheroid of cells in solution, c) a co-culture of a spheroid (red) with fibroblasts (green), grown in a three-dimensional matrix of biocompatible hydrogel (violet).

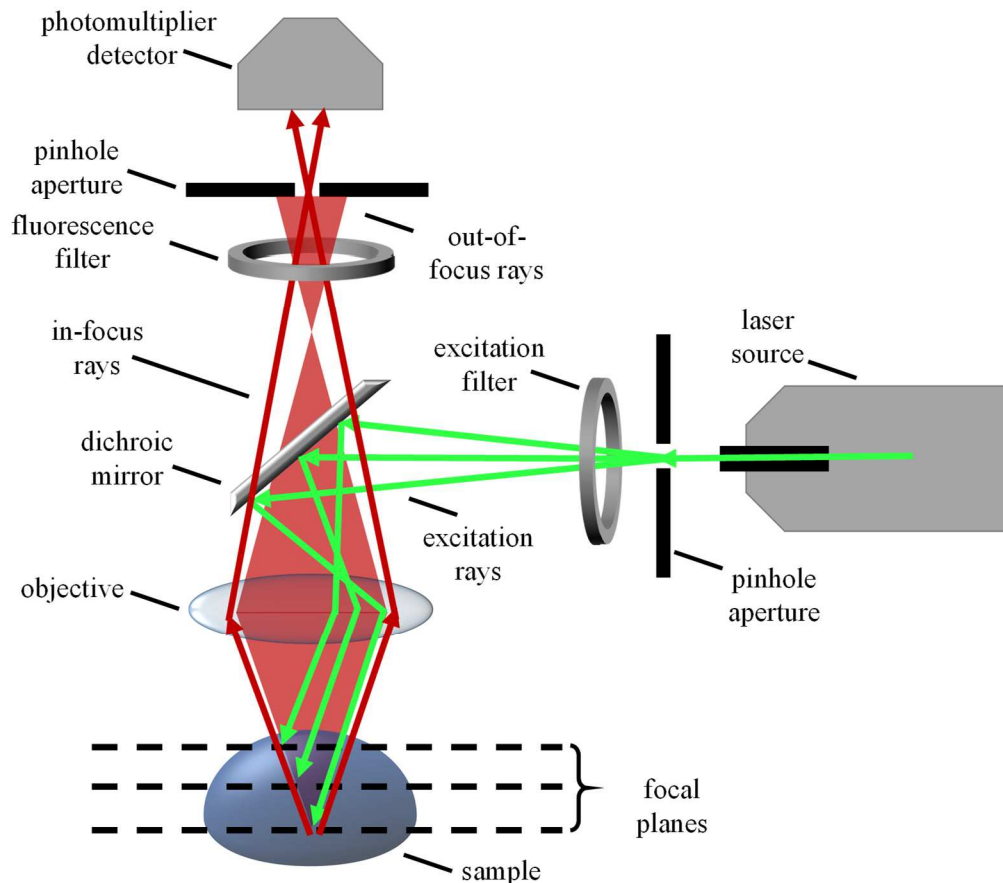
Contrary to real cancerous tissue, these microscale cell assemblies can easily be studied. The small diameter grants access to a wide range of imaging techniques, from simple total fluorescence investigations, to complex histological sections. As spheroid growth and incubation can be automated, both incubation and evaluation can readily be performed on a high throughput scale.^[132,133] As gradients of pathogens, nutrients and signalling compounds are formed in a similar manner to real tissue, intercellular communication can be established. The latter is crucial for the representation of real-life tumour behaviour: In

many cases, where cancer prevailed after seemingly successful chemotherapy, the recurring metastases and the surviving tissue showed drastically elevated resistance to the previously effective therapeutics.^[137] Results like this could be reproduced in spheroidal models, where combination cultures were fused from previously exposed spheroids and fresh untreated spheroids.^[138] Incorporation of a spheroid into larger, more diverse co-cultures extends signalling to another dimension.^[62] If co-cultured in a matrix seeded with fibroblasts or endothelial cells, the culture can profit from signalling and total interaction.^[139] Co-cultures investigated for the testing of polymeric drug-carriers in this thesis are comprised of a spheroid, embedded in a matrix of cross-linked collagen as depicted in **Scheme 2.24**. The matrix co-hosts fibroblasts to simulate a lifelike environment. 3D co-cultures of this kind can be embedded in microfluidic reactors/chips to add more features, mimicking real organisms.



Scheme 2.25: Representation of the 3D-microflow reactor in which polymeric assemblies will be tested. A 3D co-culture of spheroids and fibroblasts is grown around a semi-tubular, porous polycarbonate channel. The channel is cultured with endothelial cells, effectively mimicking a fenestrated blood vessel passing through a tumour. Samples for bio-testing can be supplied *via* the vascular circuit, simulating *in vivo* application of therapeutics. Image modified from [139] with permission from WILEY-VCH.

The final assembly to be employed in the work herein is depicted in **Scheme 2.25**. The co-culture is sandwiched between glass slides to enable direct on-line imaging. Tumour-like vascularisation is achieved by the incorporation of a micro-fabricated porous channel into the co-culture's matrix. The channel is in turn coated with a confluent culture of endothelial cells, enabling a simplified reconstruction of real tumours. The reactor setup has successfully been demonstrated to be applicable for nanoparticle-testing and delivery of small molecules. Here, it is intended to simulate the EPR effect (refer to **Section 2.4.1**).



Scheme 2.26: General setup of a confocal laser-scanning microscope (CLSM). Exciting light is provided by a laser source in a monochromatic and directional manner. The sample is reflected on a movable dichroic mirror, scanning the sample as the image is acquired. Fluorescent light enters the detector through a pinhole, which emits out-of-focus light, allowing the imaging of depth-defined planes of the sample specimen.

Optical investigation of cell cultures is carried out by confocal microscopy. A microscope setup as shown in **Scheme 2.26** allows the acquisition of depth-defined images. Sample areas outside the focus plane are omitted, allowing the precise spatially defined observation of processes in the sample. The technique enables the observer to see past structures situated around the region of interest (ROI) as long as both incident and exiting light can sufficiently penetrate the sample. The technique is of special interest for fluorescence microscopy (*confocal laser scanning microscopy*, CLSM). Observing a single plane allows to judge and compare fluorescence of an ROI in a quantitative manner, as diffracted light from areas outside of each individual ROI does not influence the investigation.

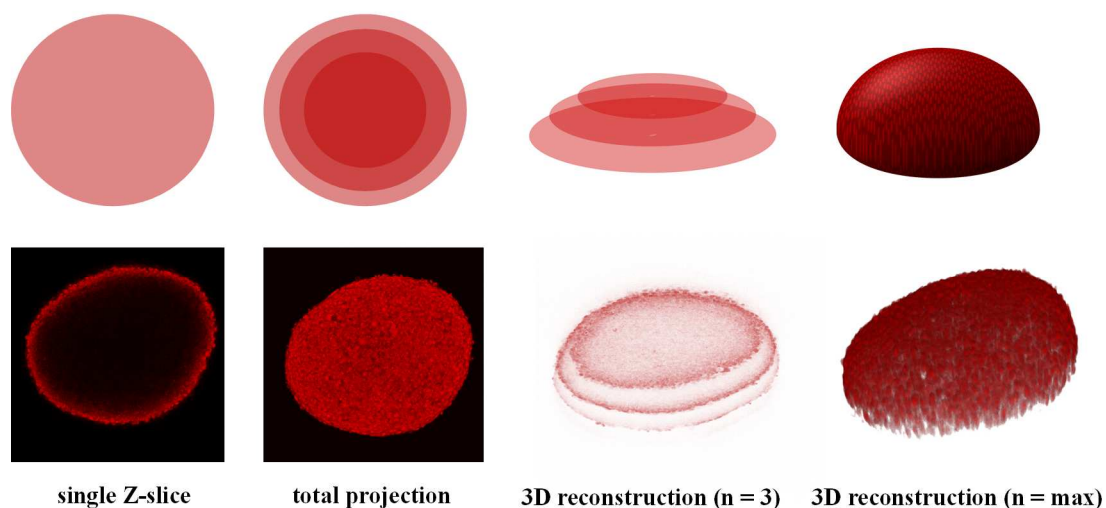


Figure 2.3: Schematic representation (top) and CLSM fluorescence images (bottom) obtained in confocal imaging of 3D cell culture. Single confocal images (Z-slices of 5-10 μm thickness) are recorded across the full depth of a sample. Slices can subsequently be concatenated into Z-stacks to yield either 2D or 3D representations of the imaged sample.

In thick samples such as histological sections or 3D cultures, the method can be exploited to generate precise three-dimensional reconstructions or representative projections of the sample (**Figure 2.3**). Individual images, acquired along the depth (Z-) axis of the sample are acquired and aligned in X/Y orientation, yielding a set of optical tomographies of the sample. Simple addition of these Z-slices yields total projection images, useful for both presentation and evaluation of sample parameters like area, density/distribution, or total fluorescence/luminosity. Since both slice-height and slice-spacing are defined acquisition parameters, 3D reconstructions of the sample can be performed by aligning acquisitions along the Z-axis. This allows both spatial representation as well as quantitative assessment of three-dimensional processes and features like direction-dependent tissue growth or molecular diffusion.

Confocal imaging was utilised to study the performance of a novel prodrug presented in this thesis. In addition, it allowed the successful refinement of methods for the assessment of drug penetration into tumour spheroids.

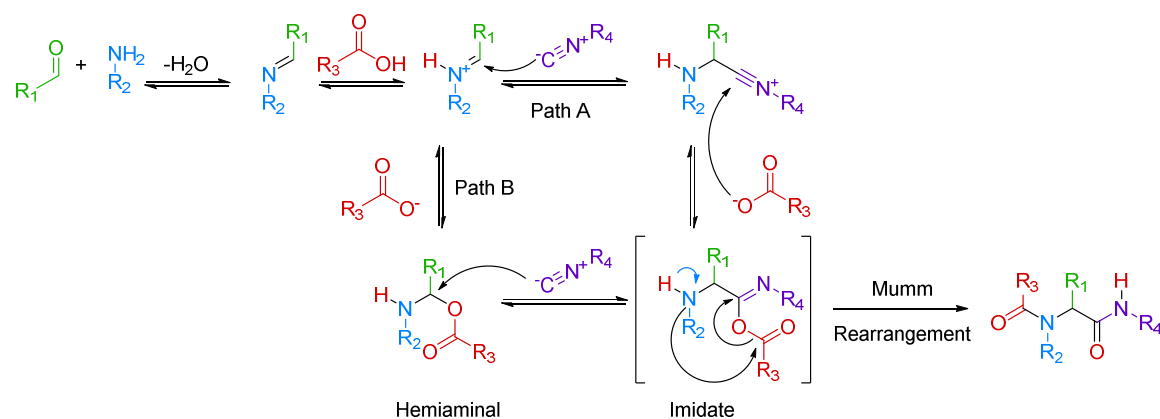
2.5 MULTICOMPONENT REACTIONS

A useful tool in the synthesis of complex polymeric architectures as presented in this thesis was the utilisation of multicomponent chemistry. Many traditional chemical methods predominantly revolve around the conversion of one moiety into another. Such approaches rely on demanding synthetic pathways or long sequences of chemical modifications. Processes like these are potentially burdened by low-yielding steps, either involving low-yielding chemical transformations due to the inherent nature of the reaction or tedious and complex purification steps. Especially in cases where different reactive groups in one molecule are present, these traditional approaches are faced with another issue: A lack of orthogonality and insufficient accessibility of different reactive groups asks for either intricate protection/deprotection strategies or highly specific catalysts. These can limit the available chemical toolkit and turn a seemingly straightforward approach into an unfeasible endeavour. When working with polymers, issues such as the formation of by-products or incomplete conversion accumulate rapidly. Traditionally the high purity of synthons along a planned synthetic route is ensured by removal of side-products, starting materials and reactants before any incompatible subsequent modification. In the case of sequential regioselective modifications of a polymeric system, this strategy cannot be universally adopted. A single polymer chain can easily bear a multitude of reactive groups. Partial conversion will inevitably carry imperfections through the entire synthetic process, oftentimes rendering certain synthetic pathways wholly inaccessible. Multicomponent reactions offer an elegant way to tackle this issue.

The elegance of multicomponent chemistry is rooted in the significant shortening of synthetic pathways on one hand, and high atom economy on the other hand. Multicomponent reactions (MCR) allow the coupling of different molecules in a single step. The products are formed in a defined fashion. In the case of MCR on polymers, the macromolecular nature of polymers can be exploited to facilitate purification. Polymers can readily be separated from small molecules *via* precipitation and size selective techniques such as SEC and dialysis. Thus reaction yields can be forced to high levels by adjustment of stoichiometry, without risking an over-complication of purification.^[8]

Discovered in 1959 by Ivar Karl Ugi as an isonitrile-enhanced Passerini reaction, it is one of the most widely known and most commonly used MCRs.^[172] It gained increasing popularity with the surfacing of combinatorial chemistry in the 1980s for the synthesis of large compound libraries. It offered a possibility to replace precisely plannable, yet lengthy

sequential two-component approaches for statistical, preparatively short multicomponent approaches.^[173,174] The Ugi reaction is a four-component reaction, forming a pseudopeptide from a carbonyl, an amine, an acid and an isocyanide. Initially considered to follow an ionic mechanism as a series of equilibria, the reaction mechanism has recently been revisited and proposed to follow an alternative route, where the isocyanide is inserted in a hemiaminal. Either way, the mechanism involves a Mumm-rearrangement,^{[175],[176]} driving the reaction equilibrium towards the product, as it poses the last and irreversible step.



Scheme 2.27: Proposed mechanisms for the Ugi reaction. Path A was initially proposed by Ugi, based upon the observation that the reaction proceeds faster in polar solvents. Path B has recently been proposed, based upon molecular simulations.^[177]

The mechanism as shown in **Scheme 2.27** relies on a sequence of equilibrium reactions. First, an imine is formed from an aldehyde and an amine. Experimentally it has been shown that purifying the imine at this point can improve yields.^[178] The imine reacts with an isonitrile and an acid to form an imidate, which subsequently undergoes a Mumm rearrangement. The exact mechanism, forming the imidate, has yet to be elucidated.^[177] A modification of the Ugi reaction, known as the Smiles-variant, has been published using phenols or amines as a replacement for the carboxylic acid.^[177] A wide palette of applications of Ugi-reactions has been published in the recent literature. Most of them exploit the great suitability for the generation of large libraries for applications such as drug discovery,^[179] the facile synthesis of monomers for functionalised polymers,^[180] molecular cryptography or steganography,^[181] or access to synthetically complex structures such as functionalised spiroindolines.^[182] In this thesis, the Ugi reaction has found an application in the immobilisation of a fluorophore/quencher pair on benzaldehyde side-chains of a RAFT polymer (refer to **Chapter 4**, page 107).

3

A Polymeric Nanocarrier for the Visualisation of pH-Triggered Release

Substantial effort has been invested into polymeric drug delivery systems and a wide range of literature-known material has found applications in modern medicine. The range of available platforms include simple PEG-conjugates,^[183] linear polymer assemblies with sidechain-loading, branched,^[32,184] or cross-linked architectures,^[32,71,184] drug-conjugates to modified proteins,^[185,186] and complex supramolecular constructs such as micelles or vesicles.^[68,187–189] Carrier architecture mostly depends on the targeted properties.^[190] Aliphatic backbones such as (meth-)acrylate or acrylamide typically provide high resistance to hydrolysis and enzymatic degradation.^[95] Their advantage, especially for large-scale applications, manifests in their compatibility with a wide range of chemical procedures and conditions, as well as commercial availability of monomers and facile chemical accessibility for modifications.^[95] As a drawback, they have been shown to aggregate in the organism, which oftentimes can have adverse or even toxic effects, especially over long term exposure or high dosage, and can only be cleared renally. Polyesters such as water-soluble polycarbonates or peptide backbones,^[191] from either (pseudo-)peptides,^[192] or template proteins,^[185,186] generally solve this issue. Their persistence in living tissue is usually limited by the rate of hydrolytic breakdown in the organism, leading to decreased circulation times and therefore potentially low efficacy. Supramolecular assemblies are often ridden by stability issues, low levels of specificity and – especially for demanding applications – complex and work-/cost-intensive analytical methods to ensure reproducible results.^[95]

Effective loading and release has been demonstrated to be achievable through a wide range of approaches too: pH-responsive linkages like hydrazones,^[113,184,193] recognition sequences for enzymatic cleavage,^[72] redox-responsive bonds such as disulfides or encapsulation in supramolecular structures,^[32] which disperse upon exposure to an external trigger have shown success over the course of the last years.^[106]

3.1 MOTIVATION AND STRATEGY

Even though substantial progress has been made in the field drug delivery, one field remains widely untouched in relation to the vast volume of published delivery and release strategies: Reporting and quantification of release can rarely be achieved in real time.^[114,141] Investigation of targeting-success is usually monitored by tracking the assembly itself, yet quantitation of the release efficiency at the site of action is rarely taken into account. Studies into release usually require off-line methods such as surgery and microscopic investigation of histological samples, or proteomic approaches from tissue- or perfusion. The overarching aim of the current thesis was to develop a system capable of carrying all aspects mentioned above. It should follow a precise and reproducible synthetic strategy, bind, deliver and release a drug in controlled fashion, exhibit properties by which tracing of the assembly should be possible, loaded or not, and lastly report an analytically readable signal upon drug release. The novelty of the last two factors lies in the timeframe, at which these properties should become relevant. The envisioned system should enable tracking and reporting in real time, in an unprecedented fashion.

Selection of the polymer backbone fell on methacrylates and methacrylamides. The determining features lie in their availability and ideal compatibility with reversible deactivation radical polymerisations. RAFT was chosen as the ideal technique to obtain defined polymer structures, for three reasons. Firstly, RAFT-polymerisation of MAs and MAAs has been studied extensively and a wide array of conditions is available to date.^[194] Secondly, the technique itself promises great levels of control over chain-length, -composition, and dispersity, the most fundamental physicochemical properties of a macromolecule for bio-applications.^[17] Thirdly, chain transfer agents for RAFT polymerisations offer end groups, which can be modified individually either *a priori* or post-polymerisation.^[19,30,195] The latter becomes an interesting feature if additional targeting, signalling or tracking handles should be incorporated in addition to the release-reporting moieties.^[71]

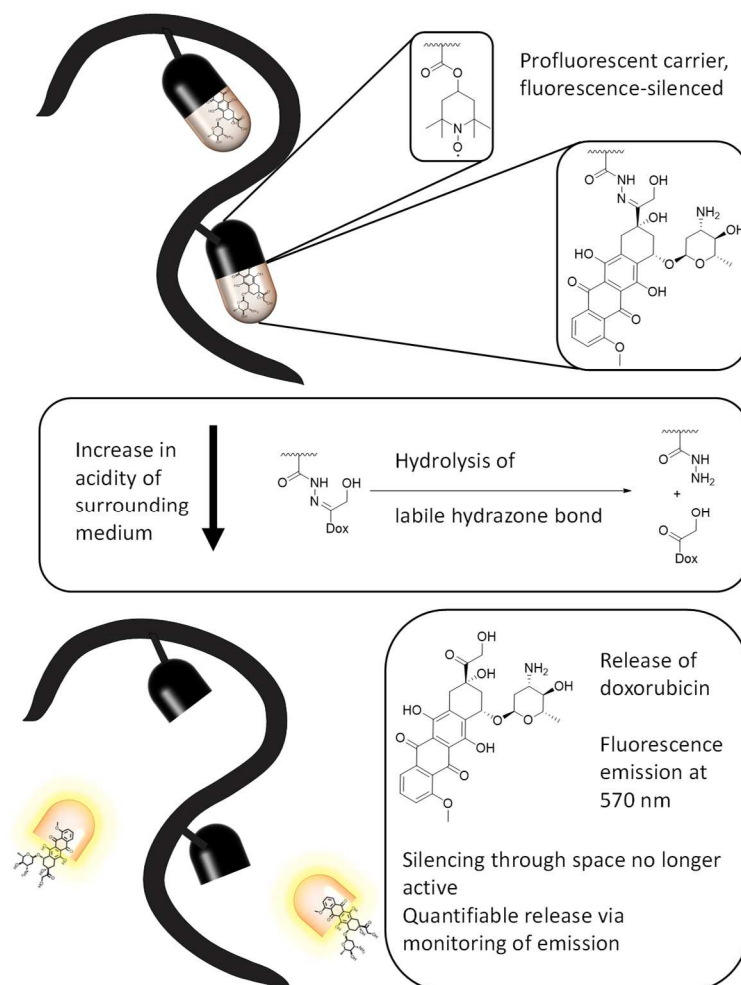
Monomers need to be selected with respect to the individual properties of the resulting polymer. First, good solubility aqueous systems at physiological conditions is critical. As a methacrylate backbone *per se* is not compatible with aqueous systems, solubility has to be achieved by the incorporation of water-soluble sidechain moieties. The literature offers a wide range of hydrophilic to (poly-)ionic solutions,^[196–198] yet many of them are inherently difficult to handle in organic solvents and thus highly problematic in GPC, NMR or MS analysis.^[199–201] Their ionic nature interferes with solubility in organic systems. Multiple charges, even before artificial ionisation occurs can lead to significant signal overlay in MS, complicating the obtained spectra to point where no useful information can be obtained from them.^[200] As synthetic and analytical accessibility was a central aspect of the project, monodisperse triethylene-glycol methacrylate was chosen, as it offers a defined number of ethylene-glycol repeat units, acceptable solubility in both organic solvents and aqueous buffers, and therefore comparatively unproblematic handling. Monodisperse monomers are crucial to mass-spectrometric investigation. Most commercial oligo-ethylene-glycol methacrylates possess narrowly distributed OEG sidechains, which will complicate the evaluation of MS spectra. Each added monomer on a chain would result in not one, but a distribution of signals patterns, potentially rendering the measurement worthless. Although shorter OEG-modified methacrylates such as the one used here do not offer the same water solubility as longer analogues, their benefits in handling, facile synthesis and purification, and great solubility in organic and inorganic solvents outweigh the benefit.^[202] In order to design a system like this, close attention needs to be paid to compatibility between synthetic and analytical methods. Linear polymers were thus selected for analytical simplicity. Statistical incorporation of anchor- and solubilisation groups were chosen over block-copolymers, in order to avoid unwanted and hard-to-predict formation of supramolecular structures.^[203]

The traceable, self-reporting system for drug release was centred on fluorescence turn-on. Drawn from the wide range of existing drugs, anthracyclines exhibit fluorescence upon irradiation in the visible spectrum, making them ideal candidates for such an undertaking.^[204] One of them, Doxorubicin (Dox), is particularly suitable for the application, as it offers a well accessible carbonyl moiety. This carbonyl can be utilised to immobilise the drug covalently on the carrier through hydrazone coupling.^[193] As hydrazone bonds are susceptible to a sensitive, pH-dependent equilibrium of closed and open forms, they have found widespread application in drug delivery. The critical pH value, at which hydrazones

are hydrolysed in the presence of water, lies at around $\text{pH} \leq 5.5$, which precisely matches the environmental conditions in either the ECM of tumour tissue or vesicular uptake in tumour cells, releasing the drug, once the assembly reaches its site of action.^[205–207]

In order to report release events, a quenching system was required, which attenuates or ideally fully silences the fluorescence signal before release. Architectures incorporating classical FRET quenchers had already been reported,^[112] yet they suffer from certain disadvantages. Firstly, typical FRET pairs need to exhibit overlapping emission- and absorption-spectra, and are highly dependent on close proximity and correct orientation.^[208] Thus, in order to design a more universally applicable system, nitroxides were chosen as quencher moieties. Nitroxides demonstrate outstanding efficiency in quenching fluorescence from both organic and inorganic fluorophores.^[154,209] They are synthetically accessible through an array of different chemistries and can be incorporated through a range of coupling techniques. Apart from their ability to silence fluorescence over comparatively long distances and across broad spectra, their unpaired electron provides additional advantages in the application at hand.^[210] On a physiological level, they have been shown to act as NO-analogues, mediating oxidative stress in their immediate environment and thus influencing or inhibiting a range of signalling cascades relevant to tumour formation and metastasis (refer to **Section 2.3**).^[166] On a macroscopic level, they have been shown to be applicable in MRI imaging approaches, making them suitable contrast agents in medical applications.^[141] MRI imaging thus offers an additional tracking handle for later applications and the combination of these properties made them the ideal compound for the application. A schematic representation of the envisioned architecture is depicted in **Scheme 3.1**.

Experimentally two approaches were explored. One approach was designed to use glycidyl methacrylate (GMA) as a single, statistically incorporated anchor unit. Through post-polymerisational nucleophilic opening of the oxirane ring in the side-chain, two chemically orthogonal coupling moieties should be generated. These would serve as attachment points for drug and nitroxide at the same time. The approach was considered to provide the highest level of control over the spatial arrangement of fluorophore and quencher, locking them in the closest proximity possible, thus ideally achieving the highest quenching efficiency possible (**Section 3.3**, page 55).



Scheme 3.1: General concept for a nanodrug, capable of reporting the release of Dox. A methacrylate based, water-soluble construct was proposed to carry nitroxides and hydrazone bound fluorescent drug moieties. Transfer of the polymeric assembly to an acidic environment would facilitate hydrolytic cleavage of the hydrazone, releasing Dox from the polymer. The inherent fluorescence of Dox, now no longer quenched by proximal nitroxides, can be used to quantify release efficiency. Reproduced from [211] with permission from the RSC.

As the single-anchor-unit approach described in **Section 3.3**, page 55, proved troublesome due to challenging precursor synthesis and the comparatively high number of post-polymerisation modification steps, another design was realised. Here, precursors for both the hydrazide and nitroxide unit were directly incorporated as *tert*-butyl-2-methacryloylhydrazine-carboxylate (bHMA), and 2,2,6,6-tetramethyl-4-piperidyl methacrylate (TMPMA), respectively (**Section 3.4**, page 66).

As Dox is costly and highly carcinogenic, a proof of concept study was carried out first, evaluating the overall synthetic strategy using acetylpyrene as a structurally analogous fluorophore. Investigations were carried out on both a small molecule system (**Section**

3.2.2, page 52) and a polymeric assembly (**Section 3.3**, page 55) in order to establish the general proof-of-concept. The obtained findings were subsequently transferred to the intended final design, which was then used to demonstrate both the ability to visualise release and exhibit measurable anti-tumour activity in both 2D- and 3D cell culture model systems (**Section 3.5**, page 83).

3.2 PRELIMINARY SMALL MOLECULE STUDIES

3.2.1 Nitroxide and Fluorescence quantification

In order to be able to quantify nitroxide density on the polymer carrier, a method for quantitation needed to be established. Literature known methods include UV/Vis-spectroscopy, which have been adapted to a number of systems. One major hindrance with photometrical quantification in general is sensitivity. While nitroxides possess specific absorption spectra, their extinction coefficients are comparatively small compared to organic dyes. Critically, as the intended architectures would incorporate a range of fluorophores with significantly higher extinction coefficients at the relevant wavelengths, another method – insensitive to such overlays and crosstalk – was required.

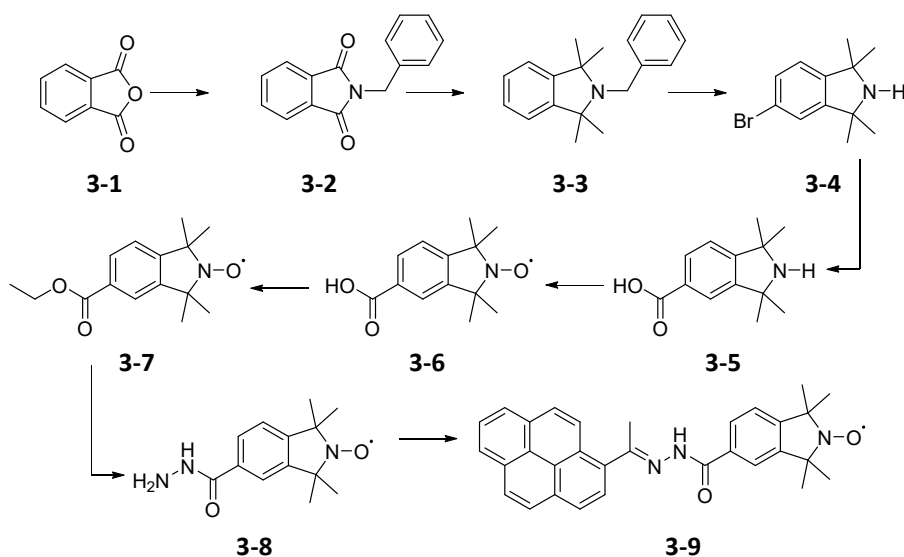
ESR spectroscopy is capable of detecting even minute concentrations of nitroxides, down to fM quantities. Double integration of the acquired spectra returns an arbitrary value, which can be used for relative quantification. In order to turn this into quantitative data, reference spectra of nitroxides in solution with known concentrations needed to be recorded. As the utilised spectrometer's output did not follow predictable trends when comparing measurements at different gain stages (i.e. doubling the detector gain did not result in a doubling of ESR double integral), yet remained linear across multiple measurements at the same gain level, calibrations for a range of gain stages were recorded. As a result, a set of reference curves (**Appendix, Table A 8.1, Figure A 8.23**) were obtained, reliably allowing the quantification of nitroxides in solution in a broad concentration-range of $45.3 \cdot 10^{-9} - 5.81 \cdot 10^{-6}$ M. Individual spectra can be found in the **Appendix, Figure A 8.13 - Figure A 8.22**.

Proof-of-concept experiments, intended to demonstrate the signalling capability and -intensity of profluorescent nitroxides with hydrolytically labile linkage were carried out using acetylpyrene. Pyrene tends to exhibit stacking and excimer formation, influencing fluorescence yields and both absorption and emission spectra.^[212] The relevance of the results is dependent on either the absence or the precise characterisation of artefacts. As excimer formation can create potential pitfalls in the analytic strategy, its prevalence needed to be ruled out. In order to avoid these effects, dilution series of acetylpyrene were recorded *via* fluorescence spectroscopy, to determine a concentration at which maximum fluorescence signal can be recorded, without reaching a concentration where excimer effects dom-

inate. Acetylpyrene in acetonitrile showed significant self-quenching at concentrations exceeding $31.5 \mu\text{M}$, and exhibited relevant levels of fluorescence starting from $1 \mu\text{M}$. (**Appendix, Figure A 8.12**).

3.2.2 A Small-Molecule Proof-of-Concept²

In order to confirm both the quenching ability of nitroxides and the release of the fluorophore in the proposed system, a small molecule model system was initially designed. A hydrazide-bearing nitroxide was synthesised, capable of linking the fluorophore directly to the quencher. The proof-of-concept serves two purposes: (i) Establish a general framework of conditions for both coupling and release experiments and (ii) provide insight into how much quenching efficiency could be expected in a minimum-distance system.



Scheme 3.2: Synthesis of the small molecule assembly to demonstrate quenching and release. Pyrene was used as a fluorescent model drug and TMIO was to be used as a quencher.

Prior to the actual synthesis of the conjugate, the nitroxide was synthesised. Previous studies had demonstrated excellent quenching efficiencies when employing indoline-based TMIO as an alternative to the widely employed TEMPO. The synthesis as shown in **Scheme 3.2** is well established and shall thus only be discussed in brief. NMR and ESI-MS spectra of each individual reaction step can be found in the **Appendix, Section 8.1**.

Firstly, N-benzyl-phthalimide **3-2** was formed *via* the condensation of phthalic anhydride **3-1** with benzylamine. The product was subsequently methylated in a Grignard-reaction, yielding the tetramethyl-isoindoline product **3-3**. The product was brominated in order

² The project was partially carried out by BSc Melissa Reith, project student to C. B.-K.

to generate a leaving-group for subsequent lithiation and carboxylation to obtain acid-functionalised isoindoline **3-5**. The non-purified reaction product was immediately oxidised, using a mixture of catalytic amounts of sodium tungstate and excess H_2O_2 , yielding the carboxy-TMIO **3-6** as an orange, crystalline solid. The product was coupled under Steglich conditions to yield the ester **3-7** and exposed to an excess of hydrazine to obtain hydrazide **3-8** as a white solid, partially reduced to the hydroxylamine form. The product was barely soluble in any organic solvent or water, thus analysis was challenging.

The final step, acidic coupling of acetylpyrene, was also challenging with regard to solubility. Both sample processing and analysis are close to impossible in this step. As the product did not exhibit sufficient levels of solubility in any available deuterated solvent or solvent mixture, NMR measurements could not be performed. ESR indicated the presence of nitroxides in solution, yet, as filtering of the sample appeared to influence sample concentration, no reliable absolute quantification could be carried out. ESI-MS, however, confirmed the successful formation of the product.

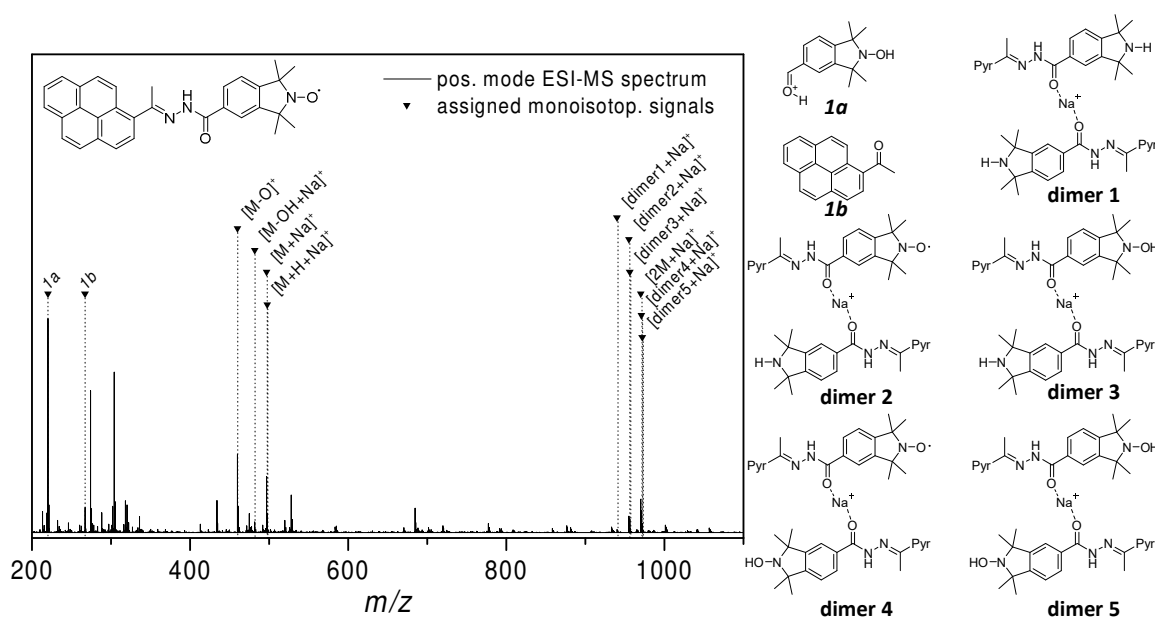
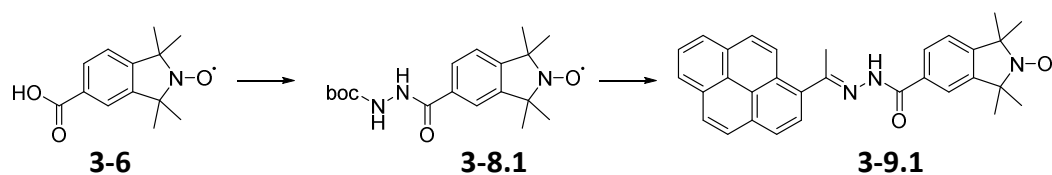


Figure 3.1: ESI-MS spectrum of **3-9**, showing almost solely product and coulomb dimers of **3-9**. Different reduction stages of **3-9** can be found as coulomb dimers, attributed to ionisation artefacts.

The absence of starting material in the spectrum shown in **Figure 3.1** indicated success. The adducts, seen in the higher mass region exhibit different stages of nitroxide reduction or loss of oxygen, which is a phenomenon that was frequently observed when measuring nitroxides in ESI-MS.^[213–215] The employed Orbitrap detector with 5 ppm reso-

lution offers sufficient precision to reliably discern elemental composition, which effectively rules out the presence of products with similar mass and different molecular composition. All of the heterodimers shown above are structurally explicable by reduction processes, occurring upon ionisation and have frequently been observed in nitroxide ESI-MS.^[214] The presence of these molecules, all stemming from the same base molecule unambiguously rules the formation of any other products than **3-9**.

Release experiments qualitatively indicated the system does report release, yet the low levels of solubility made quantification or reliable reproduction of results impossible. A possible solution would have been the incorporation of solubilizing groups. Yet, as the system had already taken an extensively complex preparative route, this was not considered a feasible option. Transfer of the findings from the small molecule study to a polymeric system was prioritised. Transition to the polymer promised to resolve solubility issues, due to the systemic presence of solubilizing groups, allowing facilitated sample handling. As modified polymers can easily be purified *via* precipitation, effectively removing small molecules and side-products, no further investigations on the small molecule system were carried out.

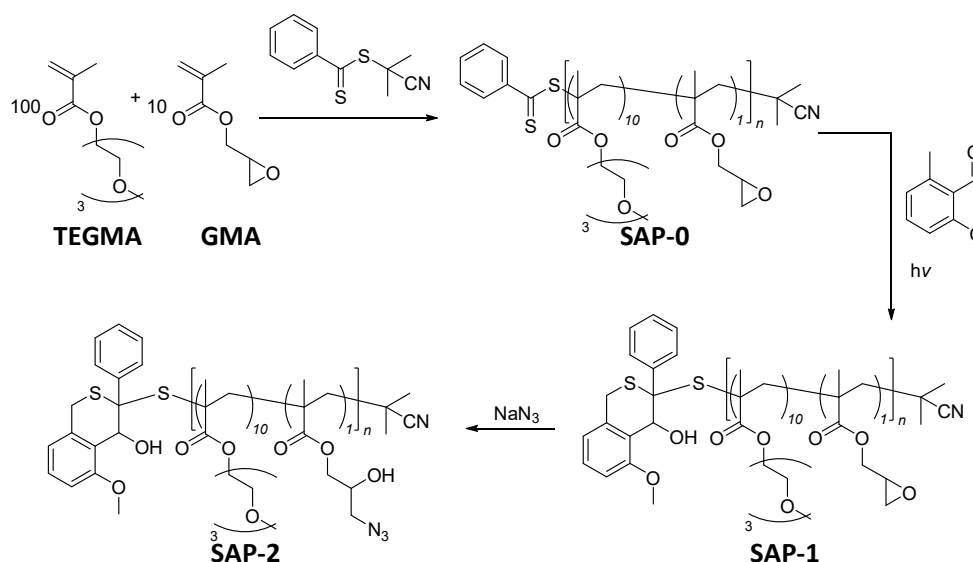


Scheme 3.3: Synthesis route for a modified approach, employing boc-hydrazido-TMIO as a synthon towards a profluorescent model system for pyrene release.

An alternative route to gain access to a more soluble intermediate by using boc-protected hydrazine was tested in an attempt to circumvent insoluble intermediates. The use of *tert*-butyl carbazate instead of hydrazine allowed larger amounts of **3-8.1** to be synthesised in one batch, yet the same problem as before was encountered during deprotection and pyrene coupling. Solubility decreased upon deprotection and the attempt to both deprotect and couple in a single step led to degradation of the fluorophore. The pyrene/nitroxide system was thus revisited in the polymeric platform described in **3.4**, page 66.

3.3 POLYMERIC APPROACH - SINGLE ANCHOR

The approach demonstrated in the previous section could successfully show the general possibility of building the intended reporter system from TMIO and a carbonyl-bearing fluorophore. The solubility issue was supposed to be conquered by the incorporation into a polymer, would shift the determining factor in solubility to the polymer's chemical composition. As one of the two explored approaches, the first one was focused on immobilizing both fluorophore and nitroxide in the same repeating unit. In agreement with recent literature, the most efficient way to achieve maximum quenching efficiency and thus a high level of fluorescence turn-on upon release, is spatially close immobilisation of quencher and fluorophore.^[147,156] Based on a published, non-water-soluble system,^[158] orthogonal coupling of nitroxide and hydrazide linker was based on ring-opened GMA (**Scheme 3.4**). In the course of the presented synthesis, an analytical protocol for the investigation of molecular composition of polymers should be established *via* SEC-ESI-MS.



Scheme 3.4: Synthetic strategy for the water soluble, single anchor platform (SAP), based on which a system for the reporting of molecular release is established. TEGMA and GMA are copolymerised *via* RAFT with CPDB as transfer agent, yielding the water-soluble copolymer **SAP-0**. In order to retain a high end group fidelity through following steps, the end group is protected with photoenol in a photo-HDA reaction, yielding **SAP-1**. In order to generate orthogonally addressable groups on the polymer, GMA is ring-opened by sodium-azide, yielding **SAP-2** as a base polymer for further modification.

Initially, TEGMA and GMA were copolymerised *via* RAFT, employing CPDB as chain transfer agent and AIBN as initiator. The resulting polymer was precipitated twice from hexanes to afford polymer **SAP-0** as a pink sticky polymer, which was analysed *via* NMR and GPC. GPC returned a molecular weight of $M_n = 12.0$ kDa, $D = 1.2$ (**Figure 3.4**).

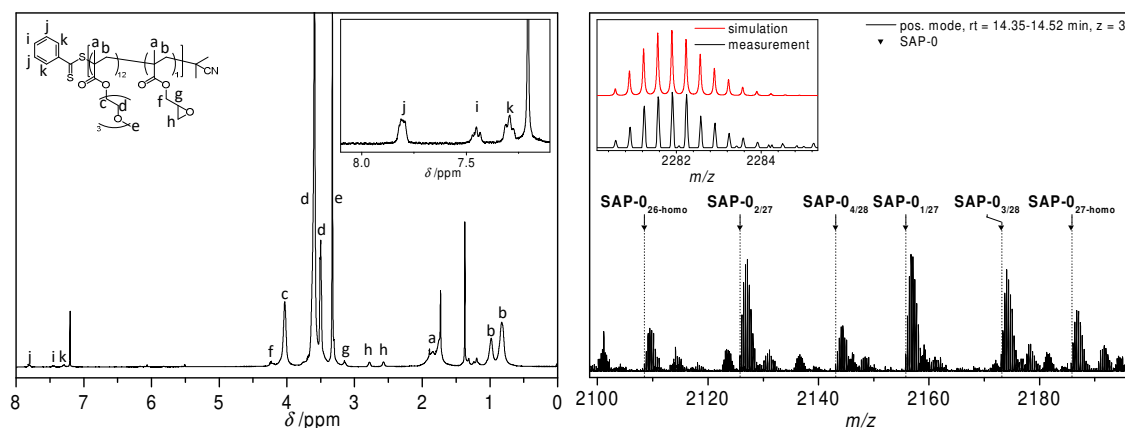


Figure 3.2: ¹H-NMR spectrum and low-molecular-weight SEC-MS slice of SAP-0. Polymer composition was determined by resonances c and h. The zoom shows the three resonances assigned to the phenyl moiety of the Z-group, used for determination of molecular weight. Right: The mass spectrum shows a zoom of one repeating unit at a chain-length of 26 to 27. Indices in the signal labels denominate the number of GMA units per total chain length. Smaller, unmarked signals could partially be assigned to salt/solvent adducts, yet overlays of patterns complicate unambiguous assignment (**Figure 2.2**). The inset shows the overlay of a comparatively undisturbed isotopic pattern and the simulation of the assigned chain composition, demonstrating the precision of the method.

Investigation *via* NMR revealed a polymer composition of 10:1 TEGMA:GMA, determined by the integrals of resonances c and h (**Figure 3.2**, left). The molecular weight was determined to be 15.0 kDa by the ratio resonances c, h and j. Additionally, the polymer was analysed *via* SEC-MS, in order to establish a high-precision analytical method for the investigation of copolymers at the molecular level. SEC-MS spectra indicated a product with high end group fidelity, as visible by the highlights in **Figure 3.2** (assignments in **Table A 8.2**). The mass spectra also demonstrate the importance of high yielding, defined synthetic protocols further down the strategic pathway: The non-modified polymer shown here already exhibits highly complex isotopic pattern overlays, caused by salt- and solvent-adducts at lower ionisation levels. Therefore, any side-reactions, even in low percentages, yielding products of unpredictable molecular composition, would complicate spectra. Such phenomena had thus to be avoided by choice of high yielding procedures.

In order to retain high end group fidelity and thus highly defined mass spectra, showing one type of polymer only, the end group had to be protected against nucleophilic attacks. The most efficient way proved to be a photochemical approach, in which the end group was reacted in a photo-HDA-reaction with 5 eq of 2-methoxy-6-methylbenzaldehyde (photoenol, PE) under 15 min of UV irradiation ($\lambda_{\text{max}} = 315 \text{ nm}$).

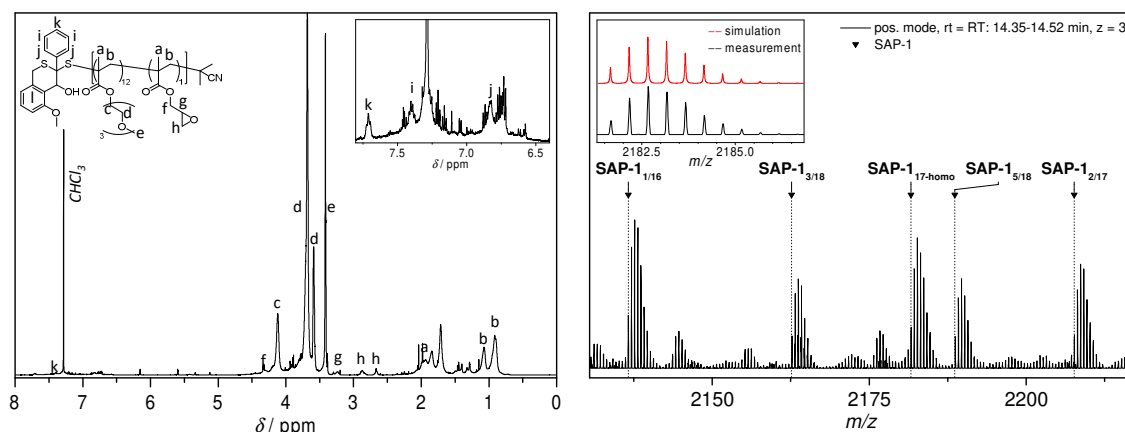


Figure 3.3: Left: $^1\text{H-NMR}$ spectrum of **SAP-1** after photo protection. The zoom shows the shift of proton resonances i, j, and k towards the low-field as a result of the HDA-reaction with the photocaged diene. Right: Zoom into one repeating unit in the SEC-MS spectrum of **SAP-1**. No signals correlated to the unprotected form of **SAP-0** were found, indicating quantitative conversion. Indices in the signal labels indicate the count of GMA units per chain length. The inset shows the overlay of a comparatively undisturbed isotopic pattern and the simulation of the assigned chain composition.

Analysis via $^1\text{H-NMR}$ spectroscopy (**Figure 3.3**) showed full disappearance of the Z-group's aromatic proton signals i, j, and k. SEC MS was employed to confirm these findings, showing a clear pattern of quantitatively PE-protected polymers (**Figure 3.3, Appendix, Table A 8.3**). GPC analysis indicated no significant change in molecular weight ($M_n = 11.0$ kDa, $D = 1.1$, **Figure 3.4**) and thus no signs of dimerisation or photo-degradation. A slight decrease in dispersity, most likely owed to repeated precipitation and inherent removal of shorter chains, could be observed by GPC (**Figure 3.4**).

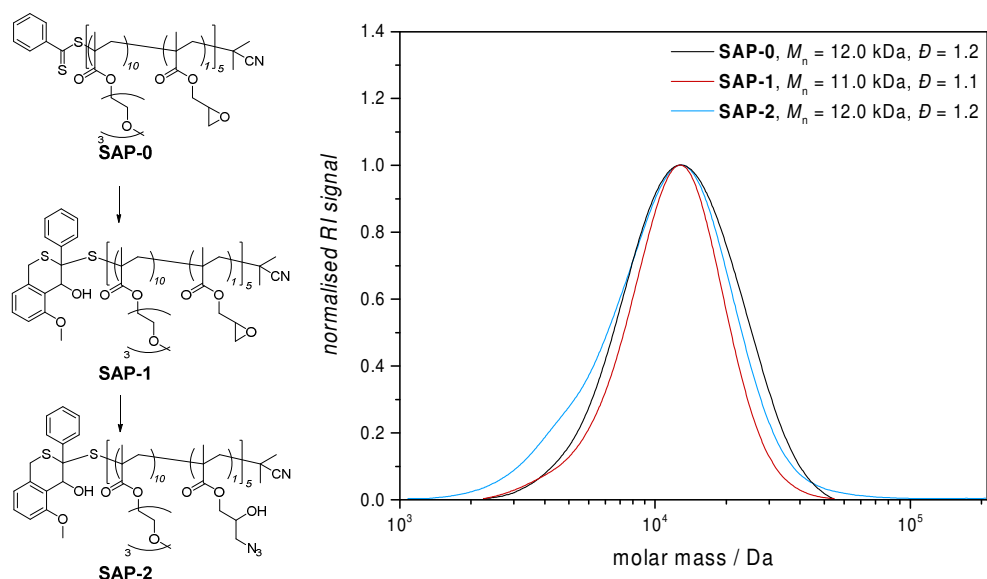


Figure 3.4: GPC-elugrams of **SAP-0** through **SAP-2**. No significant shift in molecular weight was observable. The decrease in dispersity upon photo protection (**SAP-1**) was attributed to repeated purification steps, the subsequent line-broadening of **SAP-2** most likely stems from the newly formed hydroxyl-groups, which slightly alter the both level of hydrophilicity and possible interaction with the column material.

Different strategies for functionalisation of the polymer backbone were investigated, yet only one proved to be efficient enough to be compatible with SEC-MS analysis. In the chosen approach, ring-opening of the GMA oxirane provided an organic azide as an anchor for an alkyne-bearing nitroxide, and a hydroxyl as an anchor to accommodate the hydrazide linker for drug-attachment. **SAP-1** was reacted with an excess of NaN_3 in DMF. The reaction was monitored *via* SEC-MS and NMR, with full disappearance of GMA-containing chains as a progress indicator.

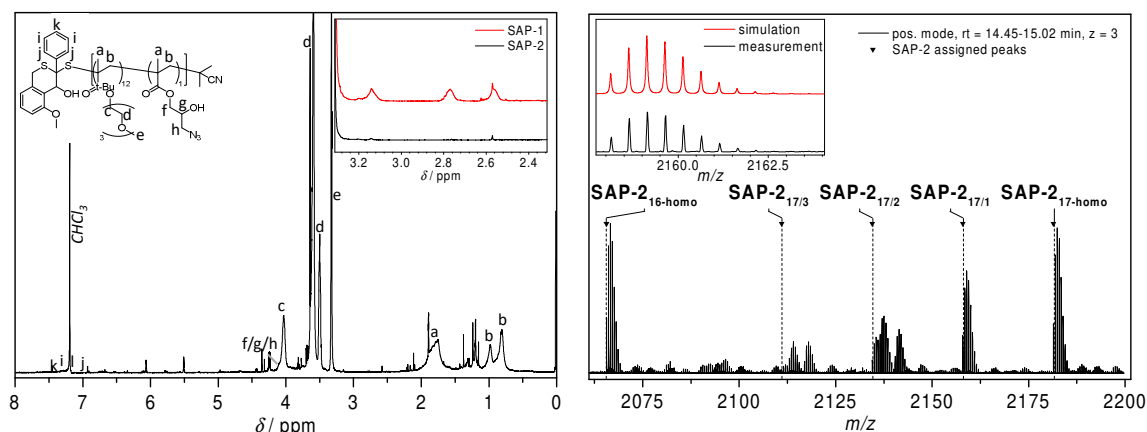


Figure 3.5: Left: $^1\text{H-NMR}$ spectrum of **SAP-2** after GMA-opening by NaN_3 . The zoom shows the shift of the resonance of protons f, g, and h upfield, now coalescing with TEG signals. Right: Zoom into one repeating unit in the SEC-MS spectrum of **SAP-2**. The spectrum shows excellent levels of conversion with no detectable precursor polymer left. The signals were unambiguously assigned to chains bearing the HDA end group from the previous step. Indices indicate the count of GMA units per chain length. The inset shows the overlay of an undisturbed isotopic pattern and the simulation of the assigned chain composition.

Analysis *via* $^1\text{H-NMR}$ showed a clear shift of resonances f, g, and h, indicating full conversion and no remaining GMA-units (**Figure 3.5**, left). Mass-spectrometric investigation *via* SEC-ESI-MS was used to demonstrate quantitative ring-opening, with no more signals associated with GMA-bearing chains visible. Only one type of polymer was identified, still bearing the PE-protected end group, confirming suitability of the PE-protection for end group capping purposes (**Figure 3.5**, **Appendix**, **Table A 8.4**). To additionally track the modification progress, ATR-FTIR spectroscopy of the sample was carried out.

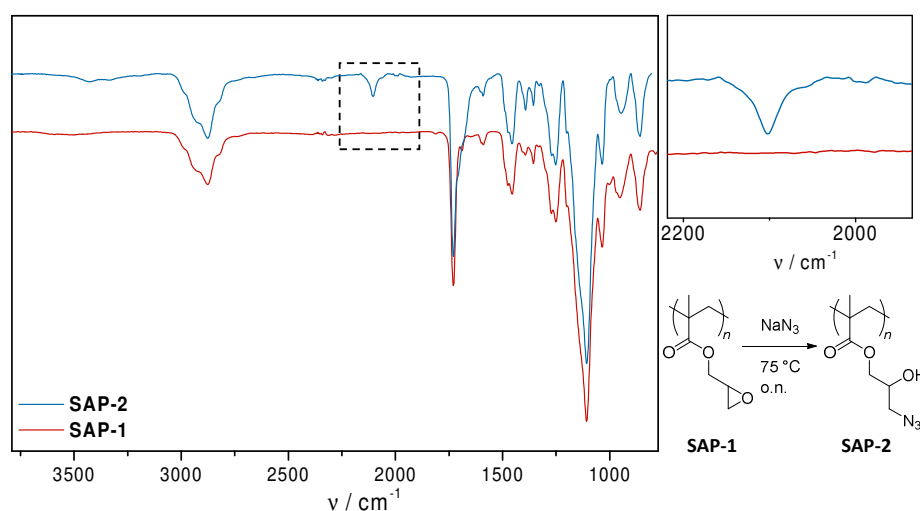
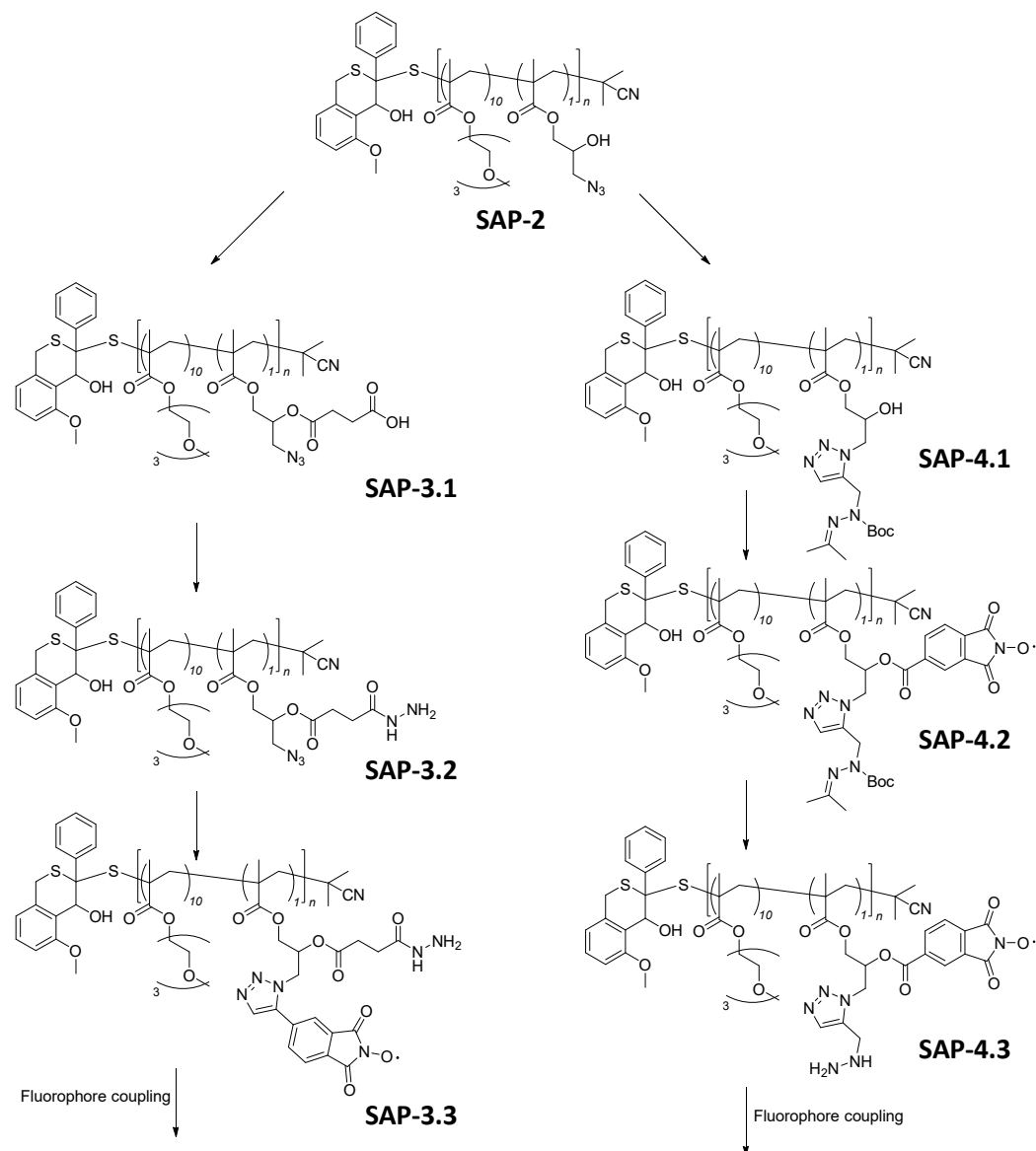


Figure 3.6: ATR- FTIR transmission spectrum of **SAP-1** and **SAP-2** to investigate the azidation reaction. A clear absorption band at 2110 cm^{-1} becomes visible upon ring-opening of GMA *via* sodium azide.^[216] The signal is characteristic for the stretching vibration of azides and was further used to monitor azide presence over the following steps.

3. A Polymeric Nanocarrier for the Visualisation of pH-Triggered Release

As shown in **Figure 3.6**, **SAP-2** clearly exhibited the typical stretching signal of organic azides in an isolated area of the spectrum at 2110 cm^{-1} .^[216]

Two functionalisation strategies were explored simultaneously from this point on, linking nitroxide to azide and hydrazine to the hydroxyl or vice versa.



Scheme 3.5: Functionalisation strategies. The left (**SAP-3**) pathway was designed to build the hydrazide linkage from a diacid and click the nitroxide. The right (**SAP-4**) pathway was designed to immobilise the nitroxide *via* esterification, clicking the hydrazine moiety in the form of a protected hydrazide.

The strategies for immobilisation of the reporter system are shown in **Scheme 3.5**. The first pathway to be explored was (i) the coupling of succinic anhydride to generate an acid for the subsequent coupling of hydrazine, (ii) clicking of alkyne-TMIO *via* CuAAC and (iii) coupling of the reporter fluorophore or drug.

SAP-2 was reacted with succinic anhydride in the presence of TEA and DMAP, to yield an acid-modified **SAP-3.1**. Presence of the acid group was confirmed by $^1\text{H-NMR}$ spectroscopy.

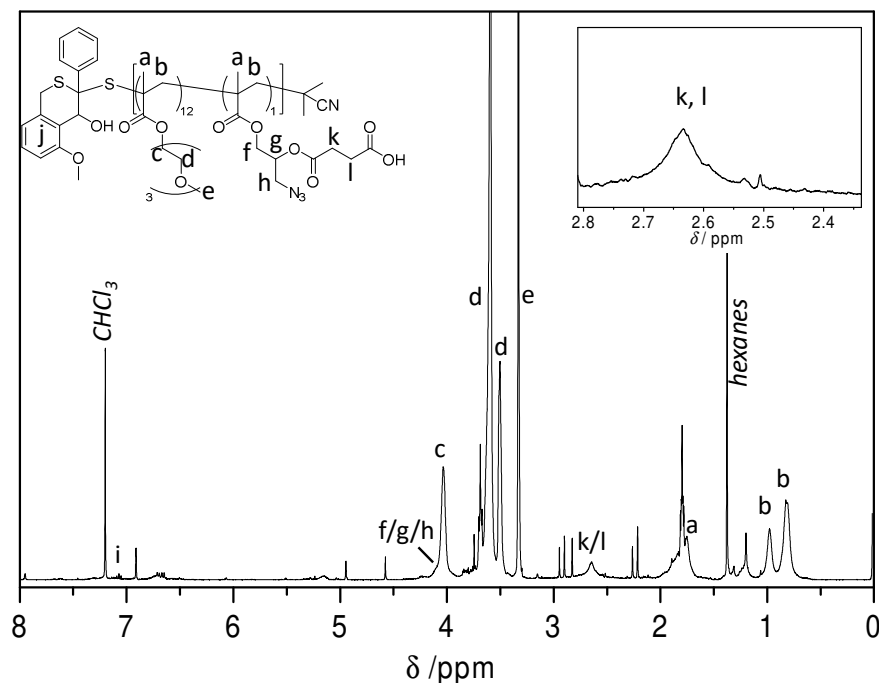


Figure 3.7: $^1\text{H-NMR}$ spectrum of **SAP-3.1**. The incorporation of succinic acid was followed by the emerging resonances k and l.

The spectrum in **Figure 3.7** shows the aliphatic resonances of the acid chain in the purified polymer. SEC-MS investigation proved difficult, as the sample did not ionise sufficiently well, and strong signal overlay complicated evaluation of the obtained mass spectra. As an alternative indicator for successful coupling, ATR-FTIR was employed to confirm a broad signal, spanning the area of $3500\text{-}2500\text{ cm}^{-1}$ (**Figure 3.8**), further underpinning the successful coupling.^[217] Attempts were made to couple either free or boc-protected hydrazine to the newly formed acid, yet sufficient coupling could not be confirmed by any analytical means.

In order to alleviate the issue, a reversed strategy was tested, wherein a hydrazine-modified alkyne is coupled *via* copper-catalysed click-chemistry, allowing the nitroxide to be later attached *via* esterification to the remaining hydroxyl group (**Scheme 3.5**, right pathway **SAP-4.x**).

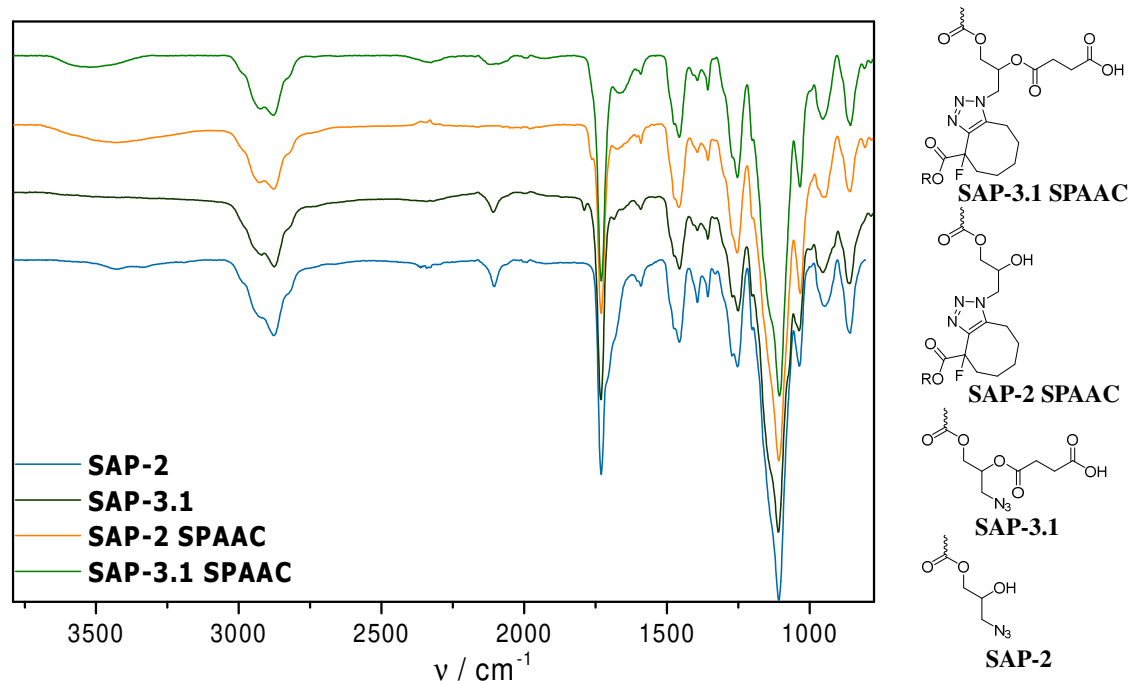


Figure 3.8: IR spectra of transformations attempted on the **SAP-2** platform towards **SAP-3**. Upon coupling of succinic anhydride, the acid becomes visible as a very broad signal spanning 3500-2500 cm^{-1} . Coupling of the acid leaves the azide signal at 2100 cm^{-1} unaffected. Clicking before coupling of the anhydride (**SAP-2 SPAAC**) led to complete disappearance of the azide band. Clicking after coupling of succinic acid shows only slight reduction of the azide signal.

The hydrazide precursor was synthesised in two steps by protecting *tert*-butyl carbamate *via* imine-formation with acetone and subsequent nucleophilic coupling to propargyl-bromine. A range of couplings were attempted to form **SAP-4.1** *via* copper-catalysed azide-alkyne click reactions (CuAAC). Coupling success was primarily evaluated *via* IR-spectroscopy. None of the attempted couplings led to a noteworthy effect on the IR spectrum of resulting products.

In order to confirm the general compatibility of the protected hydrazido-alkyne with the employed click chemistry, a test-experiment with azido-PEG was performed. The click-PEG product (**Figure 3.9**) was coupled overnight and precipitated from cold Et_2O .

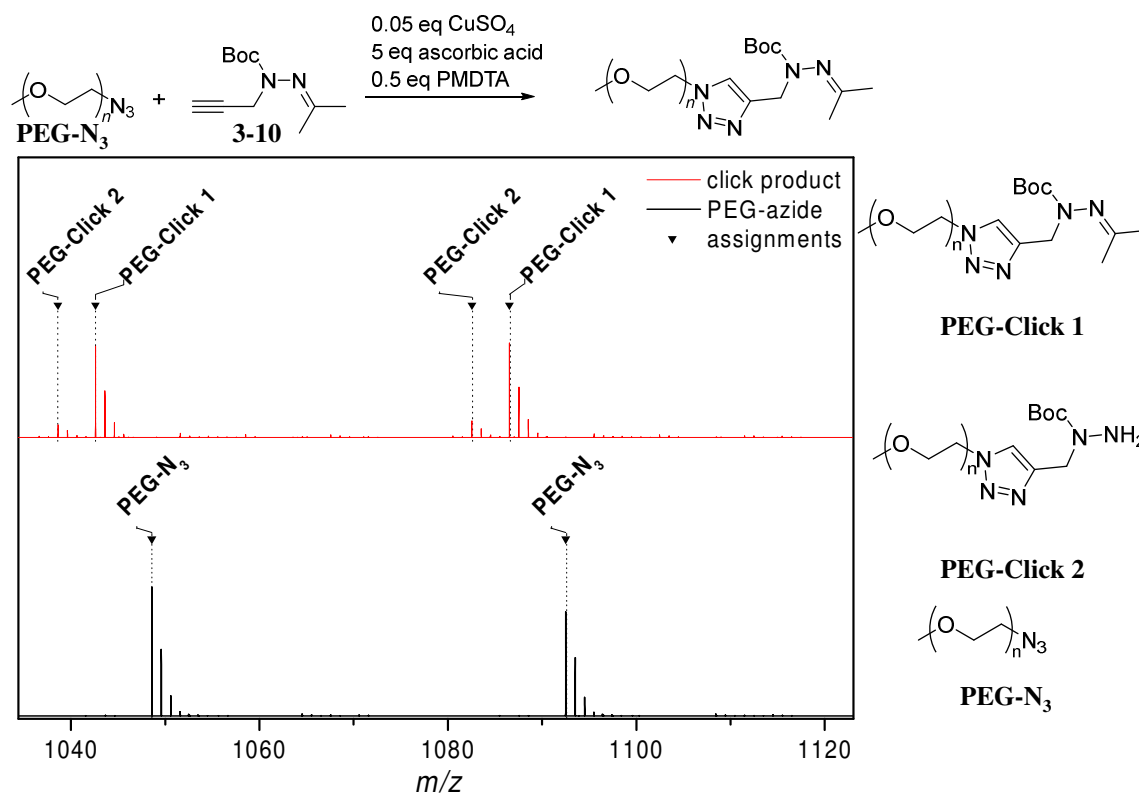


Figure 3.9: ESI-MS spectrum of PEG-N₃ and CuAAC products from the control reaction. One repeating unit of the PEG chain is shown for clarity. No azide-terminated PEG can be detected in the product (top, red), suggesting full conversion.

As shown in **Figure 3.9**, no starting material could be detected after precipitation, indicating complete conversion of the starting material. A general compatibility between substrates and the chosen chemistry could thus be confirmed. Therefore, it was assumed, the issues when transferring the click procedure to the polymeric system had to be rooted in the polymer's nature. Steric hindrance in the confined space of polymer-bound azide was assumed to interfere with the reaction, most likely blocking the copper-catalyst's bulky complex from accessing the azide.

In order to reduce steric demand in the click reaction, a strain-promoted azide-alkyne click (SPAAC) approach was tested. Such a strategy eliminated the need for a copper catalyst, and as a direct result of this, removed the bulky complex required for the formation of the triazole linkage. An assessment of the feasibility of a click approach was carried out by reacting cyclooctyne-acid with **SAP-2**. Neither NMR nor SEC-MS could unambiguously confirm the success of the coupling reaction, yet the IR spectra shown in **Figure 3.8** indicated a complete disappearance of the azide band when coupled to **SAP-2** and slight decrease when coupled to **SAP-3.1**.

A test reaction in order to evaluate the suitability of the strain-promoted click approach when used with a larger molecule was performed. For molecules exhibiting characteristic absorption spectra in UV/Vis spectroscopy, GPC can be employed to study successful coupling to polymers. Specifically, the elution traces detected by RI and have to coincide UV as shown in, when measured at $\lambda_{\text{abs}} = 360$ nm, the characteristic absorption wavelength of fluorescein. The GPC elugrams in **Figure 3.10** show clear alignment of UV- and RI signal, indicating successful loading of the polymer.

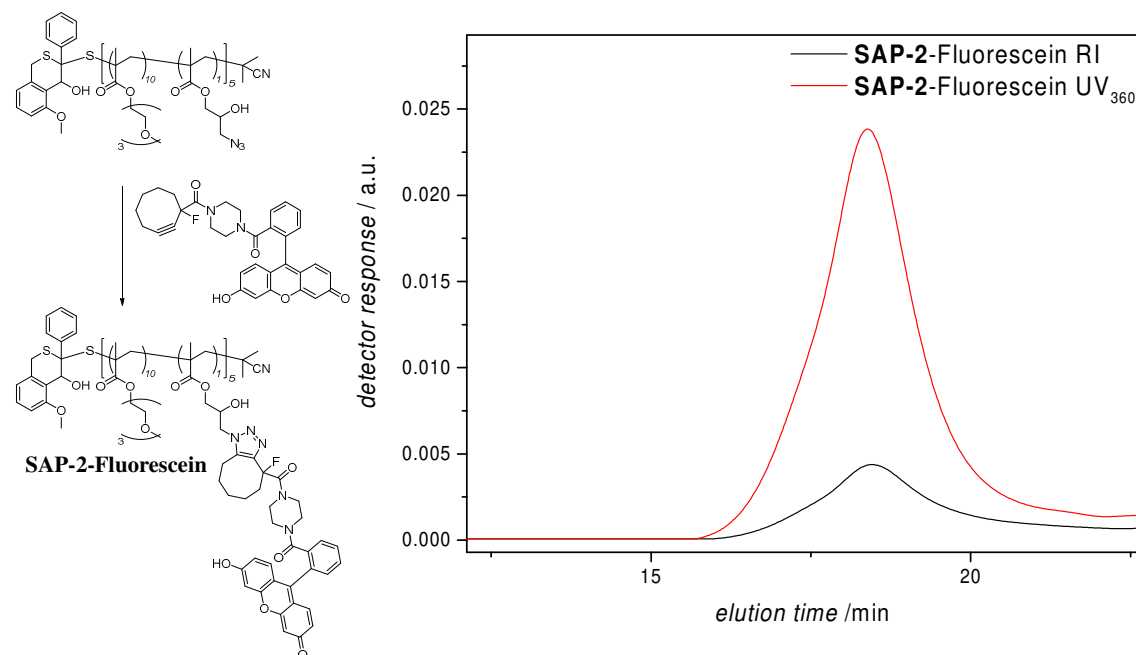


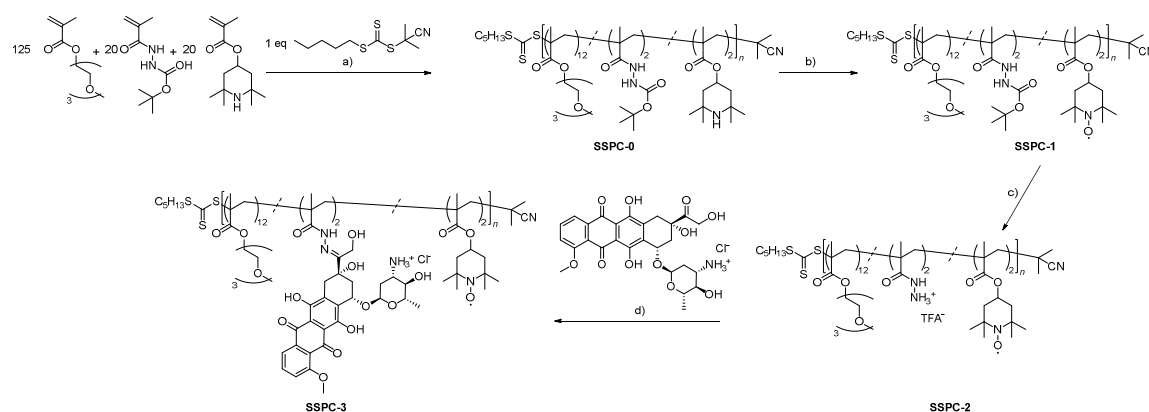
Figure 3.10: GPC of SAP-2 click product with cyclooctyne-fluorescein. A clear alignment of RI and absorption detector signal at $\lambda_{\text{abs}} = 360$ nm are clearly visible, indicating attachment of fluorescein to the polymer.

As the modification of SAP-2 proved complex for a practical application, and failed to reproducibly yield satisfying rates of conversion, the system was deemed unsuitable for biological or even medical applications. The need for synthetically challenging, specialised nitroxide- and hydrazide-moieties in this approach reduced accessibility and transferability of the system. The synthesis of functional TMIO alone involves a 5-6 step synthesis (refer to **Section 3.2.2**, page 52), with inherently low yields poses a troublesome hurdle for an actual application.^[218] To overcome this issue, the system was redesigned to incorporate precursors for hydrazide- and nitroxide-moieties directly on the monomer level. Even though no further attempts at building a highly demanding system like the one envisioned as SAP-3 or SAP-4 were undertaken, the findings and analytical techniques refined in the approach shown here were utilised to successfully construct a functioning reporter system

from an altered backbone architecture. Specifically, polymerisation conditions and analytical protocols refined on the polymeric nanocarrier based on the **SAP** structure, ultimately found application in the realisation of the platform described in **Section 3.4**, page **66**.

3.4 POLYMERIC APPROACH - DISTRIBUTED ANCHORS

The strategy outlined in the previous sections was burdened with a range of issues: Steric bulk of the chosen polymer-backbone effectively prevented the post-polymerisation incorporation of the envisioned anchor/reporter architecture. The synthesis routes towards each component of the anchor were comparatively complex and time-consuming: Both TMIO and the cyclooctyne linker,^[219,220] are subject to long, low-yielding routes (refer to the synthetic protocols in **Section 7.3**, page 135). In order to obtain high amounts of the final macromolecular architecture, simplification was required to realistically be able to reach the envisioned bio-application goals. A range of pitfalls encountered in the small molecule study (**Section 3.2.2**, page 52) and the **SAP**-type system (**Section 3.3**, page 55) had to be conquered: The small molecule study was burdened with solubility issues, which were alleviated by the conjugation to a more soluble polymer backbone. The single anchor polymeric approach described in **Section 3.3** ultimately failed due to steric hindrance in post-polymerisation of the **SAP** polymer platform. On the polymer side, GMA was replaced by bHMA as a hydrazide precursor and TMPMA as nitroxide precursor. TEGMA had already proven to be a suitable, non-toxic solubilizing unit and was therefore chosen again as the main portion of the polymer (refer to **Section 3.5**, page 83). This design sacrificed absolute control over the spatial arrangement of fluorophore and quencher, yet promised greater synthetic efficiency and thus higher yields and elevated reproducibility.



Scheme 3.6: Synthetic approach used to construct the polymeric nanodrug with a spin silencing-based reporter system. Firstly, a polymer is synthesised *via* RAFT. The incorporated nitroxide-precursors are subsequently oxidised and hydrazide-bearing sidechains are deprotected, generating a nitroxide-bearing platform for immobilisation of Dox in a pH-labile hydrazone linkage.

The remodelled concept reduced the number of modification steps to three high-yielding procedures in which (i) the nitroxide would be obtained, (ii) the hydrazide would be uncaged, and (iii) the fluorophore would be coupled, yielding a functional reporter and release system. Although this approach loses absolute control over the spatial arrangement of drug and reporter, possibly sacrificing some quenching efficiency in the process, the significantly shorter and simplified synthetic route offered a vastly increased synthetic yield. In order to establish an efficient synthetic and analytical route, first approaches were carried out as a proof of concept, using acetyl pyrene instead of Dox as a test fluorophore, due to its low cost and good commercial availability.

3.4.1 Proof of Concept

In order to construct a water-soluble backbone, bearing precursors for nitroxide and hydrazide, TEGMA, bHMA, TMPMA were copolymerised by RAFT in a 12.5:1:1 TEGMA:bHMA:TMPMA ratio. As CPDB, being susceptible to aminolysis and having proven to occasionally be incompatible with amine-bearing monomers,^[194,221,222] degraded in the presence of bHMA, it was replaced by 2-cyanoisopropyl-pentyl trithiocarbonate (PPTTC), more stable due to its trithiocarbonate structure. AIBN was employed as initiator. The resulting terpolymer was precipitated and analysed *via* GPC, SEC-MS and ¹H-NMR.

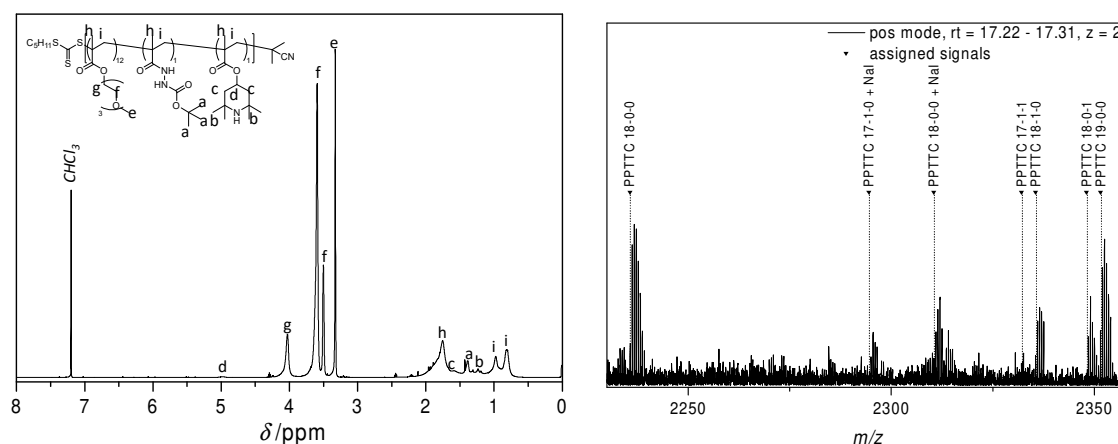


Figure 3.11: Left: ¹H-NMR-Spectrum of **PC-0**. Monomer incorporation was determined by resonances a, d and e. Right: SEC-MS spectrum, positive mode. The assigned peaks represent the exact structure on the left with numbers representing the measured TEGMA-bHMA-TMPMA ratio. Assignments mark the monoisotopic first peak of every isotopic pattern. Assignments are listed in the **Appendix, Table A 8.7**.

The ¹H-NMR Spectrum of **PC-0** (pyrene carrier) in **Figure 3.11** shows clear characteristic resonances for all monomers. Integration indicates a ratio of incorporation of TEGMA:bHMA:TMPMA 12:1:1 (refer to **Appendix, Table A 8.5**), as determined *via* resonances a, d and. Analysis *via* THF GPC was carried out based on a PMMA calibration, returning a molecular weight of $M_n = 9.0$ kDa, $D = 1.4$ (**Figure 3.15**). It is crucial to note that this value should only be used in a relative context to the following modification steps, due to the unknown Mark-Houwink parameters of the polymer in question. In addition, the high loading of accessible amines in the polymer sidechains inevitably led to interactions with the stationary phase in THF GPC. Consequentially, elution times were not directly tied to the hydrodynamic volume of the polymer, skewing the mathematical evaluation towards lower molecular weights. As homogenous incorporation of all monomers into the average chain cannot be taken for granted, the polymer was further analysed by SEC-MS, to elucidate which compositions can be found. The right hand spectrum in **Figure 3.11**

shows a late elution slice of the chromatogram. All highlighted signals correspond to chains bearing the correct end groups associated with the PPTTC RAFT agent. Incorporation was evaluated by the presence of visible repeating units with $m/z = 232.1311$ for TEGMA, $m/z = 225.1729$ for TMPMA, and $m/z = 200.1161$ for bHMA. The spectrum shows a strong prevalence of homopolymeric chains, bearing only TEGMA units, which was attributed to ionisation bias. The poly(ethylene glycol) motif generally exhibits a strong tendency to ionise in ESI-MS, due to their nature of accumulation charges.^[223] In addition, the spectrum shows a comparatively high noise floor, owed to the prevalence of charge overlays inherent to systems with a high amine content. In order to additionally validate incorporation of all units into the same polymer chain, a DOSY experiment was carried out.

The spectrum in **Figure 3.12** shows all relevant signals connected to the same diffusion coefficient, setting them clearly apart from small molecule signals (1.55 and 7.26 ppm). The DOSY result thus indicates all moieties are attached to the same size molecule, and proved the successful synthesis of the carrier platform.

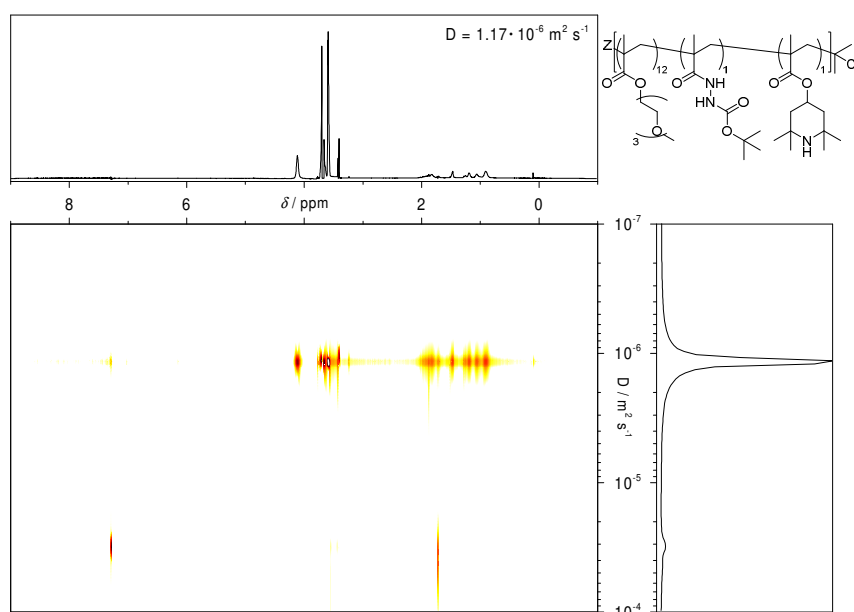


Figure 3.12: DOSY spectrum of **PC-0** in CDCl_3 . The spectrum shows all relevant polymer resonances correlated to the same diffusion coefficient close to $10^{-6} \text{ m}^2 \cdot \text{s}^{-1}$. Resonances correlated with higher diffusion coefficients were assigned to water and CHCl_3 from the NMR solvent. The inset on top shows the spectrum at diffusion coefficient of $1.17 \cdot 10^{-6} \text{ m}^2 \cdot \text{s}^{-1}$, presenting all resonances found in the 1D-spectrum measured before (refer to **Figure 3.11**). The trace on the right shows a histogram across the full 2D matrix, clearly indicating a narrow distribution along the diffusion coefficients.

In order to introduce nitroxides into the polymer architecture, **PC-0** was reacted with 15 eq of *m*CPBA, oxidizing the TMPMA units to radical-bearing TEMPOMA. The reaction's progress was monitored by ESR. The ESR spectrum in **Figure 3.14** shows the triplet shape, typical to TEMPO radicals. The double integral was compared to a previously recorded set of calibration curves with hydroxy-TEMPO (**Appendix, Figure A 8.2, Table A 8.1, Figure A 8.23**), returning quantitative oxidation of all initially present piperidyl-groups (numeric measurement data refer to **Appendix, Table A 8.5**). A noteworthy feature is the strong signal-asymmetry and line-broadening, which stems from anisotropy in the radical's orientation, additionally confirming polymer-bound radicals. The GPC analysis shown in **Figure 3.15** returned a significant shift to higher molecular weights of $M_n = 15$ kDa, $D = 1.2$ and a significant increase in elution-curve symmetry. Both observations were attributed to a significant decrease in accessible amines in the polymer sidechains and a resulting decrease in interactions with the solid phase. NMR analysis showed excessive signal distortion, especially of the low field signals belonging to protons in close proximity to the nitroxide. Spectral distortion is a commonly encountered issue in NMR spectroscopy as soon as nitroxides are present.^[145] The fact that quantitative analysis *via* NMR is not reliable in the presence of nitroxides was taken into consideration for all subsequent experiments, and additional avenues of investigation were added to the analytical protocol for each step.

In order to gain access to polymer-bound hydrazides, the boc protecting groups were removed by acidic hydrolysis. Polymer **PC-1** was deprotected by stirring in a 50% TFA solution in DCM and precipitated from cold diethyl ether. Analysis was carried out *via* NMR, ESR and GPC. The ¹H-NMR spectrum shown in **Figure 3.13** indicates the complete disappearance of the boc-resonance at 1.4 ppm, evidencing the complete removal of all boc-groups. Employing NMR spectroscopy to quantify deprotection efficiency was possible at this point, as nitroxides can form salts with strong acids, yielding the corresponding hydroxylamine salts.^[209]

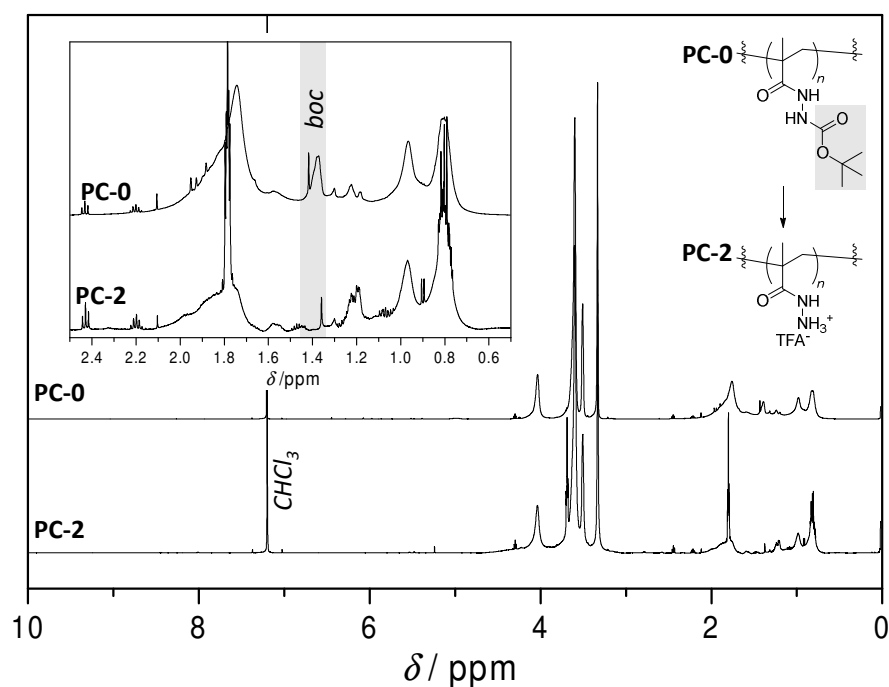


Figure 3.13: $^1\text{H-NMR}$ spectra of **PC-0** and **PC-2**, before and after boc-deprotection. The inset shows a zoom of the low-field area from 0.5-2.5 ppm. The disappearance of the highlighted resonance at 1.4 ppm indicates the complete removal of boc groups from the polymer backbone. All other resonances were unaffected, confirming the structural integrity of the polymer.

Quantitative recovery of stable radicals was vital to the following synthetic success. A full reoxidation of the TEMPO moieties could be achieved *via* the addition of small amounts of TEA, and subsequent precipitation from cold diethyl ether. Recovery was monitored *via* ESR, which showed an almost complete recovery of the ESR signal to a total loading of 89% (for numerical data refer to the **Appendix, Table A 8.6**).

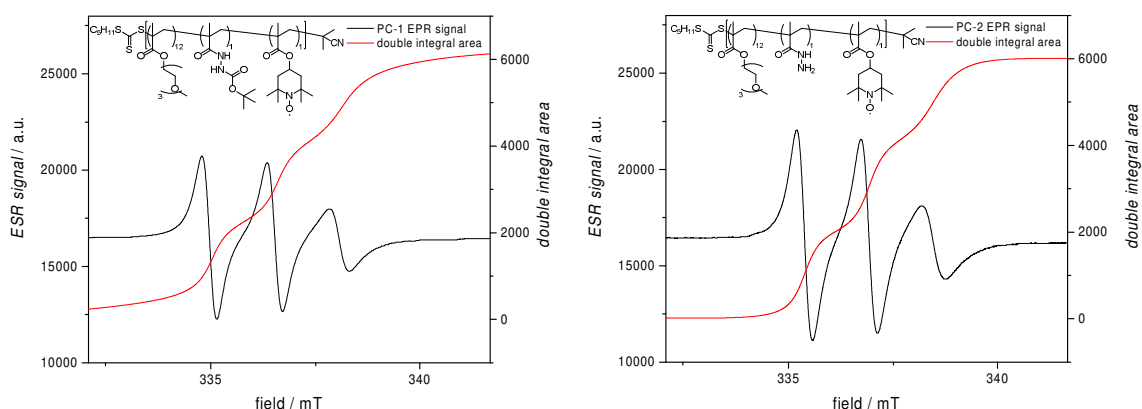


Figure 3.14: ESR spectra of the same $1 \text{ mg} \cdot \text{mL}^{-1}$ solution of **PC-1** and **PC-2** in THF before and after boc-removal. The left spectrum shows the polymer directly after oxidation *via* *m*CPBA. On the right, a slight decrease in double-integral area is visible, yet only to a minor extent. Radical densities were determined to be 99% (**PC-1**) and 89% (**PC-2**) respectively.

The ESR spectrum of **PC-2** in **Figure 3.14** additionally indicates a slight narrowing of the individual signals, compared to the precursor **PC-1**. This was attributed to increased nitroxide mobility, due to removal of the bulky *tert*-butyl groups and resulting decrease in stiffness of the polymer backbone. The deprotected polymer was also analysed *via* GPC (**Figure 3.15**). The chromatogram of **PC-2** exhibited significant line broadening, an increase in dispersity ($D = 1.4$), and a shift to lower apparent molecular weight of $M_n = 18.0$ kDa. As above, the significant increase in accessible amines and the resulting, elevated hydrophilicity, caused by the removal of *tert*-butyl groups, influences polymer shape and interaction with the solid phase and will affect elution times.

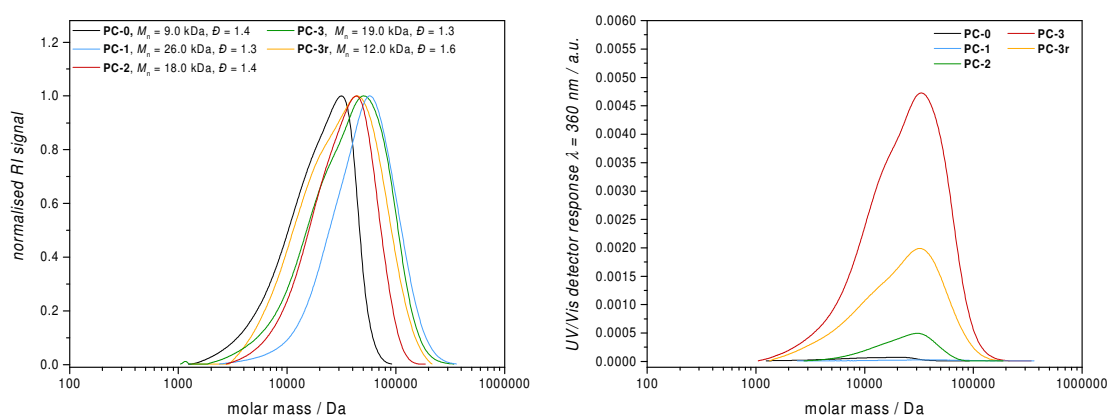


Figure 3.15: Comparison of RI and UV/-vis traces in GPC. Left: RI traces of polymers **PC-0** through **PC-3r**. Line shape and elution volumes are dominated by the chemical composition of the analytes rather than their actual molecular weight. RI traces thus predominantly served as a measure of orientation when evaluating fluorophore loading of the polymer. Right: UV/Vis-absorption of polymers **PC-0** through **PC-3r**. A strong increase of absorption is visible after loading with acetyl-pyrene (**PC-3**). Absorption visibly decreases after release (**PC-3r**), indicating removal of pyrene from the backbone.

Subsequently, pyrene loading was carried out by stirring **PC-2** in a solution of acetylpyrene in 1% acetic acid in anhydrous MeOH. The solution was neutralised with TEA and purified *via* precipitation from cold Et₂O, to remove excess acetylpyrene and TEA, yielding **PC-3** as a yellow, oily polymer. NMR analysis proved difficult due to the presence of nitroxides, yet showed weak resonances in the aromatic region above $\delta = 7.5$ ppm (**Figure A 8.24**), indicating partial, successful loading of the polymer. In order to gain more insight into the loading density of the polymer, photometrical determination of the acetylpyrene-concentration was performed. As the extinction coefficient of acetylpyrene can be influenced by pH, a concentration-calibration of acetylpyrene in ACN was obtained (**Figure A 8.12**), and the extinction coefficient was determined as $\epsilon_{354} = 17181 \text{ M}^{-1} \cdot \text{cm}^{-1}$. A $0.5 \text{ mg} \cdot \text{mL}^{-1}$ solution of **PC-3** exhibited an absorption of $A_{354} = 1.25$, indicating an

acetylpyrene-concentration of $72 \text{ nmol}\cdot\text{mL}^{-1}$ or $144 \text{ nmol}\cdot\text{mg}_{\text{PC-3}}^{-1}$, equalling a loading efficiency of 46.3% with respect to the density of hydrazide groups, determined *via* NMR in **PC-0** (**Figure 3.11**). The successful loading was additionally followed by evaluation of the UV/Vis detector chromatogram obtained from GPC shown in **Figure 3.15**. A strong increase in pyrene-specific absorption at $\lambda = 360 \text{ nm}$ became visible after pyrene loading. The coalescence of elution-times between RI and absorption traces also served as additional proof that all measured fluorophore is indeed bound to the polymer.

In order to demonstrate self reporting release from the backbone, a fluorescence experiment was carried out. A highly dilute 2 mL solution (1.5 nM) of **PC-3** in ACN was acidified by the addition of 1 mL ACN with 1% TFA and immediately measured in a fluorescence spectrometer. Release was monitored by fluorescence recovery of the quenched acetylpyrene.

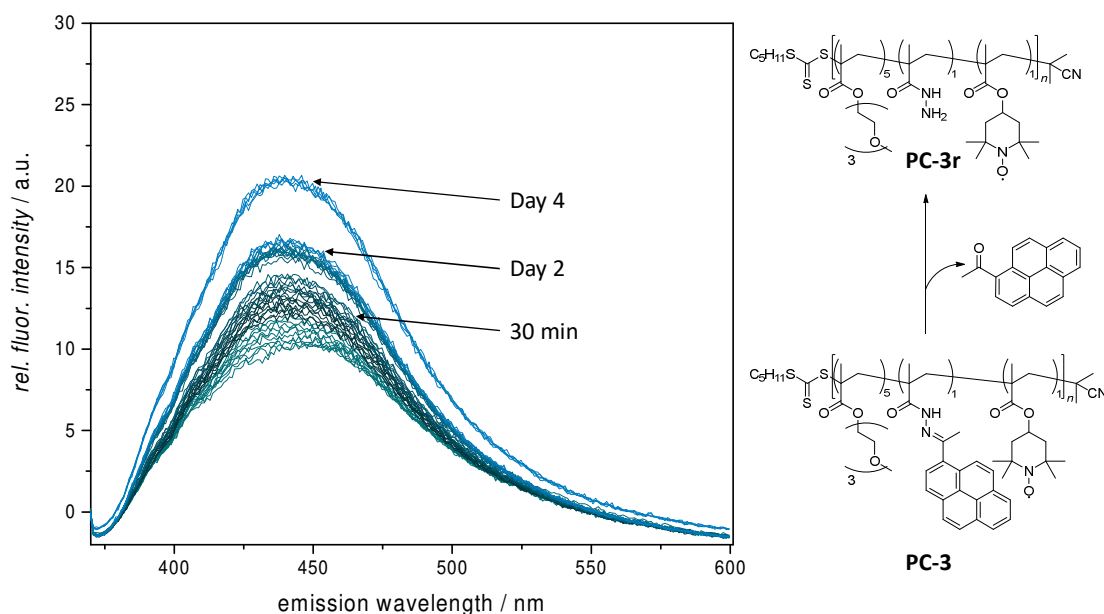


Figure 3.16: Pyrene release from a solution of **PC-3** in ACN, monitored by fluorescence spectroscopy. A strong increase in fluorescence can be observed upon acidification by the addition of $30 \mu\text{L}$ of TFA. Irradiation at $\lambda_{\text{ex}} = 360 \text{ nm}$. Increase in fluorescence slowed over time, with approximately 50% of all fluorescence recovery observed in the first 30 minutes.

As shown in **Figure 3.16**, a clear increase in signal intensity was observed, indicating the successful release of acetylpyrene from the lateral polymer chain. Initially, the release occurs almost instantaneously, gradually slowing down over time, until it ceases after close to 4 days. The overall fluorescence doubled over the course of four days. Several attempts were made to quantify the quenching- and release efficiency of the system more reliably,

yet reproducing perfectly identical polarity and pH in ACN proved inherently problematic.^[224,225] As a direct consequence, quantification of acetylpirene fluorescence became problematic: Just like pyrene, it exhibits notable sensitivity to pH and solvent polarity itself, quite drastically influencing its fluorescence quantum yield.^[224,226,227] In order to fully prove that the increase in fluorescence stems from molecular release, a bulk experiment was carried out in parallel, where the polymer was precipitated after exposure to acidic conditions to remove any released acetylpirene and subsequently analysed *via* GPC. The elugram of the released **PC-3r** showed a measureable decrease in absorption at $\lambda = 360$ nm, underpinning significant removal of the model fluorophore from the backbone. Repeated release experiments generally followed the same trend as shown above, proving the conceptual applicability of the platform, yet exhibiting error margins of a full order of magnitude. However, the fluorescence recovery was strongly influenced by the slightest impurities and water content of the sample, so further efforts were therefore focused on the establishment of an applicable, bioactive system.

3.4.2 A pH-Sensitive Nanodrug for Self-Reporting Controlled Release³

In order to construct a functioning nanodrug with self-reporting molecular release features, the findings from the proof-of-concept phase were used as a design guideline. As both loading- and quenching efficiency of the previous **PC-3** system did not exhibit quantitative loading- and quenching efficiency, and the immobilisation of Dox would prove a greater challenge in term of accessibility and steric bulk, changes to the carrier composition were made. The monomer composition was altered by doubling both nitroxide- and hydrazide content *ab initio*, providing a higher number of anchoring groups. The monomers were copolymerised *via* RAFT polymerisation in a 12.5:2:2 TEGMA:bHMA:TEMPHMA ratio, using PPTTC as transfer agent and AIBN as initiator. The resulting terpolymer **SSPC-0** (*spin silenced polymeric carrier*) was precipitated from cold Et₂O and analysed *via* GPC and NMR.

³ The results in this section have been published in *Polymer Chemistry*. Figures are reproduced from [211] with permission from the Royal Society of Chemistry (RSC).

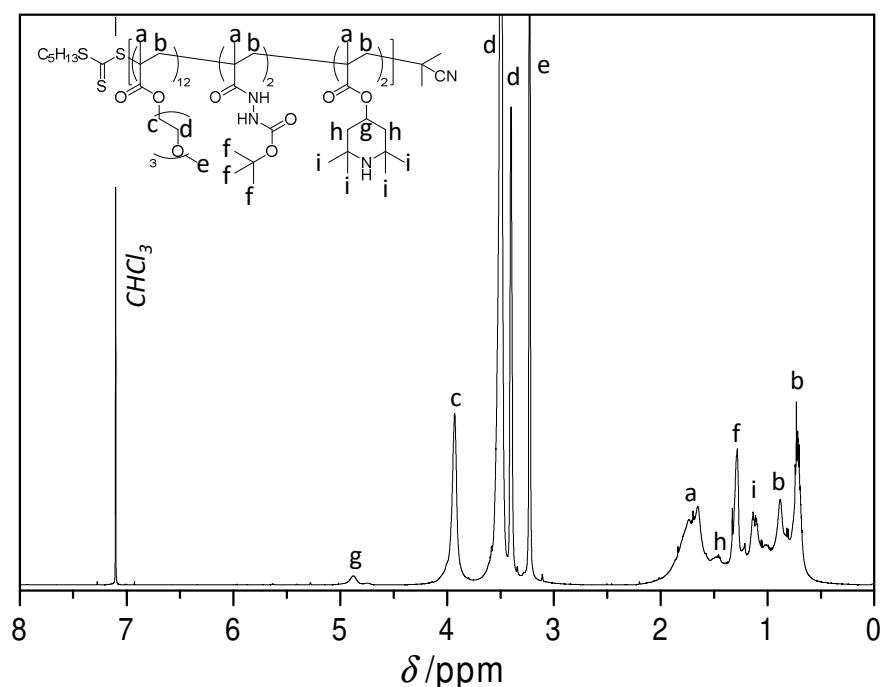


Figure 3.17: $^1\text{H-NMR}$ spectrum of **SSPC-0** in CDCl_3 , used for determination of composition. Resonances c, f, and g were utilised to calculate the ratio of incorporation for TEGMA, bHMA and TMPMA respectively. Reproduced from [211] with permission from the RSC.

The $^1\text{H-NMR}$ spectrum **Figure 3.17** clearly shows all characteristic resonances for all monomers, indicating a ratio of incorporation of 12.6:2:2 (resonances c, f and g, refer to **Appendix, Table A 8.8** for numerical data). GPC analysis was carried out using a calibration with PMMA standards, returning a molecular weight of $M_n = 7.8$ kDa, $D = 1.2$. As discussed above, these values can only be discussed in a relative context to the following modification steps, due to the molecular composition of the polymer (refer to **Section 3.4.1**). Following the same analytical protocol as established earlier, the polymer was further analysed by SEC-MS (**Appendix, Figure A 8.25**). Incorporation of all monomers into the same chain was assessed by the presence of repeating units with $m/z = 232.1311$ for TEGMA, $m/z = 225.1729$ for TMPMA, and $m/z = 200.1161$ for bHMA. The spectrum showed a strong prevalence of homopolymeric chains, bearing only TEGMA, which was attributed to ionisation bias, as the poly(ethylene glycol) motif generally exhibits a highly elevated tendency to ionize in ESI-MS, compared to other polymer chains.^[228] For numeric data of MS assignments, refer to the **Appendix, Table A 8.7**.

In order to introduce nitroxides into the assembly, **SSPC-0** was reacted with 15 eq of *m*CPBA, oxidizing the TMPMA monomer units to radical-bearing TEMPOMA. The success of the reaction was established by ESR spectroscopy.

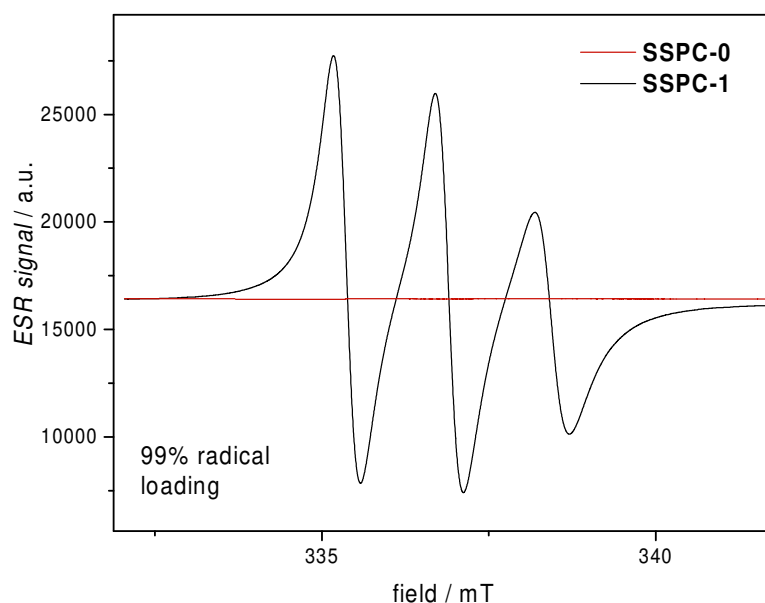


Figure 3.18: Direct comparison of **SSPC-0** and **SSPC-1** ESR spectra. A clear increase in ESR signal intensity, the triplet shape and the slight line-broadening, typical for polymer-bound nitroxides becomes visible upon oxidation. Double integration indicates quantitative conversion of TMPMA-sidechains. For numerical data refer to the **Appendix, Table A 8.8**. Reproduced from [211] with permission from the RSC.

The spectrum in **Figure 3.18** shows a clear increase from no signal before, to a strong signal after oxidation. The double integral was compared to a previously recorded set of calibration curves with hydroxy-TEMPO, returning quantitative oxidation of all initially present piperidyl-groups (**Appendix, Table A 8.8**, for calibration data refer to **Figure A 8.2, Table A 8.1, Figure A 8.23**). Clearly visible is the strong signal-asymmetry and line-broadening, stemming from anisotropy in the radical's orientation, additionally confirming polymer-bound radicals.^[144] GPC analysis returned a significant shift to higher molecular weights of $M_n = 15.0$ kDa, $D = 1.2$, and a significant increase in elution-curve symmetry. Both observations were attributed to a significant decrease in accessible amines in the polymer sidechains and a resulting decrease in interactions with the solid phase. The $^1\text{H-NMR}$ spectrum of **SSPC-1** (**Appendix, Figure A 8.28**) showed strong resonance distortions, especially of resonances associated with protons in close proximity to the nitroxide, i.e. protons g and i, previously clearly visible in **Figure 3.17**. As the high nitroxide content interferes with NMR analysis,^[145] an SEC-MS experiment was performed in order to gain more detailed insight into the polymer composition. The fact that $^1\text{H-NMR}$ spectra could not be used to quantify polymer composition in an absolute manner from this point forward was taken into consideration for the evaluation of all further modification steps. Additional analytical methods as ESR and UV/Vis spectroscopy were employed for the characterisation

of reaction products to get more reliable insight into the molecular structure of all reaction products. In order to gain access to polymer-bound hydrazides, the boc protecting group was removed by acidic hydrolysis. The polymer was deprotected by a 50% TFA solution in DCM and subsequently precipitated twice from cold diethyl ether. NMR and GPC were employed to evaluate efficiency of the reaction.

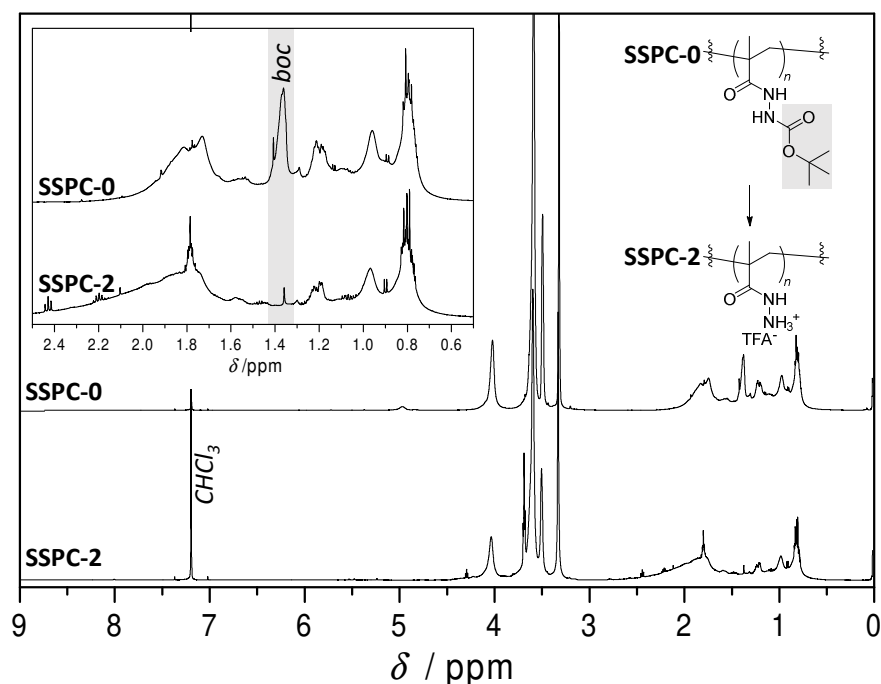


Figure 3.19: ^1H -NMR spectra comparison of **SSPC-0** and **SSPC-2** before and after boc-deprotection. The inset shows a zoom of the relevant chemical shift region from 2.5 - 0.5 ppm. The spectrum of **SSPC-2** clearly shows the disappearance of the highlighted boc-proton resonance at 1.4 ppm.

The ^1H -NMR spectrum depicted in **Figure 3.19** indicates the clear and full disappearance of the boc-associated resonance, highlighted in grey. Employing NMR spectroscopy to quantify the deprotection efficiency was deemed possible at this point, as nitroxides have the ability to react reversibly with strong acids, yielding the corresponding hydroxylamine salts. The assumption was underpinned by a strong decrease in ESR signal to 25% of theoretically available nitroxide moieties (refer to **Appendix, Figure A 8.29, Table A 8.9**), which fully returns upon recovery of the free radicals *via* TEA addition. The deprotected polymer was additionally analysed *via* GPC. The chromatogram shown in **Figure 3.20** exhibited significant line broadening, and a shift to lower apparent molecular weights. The elevated hydrophilicity, caused by the removal of butyl groups and the resulting increase in accessible amines as well as TFA-salt-formation, caused interactions with the solid phase and skewed retention times.

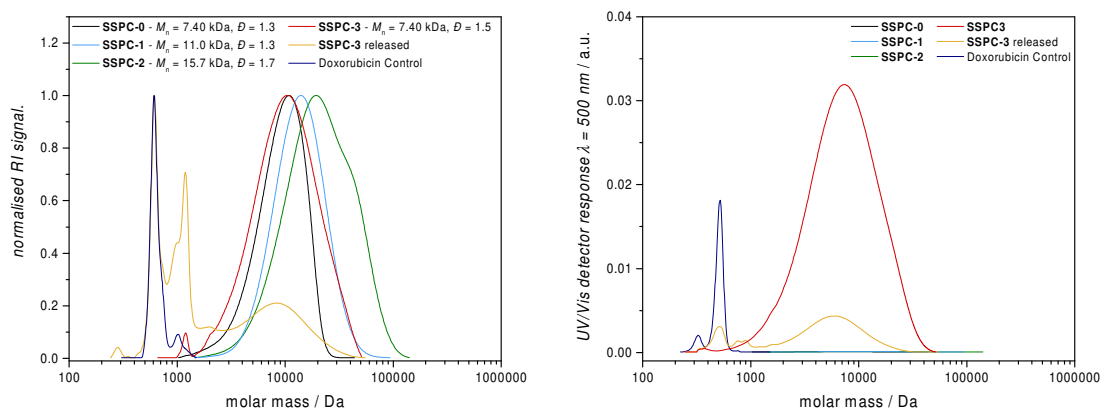


Figure 3.20: Comparison of RI and UV/Vis absorption traces in the GPC. The left shows the RI traces of all synthetic intermediates leading to the release experiment of **SSPC-3**. Additionally, Dox·HCl was assessed as a reference to identify small molecular signals in the release experiment. The latter showcases released Dox present in the analyte. The right hand graph compares absorption at $\lambda = 500$ nm across all modification steps. A significant increase in absorption can be seen in **SSPC-3** upon drug-loading, confirming the molecular architecture of the nanodrug. A decrease in absorption becomes visible upon release, as well as a small-molecular signal, which coincides with the elution of Dox, confirming successful release. Reproduced from [211] with permission from the RSC.

Drug loading was carried out by stirring **SSPC-2** for 72 h in a solution of excess Dox in 1% acetic acid in MeOH. The addition of small amounts of Na_2SO_4 as a drying agent yielded the best results. The loaded polymer was purified *via* size exclusion chromatography, using Sephadex LH-20 resin with 1% TEA in MeOH as eluent, to both remove excess small molecules and neutralise the solution to avoid cleavage upon addition of aqueous buffers later. Loaded fractions were selected by red colour, characteristic for Dox presence, and checked *via* ESR for the presence of nitroxides. Fractions with measurable ESR activity were pooled and solvent was evaporated to obtain **SSPC-3** as a dark red, oily polymer. **SSPC-3** was analysed *via* ESR, NMR, GPC and UV/Vis. GPC showed an apparent decrease in molecular weight and exhibited a slight increase in dispersity to $M_n = 7.4$ kDa, $D = 1.5$. Both were attributed to column-interactions. The important detail obtained from GPC analysis, was the loading control. As clearly visible in **Figure 3.20**, a significant increase in absorption at $\lambda = 500$ nm, the characteristic absorption maximum of Dox, becomes evident, as soon as the polymer is loaded. The elution times of RI-detectable polymer and Dox-absorption coincide exactly, proving the successful coupling of the drug to the carrier. As Dox is significantly smaller in molecular weight, it would elute at different times than the polymer. Since the **SSPC** backbone does not carry any light-absorbing groups in the same spectrum as Dox, it would not exhibit significant absorption in GPC.

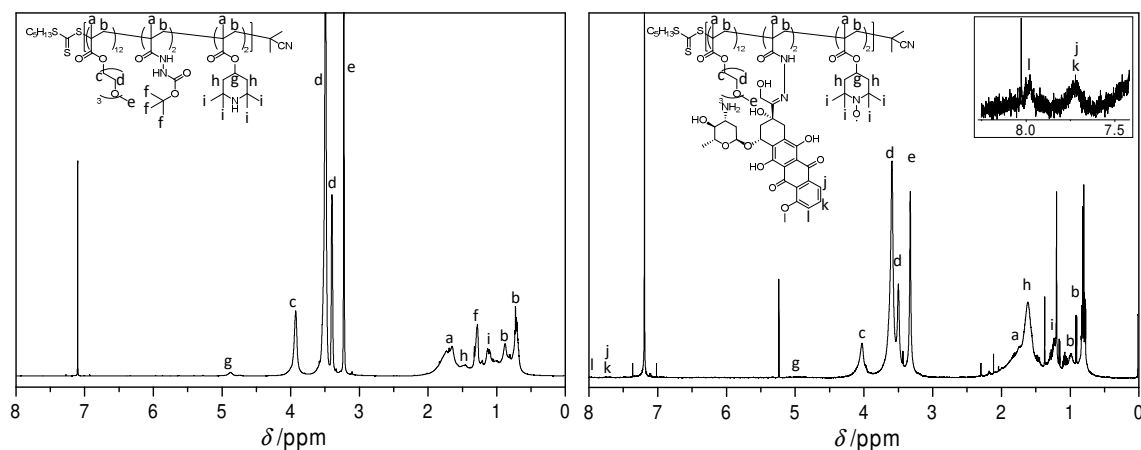


Figure 3.21: $^1\text{H-NMR}$ spectra of **SSPC-0** as a reference and **SSPC-3** after drug loading. The presence of Dox can be monitored by its characteristic aromatic resonances j, k, and l. Absolute quantification from the NMR spectrum was not possible, as nitroxide-related line-broadening leads to issues with integration. The inset on the right shows a zoom to the utilised peaks. Reproduced from [211] with permission from the RSC.

Absence of smaller molecules in both RI and absorption traces indicated high purity and no residual free drug in the analyte. Loading was investigated *via* $^1\text{H-NMR}$ and UV/Vis. The $^1\text{H-NMR}$ spectrum in **Figure 3.21** shows the appearance of resonances j, k, and l. NMR analysis suggests a degree of functionalisation of 22.5% in relation to the number of initially present hydrazides, determined from resonance f in **SSPC-0** (**Appendix, Table A 8.11**). As the spectrum shows clear evidence of nitroxide-related line broadening (signal distortion in the low field and significant broadening (e.g. barely detectable resonance g), UV/Vis spectroscopy was utilised to independently obtain a value for the grafting density. The latter indicated a loading of 25.6%, determined *via* the absorption at $\lambda = 495 \text{ nm}$ ($\epsilon_{495} = 10'000 \text{ L M}^{-1}$).^[105] In order to investigate the reporting efficiency of **SSPC-3**, a series of fluorescence measurements were carried out in a manner adapted from the protocols followed in **Section 3.4.1**, page 68. The polymer was dissolved in phosphate buffered saline (PBS) at $\text{pH} = 7.4$ and diluted to 3 mL at a final concentration of $6.25 \mu\text{g mL}^{-1}$. The concentration had to be chosen as low as possible in order to ensure both an ideal penetration by the incident light for excitation during measurement and minimal proximity quenching of released fluorophores in solution.^[218] In order to simulate the acidic conditions in a tumour, 30 μL of glacial acetic acid were added and fluorescence spectra of the solution were recorded over the course of the following seven days. **Figure 3.22** shows the fluorescence spectra as a function of time, clearly demonstrating the increase in fluorescence.

3. A Polymeric Nanocarrier for the Visualisation of pH-Triggered Release

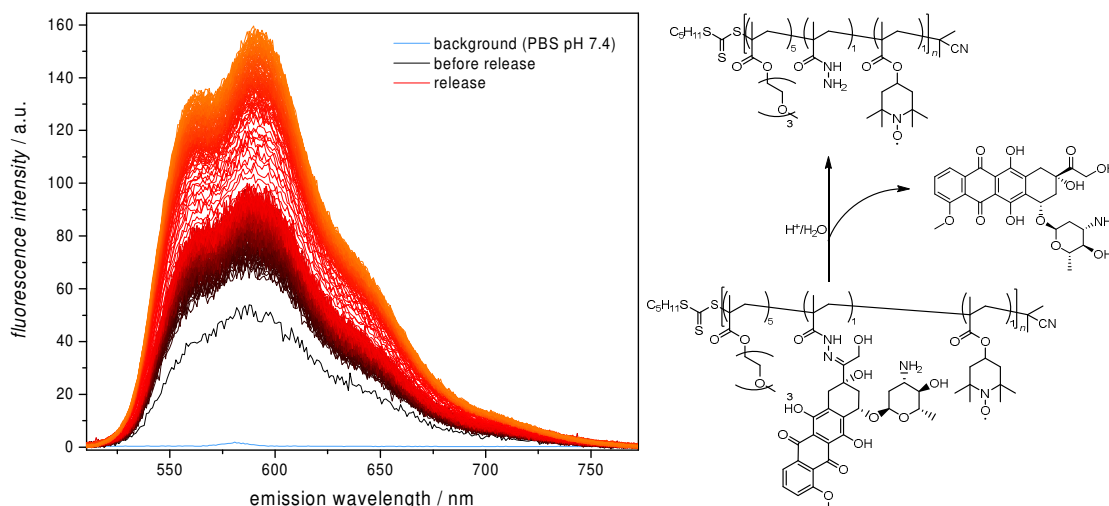


Figure 3.22: Fluorescence spectra acquired over the course of seven days. Time increments were increased every 12 h in order to be able to capture the longest uninterrupted timeframe possible. Upon acidification, a strong increase in fluorescence is observed immediately, rapidly increasing 2-fold over the course of the first hours. Lighter reds indicate later time points. Adapted from [211] with permission from the RSC.

To investigate the overall reporting efficiency, individual fluorescence spectra were integrated across the full width. The resulting values were used to investigate release rate and quenching efficiency. A negative control in PBS at pH = 7.4 was additionally measured over the same timeframe, to ensure the release is an actual response to the acidic trigger. An optically matched, freshly prepared solution of Dox·HCl was used as reference for a positive control to gain insight into the maximum fluorescence yield expectable under the employed conditions.

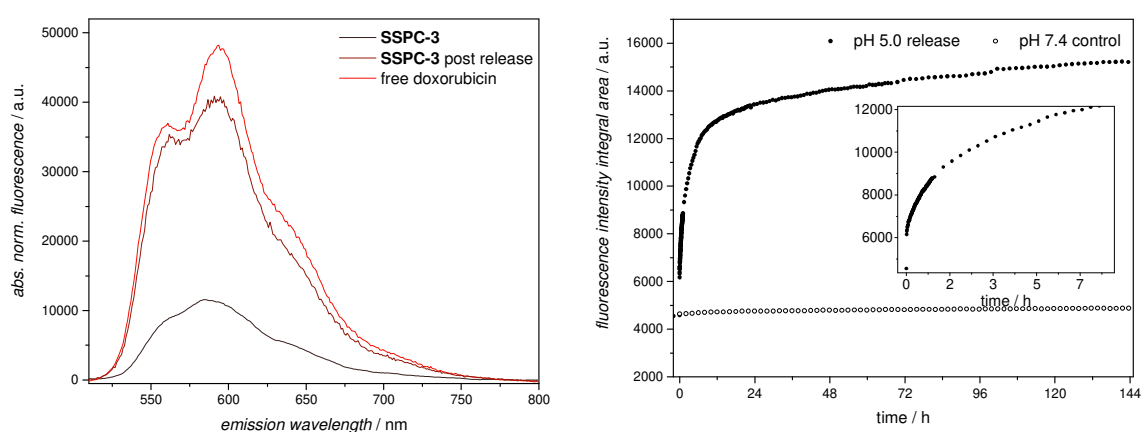


Figure 3.23: Comparison of SSPC-3 fluorescence before and after release, and free Dox in the same concentration. The graph on the right depicts the evolution of the total fluorescence integral over time in comparison to a solution at pH 7.4 (Figure 3.22). The inset shows a zoom of the first 8 h, indicating a strong burst release upon acidification. Reproduced from [211] with permission from the RSC.

Integration of the spectra in **Figure 3.23** showed a total increase in fluorescence by a factor of 3.6. A comparison with free Dox revealed a relative fluorescence yield of 23% before and 86% after release. The incomplete recovery of fluorescence was attributed to partial degradation of Dox over the course of 7 d. In addition, hydrazone formation and -cleavage are reversible processes, enabling the fluorophore in solution to reversibly interact with solute polymer and the bound nitroxides. The factor of 3.6 in quenching efficiency observed here is in perfect agreement with recent literature on covalently bound nitroxide/fluorophore pairs.^[58,146,147] To directly evidence the molecular release of Dox upon acidification, a set of bulk-release experiment was performed. For each run, 50 mg of **SSPC-3** were dissolved in 10 mL PBS at pH = 7.4 and sealed in a dialysis tube. Dialysis was carried out against a total of 7.5 L of PBS over the course of seven days, at pH = 5.0 for the release experiment, and at pH = 7.4. Dialysis solutions were exchanged daily and frozen, to avoid contamination or evaporation. After the experiments were completed, dialysis solutions for each experiment were merged and analysed *via* UV/Vis spectroscopy. As the acquired measurements turned out to almost reach the instrument's limit of detection and digital resolution, resulting spectra were smoothed with a Savitzky-Golay filter in a 20 point averaging window, in order to obtain a higher degree of precision.^[229] To ensure no data corruption by measurement error, the spectra were evaluated for more than one data point, ensuring the ratios match literature-known values (refer to the **Appendix, Table A 8.13**).^[68,230]

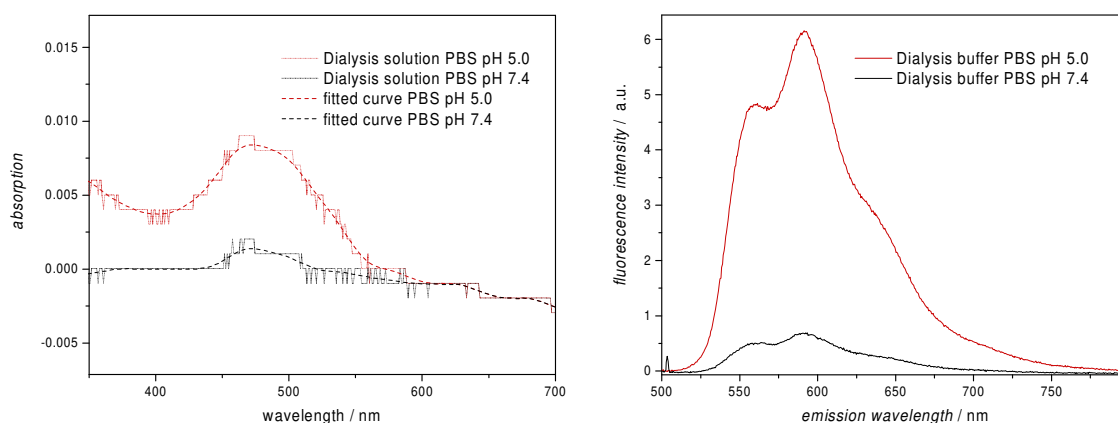


Figure 3.24: Left: UV/Vis absorption spectra employed quantify the release from 50 mg of **SSPC-3**. The spectra were smoothed in post-processing in order to obtain better resolution, as the low concentrations were just above the minimum level of detection. Right: Fluorescence measurements of the same solutions. A clearly stronger fluorescence signal can be detected for the acidic solution. Adapted from [211] with permission from the RSC.

The absorption spectra used for calculation are shown in **Figure 3.24** on the left. The acidic batch indicated a total release of 78% Dox in comparison to the total initial amount of drug bound to **SSPC-3**. The negative control at pH = 7.4 showed a mere 11% of unspecifically released Dox (refer to **Appendix, Figure A 8.32**). Additional fluorescence measurements of the buffer solutions supported this observation, with 11-fold more intense fluorescence detectable in the acidic buffer (**Figure 3.24**, right). Finally, in order to evaluate whether the results could have been influenced by polymer escaping the dialysis membranes, the dialysis solutions were analysed by ESR. Contrary to GPC, ESR provides excellent minimum levels of detection, making it an ideal method to investigate such highly dilute solutions. Neither acidic nor control solution showed any signs of nitroxide-presence, thus confirming all polymer had remained inside the dialysis tubes.

The results reported herein demonstrate an efficient way to construct a water-soluble polymer carrier for the self-reporting release of fluorescent drug-molecules. The polymeric assembly is stable over the course of weeks and exhibited high levels of stability even when transferred and handled under ambient conditions. Fluorescence turn-on occurs highly specific as soon as the polymer is exposed to an acidic environment and follows a predictable and reproducible kinetic. The ability to utilise the architecture for a broad range of fluorophores makes it a promising candidate for drug design. Fluorescence recovery is efficient enough to be detectable by the naked eye, as visible in **Figure 3.25**.

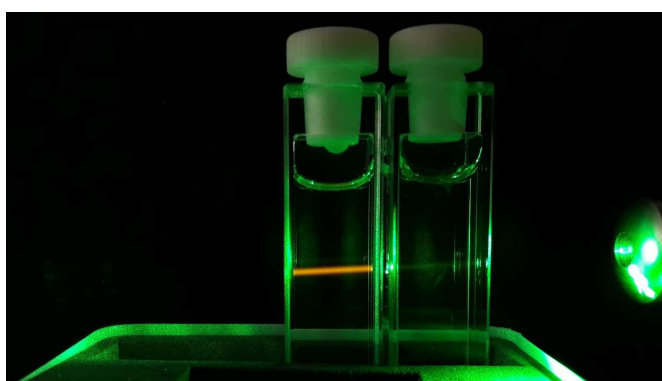
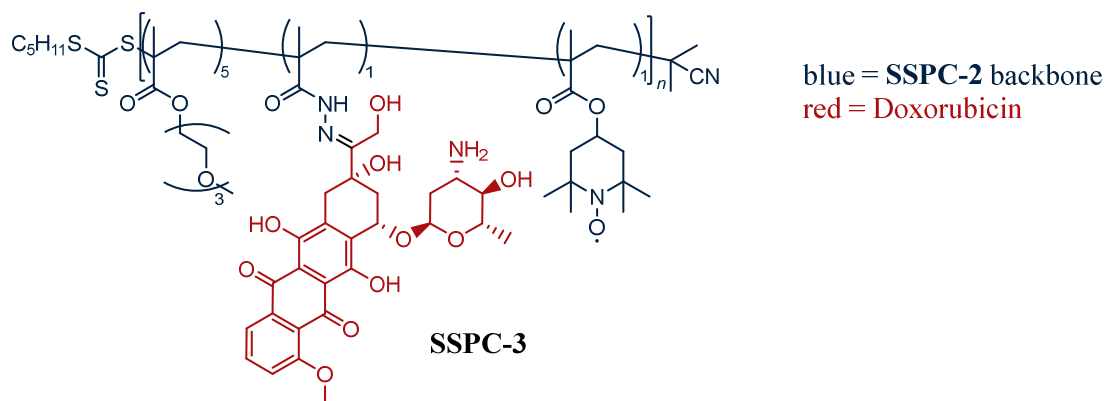


Figure 3.25: Cuvettes with **SSPC-3** before and after release. The visible orange fluorescence increases from barely visible to bright and easily detectable. Excitation was carried out with a green laser-pointer, visible on the right. Reproduced from [211] with permission from the RSC.

As the high specificity and fast release kinetics upon acidic triggering could be demonstrated too, the system was chosen to be tested in a biological application. The assembly was tested for efficacy in 2D and 3D cell culture and showed promising results in terms of uptake, distribution and toxicity (refer to **Section 3.5**).

3.5 BIOLOGICAL TESTING

After the capability to trigger and report release from the polymer backbone had been successfully established as described above, the bioapplicability of the **SSPC** assembly (refer to **Scheme 3.7**) had to be investigated.



Scheme 3.7: Chemical structure of **SSPC-3**. The **SSPC-2** backbone bears a hydrazide moiety, on which Dox is immobilised *via* hydrolytically cleavable hydrazone linkage.

Initial investigations encompassed the biocompatibility of the employed polymer backbone. Even though the general compatibility of TEGMA-based polymeric platforms has already been established in the literature numerous times, initial tests were thus carried out to evaluate the synthetic methods. As no toxicity or incompatibility between the general underlying structure of the polymer and cell-culture models could be detected (refer to **Appendix, Figure A 8.35**), the finalised nanocarrier was tested. The **SSPC-3** constructs were investigated in 2D culture in order to identify a suitable concentration-window for subsequent investigation in 3D cell cultures (refer to **Section 3.5.1**, page 84). Said 3D investigations started out with tumour spheroids to establish imaging protocols. Spheroids were subsequently co-cultured with fibroblasts, simulating more tissue-like environments for the tumour, allowing observations of **SSPC-3** efficacy in a physiological environment. Ultimately, co-cultures should be transferred to vasQchips, a vascular model reactor, developed at the ITG, Karlsruhe.^[139] The chips incorporate an artificial, porous blood vessel including cultured confluent endothelium, embedded in a hydrogel, hosting a co-culture of fibroblasts, and tumour spheroids. A detailed description of culture systems and the chip architecture is presented in **Section 2.4.3**, page 37. The setup allows for the investigation of passive and active transport of small and macromolecular assemblies from fenestrated vasculature through the surrounding tissue into the tumour. A promising attribute of 3D culture is the more tissue-like structure. Traditional cell culture approaches in polyethylene culture-

flasks or petri dishes lack interactions between different cell types, effectively depriving them of relevant environmental factors such as a naturally formed extracellular matrix and intercellular signalling.^[231] Classically this problem is solved by running tests in animal models, in which live animals, such as rodents are used to gain insight into the interaction between drugs and mammalian cells.^[133] As animal testing is earning increasing amounts of criticism for both ethical reasons (testing animals have to be sacrificed after experiments are finished) and results of inconsistent significance for medical applications, the search for alternatives has become a critical topic in recent years.^[124,232–234] As the **SSPC** platform delivers a theranostically relevant combination fluorescent anticancer drug and NO-analogue in one architecture, its applicability was investigated in spheroid systems. Bio-testing of the **SSPC-3** assembly in comparison to free Dox, as well as a novel method to quantitatively evaluate confocal laser scanning microscopy (CLSM) images is described in the following three sections.

3.5.1 2D Experiments⁴

Firstly, biocompatibility of the polymer backbone itself needed to be established. To this end, pTEGMA and **SSPC-2** were tested in HeLa cell cultures. Investigation *via* MMT viability assays returned no significant toxicity of the polymeric assembly (**Appendix, Figure A 8.35, Figure A 8.36**). In order to establish conditions for later testing of the final **SSPC-3** construct in spheroids, HepG2 and SK-MEL-28 cell lines were cultured in 2D cell culture by established protocols (refer to **Section 7.3.6**) and incubated with **SSPC-3**, free Dox·HCl for investigation of efficacy, **SSPC-2** and 5 vol% DMSO/PBS as negative controls. Concentrations (1, 5, 10, 20, and 50 μM) were normalised for Dox-content or the respective amount of polymer. Cell viability was investigated *via* MTT assay and microscopy. The main criterion for suitability was a measurable impact on cell viability, yet clearly visible remaining, to enable the microscopy of living cells. Detectability of Dox fluorescence in microscopy was an additional requirement, to enable later quantification of Dox uptake in 3D cultures *via* microscopy imaging.

⁴ Cell culture handling was carried out in collaboration with the ITG, KIT, by Dr. Bettina Olshausen (HeLa) and Dr. Vanessa Kappings (HepG2, SK-MEL-28).

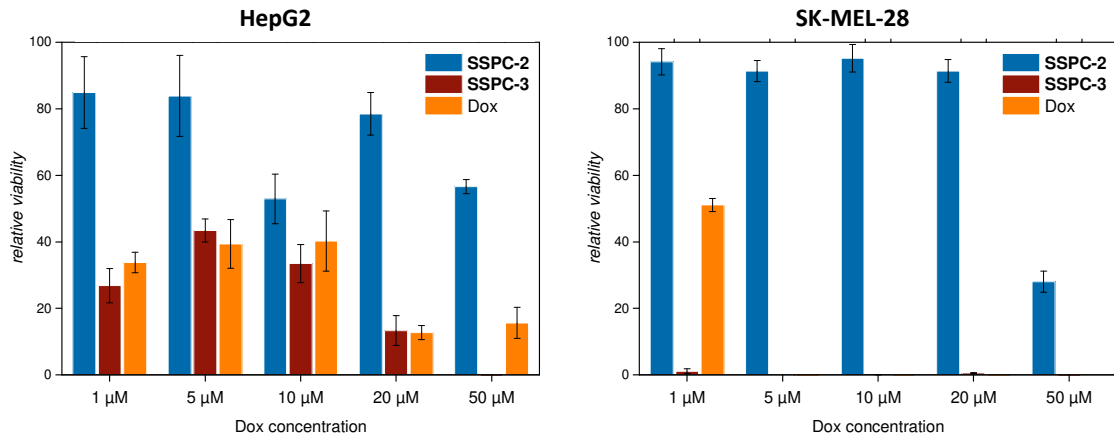


Figure 3.26: MTT viability assay results of HepG2 and SK-MEL-28 cells. A significantly elevated susceptibility of SK-MEL-28 to both free Dox and the **SSPC-3** assembly is evident in comparison to HepG2-cells. In both cell lines viability is decreased in the case of **SSPC-3** incubation. Up to the highest tested concentrations, no significant toxicity of the unloaded **SSPC-2** backbone can be detected.

MTT viability assays showed that a concentration window of 1-50 μM will fulfil the requirements of viable cells and detectable uptake. The results presented **Figure 3.26** indicate greater susceptibility of SK-MEL-28 cells to both the free drug and **SSPC-3**, with only little influence of the unloaded **SSPC-2** backbone on cell viability. As an increase of cell viability and drug resistance was to be expected in 3D experiments, the concentration range was deemed a suitable starting point for investigations in spheroidal 3D cultures.

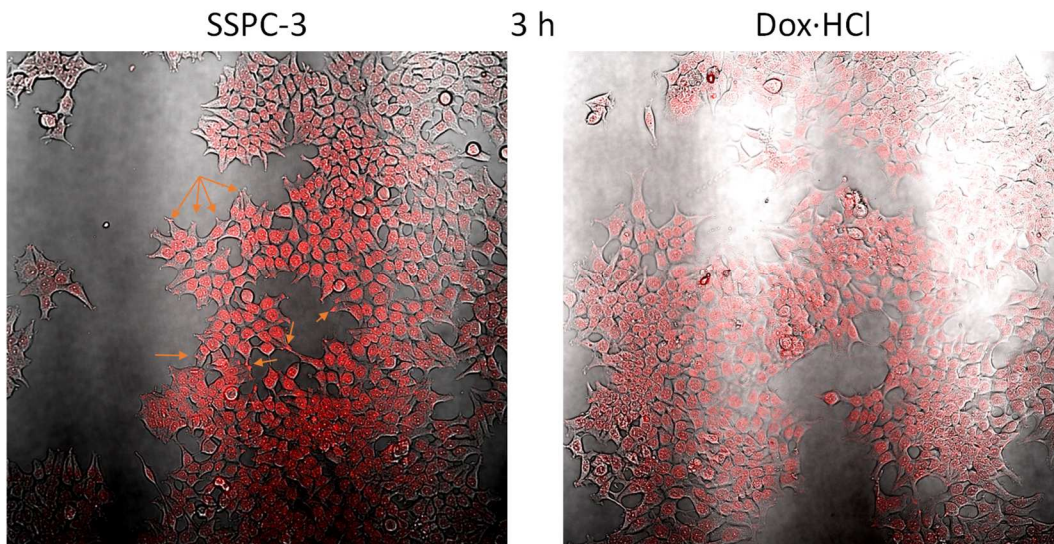


Figure 3.27: CLSM imaging of 2D HepG2 cell culture after 3h of incubation with **SSPC-3** or Dox·HCl. Arrows highlight sites of highly localised fluorescence outside the cell nuclei.

Microscopy of HepG2 cultures indicated vesicular uptake of the polymeric assembly (refer to **Figure 3.27**, highlighted by arrows), visible by highly localised fluorescent clusters in the cytosol. Fluorescence was predominantly located in the nucleus area after 3 h already, indicating release of Dox from the polymer and effective shuttling to the nucleus. Images taken after 24 h of exposure showed concentration of fluorescence in vesicles, with cell viability decreasing, as visible from a more spherical, less adherent shape.^[235]

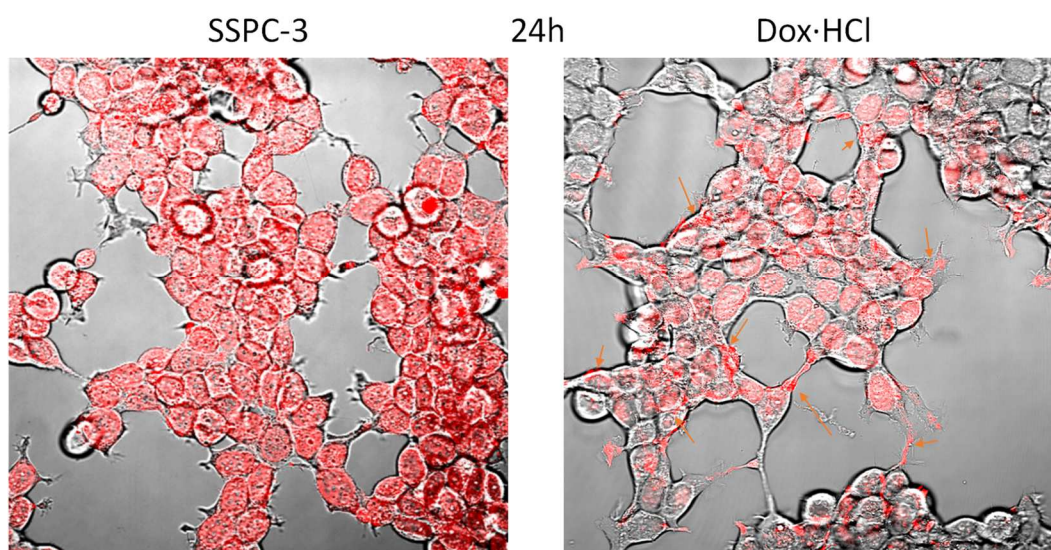


Figure 3.28: CLSM imaging of 2D HepG2 cell culture after 24 h of incubation with **SSPC-3** or Dox·HCl. Arrows highlight sites of highly localised fluorescence outside the nuclei, indicating long-term storage of Dox in vesicles.

As visible from **Figure 3.28**, long-term exposure resulted in a drastic increase of fluorescence in the nucleus of HepG2, when incubated with **SSPC-3**. Cells incubated with free Dox exhibited fluorescent nuclei, with brightly fluorescent spots visible outside of the nucleus, indicating the accumulation of Dox in vesicular structures. The results are in agreement with the viability assays (**Figure 3.26**), where **SSPC-3** exhibited slightly increased efficacy. The findings additionally suggest that either the macromolecular structure of **SSPC-3** or the presence of nitroxides on the **SSPC** platform play a role in cellular uptake and intracellular distribution.

The visible difference in fluorescence indicates that the polymeric assembly does in fact have an impact on uptake. The presence of Dox-fluorescence in the nuclei unambiguously confirms significant release from the polymer backbone. Initial *ex vivo* experiments for testing release conditions had indicated a timeframe, which should be observable by

CLSM techniques. Time-resolved observation of the release of Dox from the **SSPC-3** platform in cell culture was attempted, yet release events could not be quantified as temporally precise as in the *ex vivo* pre-tests. These findings combined indicate that a refinement of imaging-techniques would enable insight into the intracellular transport- and release-mechanism. The investigation of these processes should be tackled in future works. As the obtained results could successfully show efficacy of the polymeric assembly, further investigations were carried out in 3D culture, described in **Section 3.5.2**, page 88.

3.5.2 3D-Experiments⁵

Based on the 2D results described in **Section 3.5.1**, two lines of spheroids (HepG2 and SK-MEL-28) were investigated for their uptake of **SSPC-3** in comparison with free Dox. Spheroids were grown *via* procedures, previously established in the group of Prof. Ute Schepers, as outlined in **Section 7.3.6**. Spheroids of an average size of 500 μM , grown for a total of 7 d were employed in all experiments described in this **Section**. Exemplary specimens are shown in **Figure 3.29**.

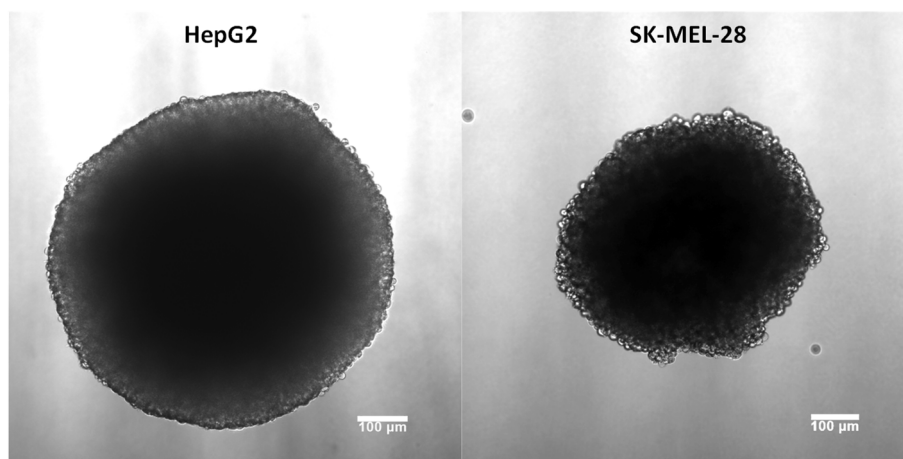


Figure 3.29: Bright-field confocal microscopy images of spheroids, grown for 7 d after 3 h of incubation with pure buffer. Differences in density and structure are clearly identifiable: HepG2 spheroids (left) form denser and more solid spheroids in direct comparison with identically treated SK-MEL-28 spheroids (right). Growth proceeds at a higher rate, yielding spheroids of 15-20% greater diameter on average. The darkened central area of both spheroids represent the necrotic core, where hypoxic conditions lead to a high prevalence of quiescent and necrotic cells.

The bright-field microscopy images in **Figure 3.29** demonstrate the spherical nature from which spheroids derive their name. An important histological feature can be observed from the outer areas of both spheroids. While HepG2 cells grow dense, highly homogenous spheroids of small, tightly connected cells, SK-MEL-28 cells assemble into more loose, slightly less ordered clusters, made up from cells of greater diameter. This attribute is of great relevance in the evaluation of molecular uptake into both the spheroid on a macroscopic and individual cells and subcellular structures on a microscopic level.^[133] HepG2 was expected to exhibit an uptake-bias for molecules of different sizes, due to decreased permeation rates of larger molecular assemblies, owed to the tighter structure of the spheroid.

⁵ Spheroid and co-culture handling was carried out in collaboration with Dr. Vanessa Kappings, ITG, KIT.

roid. As investigations presented in this section were focussed on Dox·HCl as a small molecule and **SSPC-3**, a macromolecular poly-methacrylate-based drug transporter, different effects on molecular transport, uptake and localisation were of special interest. Additionally, the images in **Figure 3.29** critically highlight an inherent phenomenon in microscopic imaging investigations of 3D cell culture. The spheroid core, being necrotic due to hypoxic conditions and insufficient supply with nutrients, mostly consists of dead and quiescent cells. Due to dense layers surrounding the core, it is potentially obscured to both confocal bright-field imaging and excitation lasers for fluorescence microscopy.^[236] During investigation of drug-penetration depths *via* fluorescence microscopy, excitation bias towards the outer regions must be taken into account. Differences between small molecules and polymeric assemblies could therefore only be evaluated in a relative fashion.^[236]

To establish transferability of the results obtained from 2D experiments and viability tests described in **Section 3.5.1**, page 84, MTT cell viability tests were carried out with both HepG2 and SK-MEL-28 spheroids and the results are shown in **Figure 3.30**.

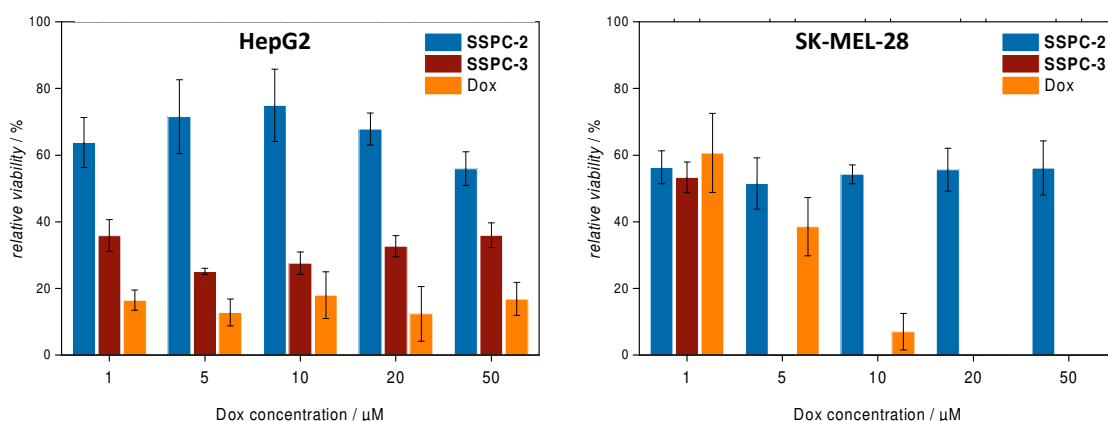


Figure 3.30: Results of MTT viability assays of HepG2 and SK-MEL-28 spheroids, used to investigate transferability of 2D-culture findings to 3D-culture experiments. Cells were incubated for 72 h in the shown concentrations (refer to **Section 7.3.6**) HepG2 spheroids (left) exhibit increased susceptibility to free Dox in comparison to **SSPC-3**. Viability appears uninfluenced by Dox concentration for both the free drug and **SSPC-3**. SK-MEL-28 spheroids exhibit overall higher susceptibility to both free Dox and **SSPC-3** in comparison to HepG2 spheroids, with increased susceptibility towards **SSPC-3**. Polymer backbone concentration does not appear to influence viability in any case.

The MTT viability assays of HepG2 spheroids indicated decreased viability in the presence of free Dox compared to **SSPC-3**. No clear influence of the total Dox concentration was observed. The result can be explained by the dense nature of HepG2 spheroids

(refer to **Figure 3.29**). Diffusion is subject to the nature of a compound's surrounding medium. In the case of HepG2 spheroids, very little room for diffusion hinders cellular uptake. As a result, the relative drug efficacy is decreased. The assumption is supported by a lack of concentration-dependence, suggesting diffusion into the spheroid to be the limiting factor. This is in agreement with recent findings, indicating that penetration plays a significant role for drug efficacy in spheroids.^[237]

The finding is underpinned by MTT results from SK-MEL-28 spheroids in **Figure 3.30**. Here, significantly increased susceptibility to Dox-exposure, in comparison to HepG2 spheroids, is indicated. The spheroids exhibit elevated susceptibility to **SSPC-3** with a clear dependence on concentration. Decreased spheroid density would promote uptake across a greater region of the spheroid. These findings additionally suggest an overall increase in uptake of the transporter, where diffusion is not a limiting factor.

As MTT assays are additionally dependent on uptake of the MTT reagent, these viability assays can only be utilised to estimate suitability of reaction. As neither actual uptake nor penetration depth can be judged from the results of a viability assay, spheroids needed to be examined *via* microscopy. Penetration depth and uptake were investigated *via* CLSM imaging and subsequent evaluation of the acquired fluorescence images. All acquired images for all tested concentrations of **SSPC-2**, **SSPC-3** and free Dox·HCl are compiled in the **Appendix, Section 8.1.9**, page 188.

Spheroids were incubated with **SSPC-3**, **SSPC-2**, Dox·HCl and buffer solutions of 1, 5, 10, 20 and 50 μM Dox concentration of **SSPC-3** equivalent polymer solution. CLSM imaging shown in **Figure 3.31** exhibited elevated overall fluorescence in spheroids incubated with **SSPC-3**. In order to gain deeper insight into distribution and obtain more quantitatively comparable data, equatorial slices were evaluated for their fluorescence intensity. Results are shown in **Figure 3.32**.

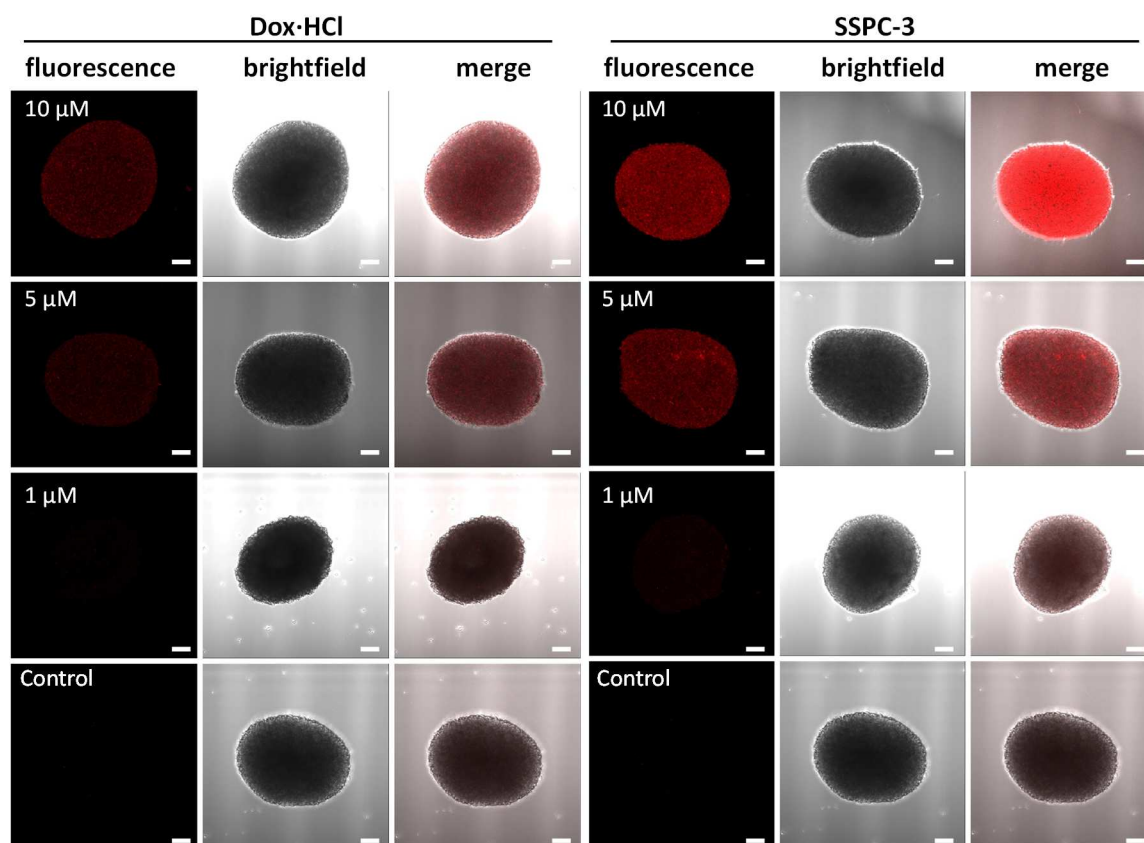


Figure 3.31: Comparison of HepG2 spheroids, DIV 7, incubated with free Dox or **SSPC-3**. Scale bars are 100 μm . An increased level of Dox-fluorescence can be observed in the case of **SSPC-3** (right), indicating elevated uptake when the drug is conjugated to the nitroxide-bearing polymer.

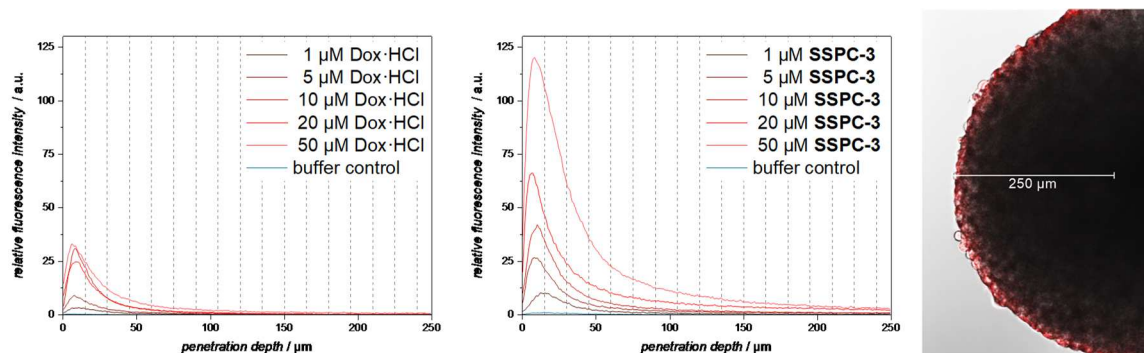


Figure 3.32: Penetration profiles of Dox·HCl and **SSPC-3** into HepG2 spheroids. The image on the right shows a spheroid incubated with 20 μM **SSPC-3** for size reference. Dashed grid lines in the graphs indicate cell layers. The profiles demonstrate strongly increased fluorescence in the case of **SSPC-3**. Fluorescence scales evenly with increasing concentration, indicating a predominantly diffusion-dependent uptake into both the spheroid and the cells.

Profiling of the acquired images showed a contrasting result to the viability assay. Dox uptake appeared to reach saturation at a comparatively low concentration around 10 μM , as clearly visible from the penetration profiles in **Figure 3.32**. Uptake of **SSPC-3** showed linear dependency on concentration with no sign of saturation effects and significantly higher overall uptake. This supports the assumption of different routes of uptake and incorporation into the spheroid for free and polymer-bound Dox. All observations from testing carried out on HepG2 cells and spheroids suggest an important involvement of the polymer bound TEMPO on intra- and intercellular of the assembly. If active transport into and possibly through the spheroids plays an important role in drug distribution, toxic effects on first contact with the drug would drastically decrease efficacy. The polymer's TEMPO moieties can suppress oxidative stress and could thus allow cellular transport mechanisms to remain functional for an extended time. The assumption drawn from these results is in agreement with previous findings from the literature and needs to be investigated in more detail in the future.^[64,75,170,238]

In order to test the assumption that spheroid penetration is not solely dependent on diffusion, but involves nitroxide interaction with the tissue, additional testing was carried out on SK-MEL-28 spheroids. The looser organisation of SK-MEL-28 spheroids suggests a decreased contribution of active transport effects on spheroid permeation of the drug. Images were acquired and evaluated in analogy to HepG2 spheroids.

Microscopy of SK-MEL-28 spheroids indicated a similar trend of elevated uptake for the polymeric drug as in HepG2 spheroids. The CLSM images shown in **Figure 3.33** indicate elevated increased levels of fluorescence even under direct observation. Spheroids grown from SK-MEL-28 exhibited slower growth-rates and generally produced smaller, spheroids of 300-400 μm in diameter. The increased cell-diameter of about 20 μm additionally resulted in less homogenous structures in comparison to HepG2 spheroids. This additionally yields an explanation for the increased susceptibility of SK-MEL-28 spheroids towards both polymeric and free drug: decreased diameter inherently increases the ratio of surface area over volume, automatically exposing a spheroid's cells to higher doses of drug molecules in the surrounding media at identical concentrations. In order to obtain deeper insight into drug penetration, fluorescence images were analysed for their equatorial fluorescence profiles.

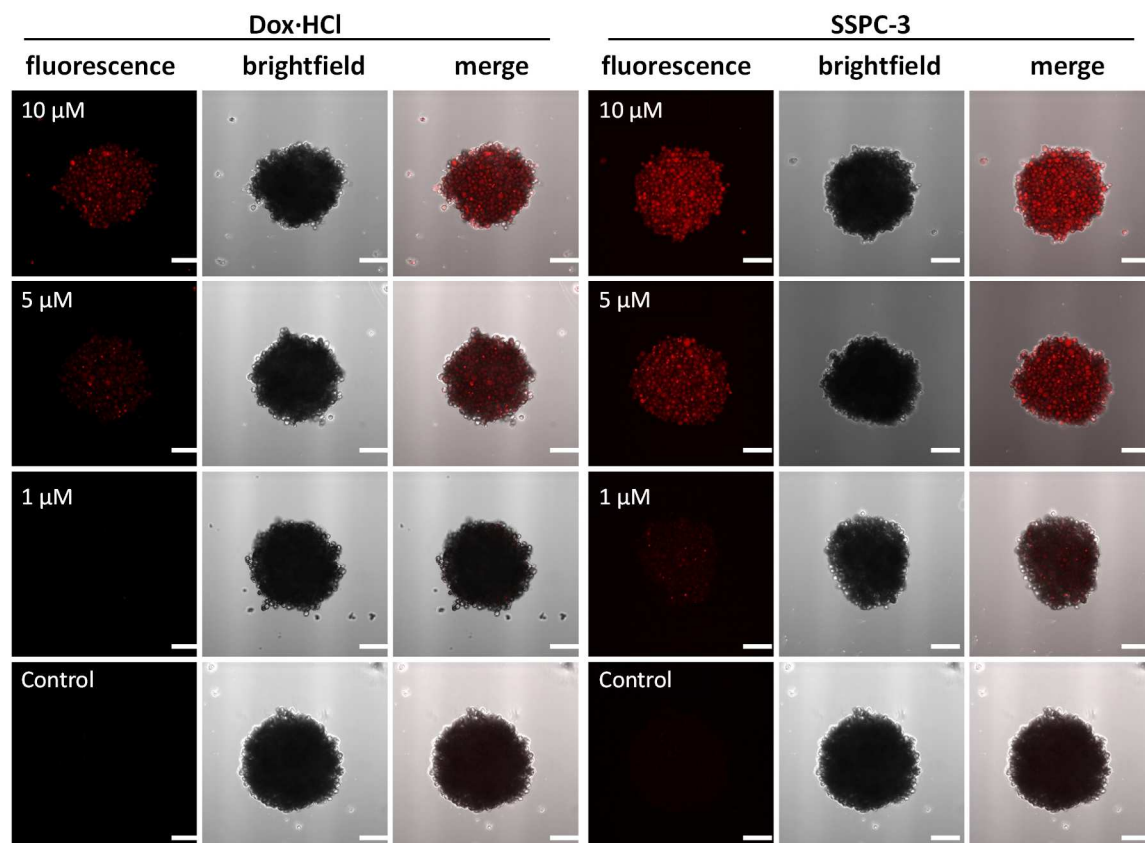


Figure 3.33: Comparison of SK-MEL-28 spheroids DIV 7, incubated with free Dox or **SSPC-3**. An increased level of Dox-fluorescence can be observed in the case of **SSPC-3** incubation, indicating elevated uptake when the drug is conjugated to the nitroxide-bearing polymer. Scale bars are 100 μm .

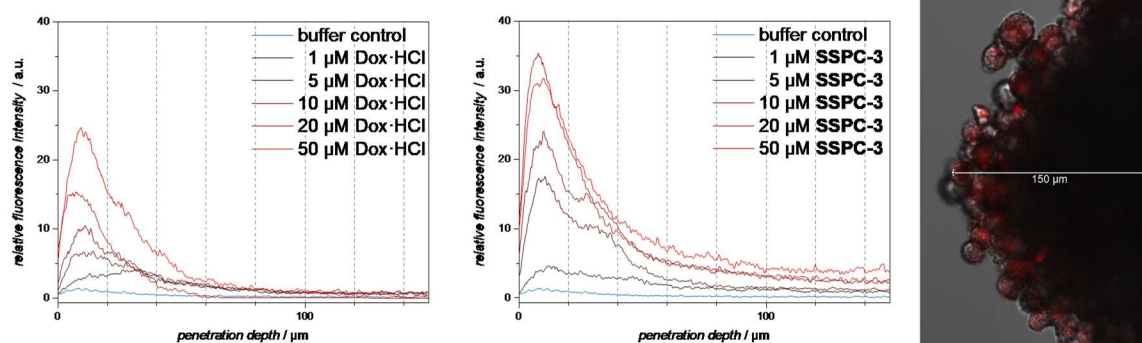


Figure 3.34: Penetration profiles of Dox·HCl and **SSPC-3** into SK-MEL-28 spheroids. The image on the right shows a spheroid incubated with 5 μM **SSPC-3** for reference. Dashed grid lines in the graphs indicate cell layers. The profiles exhibit strongly increased fluorescence in the case of **SSPC-3**. Additionally, penetration depth remains broader over a wider range of concentrations, as visible by a persistent, second mode in the distribution of ca. 20-40 μm penetration depth for the polymeric assembly. Fluorescence increase reaches a plateau at a concentration between 20-50 μM drug equivalent in the case of **SSPC-3**.

The profiles shown in **Figure 3.34** confirm the assumptions made from both MTT viability test and qualitative optical analysis of the fluorescence images: All concentrations indicated similar levels of penetration with both maxima and distribution width in the range of two cell-layers in thickness. The overall fluorescence integrals increased with higher concentrations, indicating concentration-dependent uptake in all exposed cells. Uptake rates exhibit saturation effects, with no further increase in a concentration range of ca. 50 μM for polymeric assemblies. Uptake of free Dox remained comparatively low with increasing concentration. Differences in uptake of free and polymer-bound Dox decreased to less significant levels at higher concentrations.

An interesting feature of the obtained penetration profiles can be seen in the area of the second and third cell layer towards the core (**Figure 3.34**). While areas, located in deeper regions of the spheroid readily exhibit comparatively high levels of fluorescence at low concentrations, the profile-shape does not scale with increasing concentrations. Exposure to higher concentrations of both free and polymer-bound drug predominantly influences fluorescence in the outermost layer of cells. The effect scales to higher concentrations in the case of **SSPC-3**, indicating an influence of molecular size on the rate of uptake, and likely on the pathway of uptake. As 2D experiments already indicated uptake of the **SSPC-3** assembly in a vesicular manner, this hints at a vesicular shuttling mechanism, where outside layers shuttle compounds to the inner cells *via* vesicle secretion. This would be in agreement with recent findings from the literature, where anticancer drug resistance has been linked to exosomal clearance from stromal cells.^[69,239–241]

As the results from *in vitro* spheroid experiments showed a promising trend of elevated uptake of the **SSPC** platform over free Dox, further investigations were carried out in 3D co-cultures. SK-MEL-28 and NHDF (normal human dermal fibroblast) cells were chosen for this approach, remotely recreating a 3D culture, similar to the natural environment of human skin melanoma.^[233,242] SK-MEL-28 spheroids were co-immobilised with 10%_n NHDF cells in a GelMA matrix, in order to gain insight into co-cultural behaviour. Co-cultures were incubated with 10 μM Dox equivalent by topping the co-culture with a solution of each sample (free Dox·HCl, **SSPC-2**, **SSPC-3**, buffer) for 24 h.

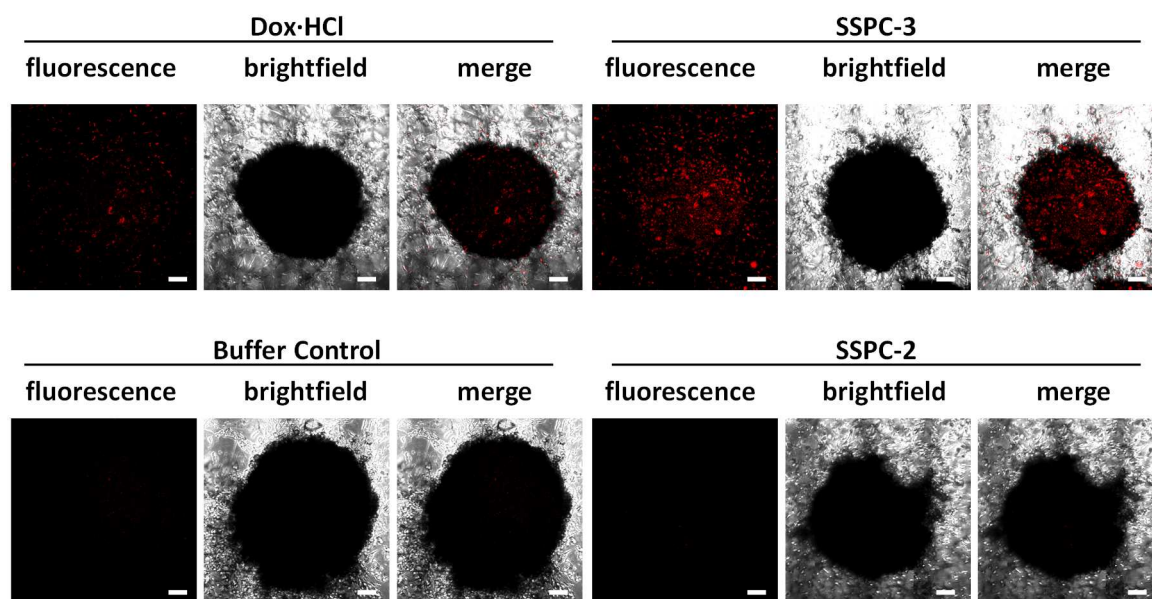


Figure 3.35: Microscopy images of SK-MEL-28 spheroids in co-culture with NHDF cells in a GelMA matrix, DIV 7. Incubation with free Dox also yields fluorescent cells in the spheroid. Spheroids show a clear increase in fluorescence in comparison to NDHF cells when exposed to the **SSPC-3** carrier. Images of the buffer control and unloaded **SSPC-2** were used for background determination.

CLSM imaging shown in **Figure 3.35** demonstrated increased fluorescence in both spheroids and fibroblasts after incubation with Dox·HCl or **SSPC-3** for 24 h. Localisation appears to be mostly homogenous in the case of Dox·HCl. Images of the co-cultures incubated with **SSPC-3** exhibited visible fluorescence bias, with elevated levels in the spheroid area, indicating elevated uptake of the polymeric assembly into the spheroid. Uptake appears to proceed in a more nucleus-directed way, visible by elevated localisation of fluorescence in comparison to more evenly distributed fluorescence seen in free spheroids (**Figure 3.31** and **Figure 3.33**). The more directed uptake was linked to more natural behaviour of the spheroids in a cultured environment, which could be demonstrated in previous works on this co-cultural composition.^[62] Precise quantitation and profile generation was not possible in the same way as in isolated spheroids due to an inherent issue of 3D imaging of co-cultures: The three-dimensional nature of the acquisitions inherently leads to brightly fluorescent NHDF cells, which are visible inside the spheroid area, and cannot be isolated in many cases. The spheroid area is determined from the bright field channel, which is unselective for spheroids or free NHDF cells, resulting in artefacts during evaluation due to overlaps. The issue can be alleviated by a staining approach, which would allow precise identification of different cell types and subdivision into different geometric regions of a

confocal image. As the clear increase in uptake of **SSPC-3** into the spheroid indicates a success in transporter design, further investigation of the assembly needs to be carried out. Real-time imaging of molecular release could not be completed and future efforts need to be focussed on the investigation thereof. This should also elucidate the conditions and pathways under which the transporter is taken up. Initial work on the construction of a directly traceable transporter to facilitate these endeavours is described in **Section 3.6**, page 100, and **Section 3.7**, page 103. The difference in uptake observed in both the comparison between SK-MEL-28 and HepG2 spheroids and the difference between free and polymer-bound Dox make the **SSPC** assembly a promising system to highlight differences in uptake. Critically, a clear increase in uptake of the **SSPC** platform in comparison to free Dox could be demonstrated in all tested systems. More work needs to be carried out on the investigation of the involvement of TEMPO incorporation in uptake-routes. Bioreactor experiments are in progress and remain subject to further investigation, ideally revealing the performance of SSPC-type polymers in a more complex biological environment.

3.5.3 Development of a Method for the Investigation of Penetration-Depth

In order to evaluate drug penetration into spheroids, a method for quantification had to be developed in parallel to imaging experiments. A reason for this is manifested in the physical nature of spheroids: structural inhomogeneity in the shape of an analysed image is inherent to naturally grown structures such as tumour spheroids can only yield inhomogeneous datasets. As reported in the literature, both size and shape of spheroids have an impact on the results obtained from spheroids and – although often neglected – need to be taken into account.^[133] Although quantification of uptake is monitored in many studies involving spheroidal 3D cultures by the total overall fluorescence integral from confocal imaging,^[93,130,243,244] distributions are only investigated in rare cases.^[133,135,136] The most commonly encountered method for quantitation of penetration are cross sections along images or profiles, taken radially from the spheroid's center.^[133,135,136] Aside from one example,^[133] where the focus was laid on the value and reproducibility of spheroid results specifically, previous works from the literature rarely discuss their quantification method in depth. One of the questions to be investigated in this thesis was the penetration profile of free Dox and the **SSPC-3** transporter assembly. In order to obtain such profiles with a higher degree of reliability than single cross-sections of the acquired microscopy images, a method needed to be developed, which would allow access more reproducible data than the traditional approach.

Based on findings from recent literature, where it has been shown that sectional imaging of spheroids of around 650 μm in diameter can be achieved in traditional CLSM imaging,^[133] a mathematical method was developed to obtain penetration profiles from CLSM cross sections. The step was crucial, as there are no readily available software solutions in existence to carry out this task. Although most software suites for confocal microscopy imaging are capable of determining fluorescence profiles along boxes or lines, these methods do not account for inhomogeneity and paths and areas need to be manually picked and adjusted for every individual measurement in every image. This process is time-consuming and has repeatedly been shown to be highly susceptible to chance and operator error.^[245] A detailed step-by-step description of the procedure can be found in **7.3.7**, page 155. The listings of the MatLab scripts used to carry out the evaluations are located in the **Appendix, Section 8.1.10**, page 194.

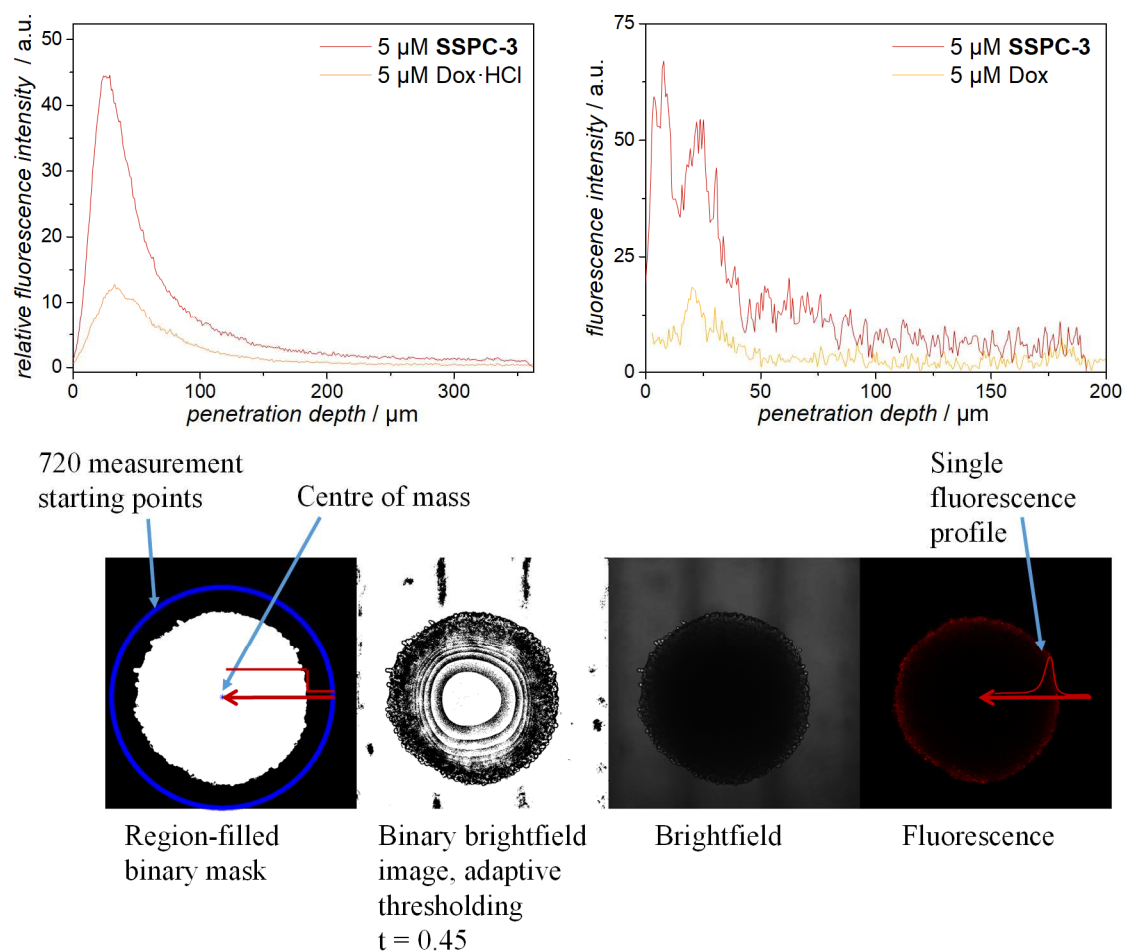


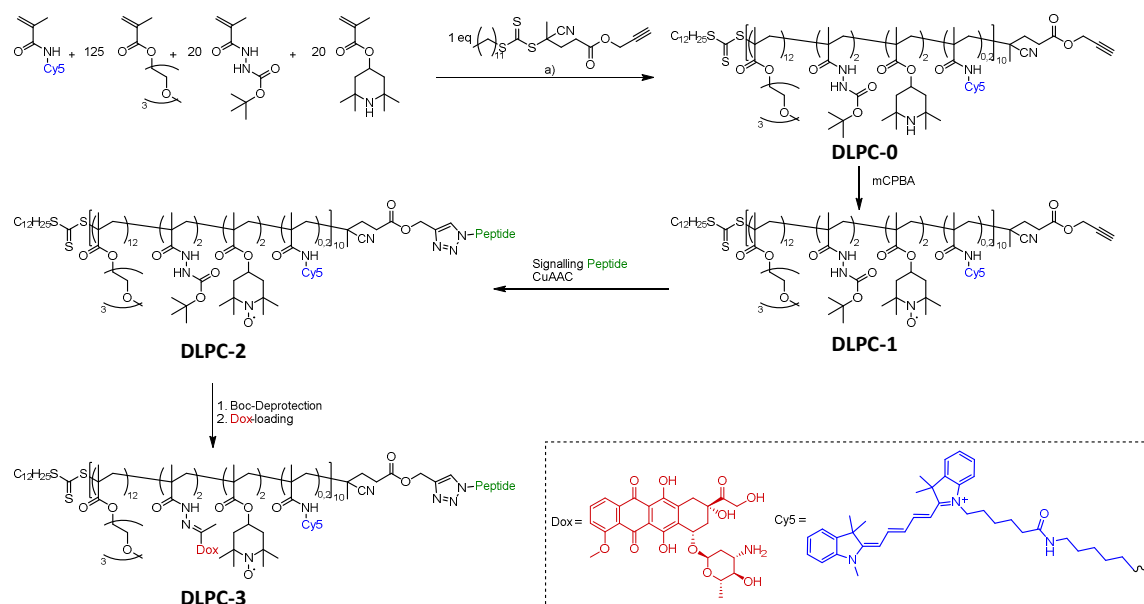
Figure 3.36: Comparison between penetration-profiles obtained by averaging eight manually measured profiles across a single HepG2 spheroid (right) and the averaging of 720, distance-aligned profiles from the same image (left). As clearly visible, manual acquisition of such profiles retains a significant level of noise. Poor alignment of measurements before averaging leads to artefacts like multiple maxima and distribution broadening. Artefacts, measurement noise and measurement background can efficiently be eliminated by acquisition of a high number of profiles before averaging, as visible on the right. Original images are shown in the bottom row, with the left two pictures representing masking layers, utilised to obtain averaged profiles. Refer to **Section 7.3.7**, page 155 for a detailed description of the procedure.

Quantification was performed on confocal images, displaying the equatorial section of each spheroid. In brief, the bright field channel of each acquisition was used to generate a binary mask *via* adaptive thresholding.^[246] The mask was subsequently used to determine the centre of mass of the spheroid (**Figure 3.36**, bottom left, blue stars) by methods from the literature.^[132] Additionally, the mask was used to designate areas of the image to spheroid (white) and background (black). Both steps were adapted from established methods automated image processing.^[133,246,247] Around the centre of mass, a circle of defined radius was chosen for evaluation (blue rings around spheroid area). Visual feedback was provided

along the whole evaluation process, in order to ensure a perfect match of mask and source image. Along the radius, penetration profiles were measured, acquiring datasets a circular manner in 0.5° increments from both fluorescent image and mask. The obtained profiles were concatenated, aligned by the information obtained from the mask image and averaged to yield penetration profiles as shown in **Figure 3.36**. Background correction was performed by firstly averaging the background segments of all profiles, determining a noise floor as the mean value across the whole background. The noise-floor was thus obtained as a constant for each image and subtracted from the profile. As clearly visible from the profiles shown in **Figure 3.36**, this could reduce noise significantly. It additionally corrected the inherent misalignment of individual measurements before quantification as an error source. The latter is of crucial, yet often neglected relevance, as it allows to judge penetration precisely from the actual interface between the outermost layer of cells and the surrounding media, instead of just the distance to the spheroid's centre. The method could reliably and reproducibly yield profiles for all evaluated microscopy images. All penetration profiles listed in this chapter have been acquired by the presented method and used for quantitation of spheroid-penetration and molecular uptake.

3.6 INCORPORATION OF A SECONDARY FLUORESCENT TRACKER

For medical purposes, an orthogonal, ideally IR-active fluorophore would be needed, as penetration depth is directly tied to wavelength, with light of longer wavelengths reaching depths of up to 5 cm in the visible spectrum.^[248,249] Based on published examples by Thurecht et. al., a system was designed to incorporate a cyanine dye *ab initio*. Amino-cyanines are commercially available, as they are widely employed in biological applications for labelling and tracking of molecular structures,^[250] thus providing an ideal precursor for methacrylamides for the statistical incorporation into the **SSPC**-type polymer backbone. The synthetic approach was designed to follow the same strategy as before, with the addition of a small amount of Cy5-MA in the first step. Additionally, the RAFT agent was changed to an alkyne-bearing trithiocarbonate, enabling the facile coupling of a signalling peptide for specific targeting of either specific organs or subcellular localisation.



Scheme 3.8: Synthetic strategy for the incorporation of targeting (green) and tracking (blue) moieties into an **SSPC**-type platform.

Cy5-MA was synthesized analogously to previous monomer syntheses and yielded good yields after purification. The RAFT agent was synthesised by literature-known protocols.^[71] Polymer synthesis was carried out in analogy to the **SSPC**-system described in **Section 3.4.2**, page 74, yielding **DLPC-0** as a blue oil. Monomer incorporation was investigated *via* ¹H-NMR.

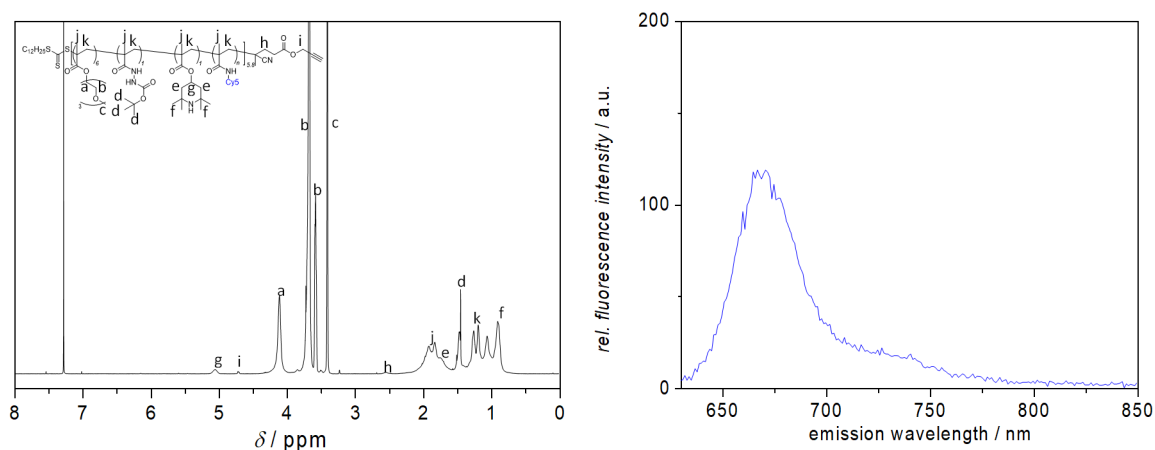


Figure 3.37: ¹H-NMR and fluorescence spectra of **DLPC-0**. As incorporation of Cy5 appeared to be too low to be visible in NMR, its incorporation was successfully confirmed by fluorescence measurement (right).

As visible from the ¹H-NMR spectrum of **DLPC-0** in **Figure 3.37**, Cy5 presence could not be quantified by NMR. The ratio of incorporation for the remaining three monomers was determined to be 6:1:1 (TEGMA:bHMA:TMPMA). The average molecular weight was determined to be $M_n = 10.5$ kDa, using the integral of resonance i as an end group signal. In order to evaluate the incorporation of the fluorophore, a fluorescence spectrum of **DLPC-0** after double precipitation was recorded, which showed the characteristic emission pattern of Cy5.

Oxidation of the TMPMA-units to TEMPOMA was supposed to follow the same chemical procedure as before, yet even the addition of stoichiometric amounts of *m*CPBA, the absolute minimum required to oxidise all nitroxides, caused the incorporated Cy5 to degrade. Protocols were adapted from the literature,^[251,252] and oxidation was attempted with Na₂WO₄/H₂O₂, *m*CPBA, Pb(OAc)₄, Ag₂O/H₂O₂. While all conditions appeared to lead to the successful formation of nitroxides, all of them also degraded the cyanine dye. Even though it was not possible to elucidate the exact effect on the dye due to the intentionally low ratio of incorporation, the structure suggests susceptibility to epoxidation of the double bonds in the fluorophore's backbone.^[253] In addition to a total loss in fluorescence, the degradation could easily be observed visually, indicated by the disappearance of the characteristic, deep blue coloration of the polymer.

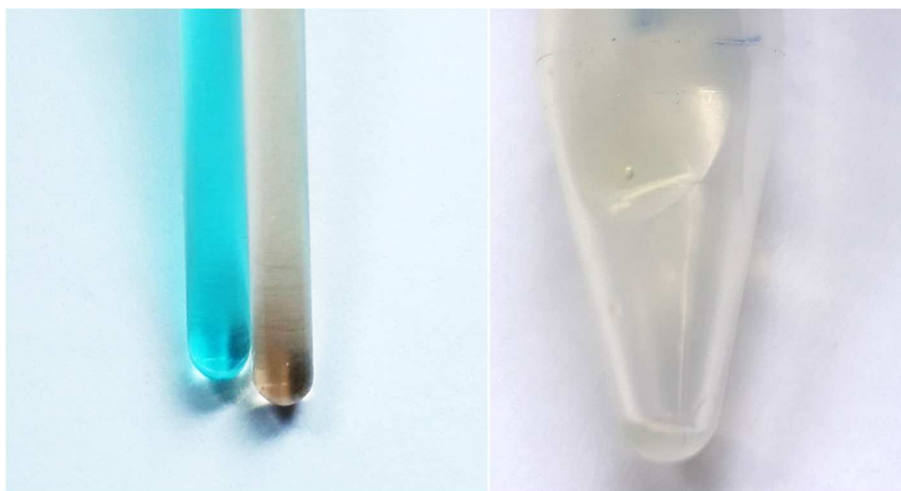


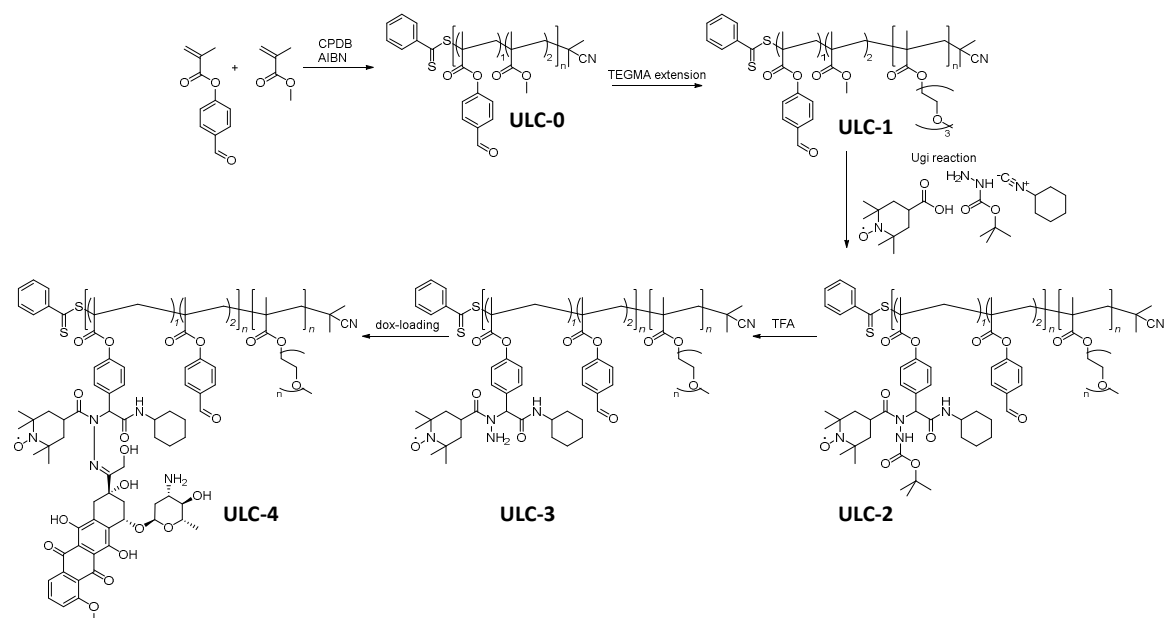
Figure 3.38: Example pictures of Cy5-degradation by the addition of *m*CPBA. Left: Photograph of **DLPC-0** solutions before and after oxidation *via m*CPBA. The solution exhibits the typical blue color of Cy5 before oxidation, which completely vanishes as soon as minute amounts of oxidizing agent are added. Right: The oxidised polyomer after precipitation.

As none of the attempts to preserve the fluorophore were successful, a different approach needs to be established, which either adds the fluorophore or the nitroxide in a post-modification step. Possible avenues may include end group modified polymers *via* thiolene chemistry employing maleimide-modified Cy5 or the attachment of a nitroxide *via* post-polymerisation modification. As experiments carried out in parallel to this project had shown promising results using a strict post-polymerisational approach with multicomponent chemistry, the project was remodelled to follow this avenue. An outlook on the project is presented in the following **Section 3.7**, page 103.

3.7 AN MCR APPROACH TO MACROMOLECULAR REPORTERS

Based on findings from the project for light-triggered self-reporting release, described in **Section 4.3**, page 112, a system based on multicomponent reactions (MCR) was designed. To gain access to all ideal attributes described above in this chapter, the Ugi-reaction provides a highly useful toolkit. An outstanding feature of the Ugi-reaction is high atom economy, enabling the highly specific anchoring of three distinctive molecules to a single repeating unit on the polymer backbone, with only few uncontrollable side reactions leading to dysfunctional end-results (refer to **Section 4.3**, page 112).

The functional platform for nitroxide- and drug anchoring was designed to utilise formylphenyl methacrylate (FPMA) to provide polymer-bound aldehyde moieties for an Ugi-attachment. Initially designed for use in visible-light triggered release as presented in **Section 4.3**, trials with a pure pFPMA backbone proved problematic, as attachment ratios and yields were extremely low. The bulky nature of Ugi-products were identified as the source of the problem, most likely stopping the reaction from proceeding beyond a certain point. As the pseudopeptide, generated in the Ugi-reaction herein would also bear three immensely bulky groups (cyclohexyl-, TEMPO- and Boc-moieties), a similar result was expected in the approach described in **Scheme 3.9**.



Scheme 3.9: Synthetic approach towards an Ugi loaded carrier (ULC) for self-reporting molecular release. A block copolymer of poly-PFMA-*stat*-MMA-block-TEGMA is synthesised *via* RAFT and subsequent chain extension. In an Ugi reaction, the polymer is loaded with carboxy TEMPO, boc-protected hydrazine and cyclohexyl isocyanide. After deprotection of the hydrazine, the polymer is loaded with Dox, analogously to approaches shown above.

In order to overcome said possible steric hindrance, the anchoring unit was designed to space anchoring points apart by two MMA units per FPMA unit, minimizing sidechain-bulk while retaining solubility of the resulting polymer in organic solvents. Based on the polymer used to generate the light responsive system described in **Section 4.3**, p. 112, an imine-loaded polymer was generated, and the incorporation of TEGMA was skipped, to first establish the feasibility of an Ugi-based approach, using a hydrazide as the amine component. **LRC-0** was reacted with tert-butyl carbazate to give **ULC-0.1**. The polymer was precipitated from cold Et₂O and analysed *via* GPC and ¹H-NMR.

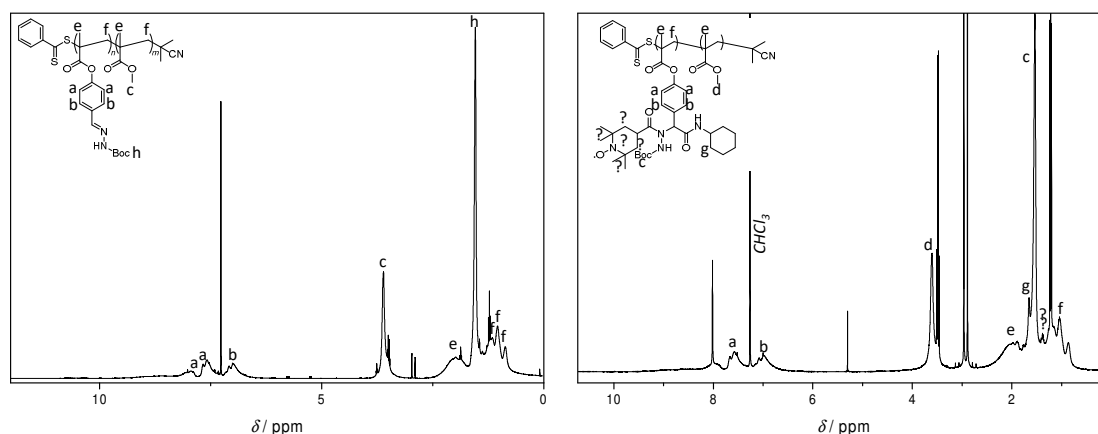


Figure 3.39: ¹H-NMR spectra of Ugi-intermediate **ULC-0.1** and -product **ULC-0.2**. Imine formation is clearly visible, indicating quantitative loading by the boc-associated resonance h. Subsequent completion of the MCR reveals additional resonances, which could be attributed to g, yet the presence of nitroxides most likely hides most relevant signals.

The NMR spectrum in **Figure 3.39** shows full disappearance of the aldehyde and quantitative imine formation as determined by the boc-associated resonance h. GPC indicates an increase to $M_n = 20.0$ kDa and no change to dispersity ($D = 1.2$) (refer to **Figure 3.40**)

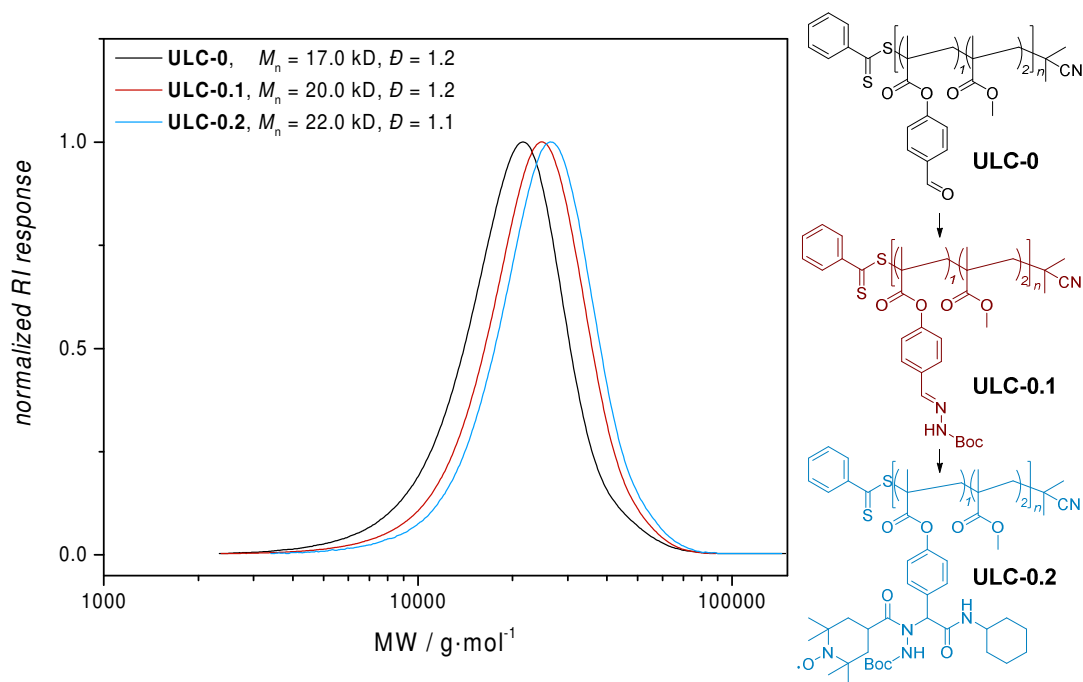


Figure 3.40: GPC elugrams of **ULC-0** – **ULC-0.2** before and after imine loading. A significant increase is visible upon imine loading. Molecular weights were determined from a PMMA calibration.

The product was reacted with cyclohexyl isocyanate and carboxy-TEMPO to complete the MCR. After precipitation, **ULC-0.2** was obtained as a sticky, yellow solid, indicating degradation of the RAFT end group and the possible presence of impurities. The sample was investigated *via* GPC, NMR and ESR. As visible from **Figure 3.40**, GPC indicated a slight increase in molecular weight to $M_n = 22.0$ kDa $D = 1.1$, indicating partial coupling. The spectrum shown in **Figure 3.39** hints at the successful incorporation of a cyclohexyl group, yet the full incorporation and success of the Ugi reaction could not be confirmed unambiguously.

The sample exhibited a strong ESR signal (refer to **Appendix, Figure A 8.34**), yet only to a fraction of what would have been expected from a high level of incorporation. Line-shape additionally indicated very little interaction between nitroxides, further confirming only little incorporation. Quantification, as described in **Section 3.2.1**, could not be performed, as the sample was insoluble in THF. An optimisation remains subject of coming works. The initial results obtained following the above avenue give an outlook on how the strategy employed here could be used in the future to complete the facile construction of a carrier platform with multiple amine-based functionalities. As imines formed by amines

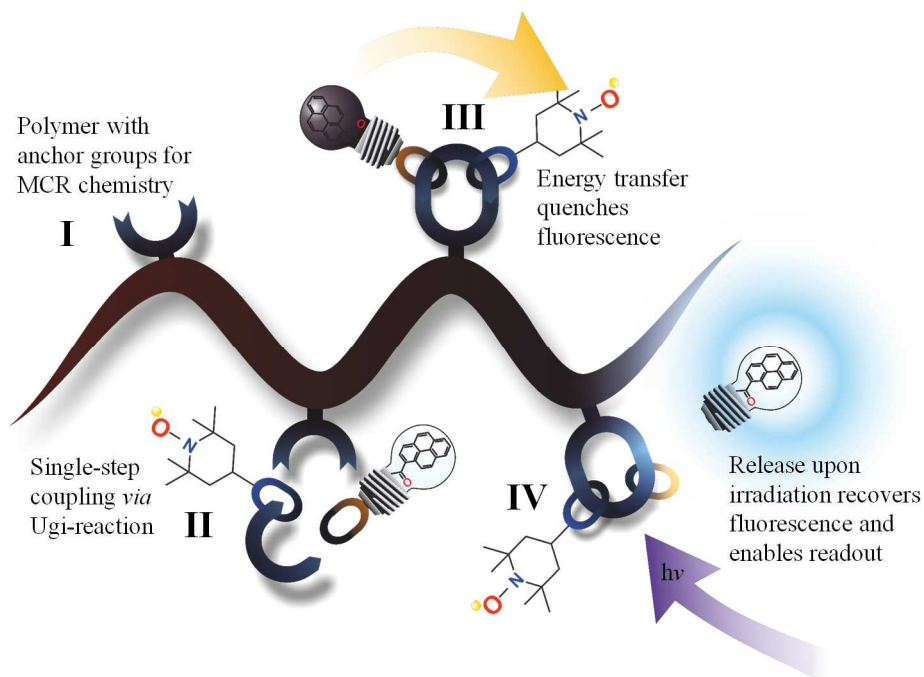
are orders of magnitude more stable than hydrazones, even low amounts of amine-functionalised alternative dyes should be able to incorporate in a similar approach as the one presented here. A block of TEGMA should be incorporated *via* chain-extension. The blocky structure of the polymer would additionally offer a chance of micelle-formation,^[254] aiding nanodrug-stability in a biological application, by encapsulating the functional part of the assembly in a shell of TEGMA chains.

4

Visible-Light Activation of Self-Reporting Molecular Release

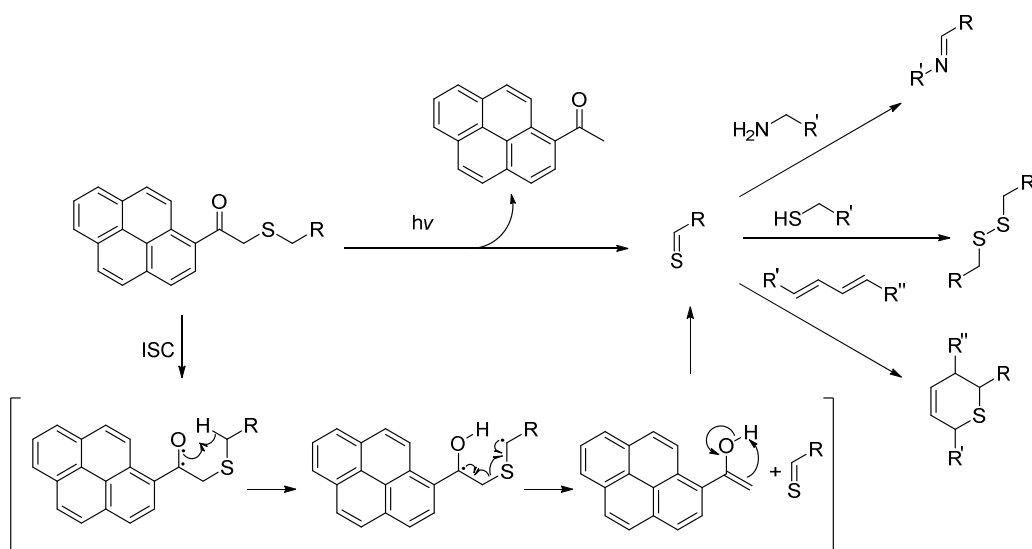
4.1 MOTIVATION AND STRATEGY

Traditional techniques in chemistry are generally burdened by waste products, environmentally harmful conditions, and high demand of solvent- and material consumption. All of these become problematic in the view of two aspects. On a macroscopic level, all of these factors tend to lead to pollution of the environment, straining global resources and stressing waste management in industry-heavy regions. On a microscopic scale, the requirement of organic solvents and side products generally poses an important point to be considered in the context of biological applications. The emergence of far-red shifted dyes and fluorophores has opened new avenues towards the application of light as an almost unlimited and ubiquitously available resource for both synthetic and therapeutic applications. Harnessing the ability to photochemically form or break bonds, paves the way for spatially and temporally controlled molecular release from nanoassemblies. Especially light from the visible spectrum becomes relevant in this context, offering mild and “green” reaction conditions.



Scheme 4.1: Illustration demonstrating the synthesis and subsequent release from a light-responsive release-reporter. First, the polymer is synthesised, bearing an anchor group (I) which allows the coupling of both fluorophore and nitroxide quencher in a single multi-component reaction (II). While bound to the backbone, the fluorophore is silenced by the nitroxide (III). Upon irradiation, the fluorophore is cleaved from the polymer backbone, escaping the effective quenching radius to the nitroxide, enabling release quantification *via* fluorescence readout (IV).

Building on the findings from the release system, described in **Chapter 3**, an additional mechanistic approach for release, using the same profluorescent reporting strategy already established, was envisioned. A fluorophore, which is spin-silenced while attached to the polymer backbone, should serve as a quantifiable signal for release. As described in previous works, light can be readily employed to facilitate molecular release on demand (refer to **Scheme 4.1**).^[55,255–257] For the application at hand, previously reported results from the pyreneacetyl sulfide (PAS) release system appear ideal. Acyl sulfide photochemistry is centred on stable, unreactive compounds, cleaving upon irradiation in a comparatively narrow spectrum, generating only little amounts of primary side-products. Pyreneacetyl sulfide, as the name implies, intrinsically provides a readily detectable fluorophore and already exhibits measurable fluorescence prior to cleavage.

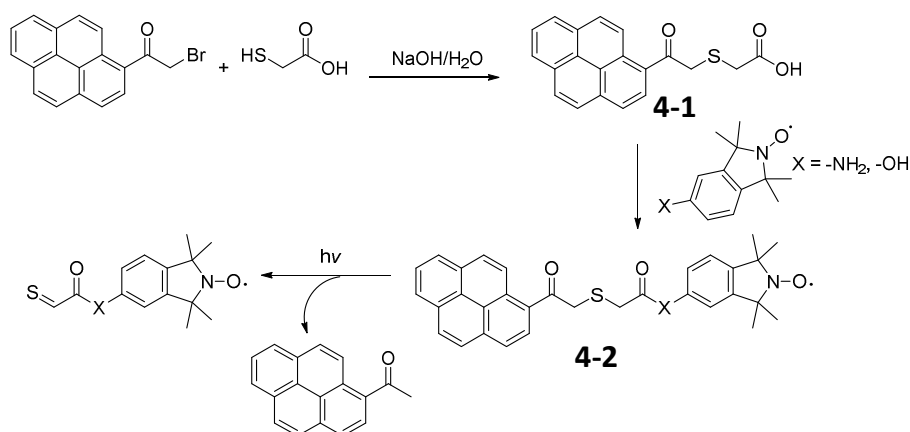


Scheme 4.2: Mechanism of pyreneacyl sulfide cleavage. Upon irradiation, the acetylpyrene portion of the molecule undergoes ISC, generating an oxygen-centred radical, which will subsequently abstract the alpha-hydrogen from the sulfide, initiating a cascade in which a thioaldehyde and enol are generated. The enol undergoes tautomerisation, back to the keto-form. The thioaldehyde can readily react with nucleophiles, thiols or dienes. Interesting for this chapter was predominantly the third pathway, where the thioaldehyde can be scavenged quantitatively in the presence of a diene forming an unreactive HDA adduct.

Upon irradiation, PAS undergoes a Norrish II type cleavage, in analogy to its well characterised structural simile phenacyl sulfide (PAS).^[258] Cleavage of PAS as shown in **Scheme 4.2**, yields fluorescent 1-acetyl pyrene and a highly reactive thiocarbonyl compound. The Thioaldehyde is readily scavenged either in a cycloaddition reaction with a diene, through reaction with an amine to an imine, or through disulfide formation with another thioaldehydes or thiol. Scavenging of the thioaldehydes was crucial to avoid side reactions and obtain defined NMR spectra. The high reactivity of free thioaldehydes can lead to a wide range of side-products, complicating analysis. Trapping by a diene was therefore chosen as an appropriate method, as the HDA product is formed irreversibly and with high efficiency. The acetylpyrene that is formed was utilised as a reporter fluorophore, readily detectable upon release. A TEMPO nitroxide derivative was chosen again as a reporting handle, silencing fluorescence through space before irradiation and releasing fluorescence upon cleavage. Initial attempts to generate a small-molecule proof-of-concept *via* conjugation of PAS-acid and a variety of small molecule nitroxides could not yield satisfactory results. A multicomponent approach was utilised applied as an alternative to successfully construct a self-reporting, visible-light triggered assembly for molecular release directly on a polymethacrylate platform.

4.2 SMALL MOLECULE STUDIES⁶

As a visible-light activated photo-release from spin-silenced constructs had never been reported before, two possible issues were identified that needed to be addressed, before transferring them to a complex polymeric system. Firstly, an insufficient ratio of silencing/turn-on would have resulted in issues with analysis, compromising the effectiveness of the self-reporting system. Secondly, the photo-release propagates *via* a reaction in excited electronic states – which were intentionally going to be influenced by unpaired electrons. At the time no in-depth studies of the proposed construct had been performed, confirming whether or not quenching of the excited state occurs before ISC and the ensuing radical cascade could take place. As polymeric systems are inherently difficult to analyse with respect to exact composition and chemical environment of individual groups, a simplified version was to be investigated first. The small molecule analogue to test this hypothesis is shown in **Scheme 4.3**.



Scheme 4.3: Synthesis and release of a small molecule reporter system for light triggered release. Thioacetic acid is reacted with bromo-acetylpyrene, yielding PAS-acid **4-1**. Coupling with modified TEMPO would yield the spin-silenced PAS-conjugate **4-2**, which then can undergo photolytic cleavage. Coupling follows established esterification or amidation protocols.

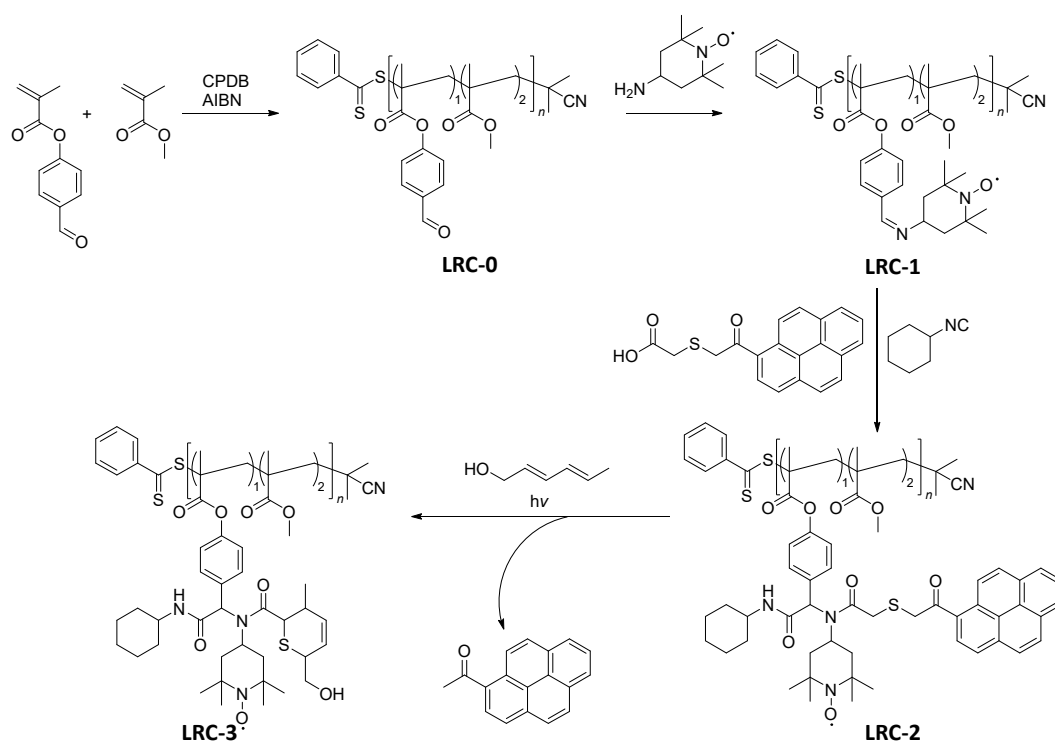
Attempts were made to couple PAS-acid to TMIO and a methylated TMIO derivative, through either esterification or amidation, using conditions akin to standard procedures from the literature. A successful formation of a product would also have allowed for optimisation of reaction conditions for polymer-postmodification in future experiments. For unknown reasons however, satisfying amounts of conjugate could not be obtained through a broad variety of coupling conditions as outlined in **Table A 8.14 (Appendix)**.

⁶ This project was partially carried out by BSc Larissa Hammer, project student to C. B.-K.

Even though extensive efforts to elucidate the cause of the problem were made *via* NMR and ESI-MS investigations, no answer could be found to overcome the issue. Attempts were made to avoid the issue by transferring the system to polymers with either hydroxyl- or amine-bearing sidechains as PAS-anchors in a similar manner to **3.4.2**, yet no advances could be achieved on that route either.

4.3 AN MCR BASED REPORTER FOR PHOTORELEASE FROM POLYMERIC NANOCARRIERS⁷

The underlying concept for a polymeric release system utilizing visible light was initially adapted from **Chapter 3**. Acetylpyrene serves as a model drug, quenched by the presence of nitroxide in its bound state with releasing and reporting groups statistically distributed along the polymer backbone. Strategies attempted to couple the PAS-acid to the backbone in a small molecule system had failed for a number of reasons, which could not be elucidated in any way. Initial attempts to generate an analogous system on a polymer, using statistically incorporated amine-bearing sidechains, also yielded exclusively problematic results. The strategy was then remodelled to give a defined, single-anchor system, accessible through a multicomponent-reaction (MCR) aided strategy.



Scheme 4.4: Synthetic approach towards a light responsive carrier (**LRC**) to demonstrate the possibilities of light-triggered release. A FPMA/MMA copolymer is synthesised *via* RAFT, yielding the aldehyde-bearing polymer platform **LRC-0**. The polymer is subsequently modified in an Ugi reaction with amino-TEMPO, cyclohexyl isocyanate, and PAS-acid. The resulting polymer **LRC-2** is then irradiated in the presence of sorbic alcohol as a thioaldehyde scavenger, to release acetylpyrene as a fluorescent reporter.

The 4-component reaction previously described by Ugi et al. utilises a carbonyl, an organic acid, a primary amine and an isocyanate, to form a pseudopeptide, anchoring all

⁷ The results presented in this section have been published in *Chemistry: A European Journal* in 2018 [259]

employed compounds in close proximity. The elegant features of this reaction, its high atom-economy, short preparative routes and the high-yielding formation of defined structures make it an ideal tool for PPM. Suitable polymers can be generated in a highly defined fashion through polymerisation of 4-formylphenyl methacrylate (FPMA) *via* a wide array of techniques for controlled polymerisation. The synthesis of PAS-acid had already been optimised as described in 4.2. The facile generation of aldehyde-bearing polymethacrylates, as well as the high-yielding synthesis of PAS-acid were complimented by good accessibility of a variety amino-nitroxides and a wide array of commercially available isocyanides.

As the successful reaction would combine a variety of sterically complex groups (TEMPO, cyclohexane and pyrene), bulk was identified as a potential issue. In order to ease the steric hindrance on the polymer backbone, MMA was statistically incorporated into the backbone, which spaced the anchoring aldehyde groups from one another by an average of two repeating units. MMA was copolymerised with FPMA in a ratio of 195:134 (feed ratio determined by NMR, refer to **Figure A 8.47**), employing CPDB as RAFT agent and AIBN as initiator. The resulting PMMA-co-FPMA **LRC-0** (*light responsive carrier*) was precipitated into cold methanol and analysed *via* NMR and GPC, the latter using 1% of TFA. Addition of TFA to GPC measurements was necessary for comparability with later modification steps. Starting from **LRC-2**, the pseudopeptide formed in the Ugi reaction would exhibit strong interactions with all tested GPC solid phase materials. Addition of 1% TFA in sample preparation alleviated the issue, most likely by shielding accessible amines with a hydrophobic trifluoromethyl group. However, values obtained from GPC measurement were only considered a referential value for relative comparison to further modification steps, as no reliable parameters for the exact calculation of molecular weight from calibrated GPC exist for this monomer combination. Yet, as NMR would become unreliable due to the presence of nitroxides and their influence on NMR,^[145] GPC evaluation was employed to monitor the polymer size in a qualitative manner.

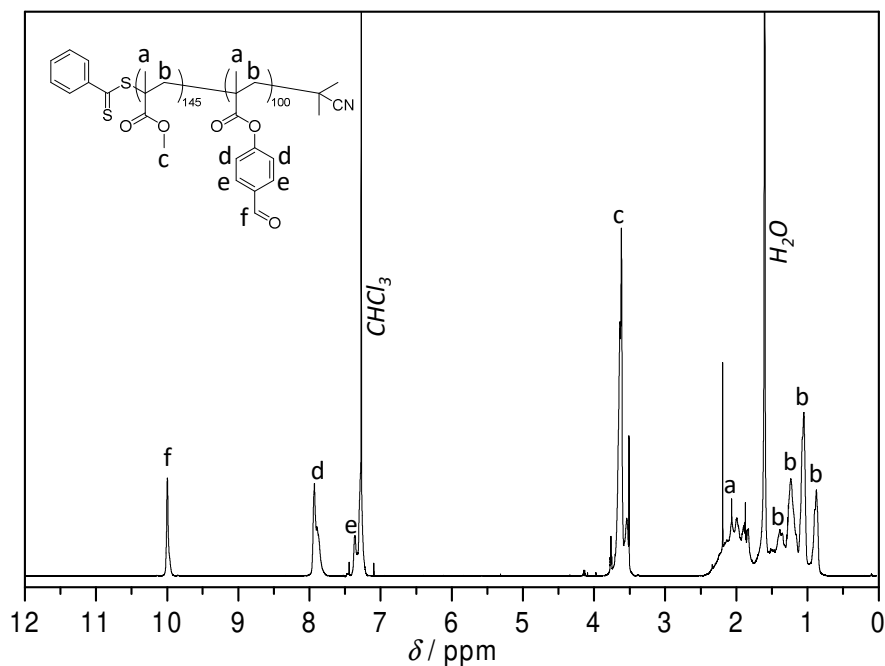


Figure 4.1: $^1\text{H-NMR}$ of **LRC-0** after precipitation. Peaks c and f were used for quantification of polymer incorporation ratios. Figure adapted from [259] with permission from Wiley VCH.

NMR analysis yielded a ratio of incorporation of 145:100 MMA:FPMA (**Figure 4.1**). GPC returned a molecular weight of $M_n = 18.8$ kDa and a dispersity of $D = 1.4$ (**Figure 4.5**). The nitroxide was coupled in a condensation reaction with 4-amino TEMPO using catalytic amounts of glacial acetic acid and Na_2SO_4 , and a small amount was precipitated into cold diethyl ether. This yielded the imine-loaded polymer **LRC-1**.

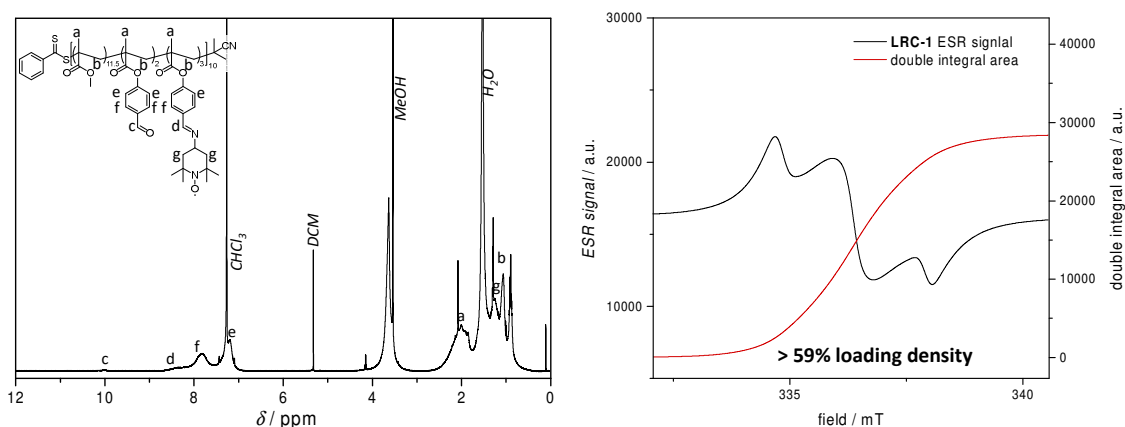


Figure 4.2: $^1\text{H-NMR}$ and ESR spectra of **LRC-1**. Almost complete disappearance of signal c indicates near-quantitative loading of available aldehydes with amino-TEMPO. Double integration of the ESR spectrum on the right indicated a total loading of 59%, yet the spectrum shows extensive broadening, stretching beyond the calibrated window. Figure adapted from [259] with permission from Wiley VCH.

The sample was analysed in NMR and ESR. The NMR spectrum of **LRC-1** is shown in **Figure 4.2**. While being subject to significant line-broadening due to the presence of unpaired electrons, the spectra showed nearly no residual signal c, indicating almost quantitative consumption of the aldehyde. The latter was confirmed *via* ESR measurement, which showed a high loading ration of over 59%, relative to aldehydes present in **LRC-0**. This was assumed the lower limit of loading, with a severely broadened signal, which stretched beyond the measured window. The broadening additionally hinted at a highly anisotropic sample with rotationally confined nitroxides and a high level of interaction between the individual nitroxide groups, typical of densely nitroxide-loaded polymers.^[144]

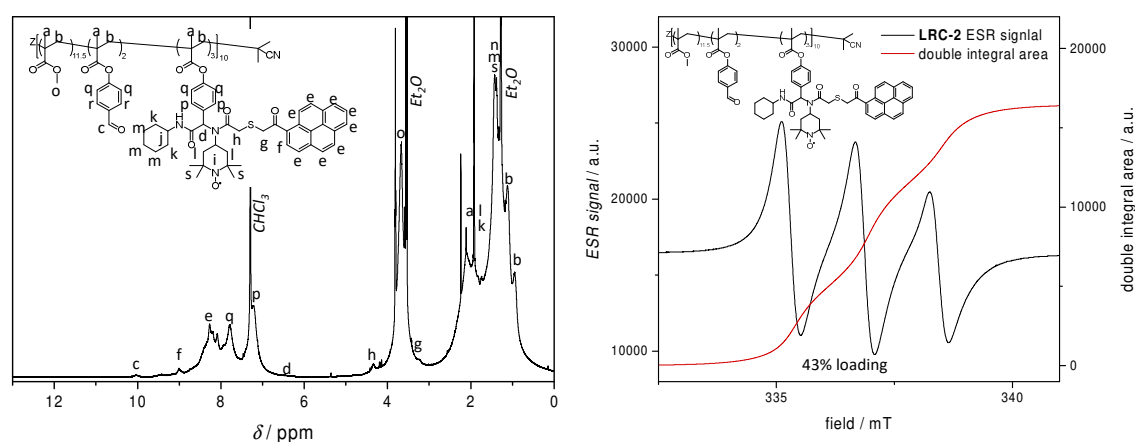


Figure 4.3: ^1H -NMR and ESR spectra of **LRC-2**. Successful coupling can be seen by the presence of signals e and f. The ESR spectrum on the right confirms nitroxide presence. Double integration of the ESR spectrum on the right indicated a total loading of 43%. Line broadening and crosstalk decreased compared to **LRC-1**, indicating stronger separation of the present nitroxides. Figure adapted from [259] with permission from Wiley VCH.

In order to complete the reporter construct, **LRC-1** was reacted with PAS-acid **4-1** and cyclohexyl-isocyanide in DMF, yielding **LRC-2** as a yellow powder. The polymer was analysed in GPC, NMR and ESR. GPC analysis showed a strong increase in molecular weight to $M_n = 28.8$ kD, $D = 1.5$, indicating successful loading of the polymer (**Figure 4.5**). ESR showed a nitroxide density of 43%, relative to the amount of aldehydes in **LRC-0**. The ESR spectrum shown in **Figure 4.3** additionally shows a decrease in line broadening, which indicates a decrease in nitroxide interactions and anisotropy, suggesting a possibly looser, more mobile organisation of the polymer backbone as well as more separated nitroxides.

Successful coupling of PAS was confirmed *via* NMR by the presence of signals e and f (**Figure 4.3**). Additionally, a solution of **LRC-2** was analysed *via* UV/Vis spectroscopy, showing the characteristic absorption spectrum of PAS (**Appendix, Figure A 8.52**).

4. Visible-Light Activation of Self-Reporting Release

After successful coupling had been established, release experiments were performed. A solution of **LRC-2** in a quartz cuvette was placed in the light-cone of a single 3 W LED, emitting a narrow spectrum of blue light in the range of 410-425 nm (refer to **Appendix, Figure A 8.53**). The complete setup is pictured in the **Appendix, Scheme A 8.1**. The solution was analysed *via* fluorescence measurements over the course of 8 h. Investigation *via* time-resolved fluorescence spectroscopy returned an increase in fluorescence immediately after irradiation.

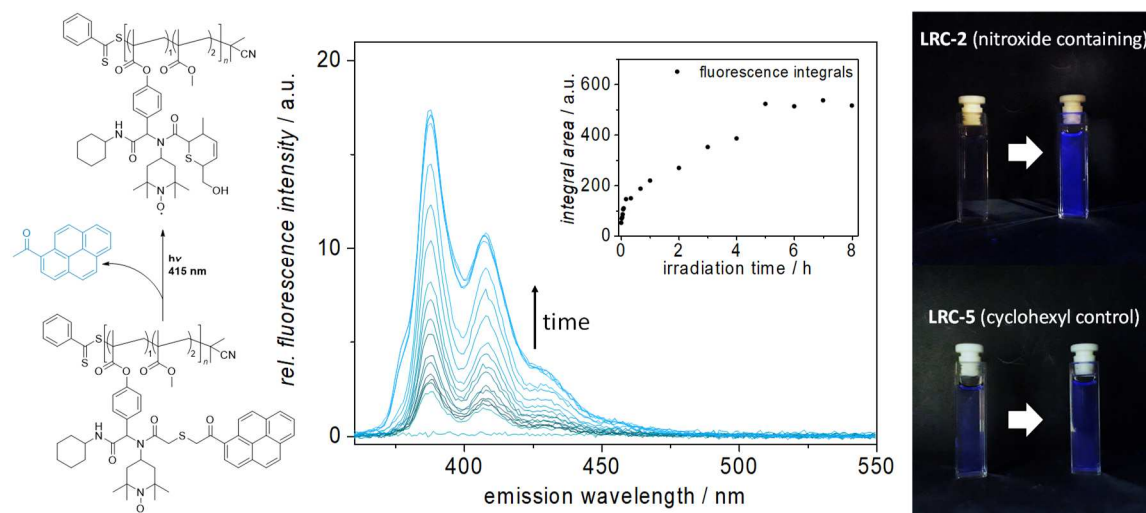


Figure 4.4: Time-resolved fluorescence spectroscopy of **LRC-2** release experiment. Over a time of 8 h, a 10.5-fold increase in total fluorescence, determined by integration of the individual spectra, could be observed. Right: side-by-side comparison of both **LRC-2** and **LRC-5** cuvettes before and after release. The change in fluorescence is intense enough to be readily observable to the naked eye in both cases, with the nitroxide-containing polymer exhibiting vastly increased quenching efficiency. Figure adapted from [259] with permission from Wiley VCH.

Integration of the fluorescence spectra in **Figure 4.4** showed a 10.5-fold increase in fluorescence, indicating the successful establishment of the proposed novel self-reporting system. The increase in fluorescence was intense enough to be readily detectable to the naked eye and could even be visually followed in real time, when irradiated with a blue-light laser pointer.^[259] Further investigation *via* UV/Vis showed a spectral shift of pyrene absorption towards the actual spectrum of free acetylpyrene, indicating a decrease in stacking-effects and an increase in fluorophore mobility (**Appendix, Figure A 8.52**). Reinvestigation of the same sample before and after removal of free fluorophore by precipitation and resolution of the polymer showed a strong decrease in absorption, fully underpinning the successful release of acetylpyrene from the polymer (**Appendix, Figure A 8.52**). In

addition to optical spectroscopy, the sample was analysed *via* GPC to monitor the change in size.

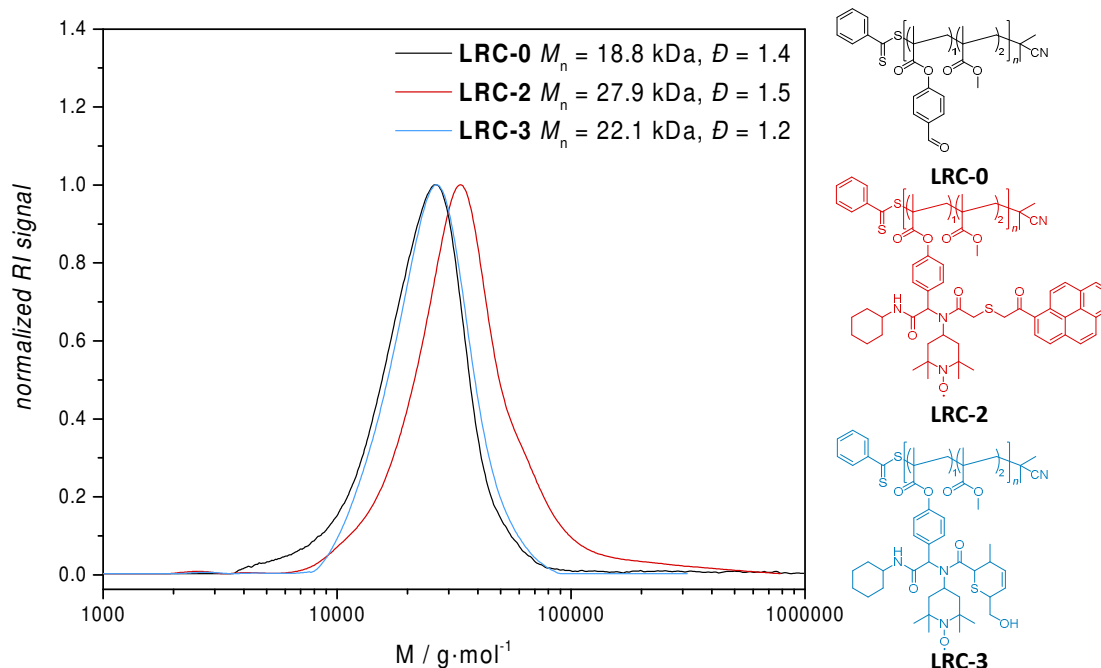
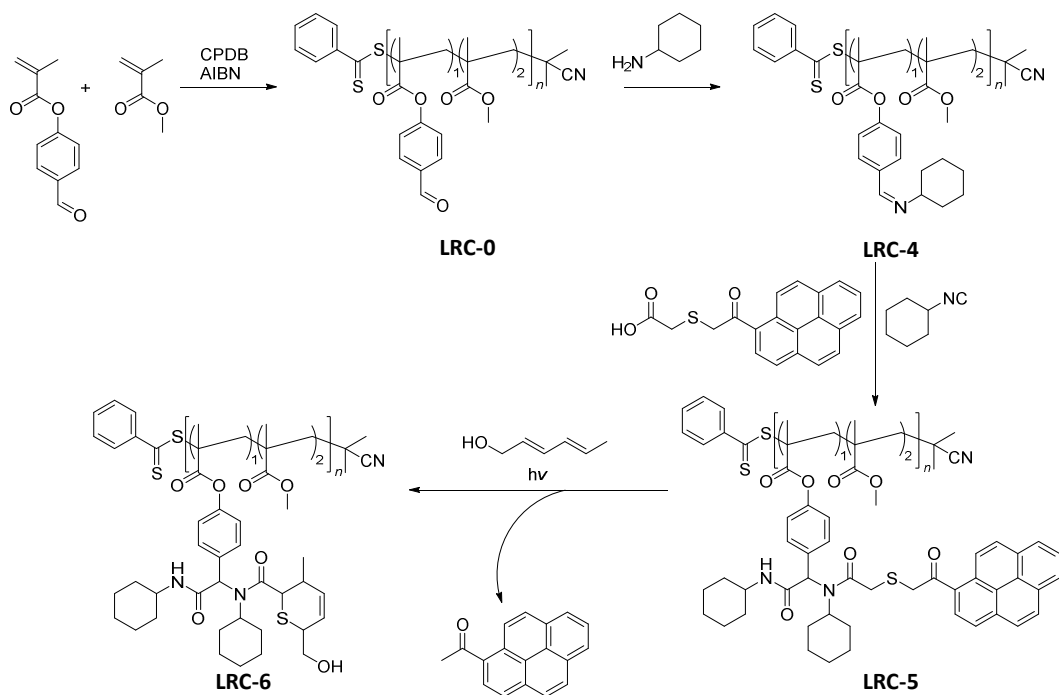


Figure 4.5: GPC elugrams of **LRC** before and after coupling as well as after photo release. A significant increase in molecular weight can be seen upon loading of the polymer, as well as a return to lower molecular weights upon cleavage of pyrene from the backbone. Figure adapted from [259] with permission from Wiley VCH.

Post-irradiation analysis of **LRC-3** *via* GPC showed a strong decrease in molecular weight ($M_n = 22.1$ kDa, $\bar{D} = 1.2$, refer to **Figure 4.5**), due to the release of acetylpyrene. In order to confirm unambiguously the applicability of the system, three crucial control experiments had to be conducted: (i) Phenomena potentially interfering with the fluorescence measurements had to be ruled out, (ii) the chemistry had to be confirmed to proceed as expected, and (iii) nitroxide-mediated quenching had to be confirmed. Firstly, the impact of mounting PAS on a polymer on fluorescence measurements had to be assessed. High density of potentially rotationally-constrained fluorophores attached to a backbone can lead to a variety of artefacts, such as self-quenching, excimer formation, or anisotropy effects, which all effect a decrease in fluorescence signal (**Figure A 8.45**) and spectral distortion in both fluorescence- and UV/Vis spectroscopy (**Figure A 8.52**).^[3,212] Predominance of such artefacts would render a reporting system like the one at hand highly ineffective. To gain insight into this, an **LRC-2** analogue was synthesised, bearing a cyclohexyl-group as a structural surrogate for the nitroxide.

4. Visible-Light Activation of Self-Reporting Release



Scheme 4.5: Synthesis of a nitroxide free analogue to investigate self-quenching effects of the pyrene moiety while attached to the polymer backbone. Cyclohexylamine was employed to generate a structural surrogate to amino-TEMPO as a building block for the MCR coupling

Synthesis followed an identical procedure, yet 4-amino-TEMPO was replaced by cyclohexylamine, providing a similarly sterically demanding synthon, without incorporating a quencher (**Scheme 4.5**). The synthetic route starting from the same **LRC-0** yielded polymer **LRC-4** and **LRC-5**. The transformation was monitored by GPC (**Figure 4.7**), showing the same trends as observed in **LRC-2** synthesis. **LRC-5** showed an increase of molecular weight to $M_n = 34.2$ kD, $D = 1.6$. As no nitroxides were present in this approach, polymer composition and therefore coupling efficiency could be monitored *via* $^1\text{H-NMR}$.

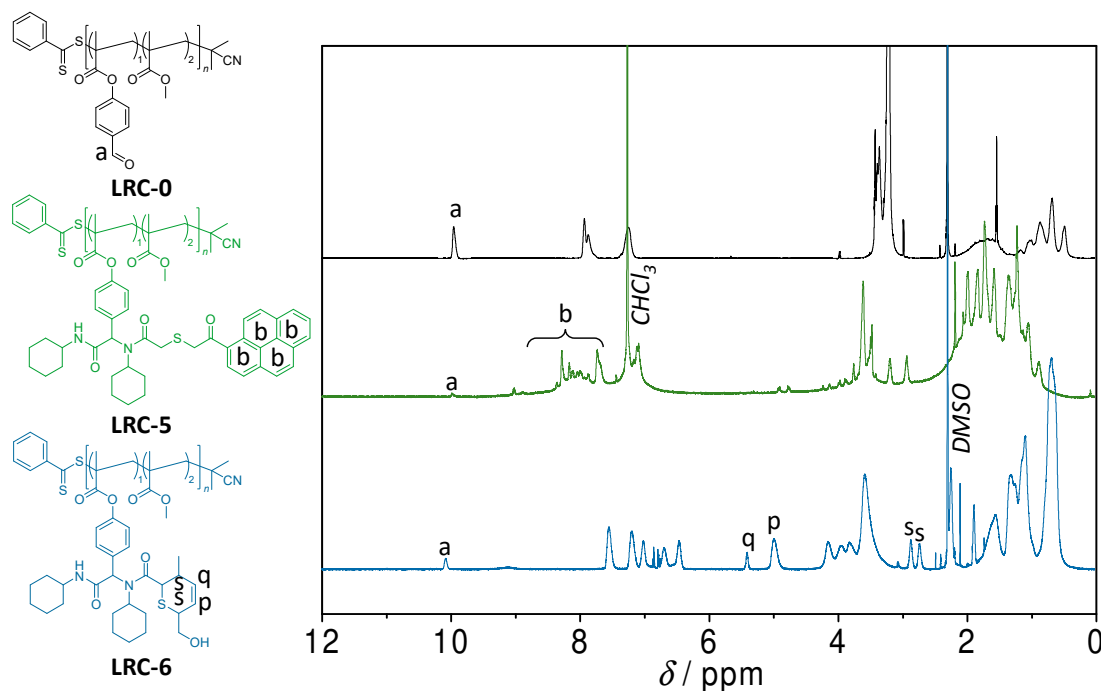


Figure 4.6: Stacked $^1\text{H-NMR}$ spectra of **LRC-0-6**. Pyrene coupling was monitored *via* both disappearance of signal a and the surfacing of pyrene signals b. Release and thioaldehyde scavenging was followed by the disappearance of pyrene signals b and the surfacing of signals p and q. Spectral assignments have been heavily simplified for clarity. Fully assigned singled out spectra can be found in the **Appendix, Section 8.1.7**, pp. 205. Figure adapted from [259] with permission from Wiley VCH.

Analysis *via* NMR indicated almost quantitative loading, judging from the disappearance of the aldehyde signal a, and the appearance of pyrene signals b (**Figure 4.6**). Release experiments from the unquenched **LRC-5** were carried out in the same manner as before for **LRC-2**. Perfectly matching predictions, a measurable increase in fluorescence could be detected, yet only to the extent of a 1.6-fold increase. Time-resolved spectra are shown in direct comparison to the quenched assembly in **Figure 4.8**. GPC investigation of the negative controls showed a decrease in molecular weight ($M_n = 27.1$ kD, $D = 1.2$) in a similar manner to **LRC-2** release (**Figure 4.7**). Release could additionally be confirmed *via* NMR, showing complete cleavage of acetylpyrene from the backbone and the quantitative consumption of photo-generated thioaldehydes by sorbic alcohol. As shown in **Figure 4.6**, the appearance of protons p and q coincides with the disappearance of all pyrene signals b after irradiation.

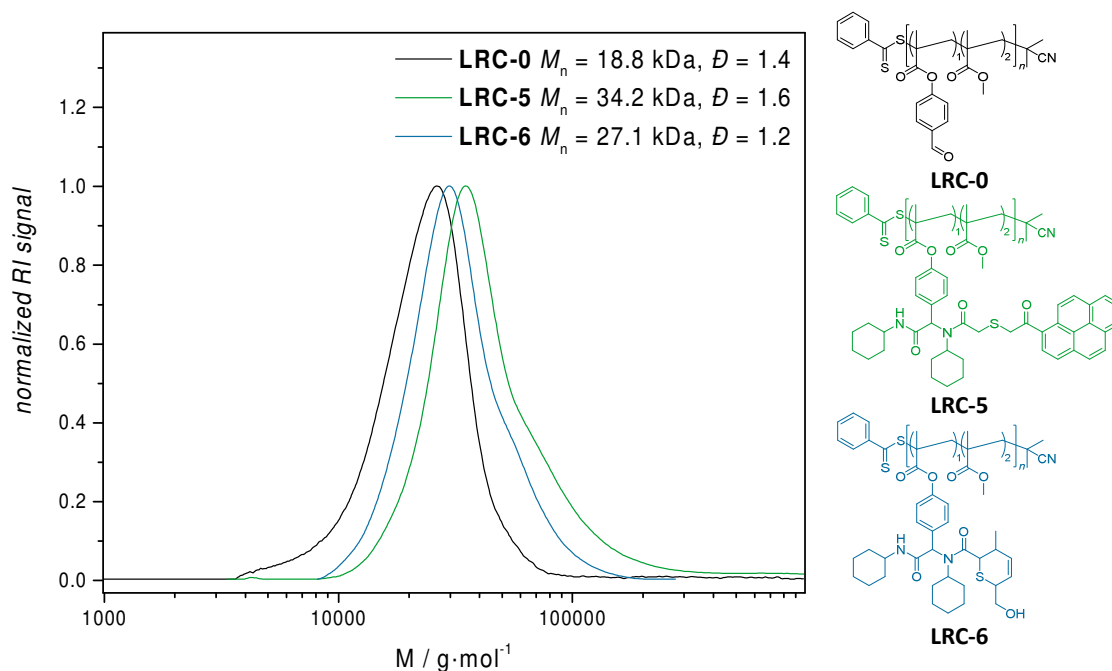


Figure 4.7: GPC elugrams of **LRC-0** through **LRC-6** before and after coupling of PAS, as well as after photo-release. A significant increase in molecular weight can be observed upon loading of the polymer, as well as a return to lower molecular weights upon cleavage of pyrene from the backbone. Figure adapted from [259] with permission from Wiley VCH.

Lastly, quenching through the actual presence of nitroxides had to be confirmed.^[209] As dialysis of released fluorophores from the nitroxide-bearing backbone was not a feasible option, nitroxides had to be rendered ineffective through reduction. In order to achieve this, 15 eq of ascorbic acid (relative to present nitroxides) were added to a solution of **LRC-2** and **LRC-5**. In the case of **LRC-5** no significant change in fluorescence could be detected, establishing no significant impact of ascorbic acid itself on the measurement. In the case of **LRC-2** reduction, a 4.5-fold increase in fluorescence could be detected immediately, confirming the fluorescence-silencing mechanism *via* nitroxide-presence (**Figure 4.8**).

In summary, the suitability of the novel system for self-reporting of photo-triggered release demonstrated herein could unambiguously be established. The increase in fluorescence by a full order of magnitude opens up a completely new toolkit for self-reporting systems, limited only by the available chemistries for release upon irradiation. The system could easily be adapted to different types of fluorophores, due to the broadband-quenching ability of nitroxides. Additionally the kinetic measurements indicate little to no negative impact of nitroxides on the overall rate or efficiency of the photoreaction, promising ideal features for broad applicability.

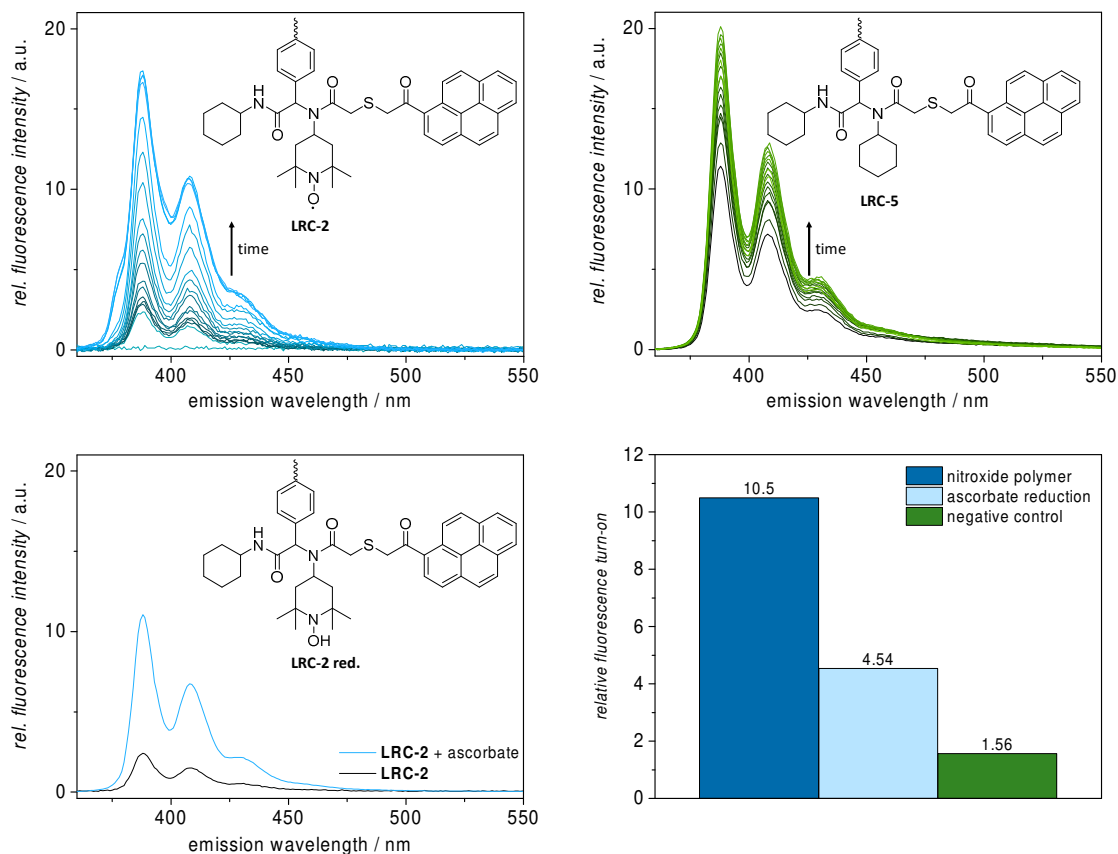


Figure 4.8: Comparison of fluorescence spectra over time. While both nitroxide-bearing **LRC-2** (top left) and negative control **LRC-5** (top right) top out at similar rates of fluorescence, intensity of the polymer is vastly different. Reduction of the nitroxides in **LRC-2** (bottom left) leads to roughly half the fluorescence recovery observed in the actual release experiment. Relative rates of fluorescence recovery are visualised on the bottom right. Figure adapted from [259] with permission from Wiley VCH.

5

Investigation of a Proof-of-Concept Dye for MSOT applications

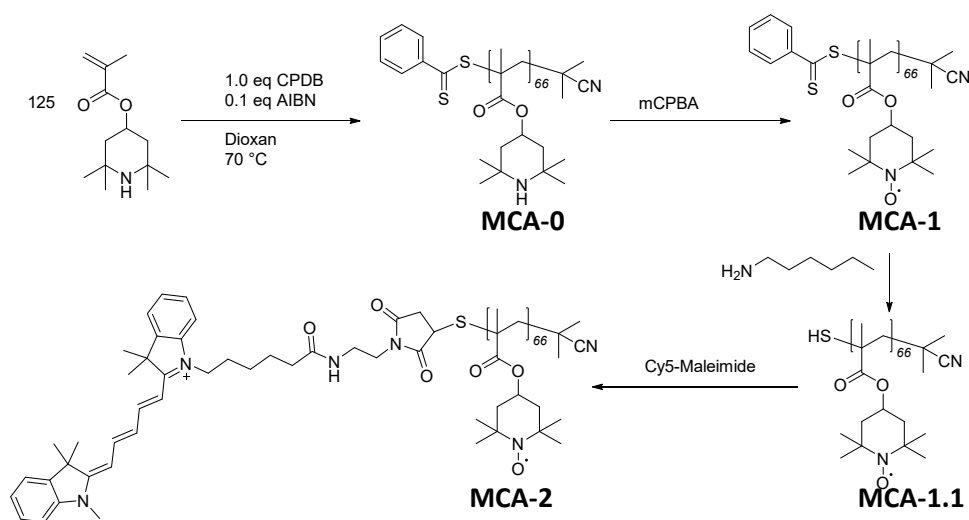
5.1 MOTIVATION AND STRATEGY

The results obtained in the release projects described above successfully demonstrated the accessibility of polymer-tethered nitroxides for the generation of profluorescent systems. Initial test-polymerisations with TMPMA had yielded narrowly distributed polymers, which upon oxidation would yield polymers of very high nitroxide-density. Release experiments shown above indicated a broad spectral range of the quenching ability of nitroxides, supported by findings from the literature, where influence on drastically shorter^[260] and longer^[60] wavelengths had been observed. The potential capability of an accessible polymeric profluorescent nitroxide assembly of long wavelength excitation offered a possible application in multispectral optoacoustic tomography (MSOT) imaging. A range of fluorophores, capable of interaction with near IR-light is readily available, which could potentially be applied in MSOT applications, yet most available fluorophores are tuned towards high fluorescence quantum yields.^[261] As MSOT relies on vibrational energy, the use of dyes with high fluorescence quantum yields is relatively inefficient. In order to employ those available compounds, fluorescence needs to be quenched as efficiently as possible. In classical fluorophore/quencher pairs, both dye and quencher have to be tuned to compatible wavelengths. This inherently limits the feasibility of many synthetic routes, as two molecules, no matter how useful towards the application, are oftentimes chemically incompatible with either synthetic steps or the environment they are later sup-

posed to be employed in. Excellent biocompatibility, accessibility, especially in a polymeric system, and the demonstrated quenching capabilities of nitroxides made them a promising candidate for MSOT applications.

5.2 SYNTHESIS AND EVALUATION

In order to construct a novel MSOT contrast agent (**MCA**, **Scheme 5.1**), a polymer backbone bearing TMP nitroxide-precursor groups was synthesised *via* RAFT. Synthetic protocols were adapted from the literature.^[31]



Scheme 5.1: Synthetic strategy for a novel MSOT contrast agent. First, a nitroxide precursor polymer is synthesised *via* RAFT and subsequently oxidised to a TEMPO bearing platform. The end group is removed *via* aminolysis and functionalised *via* thiol-ene click with Cy5-maleimide.

TMPMA was polymerised with AIBN and CPDB as a chain transfer agent. The polymer **MCA-0** was obtained as a pink, brittle solid *via* precipitation and characterised *via* ESR, GPC, SEC-MS and NMR. The high amine content caused significant issues with GPC and neither a change of solvent nor the addition of TFA as before could diminish the problem.

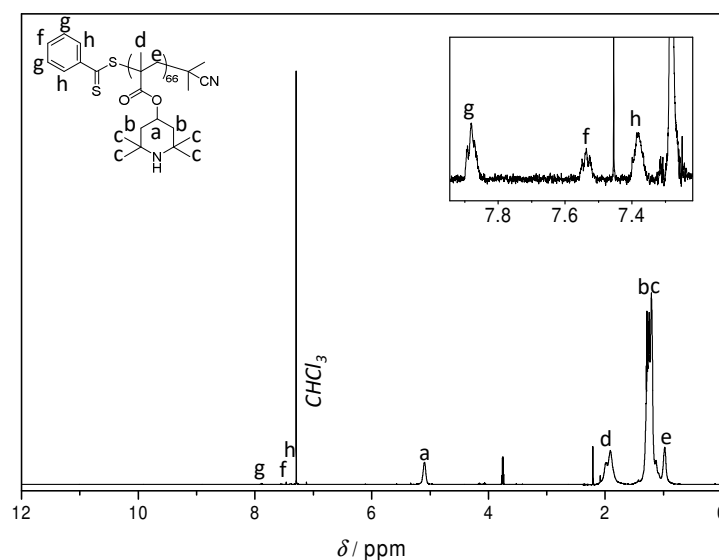


Figure 5.1: ^1H -NMR spectrum of **MCA-0**. The inset shows a zoom of the RAFT end group protons f, g, and h, which were used with the TMP signal a to calculate the average chain length.

The NMR spectrum of **MCA-0** shown in **Figure 5.1** returned an average chain length of 66, $M_n = 14.9$ kDa, determined by peaks f, g, h and a. Investigation *via* SEC-MS indicated excellent end group fidelity (**Appendix, Figure A 8.54, Table A 8.15**). The polymer was subsequently oxidised by the addition of *m*CPBA and precipitated from cold Et_2O , yielding the **MCA-1** as a bright red, brittle polymer. The sample was investigated by ESR and GPC. NMR spectra could not be obtained, as the high nitroxide content interfered with the acquisition.

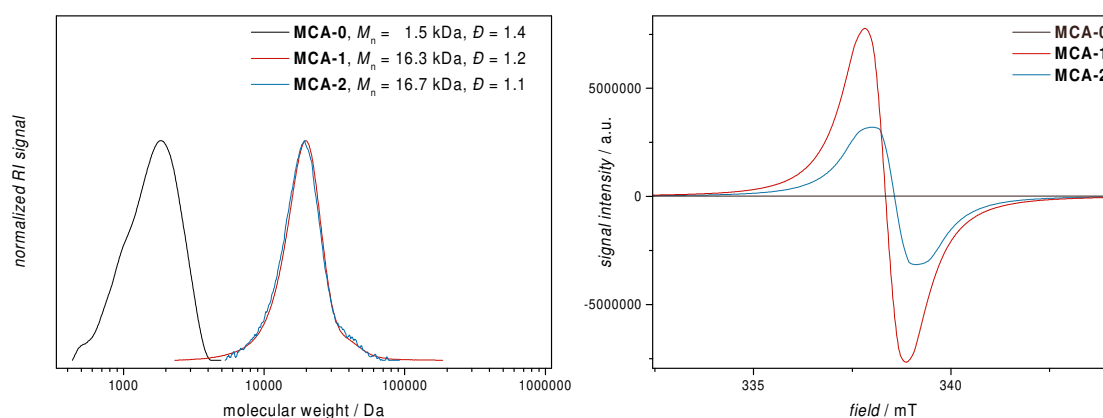


Figure 5.2: GPC elugrams and ESR spectra of **MCA-0** through **MCA-2**. Left: Clear narrowing of the elugram and a shift to the expected molecular weight can be observed upon oxidation to **MCA-1**. No significant change can be observed upon end group modification. Right: A strong increase in ESR signal, completely broadened into one single signal can be observed upon oxidation. End group modification to **MCA-2** led to a slight change in signal shape- and intensity, yet retaining the same level of oxidation.

The ESR shown in **Figure 5.2** exhibited a significantly broadened signal, indicating high levels of nitroxide interactions and sample-rigidity. Quantification with a set of TEM-POL calibration curves (**Appendix, Figure A 8.23, Table A 8.1**) indicated 75% conversion. Due to the extent of the band broadening, the spectrum potentially exceeds the calibration window in width, and actual loading was deemed even higher. The polymer was stirred with an excess of hexylamine and TEA for 30 minutes, after which Cy5-maleimide and TCEP were added with catalytic amounts of water. After an hour of stirring and repeated precipitation from MeOH, Et₂O and cyclohexane, a dark blue, powder remained. end group conversion was determined photometrically, indicating a coupling efficiency of 89%. Quenching efficiency was investigated by comparison of total fluorescence with free Cy5-maleimide. As Cy5 has an unusually high extinction coefficient of 250'000 cm⁻¹·M⁻¹, samples had to be prepared in extremely high dilutions. Thus, in order to minimise weighing- and pipetting error, samples were prepared in dilution series and plotted directly against their Cy5 absorption at $\lambda_{\text{abs}} = 650 \text{ nm}$. Individual absorption- and fluorescence-spectra can be found in the **Appendix, Figure A 8.12**.

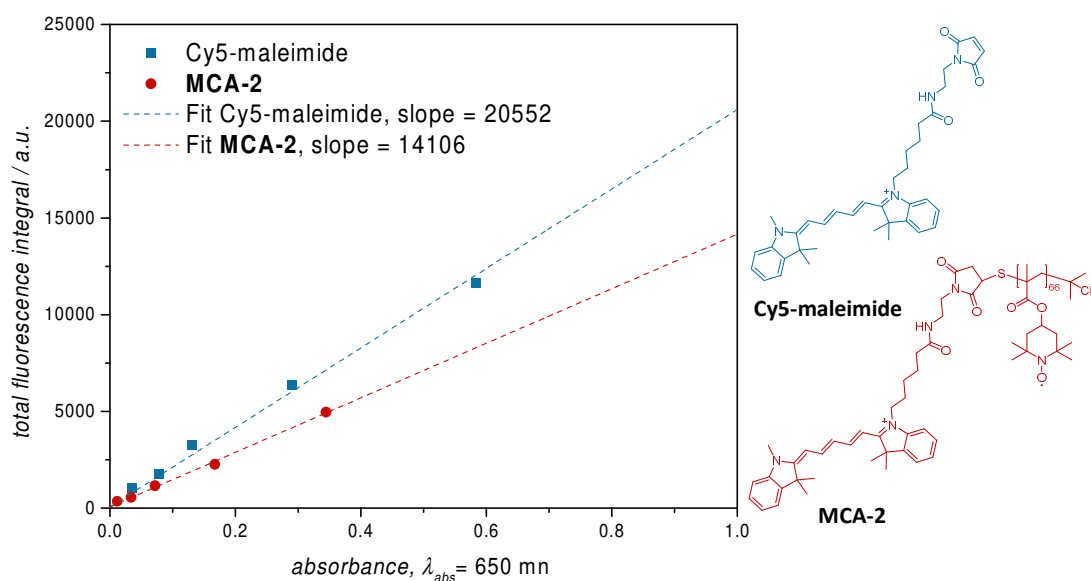


Figure 5.3: Fluorescence yield comparison. Total fluorescence integrals were plotted against the absorption maxima of Cy5 at $\lambda = 650 \text{ nm}$. Linear fitting allowed a comparison of relative fluorescence yields, returning a ratio of 1.00:0.68 Cy5-maleimide:MCA-2.

The plots shown in **Figure 5.3** demonstrate the quenching activity of the nitroxide-bearing polymer construct, yet only to the extent of a 0.68-fold reduction in overall fluorescence. Given the high nitroxide/fluorophore ratio, significantly higher quenching effi-

ciencies were expected. A range of possible reasons could be responsible for the low efficiency in this system. The polymer backbone itself is comparatively stiff, due to its bulky sidechains, which could have led to a decreased amount of interaction between fluorophore and nitroxides.^[262] Recently published profluorescent nitroxides, generated from Cyanine-type dyes required the incorporation of the nitroxide moiety directly into the absorbing system of the fluorophore to achieve high levels of fluorescence silencing.^[60] A possible way to increase the quenching efficiency of the demonstrated construct could be the incorporation into a side chain or the utilisation of multiple arms of a polymer, effectively locking the fluorophore between bulk regions of nitroxide. Investigations into the actual applicability as MSOT contrast agents are still pending and need to be evaluated in order to judge the applicability of the presented system. Regardless of the outcome of these experiments, a consequently low quenching of end group bound fluorophores would offer another avenue towards dual-dye systems as discussed in **Section 3.6**, page 3.6.

6

Concluding Remarks and Outlook

Controlled release poses one of the most crucial points in therapeutic scenarios involving drug-delivery assemblies. The current thesis presented two systems for the visualisation of controlled release. In the first part, a pH-sensitive system was constructed from a triethylene glycol methacrylate-based, water-soluble polymer backbone. Different avenues towards the envisioned structure were employed, and an efficient strategy could be identified. The reporter system, comprised of TEMPO sidechains and the inherently fluorescent anti-tumour drug doxorubicin (Dox), was successfully synthesized. The architecture utilised statistically incorporated moieties for both fluorophore and nitroxide, offering an accessible and efficiently scalable synthetic route. The release of Dox could successfully be quantified based on fluorescence turn-on and could be achieved in a precise and reproducible manner. Fluorescence turn-on was determined to be 3.6-fold. Transfer to a biological system allowed the elucidation of the bioapplicability of the assembly. The drug was tested in two- and three-dimensional cell culture systems. Especially in 3D spheroid cultures, a clear increase of efficacy and drug-penetration could be achieved. The results obtained from co-cultures of tumours spheroids and fibroblasts in collagen gels showed the same trend of elevated uptake of the polymer into spheroids. In addition to the obtained microscopy images, the computational method developed to gain insight into uptake and distribution of fluorescent assemblies into tumour spheroids proved highly reliable and adaptable, with an unprecedented level of precision. Overall, the presented system offers a feasible building block for the construction of larger assemblies for the potential application in mammalian models.

The second system presented system focussed on the utilisation of a photo-trigger in the visible spectrum. The Ugi reaction was utilised to immobilise a photo-cleavable fluorophore and a nitroxide quencher on the carbonyl sidechains of a RAFT poly(MMA-*stat*-FPMA) backbone polymer. Focus was centred on the responsiveness in the visible spectrum. Pyreneacyl sulfide was employed as both fluorophore and linker in one moiety, allowing triggered release in the blue spectrum. The system demonstrated the release of acetylpyrene upon irradiation at 415 nm in a highly controlled fashion. Release could be followed in real-time *via* monitoring of acetylpyrene fluorescence in a range of 11-fold signal-increase. The excellent quenching efficiency of the light responsive system in comparison to the architecture employed in the pH-responsive system was linked to a superior attachment strategy.

Lastly, findings from the first two sections were combined into an extension of the reporter system to add a second tracking moiety. Cy5, a red fluorophore was incorporated to gain access to a secondary tracer molecule for application in biological systems. The dye was additionally employed in an initial proof-of-concept towards a contrast agent for optoacoustic imaging. Conjugation of a single red-shifted fluorophore to a poly-TEMPOMA polymer was planned to yield a fully fluorescence-silenced construct. The system exhibited measurable decrease in Cy5-fluorescence, yet could not match the envisioned quenching efficiency.

Future works should address a number of details of the results presented in this thesis. Firstly, the pH-responsive system should further be investigated in biological tissue models. Special attention should be focussed on the role of polymer-bound nitroxides in the backbone. To investigate their involvement in the uptake process further, a range of control experiments with varying nitroxide densities should be carried out and uptake should be monitored with precise temporal and spatial resolution. Initial tests in vascularised microchips were already in progress as this thesis reached completion. The envisaged goals are to shed further light on the applicability of the presented assembly in an EPR-targeted therapeutic scenario. Investigations in such a system will ideally reveal the involvement of intercellular shuttling from the vascular lumen into tumour tissue and yield insight into the involvement of nitroxides as mediators of cellular uptake. Furthermore, an optimisation of the transporter-architecture itself, to incorporate cellular targeting peptides and a secondary, non-cleavable fluorophore, would enable precise tracking of the backbone as such and greatly facilitate the monitoring of intracellular release. Optimisation of an MCR-based

approach for the generation of biologically active block-copolymers would open a way to create larger, vesicular or tubular superstructures from comparatively small individual chains. An extension of the presented method for image evaluation would compensate the potentially inhomogeneous laser penetration depth. Three-dimensional investigations would increase reliability of the obtained penetration data and allow direct numerical comparisons between spheroids of different sizes. Specifically, necessary modifications would include a transfer to a parallel computing architecture and the implementation of conversion-free handling of primary data obtained from CSLM software.

The light triggered system successfully demonstrated how visible light poses a feasible handle for trackable, controlled release. Even though the presented system did not incorporate an active drug, it proposes a feasible handle for therapeutics. Further investigation into the utilisation of arylacylsulfides as linkers in combination with upconverting nanoparticles would open an avenue for the construction of NIR-responsive release systems.^[263] These systems could be used to both uncage drugs at a site of interest and utilise photogenerated thioaldehydes as a highly reactive handle to efficiently disrupt the cellular metabolism of tumour tissue.

In summary, presented results could show that nitroxide-based methods of fluorescence-based reporting can readily be implemented into biomedical applications. The methods developed over the course of this thesis are highly scalable and can readily be employed in larger application of larger scale, either for preliminary tests in a high-throughput scenario, or the actual incorporation into a future therapeutic.

7

Experimental

7.1 INSTRUMENTATION AND MATERIALS

GPC Measurements

SEC measurements were conducted on a PSS SECurity2 system consisting of a PSS SECurity Degasser, PSS SECurity TCC6000 Column Oven (35 °C), PSS SDV Column Set (8x150 mm 5 µm precolumn, 8x300 mm 5 µm analytical columns, 100000 Å, 1000 Å and 100 Å) and an Agilent 1260 Infinity Isocratic Pump, Agilent 1260 Infinity Standard Autosampler, Agilent 1260 Infinity Diode Array and Multiple Wavelength Detector (A: 254 nm, B: 500 nm), Agilent 1260 Infinity Refractive Index Detector (35 °C). HPLC grade THF, stabilised with BHT, is used as eluent at a flow rate of 1 mL·min⁻¹. Poly(methyl methacrylate) (M_n : 202 g·mol⁻¹ to 2.2·10⁶ g·mol⁻¹) standards (PSS ReadyCal) were used as calibrants. All samples were passed over 0.22 µm PTFE membrane filters. Molecular weight and dispersity analysis was performed in PSS WinGPC UniChrom software (version 8.2).

NMR Experiments

All ¹H-NMR spectra were recorded on a Bruker Avance 600 MHz NMR spectrometer. Samples were prepared at 10-20 mg·mL⁻¹ concentration in CDCl₃. ¹H-spectra of small molecules were recorded at 16 scans with 1 sec of d1 time. Polymer spectra were recorded at 256 scans and 5 sec d1-time in order to achieve sharper signals and a flatter baseline. ¹³C-spectra were recorded at 151 MHz at 1024 scans. Chemical shifts δ are given in ppm of 600 or 125 MHz respectively. Chemical shifts were referenced by the solvent residual

signal in CDCl₃ at 7.26 ppm in ¹H-spectra, and 77.16 ppm in ¹³C-spectra as reported in the literature.^[264]

EPR experiments

Electron paramagnetic resonance (EPR) spectroscopy was performed on a Mag-
nettech MiniScope MS400 spectrometer. Prior to integration, a baseline-correction with
pure solvent was applied.

7.2 GENERAL PROCEDURES

Data processing

NMR spectra were manually phase- and baseline-corrected in Mestrelab Mes-
treNova 11.0. Mass spectrometry data was analysed using Thermo Scientific XCal-
ibur 2.8. Fluorescence and UV-Vis data was acquired and baseline-corrected inside
the software supplied with the respective instruments. Integration of fluorescence
spectra was carried out in Originlab Origin 2016 SR2. EPR spectra were acquired
and integrated using the Miniscope Scan and Plot software supplied by the Mag-
nettech. GPC data was acquired in PSS WinGPC and processed there. All calibration
and curve evaluation operations were performed in WinGPC.

Data normalisation and plotting was carried out in Originlab Origin 2016 SR2
from plaintext-exports of all data. All calculations were performed in Originlab
Origin 2016 SR2, Microsoft Excel 2016, and Mathworks MatLab 2018r2.

EPR Calibration

Solutions of 2,2,6,6-tetramethyl-4-piperidinol-N-oxyl (TEMPOL) in THF were pre-
pared as a dilution series from 1000 – 7.81 µg·mL⁻¹. Spectra of all solutions were recorded
as 5x overscans at detector gain stages of 1, 2, 4, 8, 10, 20, 40, 80, 100, 200 and 400. Spectra
were double-integrated using a baseline of pure THF also recorded at each individual gain
stage in order to obtain data for a calibration of radical concentration in solution. Recording
calibrations for each gain stage was necessary, as signal intensity did not scale with detector
gain. For each gain-stage, spectra were recorded until a concentration where the acquisition
exceeded the detection headroom. Spectra that showed signal clipping were discarded. Rad-

ical concentration quantifications on the polymer backbone were carried out in concentrations of 0.1 – 10 mg·mL⁻¹ of polymer at the highest gain stage possible in order to acquire spectra with a maximal S/N ratio for evaluation. Sidechain conversion was calculated by comparing the concentration value obtained from EPR measurements to the concentration of piperidyl-groups present in the precursor, calculated from NMR.

Photometric Experiments

UV/Vis-absorption measurements were carried out on a Shimadzu UV-1800 spectrometer using 3 mL quartz-cuvettes of 1 cm path length. Solutions were filtered through 0.2 µm syringe filters. Absorption spectra were baseline-corrected automatically in the software from a baseline recorded using only the buffer in which experiments were carried out. Concentrations were calculated utilizing Beer-Lambert law,

$$A = \lg\left(\frac{I_0}{I_1}\right) = \varepsilon_\lambda \cdot l \cdot c$$

where A is the total absorbance, defined as the logarithm of incident light (I_0) and emitted light (I_1), the specific molar extinction coefficient ε at wavelength λ , the path length l in cm and the molar concentration c .

Fluorescence release experiments

Fluorescence measurements were carried out in a 2011 Agilent Technologies Cary Eclipse fluorescence spectrometer using 3 mL quartz cuvettes with a path length of 1 cm.

7.3 METHODS PH – RESPONSIVE NANOCARRIER

7.3.1 Monomer syntheses

Methoxy(triethyleneglycol)methacrylate (TEGMA)

Methacryloylchloride (37.6 g, 3.61 mmol, 1.2 eq) in 60 mL dichloromethane was slowly added to a solution of methoxy-(triethyleneglycol) (49.3 g, 300 mmol, 1 eq) and triethylamine (36.4 g, 300 mmol, 1.2 eq) in 280 mL dichloromethane *via* dropping funnel at 0 °C. The solution was stirred for 1 h after complete addition. The ice bath was removed

and the solution was stirred at ambient temperature overnight. Water was added until the white residue was completely dissolved. The water phase was removed and the organic layer was washed with 100 mL of 1 M HCl (2x), 100 mL saturated aqueous sodium carbonate solution (2x) and 100 mL brine (1x). The organic layer was dried over copious amounts of anhydrous Na₂SO₄. Unreacted low boiling components were removed under high vacuum for 1 h. The crude product mixed with 100 mg of phenothiazine as inhibitor and was purified by fractionated vacuum distillation (135 °C heating, 105 °C condensation temperature, 0.02 mbar). The product was obtained as a colourless clear liquid (49.2 g, 211 mmol, 70.7% yield). 20 mg of hydroquinone were added as polymerisation inhibitor for storage at -20 °C.

¹H-NMR (600 MHz, chloroform-d): δ = 6.08 (dd, J = 1.6, 0.9 Hz, 1H), 5.53 (s, 1H), 4.28 – 4.22 (t, 2H), 3.79 – 3.45 (m, 12H), 3.33 (s, 3H), 1.90 (d, J = 0.5 Hz, 3H).

¹³C-NMR (151 MHz, chloroform-d): δ = 167.42, 136.22, 125.79, 72.00, 70.72, 70.70, 70.65, 69.22, 63.95, 59.11, 18.39.

Boc-hydrazidomethacrylate (bHMA)

Methacryloylchloride (1.98 g, 18.0 mmol, 1.2 eq) in 15 mL dichloromethane was slowly added to a solution of *tert*-butyl-carbazate (1.88 g, 15.0 mmol, 1 eq) and triethylamine (1.82 g, 15.0 mmol, 1.2 eq) in 15 mL dichloromethane *via* dropping funnel at 0 °C. The solution was stirred for 1 h after complete addition. The organic layer was washed with 15 mL of 1 M HCl (2x), 15 mL saturated aqueous sodium carbonate solution (2x) and 15 mL brine (1x). The organic layer was dried over copious amounts of anhydrous Na₂SO₄. Dichloromethane was removed at the rotary evaporator under reduced pressure. The slightly yellow crude product was resolved in minimal amounts of ethyl acetate and reprecipitated by addition into 100 mL diethyl ether at -20 °C. The product was obtained as a white fine crystalline solid (1.86 g, 9.31 mmol, 62% yield).

¹H-NMR (600 MHz, chloroform-d): δ = 7.57 (s, 1H) –NH d, 6.60 (s, 1H) –NH, 5.80 (s, 1H) =CH₂, 5.46 – 5.42 (s, 1H) =CH₂, 1.99 (s, J = 1.2 Hz, 3H) –CH₃, 1.48 (d, J = 1.7 Hz, 9H) –OC(CH₃)₃.

¹³C-NMR (151 MHz, chloroform-d): δ = 167.52, 155.46, 121.40, 81.97, 77.24, 77.03, 76.81, 28.14, 18.38.

ESI-MS (negative mode): found 199.1097, calcd. 199.1083 ([M-H]⁻).

Cy5-Methacrylamide

The procedure was adapted from literature protocols.^[184] Cy5 amine Hydrochloride (5 mg, 7.65 μmol , 1 eq) was dissolved in 1 mL DMF. TEA (0.8 mg, 7.65 μmol , 1 eq) was slowly added *via* syringe. The resulting solution was agitated at 150 rpm for 15 minutes. Methacryloyl chloride (2.12 mg, 8.41 μmol , 1.1 eq) as dissolved in 500 μL DMF and added drop- wise at -20 $^{\circ}\text{C}$. The reaction mixture was agitated overnight and allowed to warm to room temperature. The monomer was purified by gradient column chromatography (silica, MeOH/DCM, 0% 3 CV, 0-10% 3 CV, 10-100% 10 CV), with the monomer eluting as the second fraction (4.1 mg, 79% yield).

ESI-MS, positive mode: $m/z = [\text{M}]^+$: found 649.4566, calcd. 649.4474; $[\text{M}+\text{HCl}]^+$: found 685.4335, calcd. 685.4243 (**Figure A 8.5**).

7.3.2 Small Molecule Studies

Synthesis of N-Benzylphthalimide (3-2)

107 g of phthalic anhydride (0.77 mol, 1.00 eq) were resolved in 500 mL glacial acetic acid. Then 120 mL benzylamine (118 g, 1.10 mol, 1.50 eq) were added slowly to the stirring solution. The solution was heated at reflux for 1 hour. The hot reaction mixture was then poured onto 1.5 L ice and resulting precipitate was collected by vacuum filtration. The solid matter was recrystallised from ethanol to give 163.32 g (0.69 mol, 96% yield).

$^1\text{H-NMR}$ (600 MHz, CDCl_3): δ (ppm) = 7.84 (dd, $J = 5.4, 3.1$ Hz, 2H, HAr), 7.70 (dd, $J = 5.5, 3.0$ Hz, 2H, HAr), 7.43 (d, $J = 7.1$ Hz, 2H, HAr), 7.32 (t, $J = 7.4$ Hz, 2H, HAr), 7.26 (t, $J = 7.3$ Hz, 1H, HAr), 4.85 (s, 2H, N-CH-CHAr).

Synthesis of 2-Benzyl-1,1,3,3-tetramethylisoindoline (3-3)

A 3-neck round bottom flask was charged with 41.0 g pre-dried magnesium turnings (1.69 mol, 8.00 eq). The whole experimental setup, consisting of a dropping funnel, a Dean Stark apparatus and a cooler, was objected to high vacuum, heated thoroughly with a heat-gun and charged with argon. Some iodine crystals were added. The setup was heated and set under argon again. The apparatus was allowed to cool down. 270 mL of dry diethyl ether were added and stirred at 250 rpm. A mixture of 80.0 mL methyl iodide (164.16 g, 1.27 mol, 6.00 eq) in 130 mL dry diethyl ether was added *via* dropping funnel until gentle

bubbling of the solution in the RBF indicated the reaction had started. The remaining methyl iodide was added slowly, maintaining a steady rate of bubbling. While the solution was left to stir, 50 g N-Benzylphthalimide **3-2** (0.211 mol, 1.00 eq) were dissolved in 500 mL dry toluene by gentle heating and then added slowly to the reaction mixture. The reaction mixture was heated to 150 °C while diethyl ether was removed constantly through the Dean-Stark apparatus. After 300 mL diethyl ether were removed in this way, the solution was refluxed for 4 hours. The reaction was allowed to cool and 350 mL dry hexane was added. The reaction mixture was left to stir overnight under argon, forming a dense, clay-like purple residue of magnesium and side-products. The reaction mixture was filtered through Celite 521 under vacuum under constant stirring with a spatula to avoid clogging of the filter. The filtrates were bubbled with compressed air until all the solvent was removed. The remaining brown solids were taken up in hexane and passed through a plug of basic alumina. The solvent was removed under reduced pressure. The product was recrystallised from 100 mL methanol to yield 8.77 g pure product as white needles (0.03 mol, 16% yield).

¹H-NMR(600 MHz, CDCl₃): δ (ppm)= 7.47 (d, J = 7.1 Hz, 2H, HAr), 7.29 (t, J = 7.5 Hz, 2H, HAr), 7.26-7.19 (m, 3H, HAr), 7.14 (td, J = 5.6, 5.1, 2.0 Hz, 2H, HAr), 3.99 (s, 2H, N-CH-CHAr), 1.30 (s, 12H, C-CH).

Synthesis of 5-Bromo-1,1,3,3-tetramethylisoindoline (**3-4**)

2-Benzyl-1,1,3,3-tetramethylisoindoline **3-3** (5.00 g, 18.8 mmol, 1.00 eq) was dissolved in 75 mL DCM and placed under argon. The reaction mixture was cooled to 0 °C. A solution of 2.02 mL bromine (39.5 mmol, 2.10 eq) in 50 mL dry DCM was added dropwise, followed by the addition of 9.02 g anhydrous AlCl₃ (67.7 mmol, 3.60 eq). Before pouring the reaction mixture onto ice, it was stirred for 1 hour at 0 °C. The reaction mixture was alkalisied with 10 M aqueous NaOH solution and extracted with DCM (3x200 mL). The organic layer was washed with brine, filtered and dried over Na₂SO₄ and the solvent was removed under reduced pressure. The resulting oil was taken up in 120 mL methanol and stirred with 377 mg sodium hydrogen carbonate. Then 2 mL aqueous hydrogen peroxide (30 wt%) was added dropwise. The solution was acidified by the addition of 2 M sulphuric acid and washed with DCM (3x125 mL). The combined organic phases were re-extracted with 2 M sulfuric acid (3x125 mL). Then the combined aqueous layers were

washed with DCM (2x50 mL). While cooling the acidic phase brought to pH = 14 by the slow addition of 10 M aqueous sodium hydroxide. The solution was extracted with DCM (3x250 mL) and the combined organic phases were washed with brine (125 mL) and dried over anhydrous sodium sulfate. The solvent was removed under reduced pressure to yield 3.78 g of a white solid (14.9 mmol, 79% yield).

¹H-NMR(600 MHz, CDCl₃): δ (ppm)= 7.38-7.34 (m, 1H, HAr), 7.24 (d, J = 1.7 Hz, 1H, HAr), 6.99 (d, J = 8.0 Hz, 1H, HAr), 1.46 (d, J = 5.5 Hz, 12H, C-CH), 1.44 (s, 1H, NH).

Synthesis of 5-Carboxy-1,1,3,3-tetramethylisoindoline (3-5)

2.00 g 5-Bromo-1,1,3,3-tetramethylisoindoline **8** (7.87 mmol, 1.00 eq) were placed under argon and dissolved in 40 mL dry THF. The solution was cooled -78 °C. A solution of *n*-butyl lithium (1.6 M in hexanes, 11.8 mL, 18.9 mmol, 2.40 eq) were added dropwise over 20 minutes. The solution was allowed to stir for 20 minutes. Dry ice pellets were mixed with dry THF to form a slurry. The slurry was poured into the reaction mixture (approx. 150 mL volume). Then the solution was allowed to warm to room temperature while stirring under argon. The solvent was removed under reduced pressure and the residue was taken up in 2 M hydrochloric acid (40 mL). The aqueous layer was washed with diethyl ether (3 x 30 mL). The aqueous phase was neutralised with sodium carbonate and washed with diethyl ether. The solvent was lyophilised to yield a white powder, which was used for the following reaction without further purification.

Synthesis of 5-Carboxy-1,1,3,3-tetramethylisoindoline-2-yloxyl (3-6)

5-Carboxy-1,1,3,3-tetramethylisoindoline **3-5** (7.87 mmol, 1.00 eq) was dissolved in a mixture of water (70 mL) and methanol (4.5 mL). Sodium hydrogen carbonate (620 mg, 7.38 mmol, 0.94 eq), 350 mg sodium tungstate dihydrate (1.06 mmol, 0.13 eq) and 6.00 mL hydrogen peroxide (30% in water, 52.9 mmol, 6.73 eq) were added. The reaction was stirred for 24 h. Further 150 mg Na₂WO₄·H₂O (450 μ mol, 0.058 eq) and 3.00 mL H₂O₂ (30% in water, 26.5 mmol, 3.36 eq) were added and the reaction was stirred for another 48 h. The solution was basified by the addition of 2 M sodium hydroxide solution and washed with diethyl ether (3 x 25 mL). The basic aqueous layer was acidified by the addition of 2 M hydrochloric acid and extracted with diethyl ether (3 x 50 mL). The combined

organic layers were washed with brine and dried over anhydrous sodium sulfate. The solvent was removed under reduced pressure to give 147 mg as yellow crystals. The aqueous phase was neutralised with NaHCO₃. An aqueous solution of 17 mL H₂O₂ (30wt%) and 140 mg Na₂WO₄·H₂O were added. Another 16 mL H₂O₂ (30wt%) were added after 5 hours. The solution was allowed to stir over the weekend. Then additional 40 mL H₂O₂ (30wt%) were added. The reaction mixture was worked up as described before to give 212.7 mg product as a yellow powdery solid. In total 359.7 mg of **3-6** could be obtained, yielding 20% over two steps (1.54 mmol).

Rf(Hex/EA (1:1), 1% AcOH, SiO₂)= 0.46

Synthesis of 1,1,3,3-tetramethylisoindoline-2-yloxyl-5-ethylcarboxylate (**3-7**)

92.5 mg of 5-Carboxy-1,1,3,3-tetramethylisoindoline-2-yloxyl **3-7** (0.395 mmol, 1.00 eq) were dissolved in 2.5 mL EtOH. Subsequently, 0.16 mL 98% sulfuric acid (2.75 mmol, 7.00 eq) were added to the solution. The reaction mixture was stirred for 96 hours at 50 °C. The solution was added dropwise to a saturated aqueous NaHCO₃ solution. The aqueous layer was extracted with DCM (3 x 25 mL). The combined organic layers were washed with brine and dried over anhydrous sodium sulfate. The solvent was removed under reduced pressure. The product was purified by column chromatography (Hex/EA (1:1), SiO₂) to yield the product as orange solid (76.4 mg, 0.291 mmol, 74%).

Rf(Hex/EA (1:1), SiO₂)= 0.95

Synthesis of 2-Yloxyl-1,1,3,3-tetramethylisoindoline-5-carbohydrazine (**3-8**)

1,1,3,3-tetramethylisoindoline-2-yloxyl-5-ethyl-carboxylate (**3-7**) (45.4 mg, 191 μmol, 1.00 eq) were dissolved in 6 mL of a 1:1 (v/v) mixture of *i*PrOH and hydrazine monohydrate. The reaction mixture was refluxed for 2 h. Diethyl ether (20 mL) was added to the reaction mixture and a white solid precipitated. The solid was isolated by filtration to yield the product as a white solid (26.3 mg, 106 μmol, 55%).

Rf (Hex/EA (1:1), SiO₂) = 0.13

Synthesis of 2-Yloxy-1,1,3,3-tetramethyl-N'-(1-pyrene-3-yl)-ethylidene)isoindoline-5-carbohydrazide (3-9)

A stock solution 7 mL of 2-Yloxy-1,1,3,3-tetramethylisoindoline-5-carbohydrazine **3-8** in toluene/*i*PrOH ($c = 0.22$ mg/mL) was prepared (0.0064 mmol, 1.21 eq). A second stock solution of 1-Acetylpyrene in *i*PrOH ($c = 1.3$ mg/mL, 1 mL, 0.0053 mmol, 1.00 eq) was added. Two drops of glacial AcOH were added and the reaction mixture was refluxed for 17 hours at 95 °C. The conversion was followed by TLC. To neutralise the solution, 1 mg Na₂CO₃ was added. The reaction mixture was dried over anhydrous sodium sulfate and filtrated. The solvent was removing under reduced pressure to give **3-9** as a yellow solid (6.3 mg 0.0133 mmol).

Synthesis of tert-butyl 2-(2-yloxy-1,1,3,3-tetramethylisoindoline-5-carbonyl)-hydrazine-1-carboxylate (3-10)

In a three neck flask 50.0 mg CTMIO **3-6** (10, 213 μmol, 1.00 eq), 34.6 mg hydroxybenzotriazole (256 μmol, 1.2 eq) and 3.9 mg DMAP (32 μmol, 0.15 eq), dissolved in 10 mL of dry DCM under argon and cooled to 0 °C. A solution of 131.8 mg DCC in 5 mL dry DCM were added slowly dropwise. The solution was allowed to warm to room temperature and stirred for 3 hours. The conversion was followed by TLC. The reaction mixture was cooled to 0 °C and a solution of 28.3 mg tert-butyl carbazate (213 μmol, 1.00 eq) in dry DCM was added dropwise. The mixture was allowed to warm to room temperature and stirred for 24 h. The solvent was removed under reduced pressure and the solid was purified *via* column chromatography (Hex/EA (1:1), SiO₂) to yield the product as an off-white solid (50.6 mg, 145 μmol, 68%).

R_f (Hex/EA (1:1), SiO₂) = 0.54

7.3.3 Single Anchor SAP-System**Small molecule synthesis****N-(prop-2-yn-1-yl)-N'-(propan-2-ylidene)pivalohydrazide (3-11)**

Protocols were adapted from the literature.^[265] **3-10** (516 mg, 3.0 mmol, 1 eq) was dissolved in 10 mL toluene and KOH (powdered, 218 mg, 3.9 mmol, 1.3 eq), and tetrabutylammonium hydrogen sulfate (100 mg, 0.3 mmol, 1 eq) were added.

Polymer synthesis and postmodification

pTEGMA-*stat-co*-GMA (SAP-1)

TEGMA and dioxane were pre-treated by running through a plug of basic alumina to remove inhibitor, residual water and peroxides. CPDB (38.1 mg, 0.172 mmol, 1 eq), TEGMA (10.0 g, 43.1 mmol, 250 eq), GMA (612 mg, 4.31 mmol, 25 eq), and AIBN (2.81 mg, 0.0172 mmol, 0.1 eq) were dissolved in 10 mL of dioxane and sealed in a 20 mm, 15 mL crimp-cap vial. The solution was degassed by gentle bubbling with nitrogen in an ice bath in the dark. Polymerisation was started by placing the vial in a preheated aluminium block at 65 °C and stirring at 800 rpm. After 6 h the reaction was quenched by opening the vial and immediate submersion in liquid nitrogen. Conversion was determined to be 25% *via* NMR. The polymer was precipitated twice from *n*-hexane at -20 °C and centrifuged at 5000 ×g for 5 min. The composition of the polymers used for further modification was determined to be 11:1 TEGMA:GMA *via* NMR from the ratio of signals c (TEGMA, 2H), g (GMA, 1H) (**Figure A 8.27**). Incorporation into the same chain was confirmed *via* SEC-MS (refer to **Appendix, Section 8.1.3**).

Photo-protection of the RAFT end group (SAP-1)

SAP-0 (50 mg) was dissolved in 10 mL of dry ACN. An excess of methoxy-photoe-nol was added (ca. 15 mg) and the solution was sealed. After degassing *via* bubbling with argon, the solution was placed in a photo reactor, equipped with four Arimed-B6 fluorescent lamps. The solution was irradiated for 15 min. after irradiation, the characteristic pink colour of **SAP-0**, owed to the dithiobenzoyl-group, had fully disappeared and the solution was completely clear. The polymer was precipitated twice from *n*-hexane at -20 °C and centrifuged at 5000 ×g for 5 min. Quantitative protection of the end group was confirmed *via* NMR (refer to **Section 3.3, Figure 3.3**). The polymer was recovered as a clear, highly viscous liquid.

GMA ring opening (SAP-2)

SAP-1 (100 mg) was dissolved in 50 mL of dry DMF, mixed with an excess of NaN_3 and sealed in a 10 mL crimp-cap vial. The solution was degassed by bubbling with argon for 15 min. After degassing, the solution was placed in an oil bath and heated to 50 °C under vigorous stirring for 2 h. The solution was allowed to cool, filtered through a PTFE membrane filter, and left to evaporate under airflow overnight. The remaining solution was taken up in THF, filtered again and precipitated from cold diethyl ether at -20 °C. **SAP-2** was recovered as slightly yellow, highly viscous liquid. Quantitative ring opening was confirmed by the disappearance of signals g, h and i from the NMR (refer to **Section 3.3, Figure 3.5**).

Succinic anhydride coupling (SAP-3.1)

SAP-2 (150 mg, 0.02 mmol, 1 eq) were dissolved in 2 mL of THF and cooled to 0 °C. Succinic anhydride (0.225 mg, 0.226 mmol, 15 eq) and DMAP (0.6 mg, 4 μmol , 0.02 eq) were added and the solution was allowed to reach room temperature overnight. **SAP-3.1** was precipitated from cold diethyl ether.

Copper click reactions general procedure

CuAAC protocols were carried out according to literature known procedures.^[266] The azide (25 mg scale) was prepared in DMF, 18 eq copper (II) sulfate, 18 eq sodium-ascorbate were added and the resulting mixture was stirred at RT for 24 h. Subsequently, the mixture was passed through an alumina column to remove copper and undissolved components. The resulting polymers were obtained by precipitation from cold diethyl ether.

7.3.4 Statistical PC-System**pTEGMA-*stat-co*-bHMA-*stat-co*-TMPMA (PC-0)**

TEGMA and dioxane were pre-treated by running through a plug of basic alumina to remove inhibitor, residual water and peroxides. CPPTTC (46.7 mg, 0.188 mmol, 1 eq), TEGMA (2.33 g, 10.1 mmol, 125 eq), TMPMA (192 mg, 0.851 mmol, 10 eq), bHMA

(173 mg, 0.851 mmol, 10 eq) and AIBN (2.21 mg, 0.0133 mmol, 0.1 eq) were dissolved in 3 mL of dioxane and sealed in a 20 mm, 15 mL crimp-cap vial. The solution was degassed by gentle bubbling with nitrogen in an ice bath in the dark. Polymerisation was started by placing the vial in a preheated aluminium block at 65 °C and stirring at 800 rpm. After 12 h, the reaction was quenched by opening the vial and immediate submersion in liquid nitrogen. Conversion was determined to be 64% *via* NMR as an average of the ratio of signals e/b', g/g' and c/c'. The polymer was precipitated twice from ether at -20 °C and centrifuged at 5000 ×g for 5 minutes to obtain the polymer as a clear, yellow highly viscous material. The composition of the polymers used for further modification was determined to be 12.5:1:1.01 *via* NMR from the ratio of signals c (TEGMA, 2H), g (TMPMA, 1H), and f (bHMA, 9H) (**Figure 3.11**). Incorporation into the same chain containing the correct end group was confirmed *via* DOSY (**Figure 3.12**) and SEC-MS (**Figure 3.11, Table A 8.7**).

pTEGMA-*stat-co*-bHMA-*stat-co*-TEMPOMA (PC-1)

To a solution of 150 mg of **PC-0** in 10 mL dichloromethane 10 eq of *m*CPBA were added (stoichiometry relative to the amount of TMPMA groups). The solution was sealed in a 20 mm, 15 mL crimp-cap vial and stirred at 1000 rpm for 3 h. The solvent was removed under reduced pressure using a rotary evaporator. *m*CPBA was removed by precipitating the polymer from a mixture of ether/hexanes (10/1) at -20 °C and centrifugation at 3500 g, yielding a clear red viscous material. Nitroxide loading was determined *via* the ESR from 4.4 mg of polymer in 1.5 mL THF using a calibration dataset acquired from defined TEM-POL solutions at gain 2 (**Table A 8.5**). Conversion was determined to be quantitative.

pTEGMA-*stat-co*-HMA-*stat-co*-TEMPOMA (PC-2)

The precipitate from **SSPC-1** was resolved in 7 mL of dichloromethane, cooled to 0 °C and 7 mL of concentrated trifluoroacetate were added under 1000 rpm stirring. The solution was allowed to reach room temperature and stirred for another 30 minutes in a ventilated vial. Solvent and trifluoroacetate were removed under reduced pressure at the rotary evaporator. A 5 mg sample was taken to confirm full boc-group removal *via* NMR. A few drops of triethylamine were added until no more white fumes formed to neutralise the crude product and restore nitroxide functionalities to their oxidised form. The polymer was precipitated from a mixture of ether/hexanes (10/1) at -20 °C and centrifugation at

3500 $\times g$, yielding a dark orange, slightly cloudy viscous material. Investigation of nitroxide density *via* ESR showed a strong decrease in signal strength (**Table A 8.6**), indicating the formation of the TFA salt by the nitroxide. All material was immediately employed in subsequent drug loading.

Pyrene loading (PC-3)

The remaining **PC-2** (ca. 50mg) was resolved in 5 mL of anhydrous methanol and 200 mg of anhydrous sodium sulfate were added. The solution was stirred for 15 minutes and 30 mg of Acetylpyrene were added (ca. 5 eq in relation to present hydrazides). The solution was sealed in a 20 mm, 15 mL crimp-cap vial and purged with nitrogen for 15 minutes. 75 μL of glacial acetic acid were added and the sealed vial was placed in a preheated aluminium block at 70 $^{\circ}\text{C}$ and stirred at 250 rpm for three days. The solution was neutralised by careful addition of dry TEA and filtered. The residual sodium sulfate was thoroughly washed with methanol until no more red colour would elute from the filter. The solution was reduced to 3.5 mL under reduced pressure at room temperature. Residual Pyrene was removed by running size exclusion chromatography with ca. 50 g of Sephadex LH-20 resin and methanol with 0.5% TEA as eluent. Fractions were checked for presence of nitroxide-containing polymer *via* GPC and ESR. All fractions exhibiting a polymer peak in the GPC RI trace also exhibited strong absorption at a wavelength of 360 nm, matching the elution times in the RI signal, indicating successful polymer coupling. All fractions confirmed for presence of Pyrene conjugate exhibited strong ESR signals. The polymer was obtained as a yellow, sticky solid.

Pyrene loading was quantified *via* NMR spectroscopy and photometry. UV/Vis ($\lambda_{\text{max}} = 360 \text{ nm}$) yielded an overall loading of 46.3%.

GPC Investigation of Dox Loading

Pyrene loading was tested by the increase of light-absorption at 360 nm in the UV detector. RI traces of each individual run were normalised, and UV spectra were scaled by the according factor, in order to make sure concentration fluctuations from filtering do not influence the outcome, footing on the assumption that each sample's difference in refractive index is negligible, compared to the change in extinction at 360 nm. Absorption-traces

showed multiple orders of magnitude difference in intensity, independent of the processing method, when comparing samples before and after loading.

Release kinetics

Fluorescence experiments were carried out in a 3 mL quartz cuvette. **PC-3** was dissolved to a concentration of $0.4 \text{ mg}\cdot\text{mL}^{-1}$, 64x diluted in ACN and 10 μL of acetic acid were added. Spectra were acquired in 30 s increments for 100 measurements and 20 min increments for another 100 measurements. As fluorescence-increase slowed down from there following spectra were acquired in 120 min increments to a total acquisition time of 4 d. Repeated experiments would unsatisfyingly yield widely varying amounts of fluorescence turn-on of more than an order of magnitude of variation. The issue was identified to be mostly dependent of pyrene's sensitivity to different levels of polarity. Different batches of **PC-3** would occasionally indicate differing amounts of residual TEA, impossible to be removed from solution. A shift to a buffered system in PBS was attempted, but exhibited precipitate of unknown composition, interfering strongly with fluorescence measurements. The system was remodelled to utilise Dox as a fluorophore, as this would allow access to a water-soluble system.

7.3.5 Statistical SSPC System

Polymer synthesis and postmodification

pTEGMA-*stat*-co-bHMA-*stat*-co-TMPMA (SSPC-0)

TEGMA and dioxane were pre-treated by running through a plug of basic alumina to remove inhibitor, residual water and peroxides. CPPTTC (46.7 mg, 0.188 mmol, 1 eq), TEGMA (2.33 g, 10.1 mmol, 125 eq), TMPMA (385 mg, 1.71 mmol, 20 eq), bHMA (346 mg, 1.71 mmol, 20 eq) and AIBN (2.21 mg, 0.0133 mmol, 0.1 eq) were dissolved in 3 mL of dioxane and sealed in a 20 mm, 15 mL crimp-cap vial. The solution was degassed by gentle bubbling with nitrogen in an ice bath in the dark. Polymerisation was started by placing the vial in a preheated aluminium block at 65 °C and stirring at 800 rpm. After 12 h, the reaction was quenched by opening the vial and immediate submersion in liquid nitrogen. Conversion was determined to be 70% *via* NMR as an average of the ratio of signals

e/b', g/g' and c/c' (**Figure A 8.26**). The polymer was precipitated from ether at -20 °C and centrifuged at 5000 ×g for 5 minutes. As NMR still showed residual monomer the polymer was reprecipitated from a mixture of ether/hexanes (10/1) and centrifuged again to obtain at 5000 ×g for 5 min to obtain the polymer as a clear, yellow highly viscous material. The composition of the polymers used for further modification was determined to be 6.26:1:1.01 *via* NMR from the ratio of signals c (TEGMA, 2H), g (TMPMA, 1H), and f (bHMA, 9H) (**Figure A 8.27**). Incorporation into the same chain containing the correct end group was confirmed *via* mass spectrometry in an SEC-MS experiment.

pTEGMA-*stat-co*-bHMA-*stat-co*-TEMPOMA (SSPC-1)

To a solution of 150 mg of **SSPC-0** in 10 mL dichloromethane 10 eq of *m*CPBA were added (stoichiometry relative to the amount of TMPMA groups). The solution was sealed in a 20 mm, 15 mL crimp-cap vial and stirred at 1000 rpm for 3 h. The solvent was removed under reduced pressure using a rotary evaporator. *m*CPBA was removed by precipitating the polymer from a mixture of ether/hexanes (10/1) at -20 °C and centrifugation at 3500 g, yielding a clear red viscous material. Nitroxide loading was determined *via* the ESR from 4.4 mg of polymer in 1.5 mL THF using a calibration dataset acquired from defined TEM-POL solutions at gain 2 (**Table A 8.1**). Conversion was determined to be quantitative.

pTEGMA-*stat-co*-HMA-*co*-TEMPOMA (SSPC-2)

The precipitate from **SSPC-1** was resolved in 7 mL of dichloromethane, cooled to 0 °C and 7 mL of concentrated trifluoroacetate were added under 1000 rpm stirring. The solution was allowed to reach room temperature and stirred for another 30 minutes in a ventilated vial. Solvent and trifluoroacetate were removed under reduced pressure at the rotary evaporator. A 5 mg sample was taken to confirm full boc-group removal *via* NMR. A few drops of triethylamine were added until no more white fumes formed to neutralise the crude product and restore nitroxide functionalities to their oxidised form. The polymer was precipitated from a mixture of ether/hexanes (10/1) at -20 °C and centrifugation at 3500 ×g, yielding a dark orange, slightly cloudy viscous material. Investigation of nitroxide density *via* ESR showed a strong decrease in signal strength, indicating the formation of the TFA salt by the nitroxide. All material was immediately employed in subsequent drug loading.

Doxorubicin loading (SSPC-3)

The remaining **SSPC-2** (ca. 100 mg) was resolved in 5 mL of anhydrous methanol and 200 mg of anhydrous sodium sulfate were added. The solution was stirred for 15 minutes and 30 mg of doxorubicin hydrochloride were added (ca. 2 eq in relation to present hydrazides). The solution was sealed in a 20 mm, 15 mL crimp-cap vial and purged with nitrogen for 15 minutes. 75 μ L of glacial acetic acid were added and the sealed vial was placed in a preheated aluminium block at 70 °C and stirred at 250 rpm for three days. The solution was neutralised by careful addition of triethylamine and filtered. The residual sodium sulfate was thoroughly washed with methanol until no more red colour would elute from the column. The solution was reduced to 3.5 mL under reduced pressure at room temperature. Residual Dox was removed by running size exclusion chromatography with ca. 50 g of Sephadex LH-20 resin and methanol with 0.5% TEA as eluent. Fractions were checked for presence of nitroxide-containing polymer *via* GPC and ESR. All fractions exhibiting a polymer peak in the GPC RI trace also exhibited strong absorption at a wavelength of 500 nm, matching the elution times in the RI signal, indicating successful polymer coupling. All fractions confirmed for presence of Dox conjugate exhibited strong ESR signals. Fractions exhibiting ESR signal were added to an equal volume of phosphate buffered saline (PBS) at pH = 7.4 and dialysed against 3x 500 mL of PBS at pH = 7.4 to remove residual TEA and methanol. The final polymer was obtained *via* extraction with dichloromethane until the aqueous phase showed no more red colouring. The polymer was obtained as a dark red, sticky solid.

Drug loading was quantified *via* NMR spectroscopy and photometry. NMR quantification yielded an overall loading of 22.5% determined from the integrals of the aromatic proton resonances associated with doxorubicin relative to the initial amount of bHMA. TEGMA resonances were used as a reference and loading was calculated as the ratio of both incorporation ratios, given in **Table A 8.12**. Photometry indicated a slightly higher loading density of 25.6%, calculated from Lambert-Beer's law with a path-length of 1 cm and an absorption coefficient of $\epsilon_{495} = 10'000 \text{ L}\cdot\text{M}^{-1}$ (**Figure A 8.31**). Lower loading densities determined *via* NMR-based calculations were attributed to line broadening from the presence of nitroxides and the weak signals of Dox.

Determination of Dox loading density

Dox loading was photometrically determined by recording a background-corrected spectrum in PBS. The absorption value at 495 nm was utilised to calculate the total Dox concentration in solution. The value was recalculated as Dox amount per milligram of sample. The amount was subtracted from the total amount of material weighed in to give the amount of polymer per milligram of sample. The total amount of hydrazides present was taken from the NMR measurements obtained from the starting material as the molar fraction of boc-groups present. Loading density was given as a fraction of Dox amount and hydrazide groups present. Spectra and numeric values can be found in the **Appendix, Figure A 8.31** and **Table A 8.12**.

GPC Investigation of Dox Loading

Drug loading was tested by the increase of light-absorption at 500 nm in the UV detector. RI traces of each individual run were normalised, and UV spectra were scaled by the according factor, in order to make sure concentration fluctuations from filtering do not influence the outcome, footing on the assumption that each sample's difference in refractive index is negligible, compared to the change in extinction at 500 nm. Absorption-traces showed multiple orders of magnitude difference in intensity, independent of the processing method, when comparing samples before and after loading.

Release kinetics

Fluorescence experiments were carried out in a 3 mL quartz cuvette. **SSPC-3** was dissolved to a concentration of $0.4 \text{ mg}\cdot\text{mL}^{-1}$, 64x diluted in PBS at pH = 7.4 and 30 μL of acetic acid were added. Spectra were acquired in 30 s increments for 100 measurements and 20 min increments for another 100 measurements. As fluorescence-increase slowed down from there following spectra were acquired in 120 min increments to a total acquisition time of 7 d. Fluorescence was quantified by numeric integration between 500 – 800 nm of each individual spectrum. Integral values were plotted over time and revealed a 3.6x increase in fluorescence yield. A direct comparison with an identically treated sample of Dox-hydrochloride after absorption-matching revealed relative fluorescence yields of 23% prior to release and 86% after full release. The difference in fluorescence yield was at-

tributed to possible partial degradation of Dox-HCl, different present Dox-species, stemming from the preparation procedure (see below) and slight residual quenching by nitroxide-bearing polymer in the solution.

In addition to the actual release experiment, a control experiment was conducted, applying the same time in solution, yet without lowering the pH. The control sample showed an increase of 7% in fluorescence over the course of a week measured by the overall fluorescence integral, which was attributed to unspecific hydrolysis of hydrazone linkages. Spectra are shown in **Figure A 8.32**.

Bulk Release Quantification

To estimate total release 50 mg of conjugate were dissolved in 10 mL of PBS at pH 7.4 and dialysed against 3x2.5L PBS at pH 5.0 for 7 days at 4°C. Buffers were exchanged every 48 h The overall release was quantified *via* photometry and the amount of released Dox was calculated from the volume and concentration of Dox, determined from the absorption at 495 nm ($\epsilon = 10'000 \text{ L}\cdot\text{M}^{-1}$). As concentrations were extremely low and spectrometer resolution was as low as 0.001, spectra were mathematically smoothed to obtain more precise values. A Lowess filter, fitting splined traces to every dataset, yielded spectra that actually matched Dox absorption spectra. To check for the validity of the fit, absorption ratios at 495 and 480 nm were compared to their respective literature-reported extinction coefficients. The absorbance ratio 480/495 nm was determined to be 0.78, almost exactly matching the reported extinction coefficient ratio of 0.8 ($12'500 \text{ L}/\text{M}^{[68]}$ and $10'000 \text{ L}/\text{M}^{[230]}$ respectively). To confirm that the release was actually pH sensitive a control experiment 50 mg of polymer was conducted with dialysis Buffer at pH7.4. Release was determined to be 78% at pH 5.0 and 11% at pH 7.4. Values were calculated from absorption at 480 and 495 nm and averaged

7.3.6 Biological Testing

Microscopy

CLSM images were acquired using a Leica SPE (DMI4000B inverted microscope) with ACS APO 10.0x0.30 CS DRY objective, set as: Pinhole: HC PL FLUOTAR 10.0x0.30

DRY Airy (94,3 μm) @ 8 bit resolution, 1024 \times 1024 pixels, 400 Hz. Excitation laser 488 nm (15% power), Emission bandwidth PMT2 (488) 550 nm – 650 nm.

Cell culture instrumentation

Vacuum pump Integra Vacusafe (INTEGRA Biosciences GmbH), ENVAIReco® clean-bench ENVAIR, Ex Demo Units Incubator C170 (Binder), Incubator UN55 (Memmert GmbH + Co. KG), Centrifuge: Megafuge 2.0R Heraeus Sepatech (SEPATECH)

Materials and cell lines

HepG2: human hepatocellular carcinoma cell line

HUVEC: human umbilical vein endothelial cells (C-12200, PromoCell)

NHDF: normal human dermal fibroblasts (CC-2511, Lonza)

SK-MEL-28: skin-melanoma-28 (300337, CLS Cell Lines Service GmbH)

Culture media and additives

Agarose, peqGold Universal Agarose (35-1020, PeQlab, VWR International), DMEM, Dulbecco's Modified Eagle Medium (41966-029, Gibco®, Life Technologies™), DMSO, Dimethylsulfoxide (D2650-100ML, Sigma-Aldrich®), DPBS, Dulbecco's Phosphate Buffered Saline (1x, -CaCl₂, -MgCl₂, 14040-091, Gibco®, Life Technologies™), EGM®-2 Endothelial Cell Growth Medium-2 BulletKit (CC-3162, Lonza), FCS, Newborn Calf Serum, Heat-inactivated, 500 mL (26010-074, Gibco®, Life Technologies™), FGM®-2 Fibroblast Growth Medium-2 BulletKit (CC3132, Lonza), Gelatin (G2500-100G, Sigma-Aldrich®), Lithium Phenyl (2,4,6-trimethylbenzoyl) phosphinate (L0290, Tokyo Chemical Industry), Methacrylic Anhydride (276685-500ml, Sigma-Aldrich®), Penicillin/Streptomycin (P/S) (15140-122, Gibco®, Life Technologies™), Trypsin-EDTA, 0,25% (25200056, Gibco®, Life Technologies™)

Preparation of agarose plates for spheroid growth

Wells of a 10 mm flat bottom 96-well plate were incubated with 50 μL of a 1.5% agarose solution in Dulbecco's Phosphate Buffered Saline (DPBS^{-/-}) and left for gelation for 15 min at ambient temperature. Subsequently, the coated wells were filled with 100 μL of DPBS^{-/-} and either stored at 4 °C or used directly.

Cell lines were stored at -196 °C. After thawing, cells were taken up in 75 cm² cell culture bottles in 15 mL DPBS^{-/-} and cultured at 37 °C at 5% CO₂ atmosphere. After reaching 90% confluence, cells were washed with 10 mL DPBS^{-/-} and removed from the surface by the addition of 1 mL of 0.25% Trypsin-EDTA solution. Subsequently, trypsination was quenched by the addition of cell culture medium and the cell suspension was transferred to a 50 mL centrifuge tube. The cell count was determined microscopically in a Neubauer counting chamber. Cells were resuspended in culture medium and used for experiments directly (see below).

Preparation of tumour spheroids on agarose plates

Spheroids were prepared from HepG2 and SK-MEL-28 cell lines, cultured by the protocol described above. Harvested cells were resuspended and the cell count was adjusted to $1 \cdot 10^5 \text{ mL}^{-1}$. For each batch, 40 μL of cell suspension were added to each well of an agarose-coated 96-well plate, prepared as described above. Plates were incubated at 37 °C in a 5% CO₂ atmosphere. The medium was topped up by the addition of 10 μL every other day. Spheroids were harvested by removal of the full volume of medium and transfer to either 1.5 mL centrifuge tubes or μ -slide wells.

Incubation of spheroids with Dox/SSPC-3

Spheroids were grown for a total of 7 days, harvested and collected in 1.5 mL centrifuge tubes. Next, singled out spheroids were taken up in 50 μL of medium and transferred to a well in an agarose-coated plate, freshly prepared by the protocol outline above. Subsequently, 50 μL of sample solution (free Dox, **SSPC-3**, **SSPC-2**, and buffer only) were added in concentrations of 100 μM , 40 μM , 20 μM , 10 μM and 2 μM Dox-equivalent, bringing the final concentration in solution to 50 μM , 20 μM , 10 μM , 5 μM and 1 μM . Concentrations were chosen in this order of magnitude from MTT tests performed prior to

spheroid experiments, in order to determine a window where cell viability showed an impact by the drug, yet cells survived the incubation. All incubations were carried out in triplicates.

Visualisation of cellular uptake

Spheroids, incubated as described above, were taken up in a 1.5 mL centrifuge tube pre-charged with DPBS^{-/-}. Spheroids were washed and transferred to an ibidi-microscopy slide and investigated *via* microscopy. Imaging was carried out using an inverted confocal laser microscope. In order to achieve maximum comparability of the obtained images, all acquisitions were carried out using the exact same microscope settings (10x objective, excitation laser $\lambda_{\max} = 488$ nm at 14.6% intensity, emission filter 550 nm, z-stack slice thickness of 5-10 μm)

Toxicity testing on spheroids

Spheroids were incubated with sample solutions according to the protocol described above for 72 h at 37 °C under 5% CO₂ atmosphere (concentrations 50 μM , 20 μM , 10 μM , 5 μM and 1 μM Dox). Subsequently, incubated spheroids were washed with DPBS^{-/-} and transferred to a fresh, agarose-coated plate. Dead-controls were incubated with either the highest substance concentration or pure buffer under the same condition and subjected to 10 μL of Triton-X for 30 min. Live-controls were taken, using eight untreated spheroids in each run. For the quantification of cell viability, spheroids were incubated with 15 μL MTT reagent and incubated for 2 h at 37 °C under 5% CO₂ atmosphere. The MTT reaction was stopped by the addition of 100 μL of stopping-buffer. After 24 h, samples were measured by light absorption spectroscopy ($\lambda_{\text{abs}} = 595$ nm, $n = 5$) and investigated for viability. Values were normalised by the live-/dead-controls and evaluated in Microsoft Excel 2016.

Toxicity testing of 2D-cultures (HepG2, SK-MEL-28, NHDF- HUVEC)

Cells were cultured as described above and harvested. HepG2 and SK-MEL-28 cells were seeded to agarose plates at $1 \cdot 10^4$ cells per well, NHDF and HUVEC were seeded at $2 \cdot 10^4$ cells per well. Cells were incubated with sample solutions according to the protocol described above for 72 h at 37 °C under 5% CO₂ atmosphere (concentrations 50 μM ,

20 μM , 10 μM , 5 μM and 1 μM Dox). Subsequently, incubated spheroids were washed with DPBS^{-/-} and transferred to a fresh, agarose-coated plate. Dead-controls were incubated with either the highest substance concentration or pure buffer under the same condition and subjected to 10 μL of Triton-X for 10 min. Live-controls were taken, using untreated wells in each run. For the quantification of cell viability, spheroids were incubated with 15 μL MTT reagent and incubated for 2 h at 37 °C under 5% CO₂ atmosphere. The MTT reaction was stopped by the addition of 100 μL of stopping-buffer. After 24 h, samples were measured by light absorption spectroscopy ($\lambda_{\text{abs}} = 595 \text{ nm}$, $n = 5$) and investigated for viability. Values were normalised by the live-/dead-controls and evaluated in Microsoft Excel 2016.

3D-Cocultures of SK-MEL-28 spheroids with NHDF in GelMA hydrogels

SK-MEL-28 spheroids were generated over a course of 7 days and harvested as described above. For each experiment, three spheroids were co-embedded with $5 \cdot 10^5$ NHDF cells in a hydrogel (5% GelMA, cross-linked *via* 0.3% LAP in an Omnicure®, 40 sec, 800W/cm²). The hydrogel was formed by suspension of $5 \cdot 10^5$ cells in 50 μL FGM-2 medium in a 1.4 mL centrifuge tube. The suspension was gently mixed with 100 μL of a 10% (w/v) GelMA solution in DPBS^{-/-}. The spheroids were taken up in 44 μL FGM-2 and added to the centrifuge tube. Lastly, 6 μL of LAP-photoinitiator were added to the solution and the solution was gently mixed, avoiding the formation of air bubbles at all times, and transfer to a well of a μ -slide. After irradiation in an Omnicure (40 sec, 800W/cm²), the cured gel was topped with 200 μL FGM-2.

Incubation of 3D-Cocultures

Stock solutions of **SSPC-3**, Dox·HCl, and **SSPC-2** were prepared in a concentration of 10 μM in FGM-2. Co-cultures, grown for 7 d as described above were washed, covered with 200 μL of stock solution each, and incubated at 30 °C for 3 h. Cultures were imaged *via* CLSM (10x objective dry, excitation laser $\lambda_{\text{max}} = 488 \text{ nm}$ at 14.6% intensity, emission filter 550-650 nm, Z-stack slice thickness of 5 μm , $n = 100$). Co-cultures were incubated for another 21 h, washed with DPBS^{-/-}, covered with FGM-2 and imaged again.

7.3.7 Automated Evaluation of Microscopy images

Automated evaluation of CLSM slices was carried out using Mathworks MatLab 2018a under the KIT institution academic license. Inspiration and background was drawn from AnaSP, a MatLab based open source software for determination of statistical parameters of spheroids, freely available *via* Sourceforge.^[132] The developed script lets the operator pick an input directory of image exports from the LasX microscopy suite by Leica. Channels are automatically designated, with the first channel ('*ch00') used for fluorescence evaluation and the second channel ('*ch01') used for mask generation. Mask generation itself is based on the `binarize()` function supplied with MatLab, determining image areas *via* adaptive thresholding. The individual threshold factor is supplied by the operator, with visual feedback returned in real time. The image obtained from adaptive thresholding is binarised, transferred into a logical array and subdivided by an array of identical dimensions, designating different areas. As the largest area in the microscopy images analysed was the spheroid itself in all cases, all but the largest areas were omitted and the largest coherent area was filled to yield a binary mask, fully covering the spheroid in the image. In analogy to [132] and empirical findings from the experiments carried out in the course of spheroid generation, a spheroid's centre of mass was chosen as a suitable end-point for diffusion. The centre of mass was obtained from the bright-field image after omitting all pixels outside of the spheroid area. In order to evaluate drug penetration, measurements were carried out along a vector of steady length, outranging the spheroid's maximum radius, cycling around the centre of mass. Vector length was adjusted for each image if necessary, by presence of the full mask area inside of the radius. Results were pre-selected by the centre of mass position: Acquisitions, where the centre of mass deviated by more than one third of the mean radius were deemed unsuitable for the evaluation in question, and evaluation was carried out on different images from the same run of experiments. Profiling was carried out at 4x image resolution along the vector, using nearest-neighbour averaging without image filtering, as both available bilinear and bicubic filtering techniques introduced over-and under-emphasis of fluorescence, where the vector would traverse more than two data-points between pixels, after traversing two valid pixels of high relative numeric differences. This effect proved problematic in mask border-areas during mask profiling in particular, where only binary values are available and extrapolation returns invalid datasets. Profiles were recorded from the maximum radius towards the centre of mass, with the ac-

quisition angle rotating by 0.5° per evaluation, totalling at 720 individual profiles per image. In parallel, the same evaluation was carried out on the mask, yielding a binary vector, allowing to separate the acquired profiles into outside [0] and inside [1] areas of the spheroid. Obtained profiles were aligned by cycling dataset vector arrays by the total of “outside” data points, obtained from the mask profile vector. Averaging was carried out by adding the aligned spectra and division by the total number of profiles. Spectra were background-corrected by determination of a noise floor and subsequent subtraction of a noise-floor constant. Noise floor was determined by averaging the “outside” segments of the obtained profiles, and calculation of the mean value. As image resolution in μm was known and consistent across all acquisitions, profiles were stored in relation to their actual spatial resolution and plotted as relative fluorescence along the measurement vector. The complete, commented listings of the four scripts (file handling, mask creation, profiling parametrisation, profiling) are presented in the **Appendix, 8.1.10, page 194**.

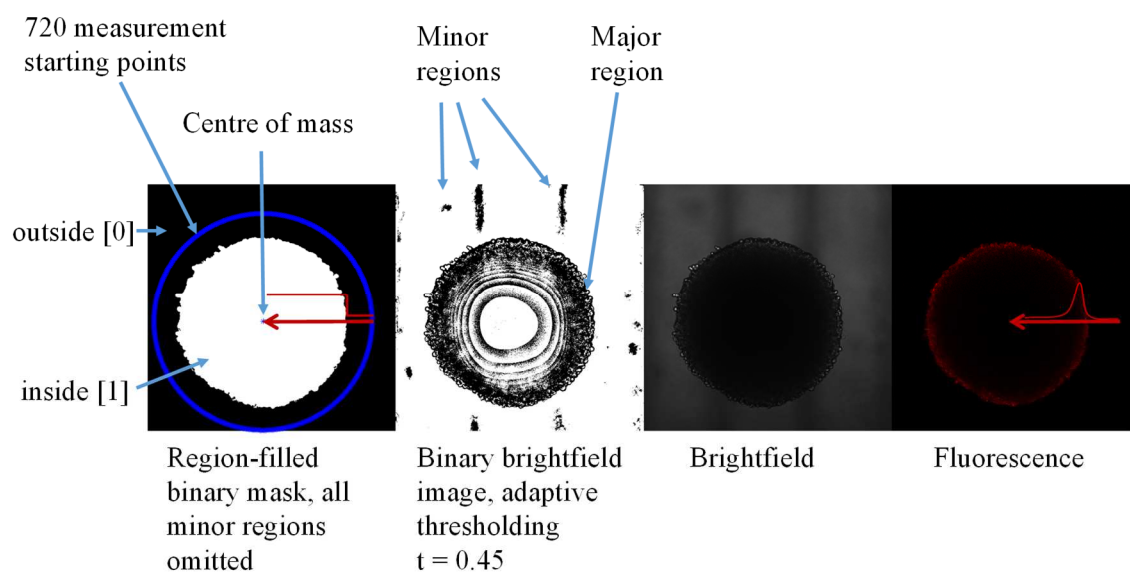


Figure 7.1: Mask creation and evaluation process. Red arrows indicate the evaluation vector at the starting angle of 0° . Red lines indicate a stylised representation of the profile acquired from the evaluation.

Data plotting and curve fitting to obtain data for penetration depths was carried out in Originlabs Origin, using the inbuilt ‘GaussMod’ fitting function with a maximum of 400 iterations and $R^2 \geq 0.99$ as convergence criterion. The function, a Gauss-distribution with an asymmetry-modifier, was selected over a simple Gauss-distribution, as results proved consistently convergent with the obtained data.

7.3.8 DLPC-System

Alkyne-Trithiocarbonate (**3-13**)

Under inert atmosphere, 1.65 g of *t*BuOK were prepared in 12 mL THF and cooled to 5 °C. Mercapto docecane (3.5 mL, 2.97 g, 14.7 mmol, 2 eq) were added over the course of 10 min. the solution was stirred for 45 min and 0.88 mL of CS₂ (14.65 mmol, 2 eq) were added slowly (15 min). Iodine (2 g, 7.33 mmol, 1 eq) was added over the course of 30 min. The solution was stirred overnight. Water (100 mL) was added and the solution was washed with saturated sodium thiosulfate solution and brine. The organic phase was dried over sodium sulfate and recrystallised from ether at -20 °C over night. The resulting yellow precipitate (3.64 g, 5.56mmol, 1 eq) was dissolved in EtOAc and 3.1 g ACVA initiator (11.1 mmol, 2 eq) were added. The solution was refluxed for 22 h. The solvent was removed under reduced pressure and the product was obtained *via* recrystallisation from hot *n*-heptane. The resulting trithiocarbonate (500 mg, 1.24 mmol, 1 eq) was dissolved in propargyl alcohol, and EDC·HCl (356.2 mg, 1.86 mmol, 1.5 eq) and DMAP (30.3 mg, 24.8 μmol, 0.2 eq) were added. The solution was stirred overnight. propargyl alcohol was removed under reduced pressure. The raw product was taken up in EtOAc and washed with 1 M HCl and brine. The organic phase was dried over sodium sulfate. The product was evaporated onto Celite and dry loaded on a 40 g silica column and purified *via* gradient chromatography (EA/Hex 0% (3 CV), 0-5% (3 CV), 5% (3 CV), 5-10% (3 CV), 10-100% (10 CV)). The product was characterised *via* NMR and MS (**Figure A 8.33**).

pTEGMA-*stat*-bHMA-*stat*-TMPMA-*stat*-Cy5MAA (DLPC-0)

TEGMA and dioxane were pre-treated by running through a plug of basic alumina to remove inhibitor, residual water and peroxides. **3-13** (126.8 mg, 0.375 mmol, 1 eq), TEGMA (2.33 g, 10.1 mmol, 125 eq), TMPMA (385 mg, 1.71 mmol, 20 eq), bHMA (346 mg, 1.71 mmol, 20 eq), Cy5-MAA (1.2 mg 0.0454 mmol, 0.5 eq), and AIBN (2.21 mg, 0.0133 mmol, 0.1 eq) were dissolved in 3 mL of dioxane and sealed in a 20 mm, 15 mL crimp-cap vial. The solution was degassed by gentle bubbling with nitrogen in an ice bath in the dark. Polymerisation was started by placing the vial in a preheated aluminium block at 65 °C and stirring at 800 rpm. After 12 h the reaction was quenched by opening the vial and immediate submersion in liquid nitrogen. The polymer was precipitated

from ether at -20 °C and centrifuged at 5000 ×g for 5 minutes. As NMR still showed residual monomer the polymer was reprecipitated from a mixture of ether/hexanes (10/1) and centrifuged again to obtain at 5000 ×g for 5 min to obtain the polymer as a clear, yellow highly viscous material. The composition of the polymers used for further modification was determined to be 6:1:1 *via* NMR from the ratio of signals c (TEGMA, 2H), g (TMPMA, 1H), and f (bHMA, 9H) (**Figure 3.37**). The average molecular weight was determined to be $M_n = 10.5$ kDa, using the integral of resonance i as an end group signal.

TMPMA sidechain oxidation general protocol (DLPC-1)

50 mg **DLPC-0** was dissolved in 5 mL solvent. Oxidizing agent was added and the solution was stirred. The polymer was precipitated by the addition of 10 mL of cold diethyl ether and centrifuged at 5000 ×g. Potentially co-precipitated salts were removed by redissolution and centrifugation. Polymers were precipitated from cold diethyl ether and recovered *via* centrifugation. Conditions are listed in **Table A 7.1**.

Table A 7.1: Oxidation conditions for the attempted synthesis of **DLPC-1**.

#	solvent	oxidizing agent	T / °C	duration
1	DCM	5 eq <i>m</i> CPBA	RT	60 min
2	DCM	1 eq <i>m</i> CPBA	RT	10 min
3	DMF	0.1 eq Na ₂ WO ₄ / 5 eq H ₂ O ₂	RT	12 h
4	DMF	0.1 eq Na ₂ WO ₄ / 1 eq H ₂ O ₂	RT	60 min
5	DMF	0.1 eq Ag ₂ O / 1 eq H ₂ O ₂	RT	60 min
6	DMF	Pb(OAc) ₄	RT	60 min

7.3.9 ULC-System

Procedure for RAFT polymerisation of ULC-0

Prior to polymerisation, both FPMA and dioxane were passed through a short column of basic alumina to remove inhibitor, residual water and peroxides. 2-Cyano-2-propyl benzodithioate (CPBD) (15 mg, 0.0682 mmol, 1 eq), FPMA (870 mg, 4.57 mmol, 67 eq), methyl methacrylate (958 mg, 9.53 mmol, 139 eq), and azoisobutyronitrile (AIBN) (1.5 mg, 9.91 μmol, 0.1 eq) were added to 2.1 mL of dioxane and sealed in a 15 mL crimp-cap photo vial. The solution was wrapped in aluminium foil, placed in an ice bath and degassed by

gentle bubbling with argon for 20 min. Polymerisation was initiated by placing the vial in a preheated aluminium block at 70 °C and stirring at 800 rpm. After 4.5 h, the reaction mixture was removed from the heating block, opened to quench the reaction by exposure to atmospheric oxygen and immediately submerged in liquid nitrogen. Conversion was determined *via* NMR (**Figure A 8.47**) to be 80%. The polymer was precipitated from ether at -20 °C and filtered. The polymer was then further purified *via* reprecipitation into cold methanol at -20 °C, yielding the polymer as a pink, flaky and brittle solid. Monomer incorporation was determined to be 145:100 MMA:FPMA from the ratio of the NMR resonances f (FPMA, 1 H) and c (MMA, 3 H) (**Figure A 8.48**).

Ugi post-polymerisation modification procedure (ULC-1)

ULC-0 (62.4 mg, 0.162 mmol aldehydes, 1 eq) was dissolved in 0.3 mL anhydrous DMF containing 1% TFA and a small amount of anhydrous Na₂SO₄ was added. *Tert*-butyl carbazate (38.3 mg, 0.332 mmol, 2 eq) was dissolved in 0.2 mL of anhydrous DMF and added *via* syringe. The reaction was left to shake at 100 rpm for 30 min at ambient temperature. Carboxy-TEMPO (49.3 mg, 0.246 mmol, 1.5 eq) was dissolved in 0.2 mL DMF and added to the solution. Subsequently, cyclohexyl isocyanide (36.2 mg, 0.332 mmol, 2 eq) was added directly and the solution was left to shake at 100 rpm for another 30 min at ambient temperature. The product was precipitated from 10 mL methanol, centrifuged at 5000 ×g, dissolved in 5 mL THF and reprecipitated over night from 25 mL methanol at -20 °C. The product was recovered *via* centrifugation and dried at RT under reduced pressure.

7.4 METHODS LIGHT-RESPONSIVE NANOCARRIER

Synthetic protocols

Synthesis of pyreneacyl sulfide acid (PAS)

The synthesis was adapted from literature-known procedures.^[257] A round bottom flask was charged with NaOH (0.78 g 19.5 mmol) in water (30 mL) was submerged in an ice bath. After all NaOH was dissolved, thioglycolic acid (0.65 mL, 9.75 mmol, 1 eq) was added dropwise to the stirred solution *via* syringe. After that, 1-bromoacetylpyrene (3.00 g, 9.28 mmol, 1 eq.) was dissolved in THF (90 mL) and added *via* dropping from a syringe at a rate of 5 to 10 drops per second. As soon as all starting material was added, the round bottom flask was covered in aluminium foil, removed from the ice bath and allowed to reach ambient temperature, and stirred overnight. Next, the solution was poured onto 100 g of ice, and acidified by the addition of 20 mL of 12 M hydrochloric acid, yielding a solid yellow precipitate. The precipitate was filtered, washed with water (approximately 80 mL) and allowed to dry in the dark. The yellow filtrate was redissolved in THF, dried at 4 °C over Na₂SO₄ and residual solvent was removed under reduced pressure. The yellow solid was triturated against chloroform and left overnight in the freezer, allowing the product to recrystallise. The product was obtained by filtration and subsequent drying at 50 °C as a yellow semicrystalline solid (2.09 g, 67.4%).

Synthesis of 4-formylmethacrylate (FPMA)

The following procedure was adapted from a known literature protocols.^[267] Methacryloylchloride (37.6 g, 361 mmol, 1.2 eq) in dichloromethane (60 mL) was slowly added *via* dropping funnel at 0 °C to a solution of 4-hydroxubenzaldehyde (36.1 g, 300 mmol, 1 eq) and TEA (36.4 g, 300 mmol, 1.2 eq) in 280 mL dichloromethane. The solution was stirred for 1 h after complete addition. The ice bath was removed and the solution was left to stir overnight at ambient temperature. Water was added until no more white precipitate was visible. The aqueous phase was removed and the organic layer was washed with 100 mL of 1 M HCl (2x), 100 mL saturated aqueous NaHCO₃ (2x) and 100 mL saturated aqueous NaCl solution (1x). The organic layer was subsequently dried over anhydrous

Na₂SO₄ and unreacted low boiling components were removed under high vacuum distillation (< 10⁻² mbar). The crude product was mixed with 100 mg of phenothiazine (PTZ) as inhibitor and was purified by fractionated vacuum distillation (180 °C heating, 145 °C condensation temperature, 0.02 mbar). The product was obtained as a colourless clear liquid (25.2 g, 134 mmol, 44.7% yield), which would solidify just under ambient temperature. 20 mg of hydroquinone were added as a polymerisation inhibitor and the product was stored in the dark at -20 °C.

¹H-NMR (chloroform-d): δ = 10.00 (d, J = 1.1 Hz, 1H), 7.93 (dd, J = 8.7, 1.0 Hz, 2H), 7.53 – 7.04 (m, 2H), 6.38 (d, J = 1.1 Hz, 1H), 5.81 (t, J = 1.4 Hz, 1H), 2.07 (s, 3H).

¹³C-NMR (chloroform-d): δ = 191.11, 165.25, 155.82, 135.56, 134.08, 131.35, 128.24, 122.56, 18.44

Procedure for RAFT polymerisation of LRC-0

Prior to polymerisation, both FPMA and dioxane were filtered through a short column of basic alumina to remove inhibitor, residual water and peroxides. 2-Cyano-2-propyl benzodithioate (CPBD) (15 mg, 0.0682 mmol, 1 eq), FPMA (870 mg, 4.57 mmol, 67 eq), methyl methacrylate (958 mg, 9.53 mmol, 139 eq), and azoisobutyronitrile (AIBN) (1.5 mg, 9.91 μmol, 0.1 eq) were added to 2.1 mL of dioxane and sealed in a 15 mL crimp-cap photo vial. The solution was wrapped in aluminium foil, placed in an ice bath and degassed by gentle bubbling with argon for 20 min. Polymerisation was initiated by placing the vial in a preheated aluminium block at 70 °C and stirring at 800 rpm. After 4.5 h, the reaction mixture was removed from the heating block, opened to quench the reaction by exposure to atmospheric oxygen and immediately submerged in liquid nitrogen. Conversion was determined *via* NMR (**Figure A 8.47**) to be 80%. The polymer was precipitated from ether at -20 °C and filtered. The polymer was then further purified *via* reprecipitation into cold methanol at -20 °C, yielding the polymer as a pink, flaky and brittle solid. Monomer incorporation was determined to be 145:100 MMA:FPMA from the ratio of the NMR resonances f (FPMA, 1 H) and c (MMA, 3 H) (**Figure A 8.48**).

Ugi post-polymerisation modification procedure (LRC-1 and LRC-4)

LRC-0 (62.4 mg, 0.162 mmol aldehydes, 1 eq) was dissolved in 0.3 mL anhydrous DMF containing 1% TFA and a small amount of anhydrous Na₂SO₄ was added. 4-Amino

TEMPO (57.6 mg, 0.332 mmol, 2 eq) (cyclohexylamine for **LRC-4**) was dissolved in 0.2 mL of anhydrous DMF and added *via* syringe. The reaction was left to shake at 100 rpm for 30 min at ambient temperature. Pyreneacyl sulfide (82.0 mg, 0.246 mmol, 1.5 eq) was dissolved in 0.2 mL DMF and added to the solution. Subsequently, cyclohexyl isocyanide (36.2 mg, 0.332 mmol, 2 eq) was added directly and the solution was left to shake at 100 rpm for another 30 min at ambient temperature. If the solution did not clear at this point, DCM (500 μ L) was slowly added until the solution cleared. The product was precipitated from 15 mL methanol, centrifuged at 5000 g, dissolved in 5 mL THF and reprecipitated over night from 45 mL methanol at -20 °C. The product was recovered *via* centrifugation and dried at 40 °C under reduced pressure.

Release under blue-light irradiation

Samples of 3.33 mg·mL⁻¹ **LRC-2** or **LRC 5** in THF were irradiated in 3 mL quartz fluorescence cuvettes. The cuvette was placed inside a cylindrical chamber of 10 cm diameter and 15 cm length and fixed in a 3D-printed custom cuvette holder in order to standardize sample positioning. A 3 W LED (Avonec, 410-420 nm, 3 W, ‘actinic blue’) was placed a distance of 1 cm from the sample for irradiation. The temperature in the cylinder was kept at ambient by airflow. Between measurements of fluorescence data points and irradiation increments, the cuvette was kept in the dark in order to avoid ambient irradiation.

7.5 METHODS MSOT CONTRAST AGENT

Polymerisation of RAFT poly-TMPMA (MCA-0)

Dioxane was pretreated by running through a plug of basic alumina. CPDB (27.7 mg, 0.125 mmol, 1 eq), TMPMA (2.82 g, 12.5 mmol, 100 eq) and AIBN (2.05 mg, 0.0125 mmol, 0.1 eq) were dissolved in 7.5 mL of pretreated dioxane and sealed in a 10 mL crimp-cap vial. The solution was degassed *via* bubbling with argon for 15 min. After all solids had dissolved, the vial was placed in an oil bath, preheated to 65 °C and stirred vigorously. After 2 h polymerisation was quenched by submersion in liquid nitrogen. The polymer was precipitated from cold diethyl ether (-20 °C) and recovered *via* filtration. NMR

indicated a molecular weight of 16.9 kDa. GPC could not yield reliable results due to significant interactions with the gel bed.

Oxidation of TMPMA sidechains to TEMPOMA (MCA-1)

To a solution of 150 mg of **MCA-0** in 10 mL dichloromethane 10 eq of *mCPBA* were added (stoichiometry relative to the amount of TMPMA groups). The solution was sealed in a 20 mm, 15 mL crimp-cap vial and stirred at 1000 rpm for 3 h. The solvent was removed under reduced pressure using a rotary evaporator. *mCPBA* was removed by precipitating the polymer from a mixture of ether/hexanes (10/1) at -20 °C and centrifugation at 3500 \times g, yielding a brittle red. Nitroxide loading was determined *via* the ESR in 1.5 mL THF using a calibration dataset acquired from defined TEMPOL solutions at gain 1 (**Table A 8.1**). Conversion was determined to be quantitative (**Figure 5.2**).

Cy5-coupling (MCA-2)

In a two-necked 15 mL round bottom flask 25 mg of **MCA-1** were dissolved in 5 mL THF. Ethanolamine (2 mL) was added and the solution was heated to 50 °C for 5 h. An excess of Cy5 and TCEP (ca. 10 eq) was added and the solution was stirred overnight. The polymer was precipitated from cold diethyl ether. Subsequently, the polymer was taken up in 10 mL MeOH and purified *via* size exclusion chromatography, using 25 g Sephadex LH-20 resin and 1% AcOH in MeOH (v/v) as eluent. MeOH was removed under reduced pressure and the polymer was recovered as a blue brittle solid.

8

Appendix

8.1 PH-SENSITIVE RELEASE SYSTEMS

8.1.1 Monomers

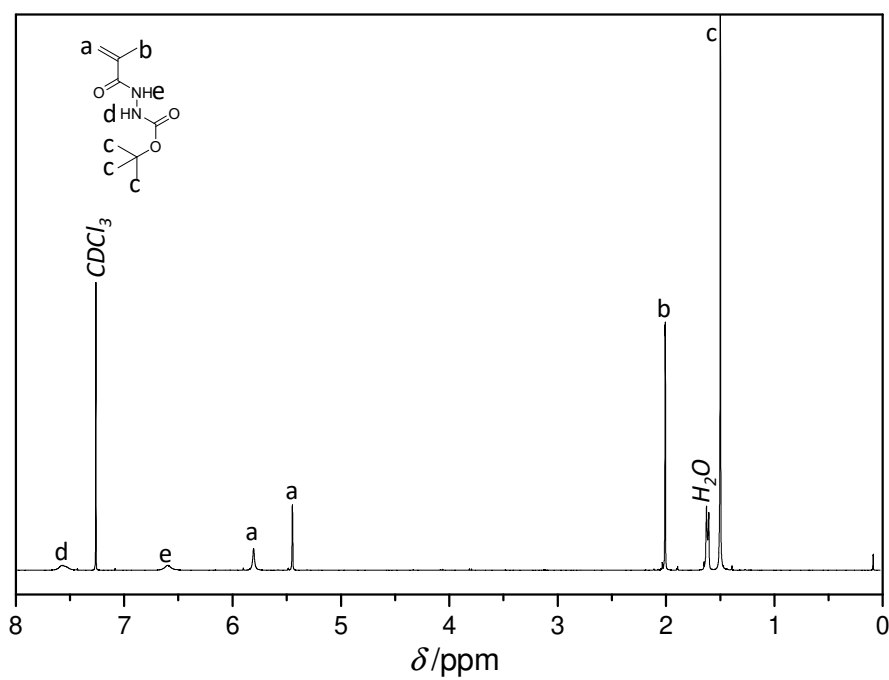


Figure A 8.1: $^1\text{H-NMR}$ (600 MHz, chloroform-d) of bHMA.

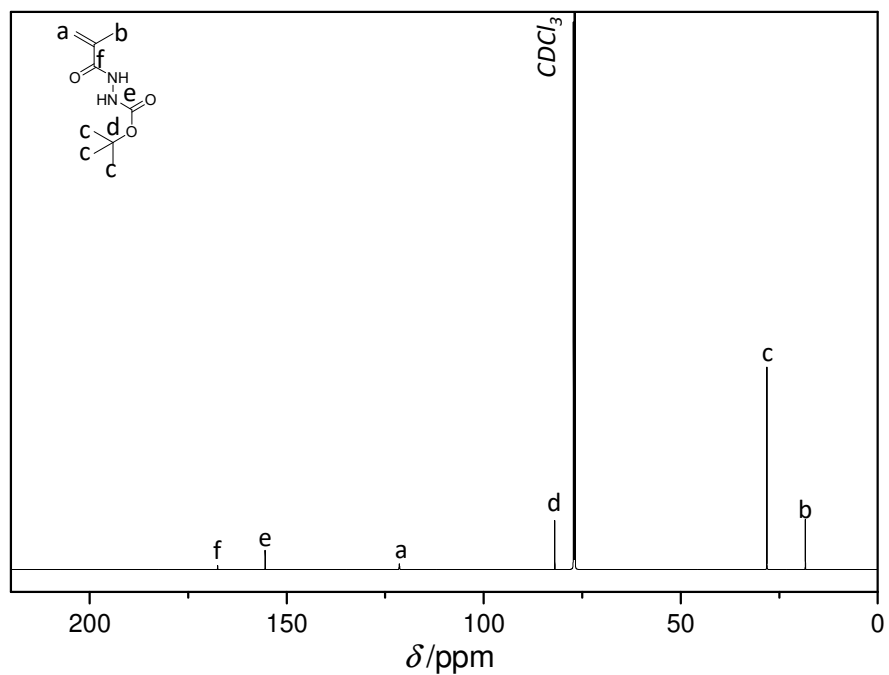


Figure A 8.2: ^{13}C -NMR (151 MHz, chloroform-d) of bHMA.

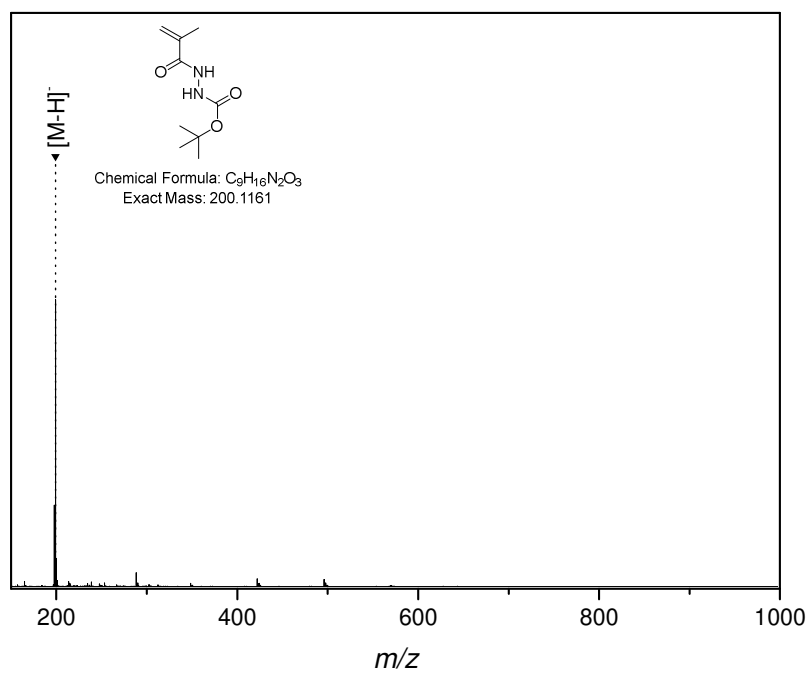


Figure A 8.3: ESI-MS spectrum of bHMA (negative mode).

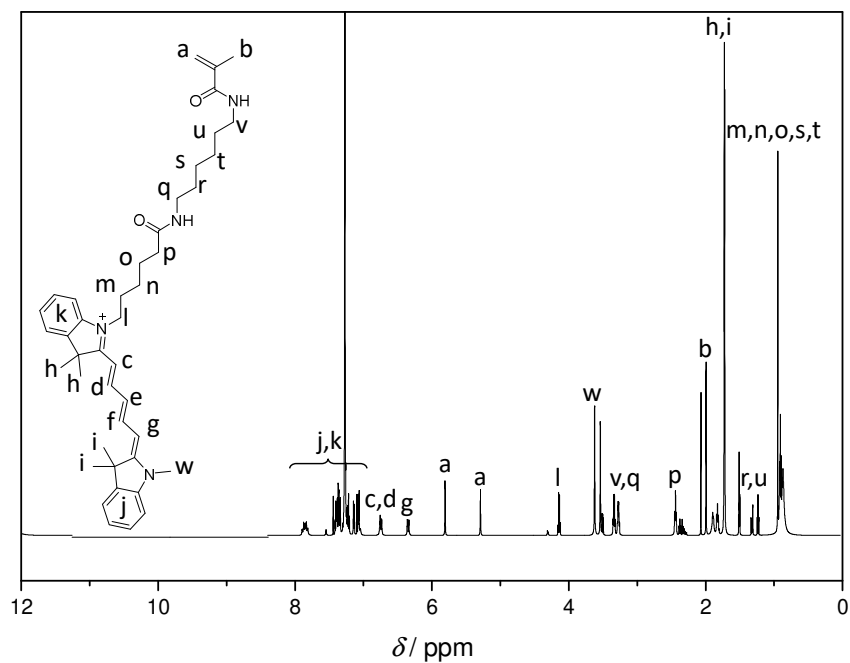


Figure A 8.4: $^1\text{H-NMR}$ (400 MHz, chloroform-d) of Cy5-MAA.

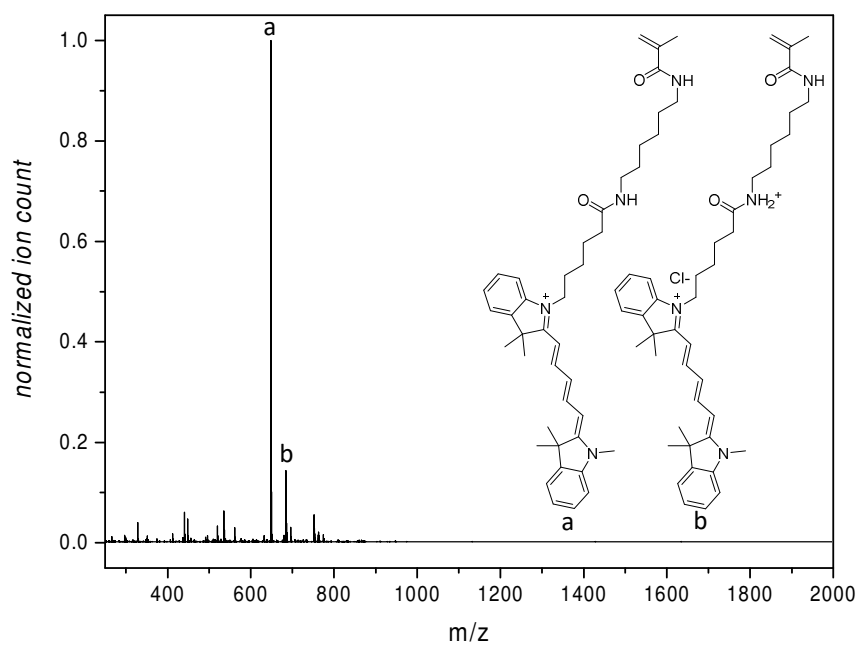
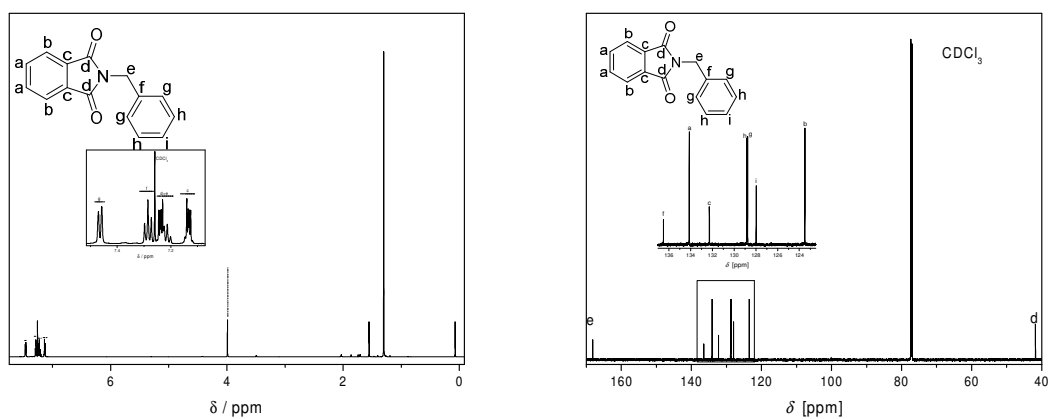
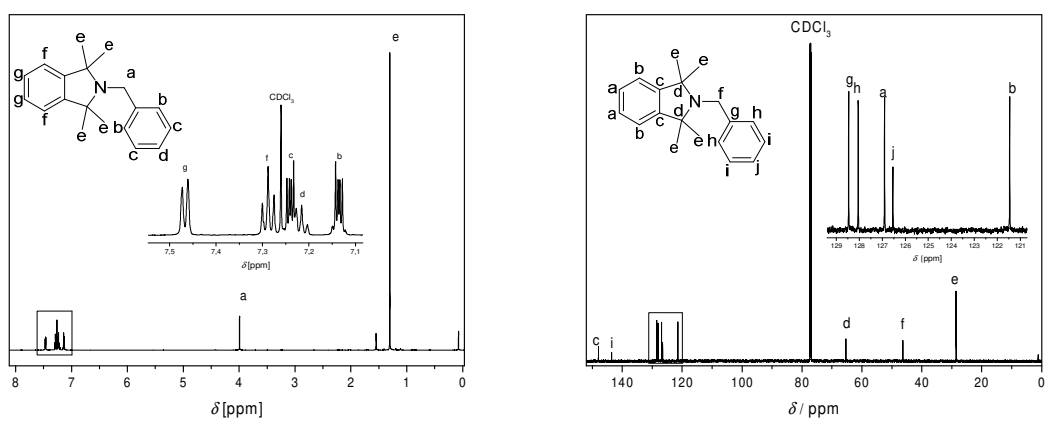
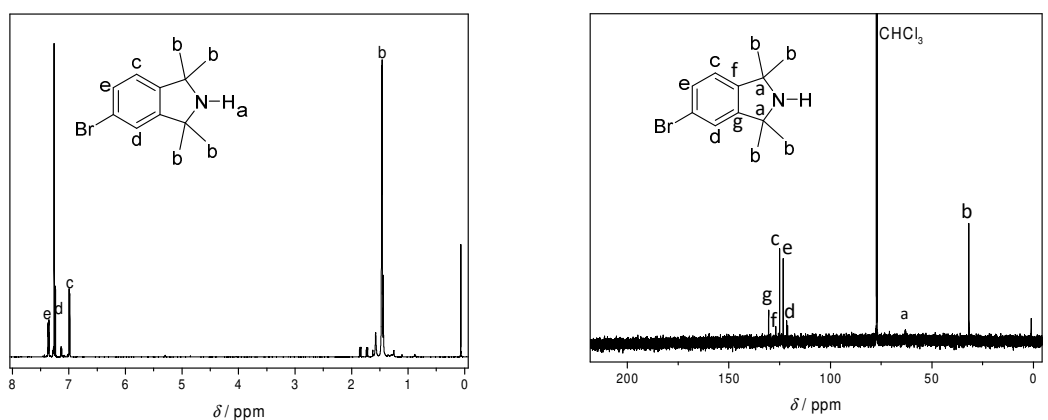


Figure A 8.5: ESI-MS spectrum of Cy5-MAA.

8.1.2 Small Molecules

Figure A 8.6: ^1H - and ^{13}C NMR spectra of 3-3.Figure A 8.7: ^1H - and ^{13}C NMR spectra of 3-3.Figure A 8.8: ^1H - and ^{13}C NMR spectra of 3-4.

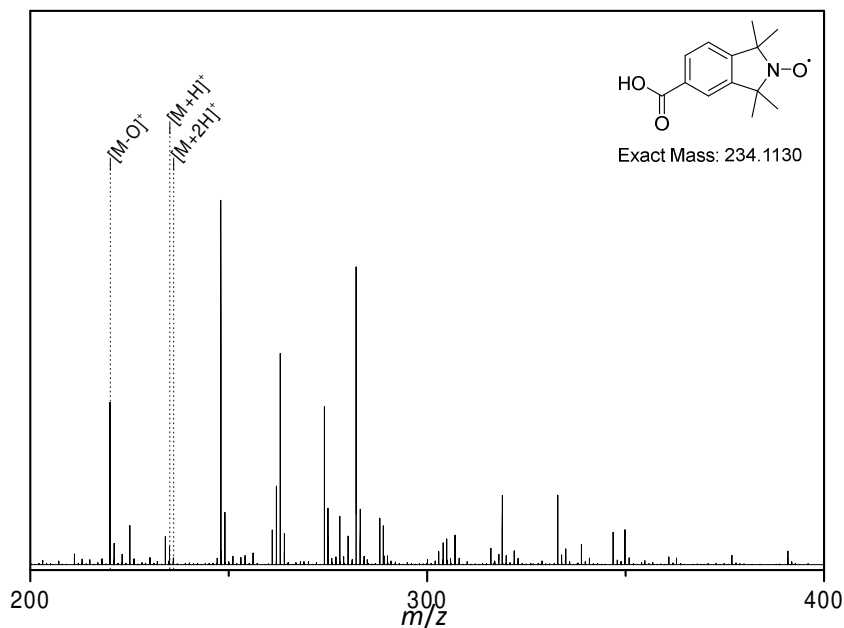


Figure A 8.9: ESI-MS spectrum of **3-6**. Molecule peaks are marked. Due to the acid-group, the molecule ionised poorly in positive mode, showing many background contaminations. Negative mode spectra could not be acquired at the time.

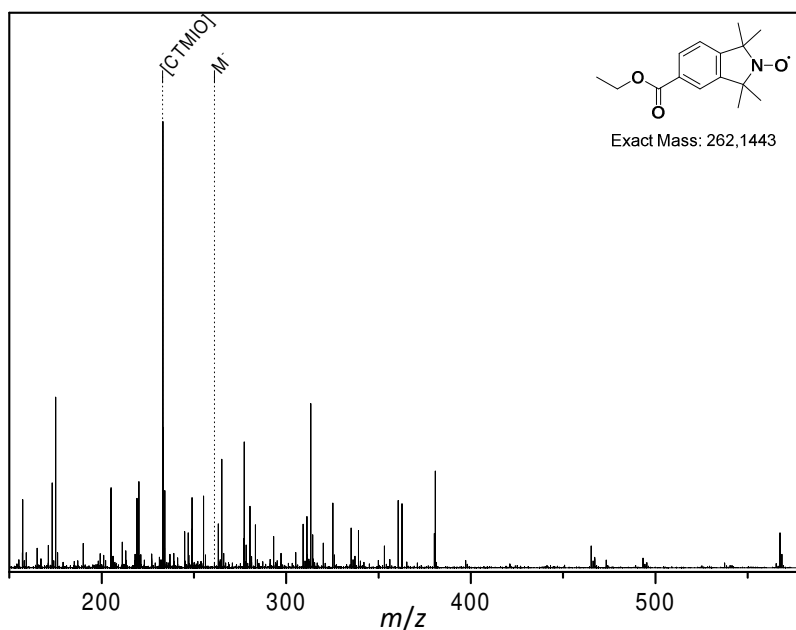


Figure A 8.10: ESI-MS spectrum of **3-7**. Molecule peaks are marked. The molecule did not ionise well in both positive and negative mode, showing strong background contamination signals.

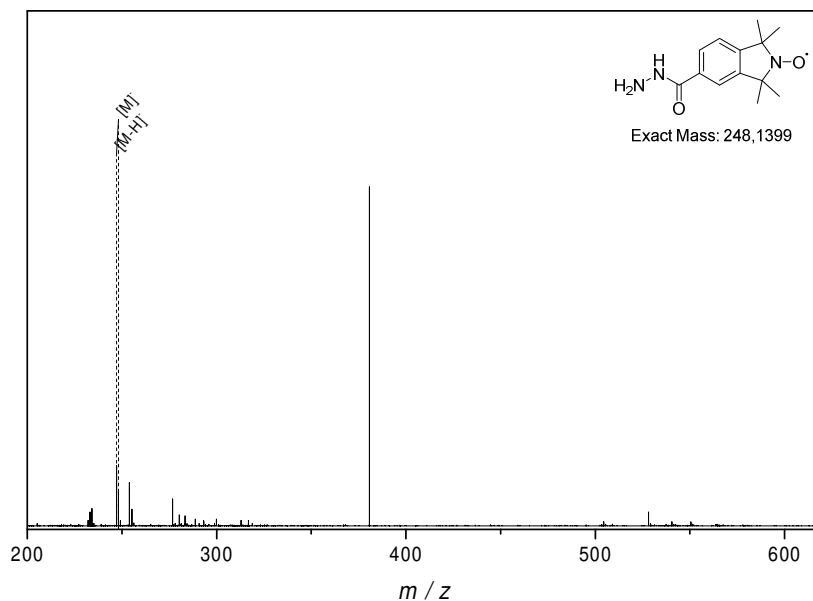


Figure A 8.11: ESI-MS spectrum of **3-8**.

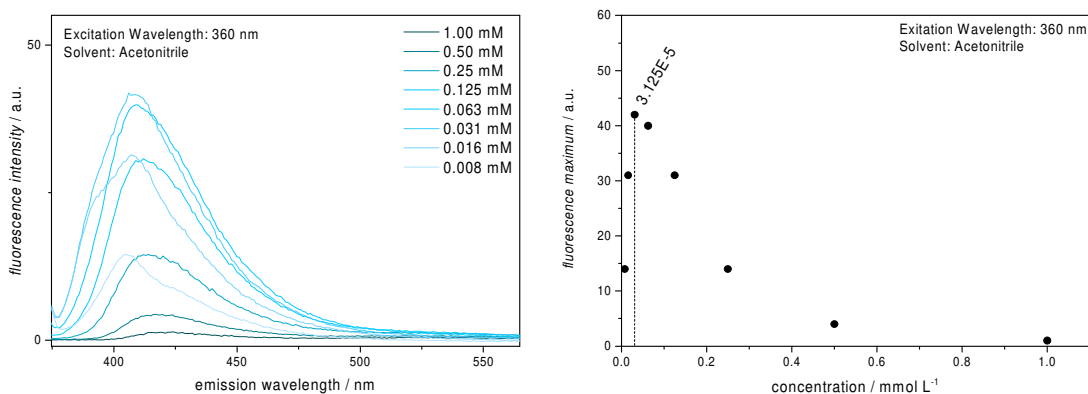


Figure A 8.12: Concentration dependence of Acetylpyrene fluorescence. Fluorescence shows a significant drop in intensity at concentrations greater than approximately $31.5 \mu\text{M}$. Additionally, a distortion of the fluorescence spectrum is visible at higher concentrations, indicating molecular interactions of the fluorophore. Lighter colours indicate higher concentrations.

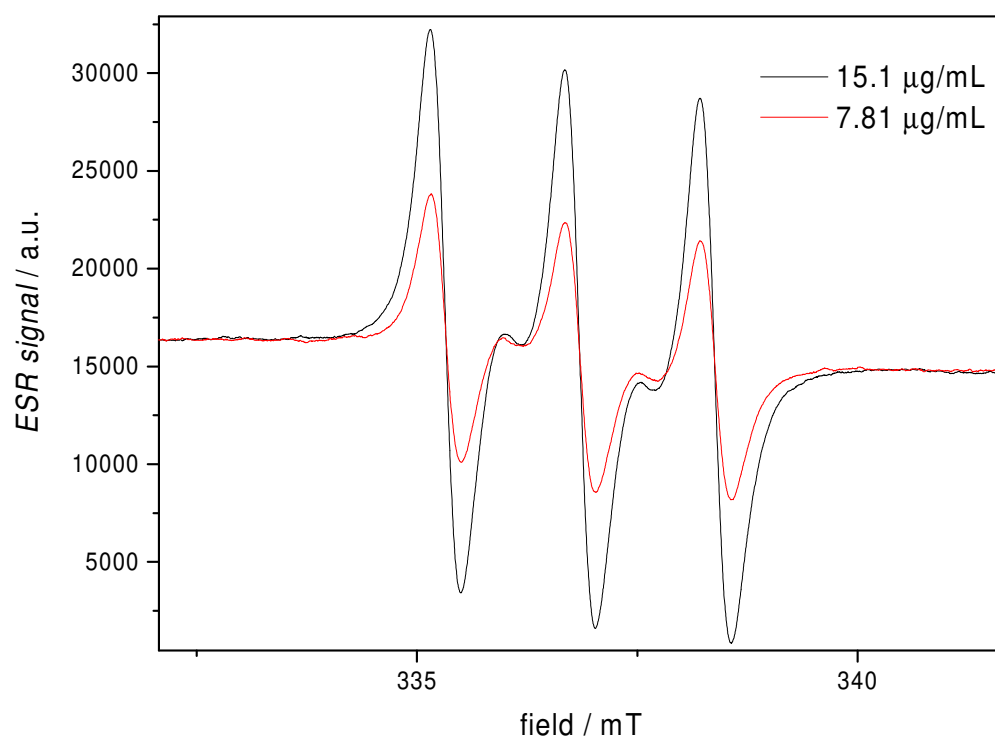


Figure A 8.13: ESR spectra of TEMPOL at gain 200.

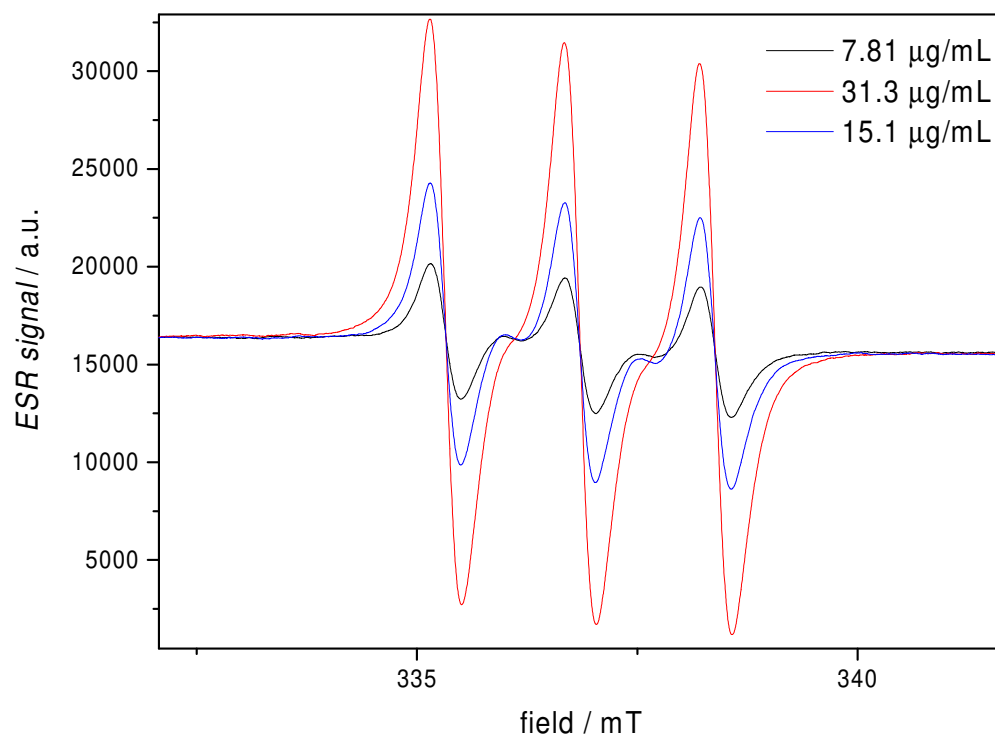


Figure A 8.14: ESR spectra of TEMPOL at gain 200

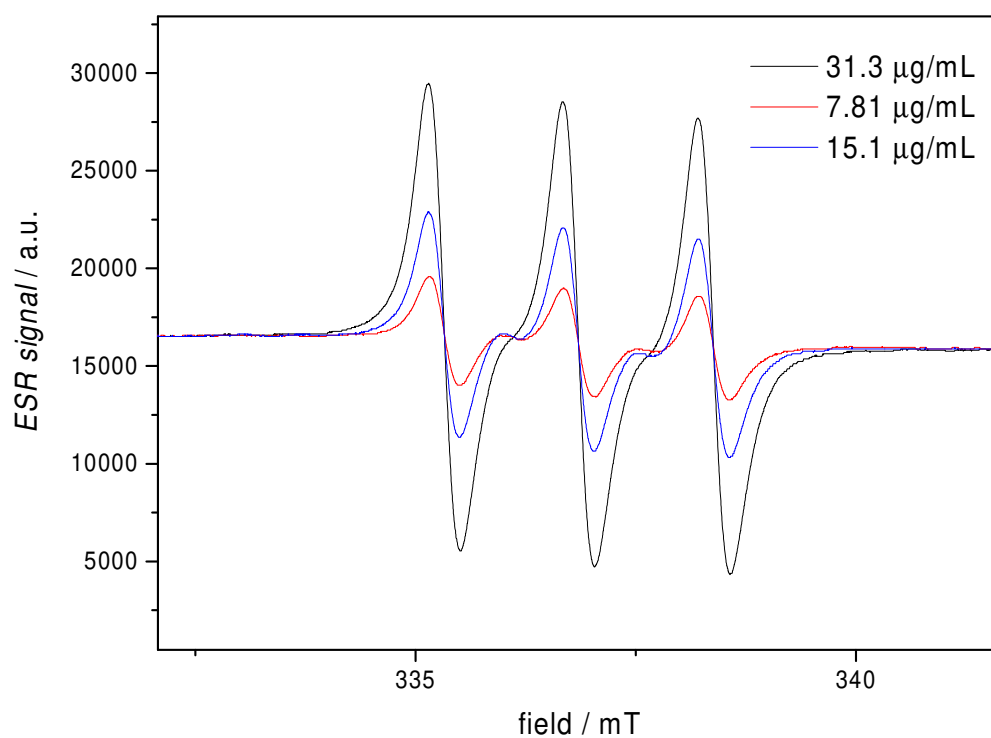


Figure A 8.15: ESR spectra of TEMPOL at gain 80.

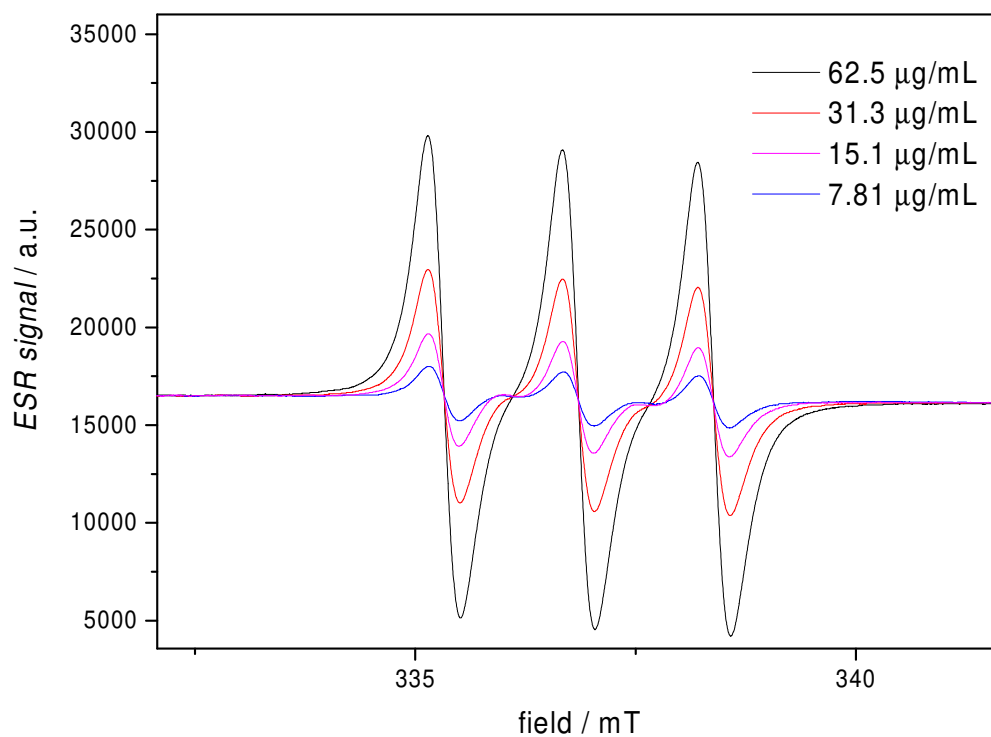


Figure A 8.16: ESR spectra of TEMPOL at gain 40.

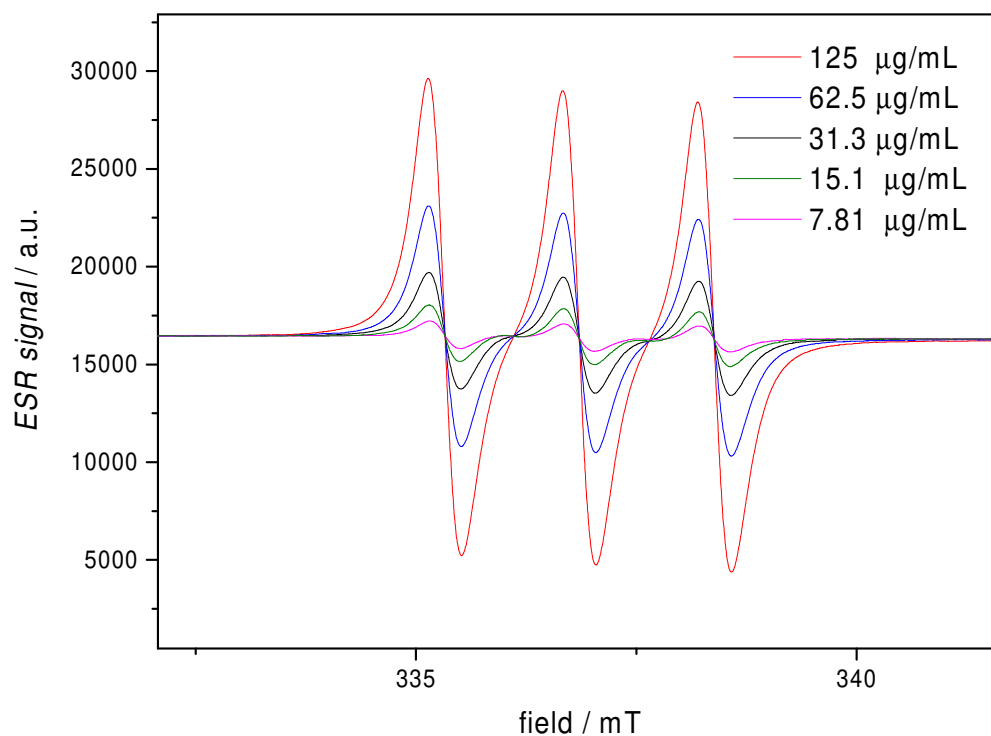


Figure A 8.17: ESR spectra of TEMPOL at gain 20.

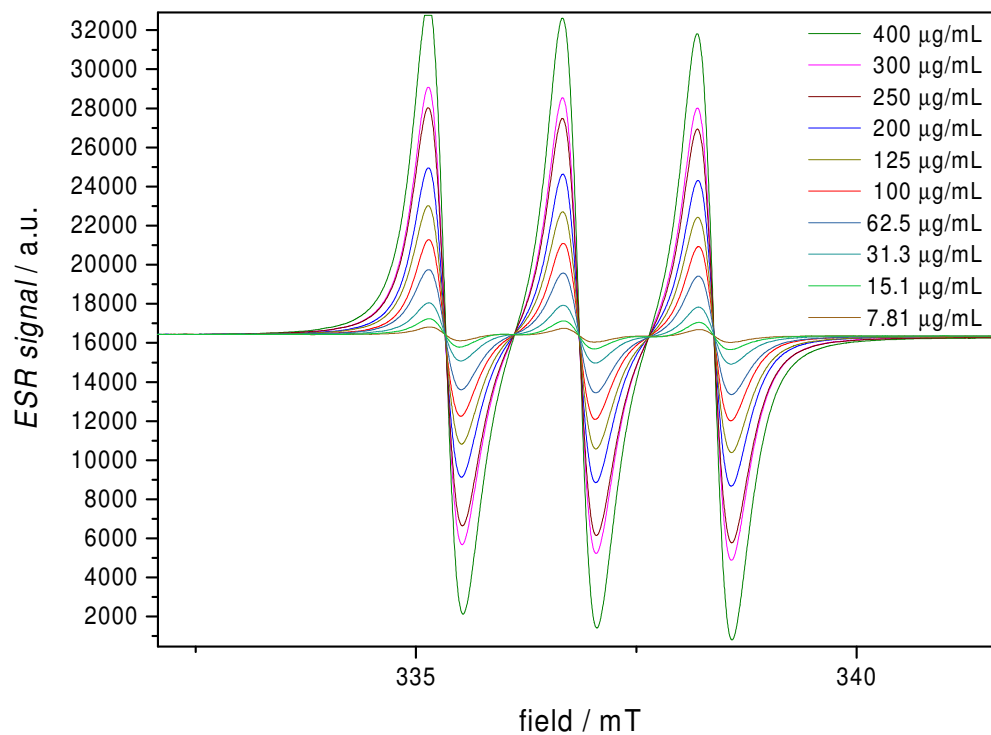


Figure A 8.18: ESR spectra of TEMPOL at gain 10.

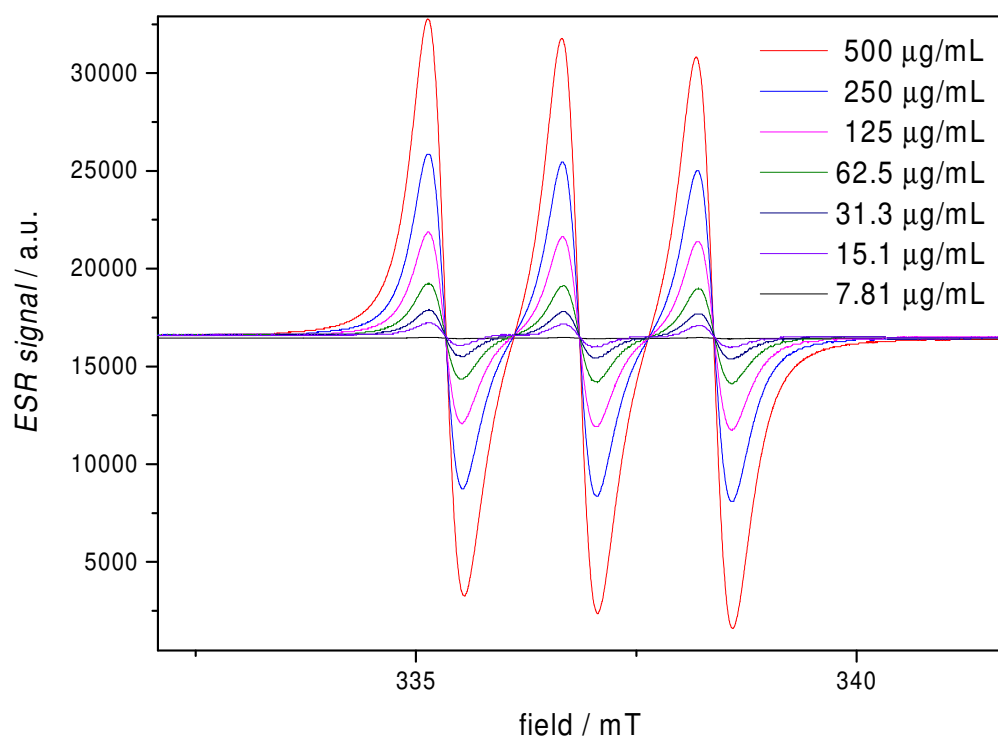


Figure A 8.19: ESR spectra of TEMPOL at gain 8.

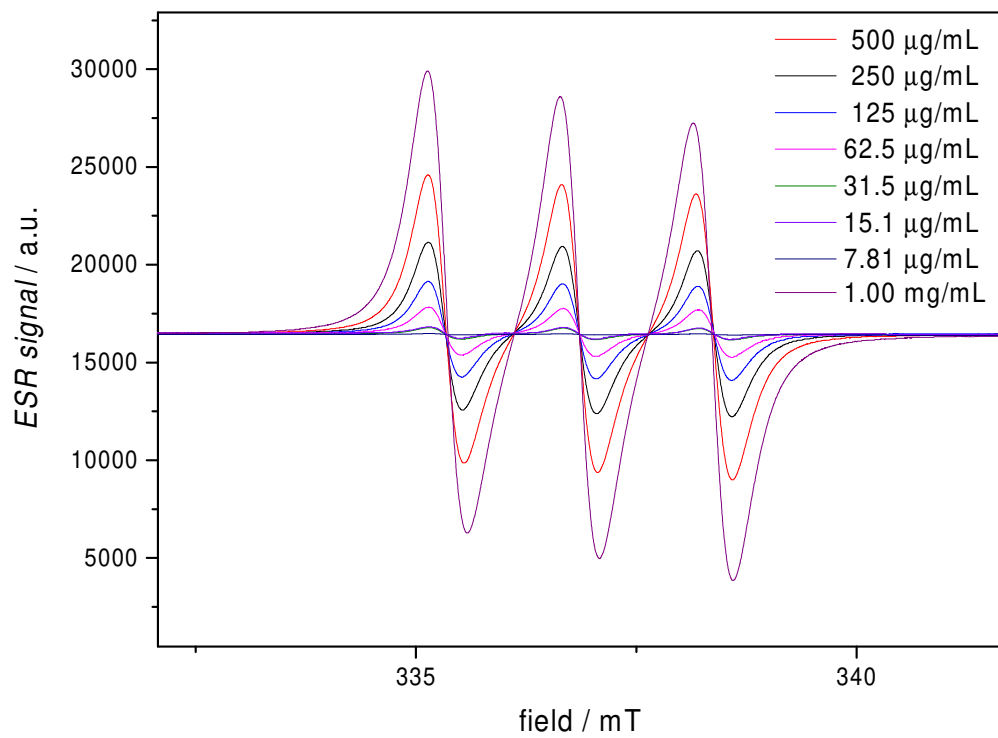


Figure A 8.20: ESR spectra of TEMPOL at gain 4.

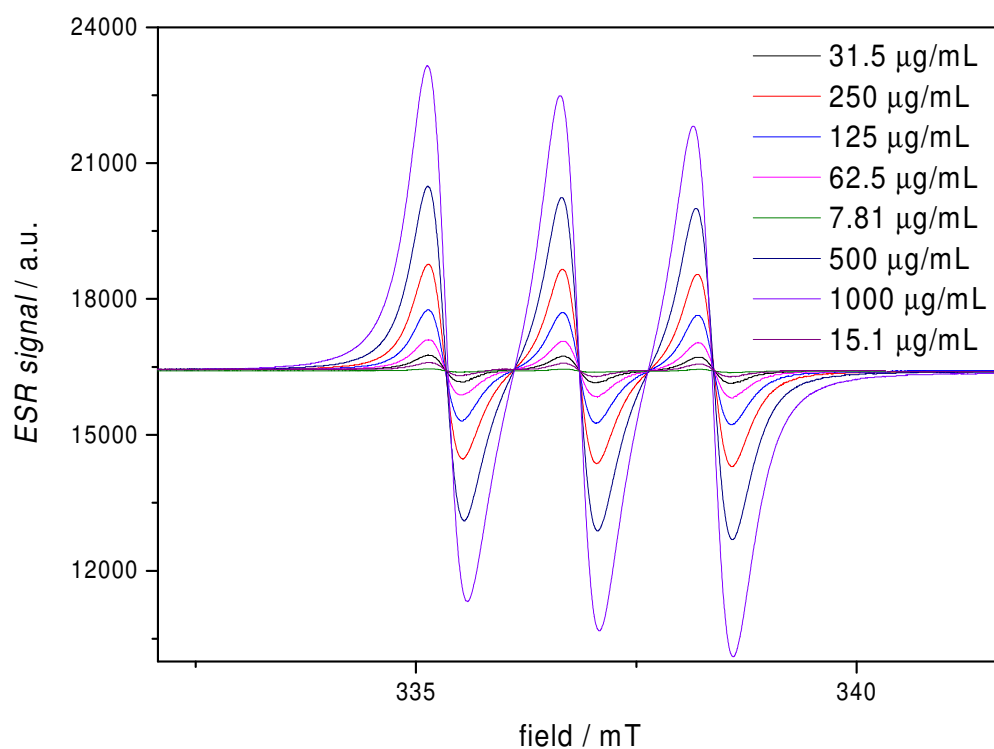


Figure A 8.21: ESR spectra of TEMPOL at gain 2.

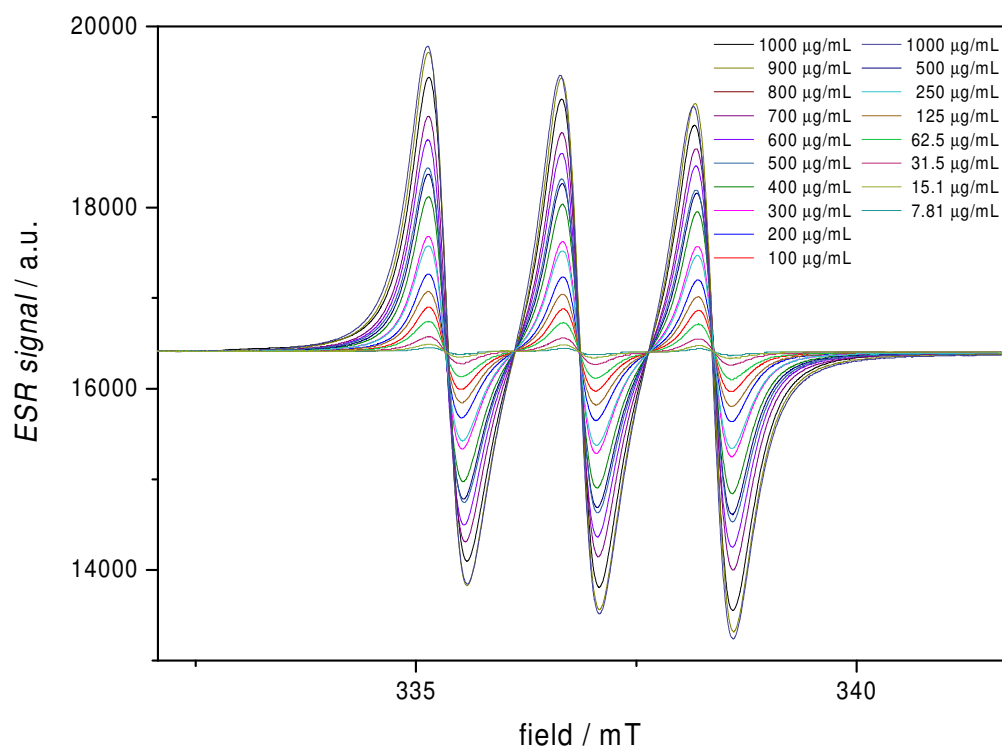


Figure A 8.22: ESR spectra of TEMPOL at gain 1.

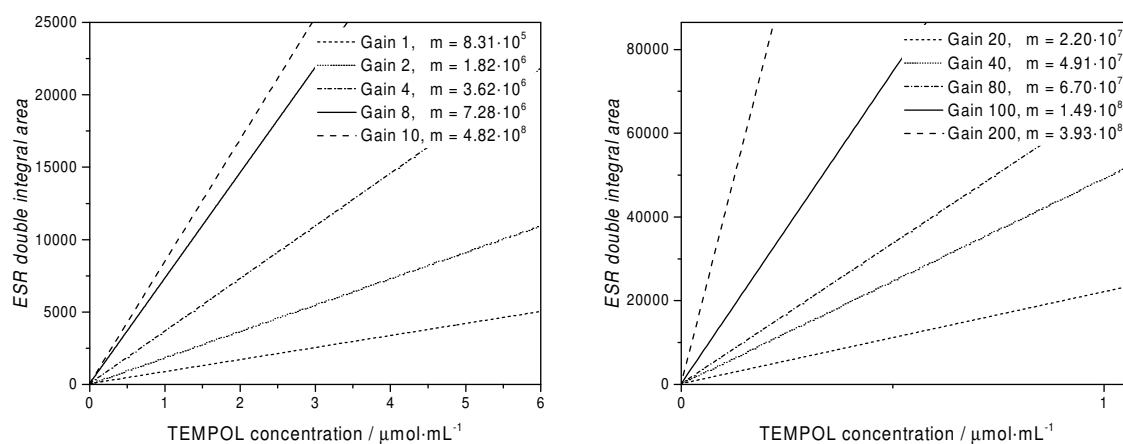


Figure A 8.23: ESR calibration curves of TEMPOL, used to evaluate nitroxide content of polymers. Slopes are listed in . Modified from [259] with permission from Wiley VCH.

Table A 8.1: Correlation of TEMPOL concentration and double integral area. Increasing receiver gain values led to a strong increase in ESR signal. A range of calibration coefficients for a selection of gain stages 1-200 was recorded, since gain and signal did not scale in a consistent fashion.

	<i>slope / L·mmol⁻¹</i>
Gain 1	$8.31 \cdot 10^5$
Gain 2	$1.82 \cdot 10^6$
Gain 4	$3.63 \cdot 10^6$
Gain 8	$7.28 \cdot 10^6$
Gain 10	$8.42 \cdot 10^6$
Gain 20	$2.20 \cdot 10^7$
Gain 40	$4.91 \cdot 10^7$
Gain 80	$6.70 \cdot 10^7$
Gain 100	$1.49 \cdot 10^8$
Gain 200	$3.93 \cdot 10^8$

8.1.3 SAP system

Table A 8.2: MS values obtained from SEC-MS of **SAP-0** and calculated values for comparison. Column “Label” denotes the chain composition and label in the spectrum. $\Delta\Delta m/z$ max. denotes the theoretical maximum deviation in m/z by instrument parameters.

<i>Label</i>	<i>m/z exp.</i>	<i>m/z calcd.</i>	$\Delta\Delta m/z$	$\Delta\Delta m/z$ max.
SAP-0 ₂₆ -homo	2108.4819	2108.4701	0.0117	0.05271
SAP-0 _{5/28}	2113.1240	2113.1107	0.0133	0.05283
SAP-0 _{2/27}	2125.8112	2125.8017	0.0095	0.05315
SAP-0 _{4/28}	2143.1394	2143.1334	0.0059	0.05358
SAP-0 _{1/27}	2155.8391	2155.8244	0.0146	0.05390
SAP-0 _{3/28}	2173.1735	2173.1561	0.0174	0.05433
SAP-0 ₂₇ -homo	2185.8569	2185.8471	0.0097	0.05465

Table A 8.3: MS values obtained from SEC-MS of **SAP-1** and calculated values for comparison. Column “Label” denotes the chain composition and label in the spectrum. $\Delta\Delta m/z$ max. denotes the theoretical maximum deviation in m/z by instrument parameters. Single values slightly exceeding deviation maximum were due to poorly resolved peaks.

<i>Label</i>	<i>m/z exp.</i>	<i>m/z calcd.</i>	$\Delta\Delta m/z$	$\Delta\Delta m/z$ max.
SAP-1 _{homo17}	2181.6546	2181.6612	0.0066	0.0130
SAP-1 _{1/16}	2136.6205	2136.6271	0.0065	0.0128
SAP-1 _{4/19}	2233.5795	2233.7373	0.0178	0.0134
SAP-1 _{3/18}	2162.6180	2162.6279	0.0099	0.0129
SAP-1 _{2/17}	2207.6521	2207.6596	0.0075	0.0132
SAP-1 _{5/18}	2188.5454	2188.7031	0.0176	0.0131

Table A 8.4: MS values obtained from SEC-MS of **SAP-2** and calculated values for comparison. Column “Label” denotes the chain composition and label in the spectrum. $\Delta\Delta m/z$ max. denotes the theoretical maximum deviation in m/z by instrument parameters. Single values slightly exceeding deviation maximum were due to poorly resolved peaks.

<i>Label</i>	<i>m/z exp.</i>	<i>m/z calcd.</i>	$\Delta\Delta m/z$	$\Delta\Delta m/z$ max.
SAP-2 _{17 homo}	2181.6703	2181.6546	0.0205	0.0152
SAP-2 _{17/1}	2158.1455	2158.1290	0.0165	0.0186
SAP-2 _{17/2}	2134.6188	2134.6035	0.0153	0.0185
SAP-2 _{17/3}	2111.0935	2111.0780	0.0155	0.0184
SAP-2 _{16 homo}	2065.6046	2065.5890	0.0156	0.0183

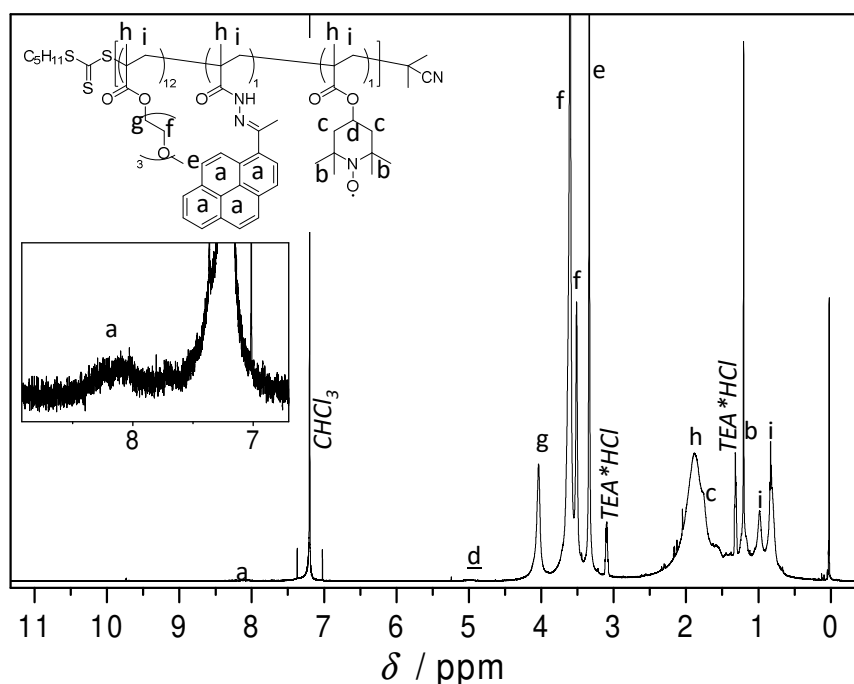
8.1.4 PC system

Table A 8.5: NMR and ESR numerical results of **PC-1** oxidation. Measured at $2.4 \text{ mg} \cdot \text{mL}^{-1}$ in DCM at gain 2. Monomer integrals and ratios determined from **PC-0** NMR.

Monomer	Integral	molar ratio	n per $2.4 \text{ mg} / \mu\text{mol}$	$c / \mu\text{mol} \cdot \text{mL}^{-1}$	I_{theo}	I_{measured}	Conversion
bHMA	1.03	0.070	0.73	0.733	---	---	---
TEGMA	12.35	0.860	8.96	8.962	---	---	---
TMPMA	1	0.070	0.73	0.726	6114	6085	99.4%

Table A 8.6: ESR numerical results of **PC-2** after TEA addition. Measured at $2.7 \text{ mg} \cdot \text{mL}^{-1}$ in DCM at gain 2. Monomer integrals and ratios determined from **PC-0** NMR.

Monomer	Integral	molar ratio	n per $2.7 \text{ mg} / \mu\text{mol}$	$c / \mu\text{mol} \cdot \text{mL}^{-1}$	I_{theo}	I_{measured}	Conversion
bHMA	1.03	0.070	0.82	0.82	---	---	---
TEGMA	12.35	0.860	10.01	10.01	---	---	---
TMPMA	1	0.070	0.81	0.81	6827	6052	88.6%

**Figure A 8.24:** ^1H -NMR of **PC-3** in CDCl_3 . The inset shows a zoom of the aromatic area. Signals are heavily influenced by the presence of nitroxides, most likely losing a lot of signal intensity to line broadening and distortion

8.1.5 SSPC system

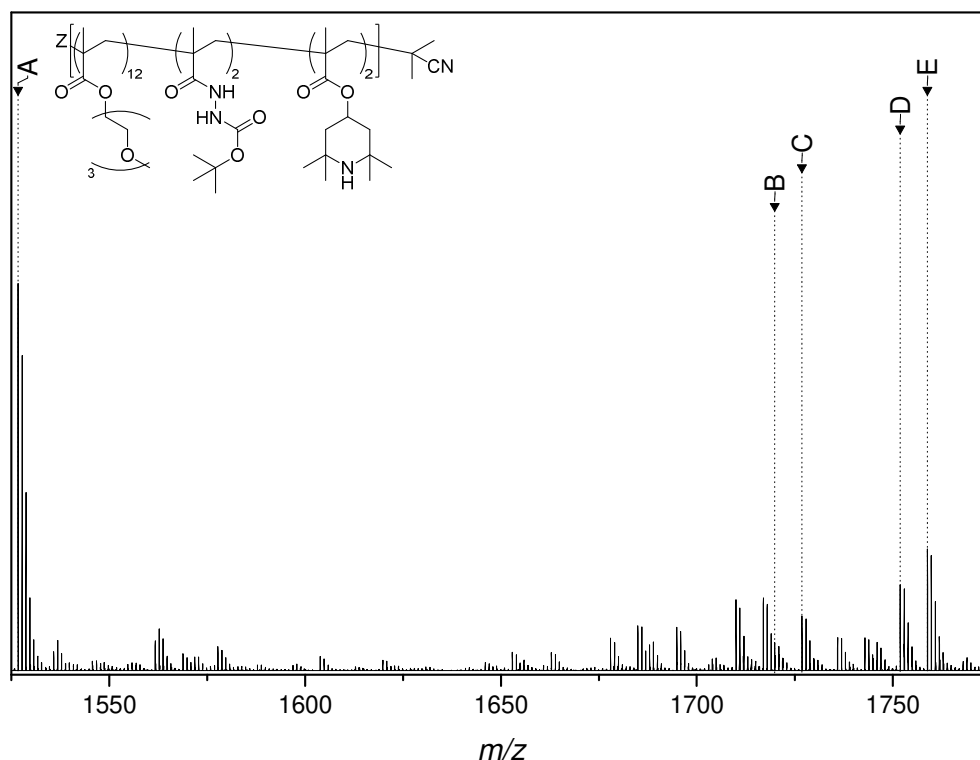


Figure A 8.25: SEC-ESI-MS Spectrum recorded of **SSPC-0**. Monomer incorporation into the same chain was confirmed by mass difference of peaks from base peak A. Values are listed below in **Table A 8.7**. Reproduced from [211] with permission from the RSC.

Table A 8.7: ESI-MS values obtained from SEC-MS of **SSPC-0** and calculated values for comparison. Column “rep. unit” denotes the repeating unit responsible for the indicated mass difference from base-signal A. $\Delta\Delta m/z$ max. denotes the allowed maximum deviation in m/z by instrument parameters.

Label	m/z	rep. unit	$\Delta m/z$ calcd	$\Delta m/z$ found	$\Delta\Delta m/z$	$\Delta\Delta m/z$ max.
A	1526.7518	base peak	---	---	---	---
B	1719.9104	- TEGMA + bHMA + TPMA	193.1578	193.1586	-0.0008	0.0039
C	1726.8683	+ bHMA	200.1160	200.1165	-0.0005	0.0040
D	1751.9254	+ TMPMA	225.1729	225.1736	-0.0007	0.0045
E	1758.8828	+ TEGMA	232.1311	232.1310	0.0001	0.0046

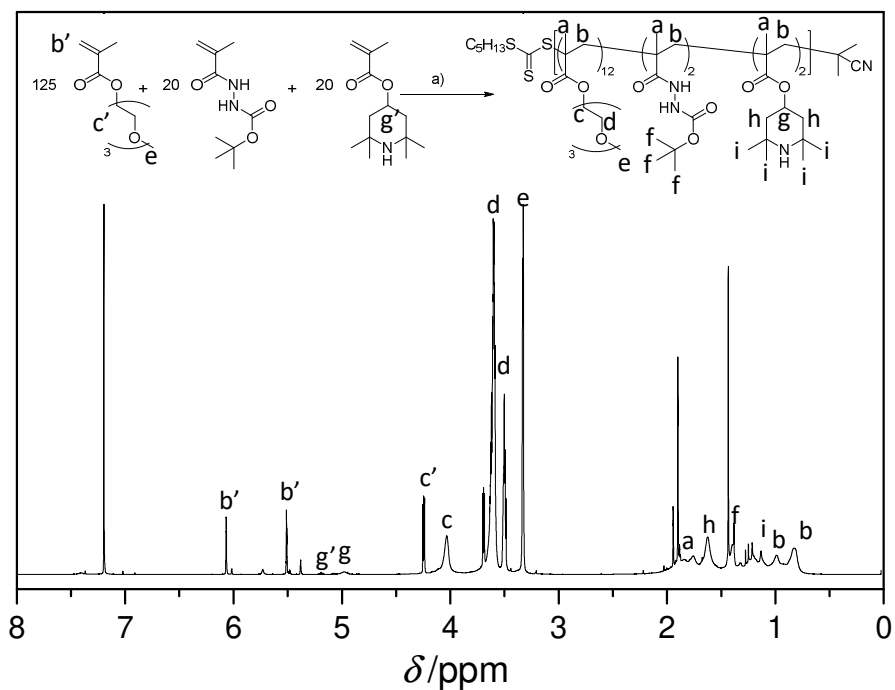


Figure A 8.26: $^1\text{H-NMR}$ (600 MHz, CDCl_3) spectrum of **SSPC-0** reaction mixture used to determine conversion. Ratio was determined from integrals c/c' and g/g' . Reproduced from [211] with permission from the RSC.

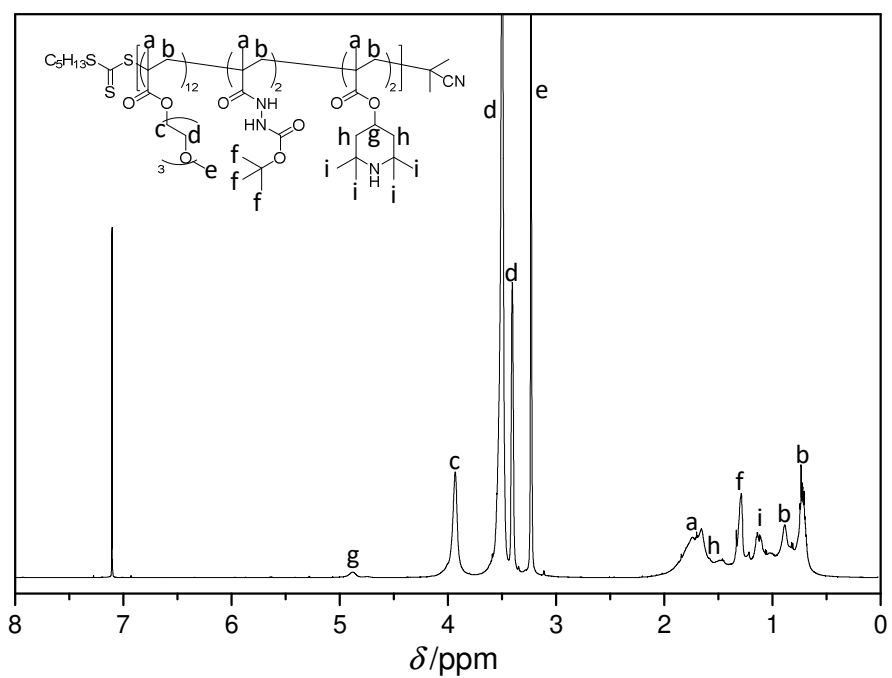


Figure A 8.27: $^1\text{H-NMR}$ (600 MHz, CDCl_3) spectrum of **SSPC-0**. Polymer composition was determined from the ratio of the signals g , c , and f . Reproduced from [211] with permission from the RSC.

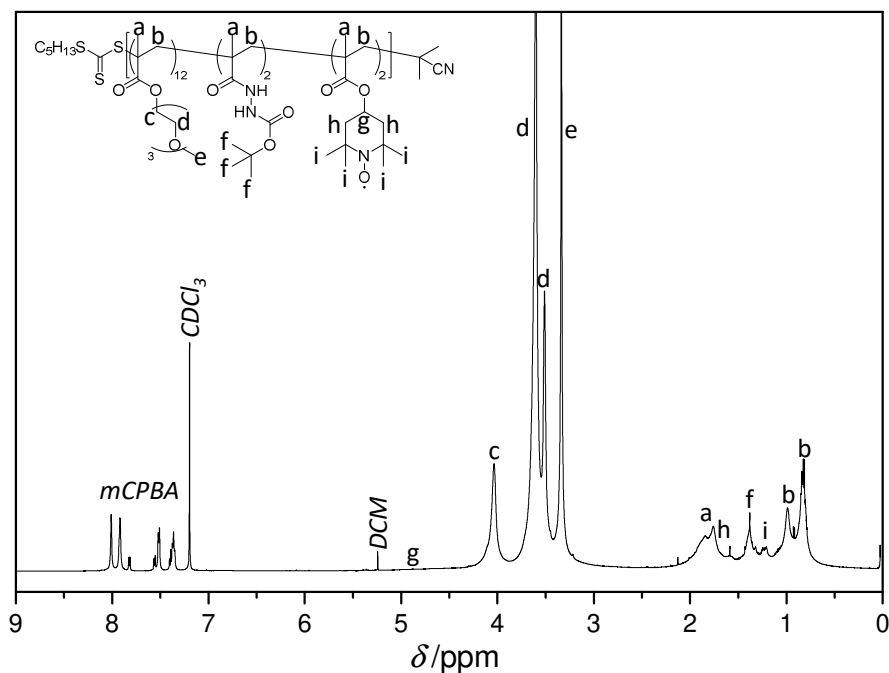


Figure A 8.28: $^1\text{H-NMR}$ (600 MHz, CDCl_3) spectrum acquired from a crude sample of **SSPC-1**. The spectrum shows a clear increase in band broadening of signals g, h, and i, stemming from nitroxide presence. Reproduced from [211] with permission from the RSC.

Table A 8.8: Calculated conversion from EPR. Monomer ratios were taken from **SSPC-0** NMR spectra.

Monomer	NMR Integral	molar ratio	$c / \mu\text{mol}\cdot\text{mL}^{-1}$	EPR I_{theo}	I_{measured}	Conversion
bHMA	1.01	0.069	2.35	---	---	---
TEGMA	6.26	0.876	14.5	---	---	---
TMPMA	1	0.055	2.32	22237	22032	99%

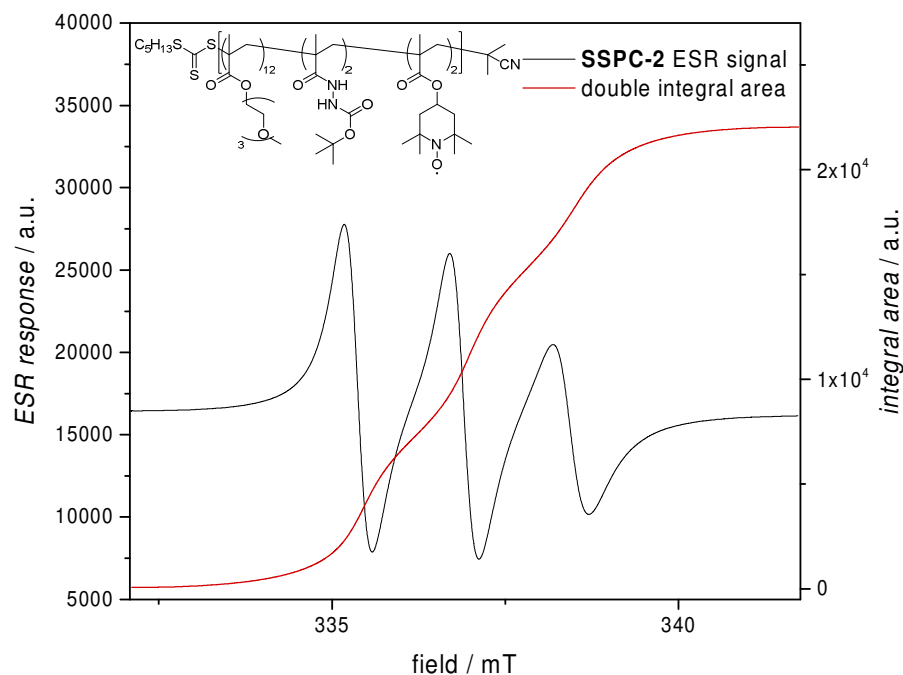


Figure A 8.29: ESR spectrum recorded of **SSPC-2**. The line broadening clearly indicates polymer bound-nitroxides. Partial formation of the TFA-salt with the nitroxide was assumed as the signal had decreased to 7032, where a theoretical maximum of 27248 indicated only 25.2% of radicals left. Reproduced from [211] with permission from the RSC.

Table A 8.9: Nitroxide density after boc-deprotection of **SSPC-2**. Spectrum was measured at a gain of 40.

<i>Monomer</i>	<i>Integral</i>	<i>molar ratio</i>	<i>n / μmol</i>	<i>c / μmol·mL⁻¹</i>	<i>I_{theo}</i>	<i>I_{measured}</i>	<i>rad. loading</i>
bHMA	1.01	0.069	3.27	3.27	---	---	---
TEGMA	6.26	0.876	20.2	20.2	---	---	---
TMPMA	1	0.055	3.23	3.23	27248	7032	26%

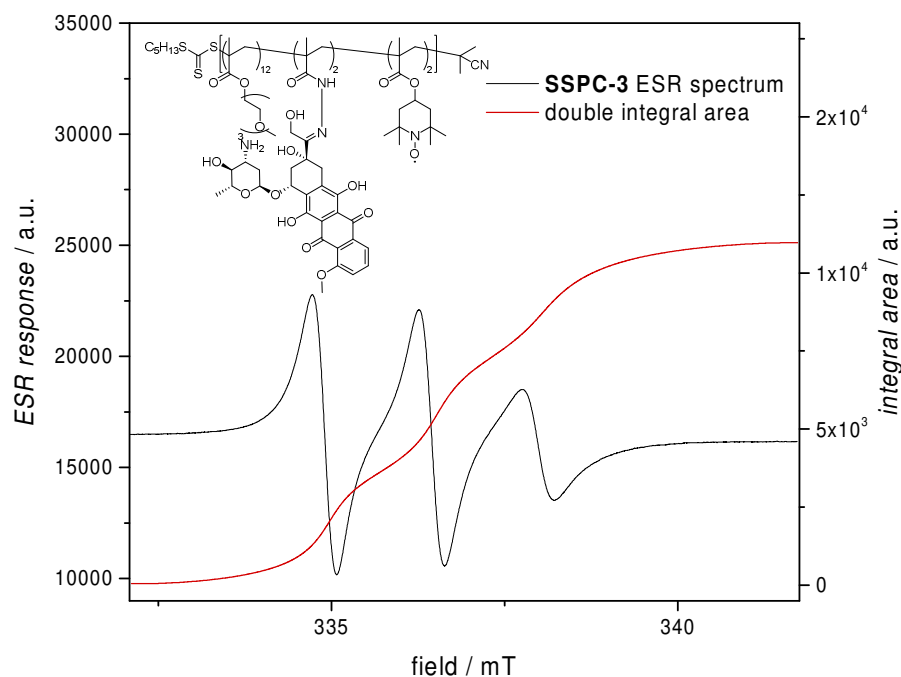


Figure A 8.30: ESR spectrum of **SSPC-3** recorded after Dox-loading clearly shows the preservation of polymer-bound nitroxides. Reproduced from [211] with permission from the RSC.

Table A 8.10: ESR evaluation data after Dox-loading of **SSPC-3** indicated a preservation of 52%.

<i>Monomer</i>	<i>rel. Integral</i>	<i>molar ratio</i>	<i>n / mmol</i>	<i>c / μmol·mL⁻¹</i>	<i>I_{theo}</i>	<i>I_{measured}</i>	<i>rad. loading</i>
bHMA	1.01	0.12	$4.35 \cdot 10^{-4}$	$4.35 \cdot 10^1$	---	---	---
TEGMA	6.26	0.76	$2.69 \cdot 10^{-3}$	$2.69 \cdot 10^0$	---	---	---
TMPMA	1	0.12	$4.30 \cdot 10^{-4}$	$4.30 \cdot 10^{-1}$	21128	10959	52%

Table A 8.11: Dox-loading density of **SSPC-3** as determined *via* NMR. *x* represents the relative incorporation of TEGMA and either the boc- or Dox-bearing hydrazide in **SSPC-0** and **SSPC-3**. **SSPC-0** shows a hydrazide density of 1 mol hydrazide per 6.25 mol TEGMA. **SSPC-3** shows a ratio of incorporation of 1 mol Dox per 27.78 mol of TEGMA. This results in a loading density of 22.5% loaded hydrazide anchors.

<i>Polymer</i>	<i>Signal</i>	<i>Group</i>	<i>I_{abs.}</i>	<i>I_{rel.}</i>	<i>n_{protons}</i>	<i>H per rep. unit</i>	<i>x</i>
SSPC-0	c	boc	1886124	1.00	9.00	9	1.00
	f	TEG-C ¹	2618534	1.39	12.49	2	6.25
SSPC-3	c	Dox	62234	1.00	1.00	1	1.00
	l	TEG-C ¹	3457426	55.56	55.56	2	27.78

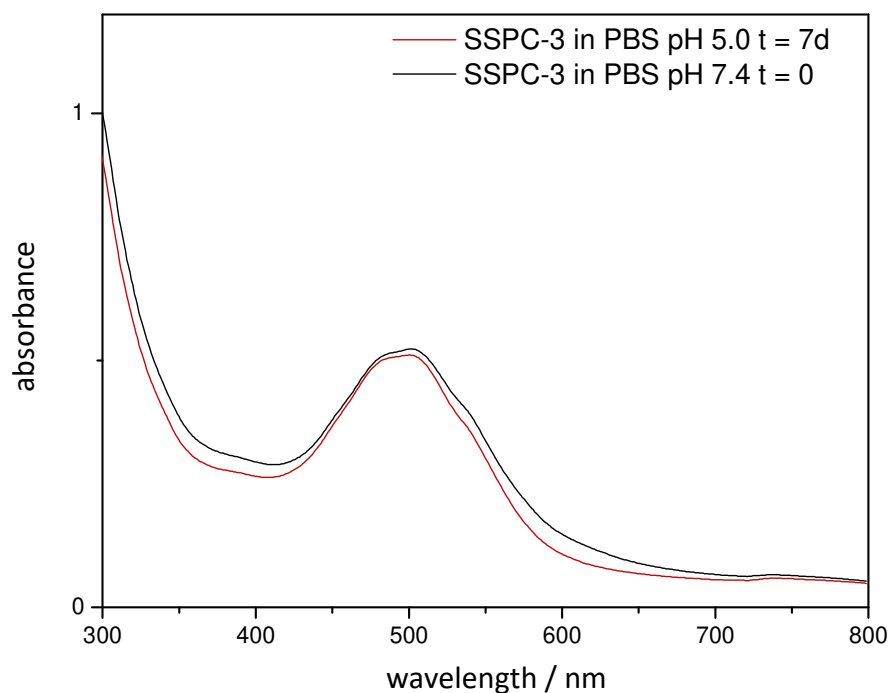


Figure A 8.31: UV-Vis-absorption spectrum of $0.4 \text{ mg}\cdot\text{mL}^{-1}$ **SSPC-3** in PBS. Loading was determined from the absorption at 495 nm at $\text{pH} = 7.4$. The second measurement after acidification was conducted as a reference measurement to obtain a reliable reference for possible changes in absorptive properties. A slight change towards shorter wavelengths and a minute decrease in absorption are visible as a result of the slight increase in volume. Reproduced from [211] with permission from the RSC.

Table A 8.12: Calculation of loading density. The molar hydrazide content X_{HMA} was obtained from boc-signals' integral based on the NMR spectra of **SSPC-0**.

	Abs ₄₉₅ / AU	c_{polymer} / $\text{mg}\cdot\text{mL}^{-1}$	c_{dox} / $\text{mg}\cdot\text{mL}^{-1}$	X_{dox} / $\mu\text{g}_{\text{dox}}\cdot\text{mg}_{\text{polymer}}^{-1}$	X_{HMA}	n_{HMA} / μmol	n_{Dox} / μmol	loading density
SSPC-3	0.5	0.4	0.0290	72.5	0.121	0.488	0.125	25.6%

Table A 8.13: Spectrometric data used for calculation of release efficiency.

	<i>pH 7.4</i>		<i>pH 5.0</i>	
	<i>495 nm</i>	<i>480 nm</i>	<i>495 nm</i>	<i>480 nm</i>
<i>absorption</i>	$9.30\cdot 10^{-4}$	$1.26\cdot 10^{-3}$	$7.02\cdot 10^{-3}$	$8.28\cdot 10^{-3}$
ϵ	$1.00\cdot 10^4$	$1.25\cdot 10^4$	$1.00\cdot 10^4$	$1.25\cdot 10^4$
$c_{\text{dox}} / \text{mol}\cdot\text{L}^{-1}$	$9.30\cdot 10^{-8}$	$1.01\cdot 10^{-7}$	$7.02\cdot 10^{-7}$	$6.62\cdot 10^{-7}$
$n_{\text{dox}} / \mu\text{g}$	$6.98\cdot 10^{-1}$	$7.56\cdot 10^{-1}$	5.27	4.97
$m_{\text{dox}} / \mu\text{mol}$	$4.05\cdot 10^2$	$4.04\cdot 10^2$	$3.05\cdot 10^3$	$2.65\cdot 10^3$
$m_{\text{dox polymer}} / \mu\text{g}$	$3.71\cdot 10^3$	$3.71\cdot 10^3$	$3.61\cdot 10^3$	$3.61\cdot 10^3$
release efficiency	11%	11%	84%	73%

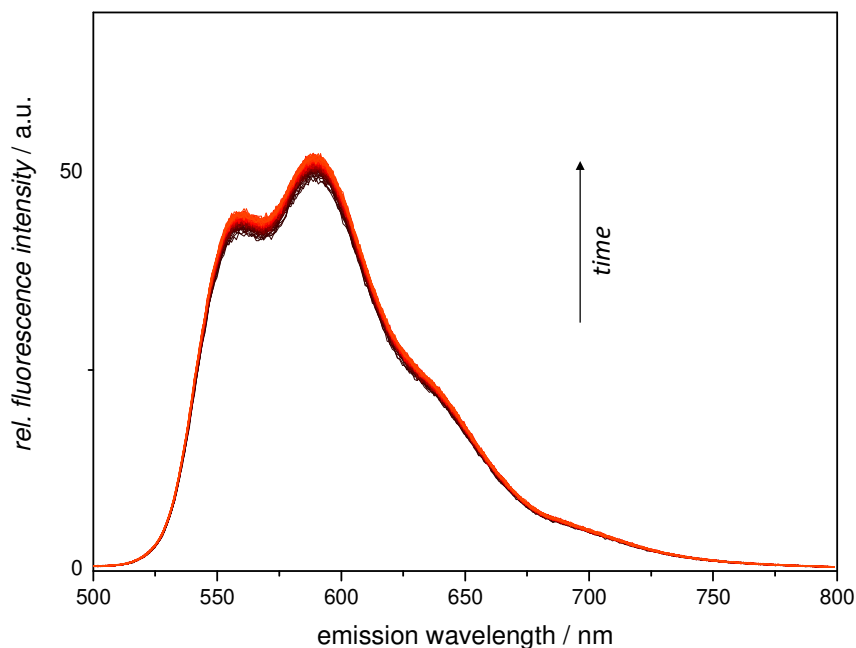


Figure A 8.32: Time-resolved fluorescence spectra of **SSPC-3** in PBS at pH = 7.4. In comparison to the release experiment at pH = 5.0 only a small increase in fluorescence can be observed. Lighter reds indicate later time-points. Reproduced from [211] with permission from the RSC.

8.1.6 DLPC System

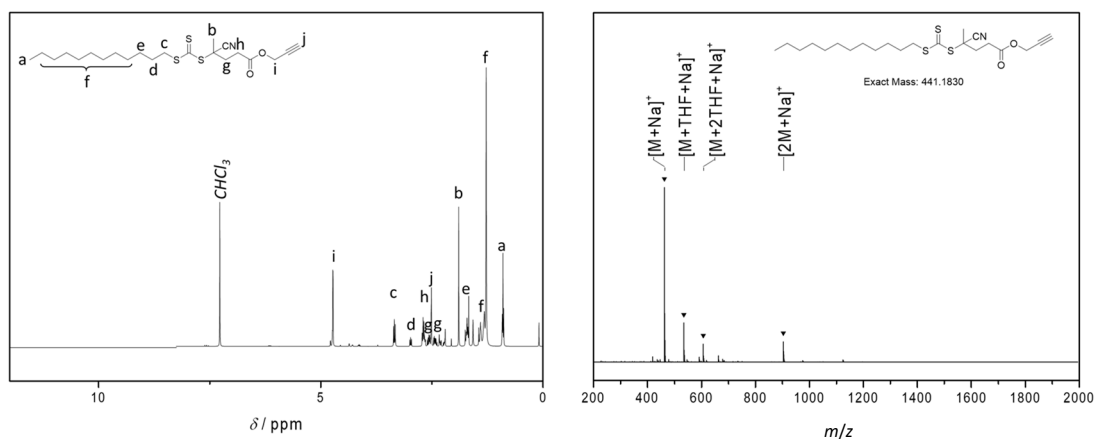


Figure A 8.33: $^1\text{H-NMR}$ (400 MHz, CDCl_3) and ESI-MS (positive mode) of alkyne-RAFT agent (**3-13**)

8.1.7 ULC-system

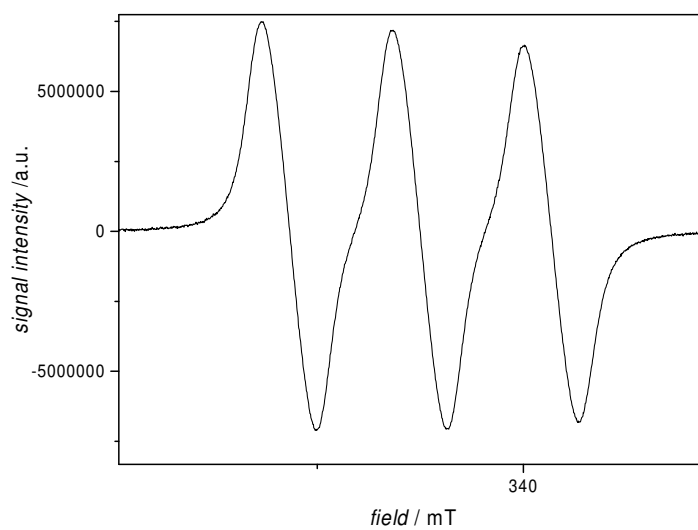


Figure A 8.34: ESR spectrum of **ULC-0.2**. The spectrum exhibits very slight line broadening and asymmetry, indicating polymer bound nitroxides. A proper quantification could not be performed, yet a lot more signal would have been expected from the assembly at high levels of incorporation.

8.1.8 2D Bio-Testing

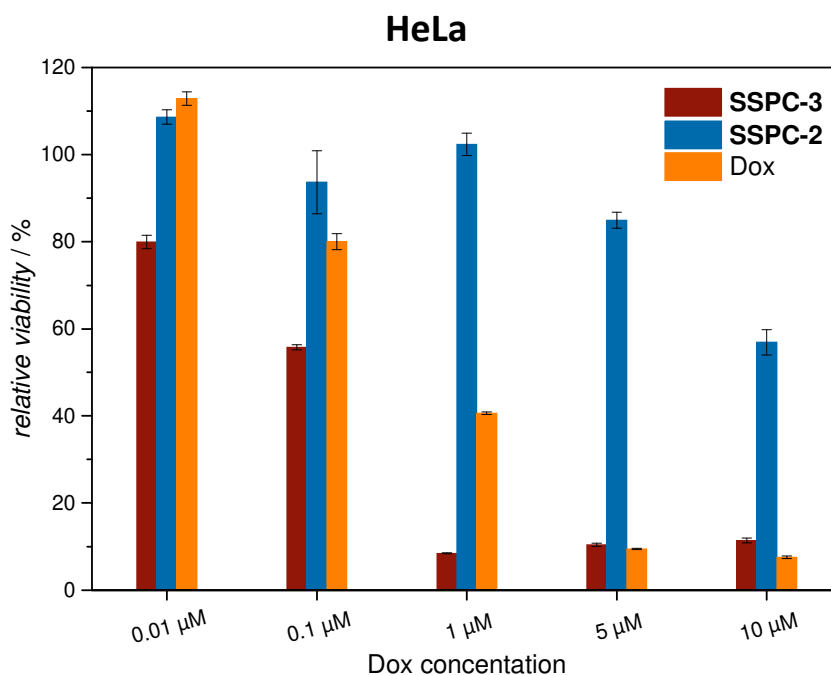


Figure A 8.35: MTT viability test in HeLa cells. As it is clearly visible, no impact on cell viability of the **SSPC-2** backbone is observed. The loaded **SSPC-3** carrier exhibits slightly increased efficacy over free Dox.

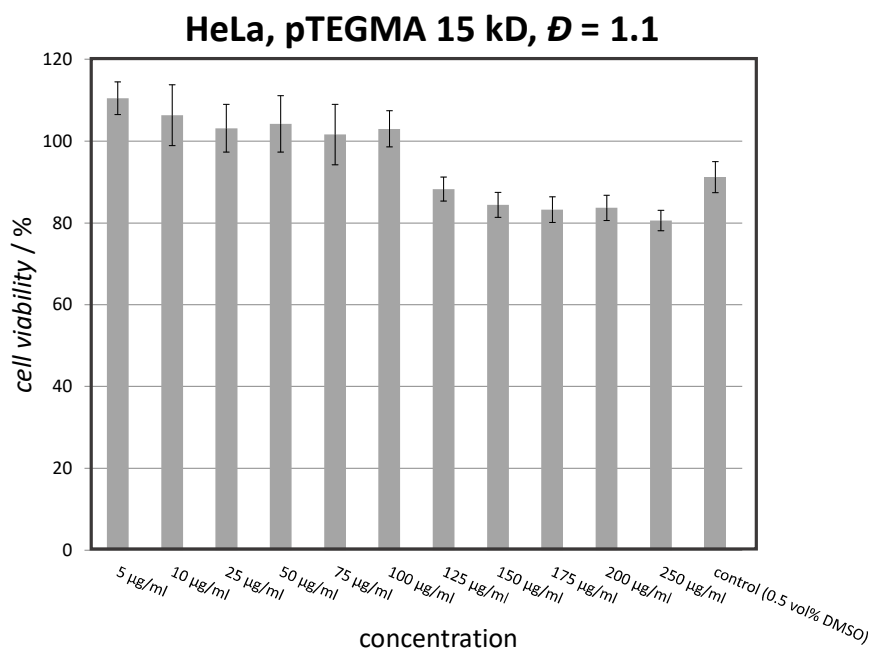


Figure A 8.36: MTT viability test in HeLa cells. As it is clearly visible, no impact on cell viability of the pTEGMA is evident.

8.1.9 3D Bio-Testing

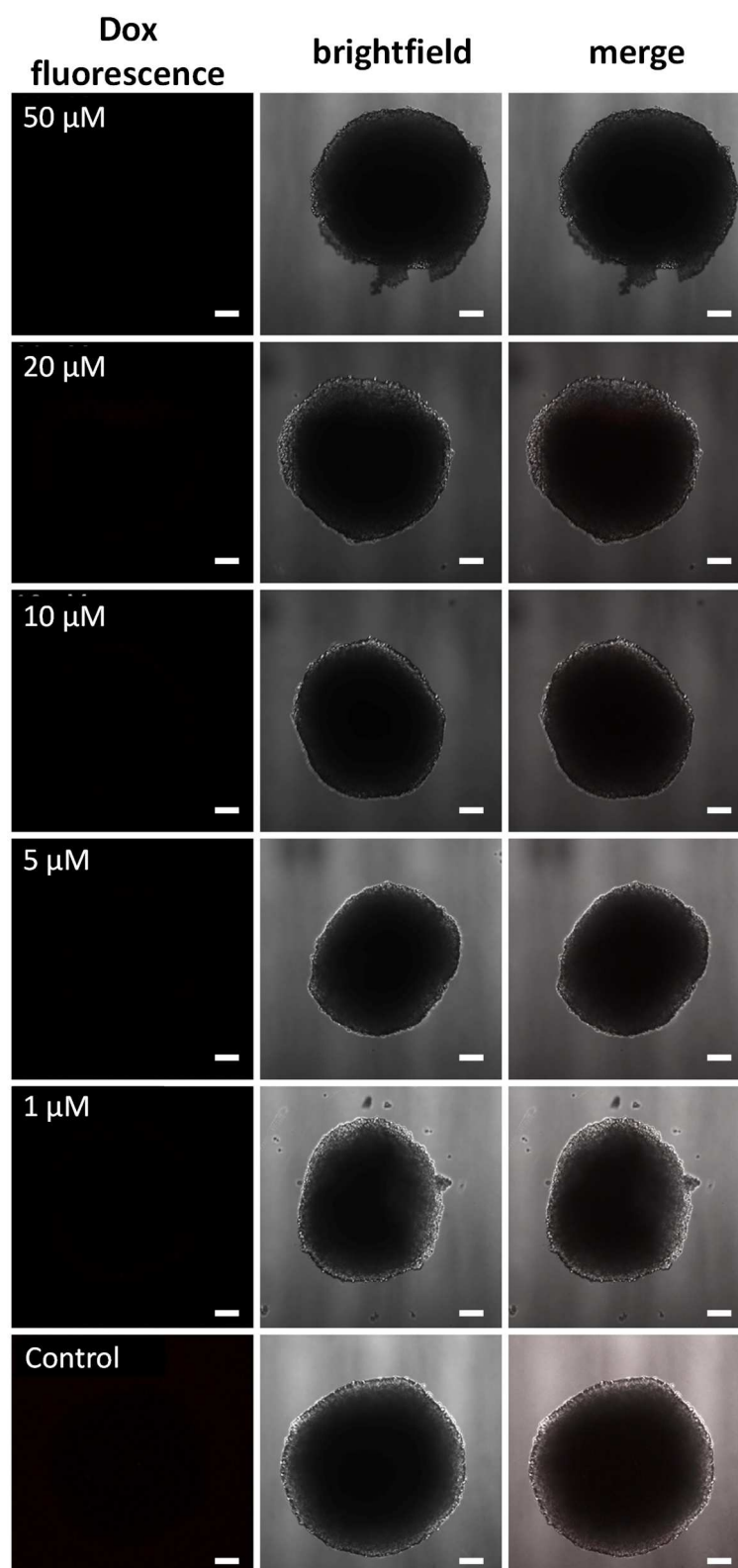


Figure A 8.37: HepG2 spheroids, DIV 7, 3 h incubation with **SSPC-2**. Scale bars are 100 μm .

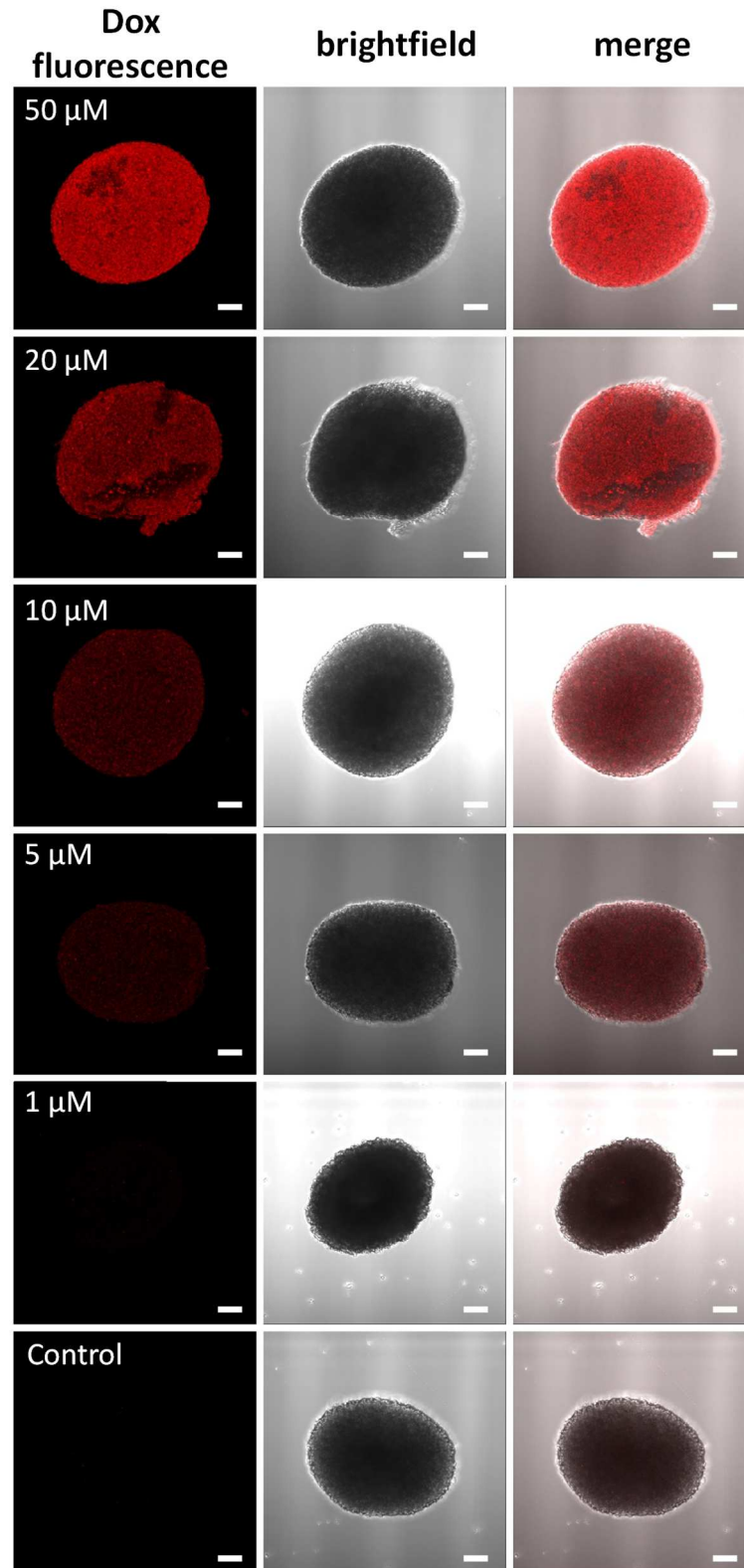


Figure A 8.38: HepG2 spheroids, DIV 7, 3 h incubation with Dox·HCl. Scale bars are 100 μm .

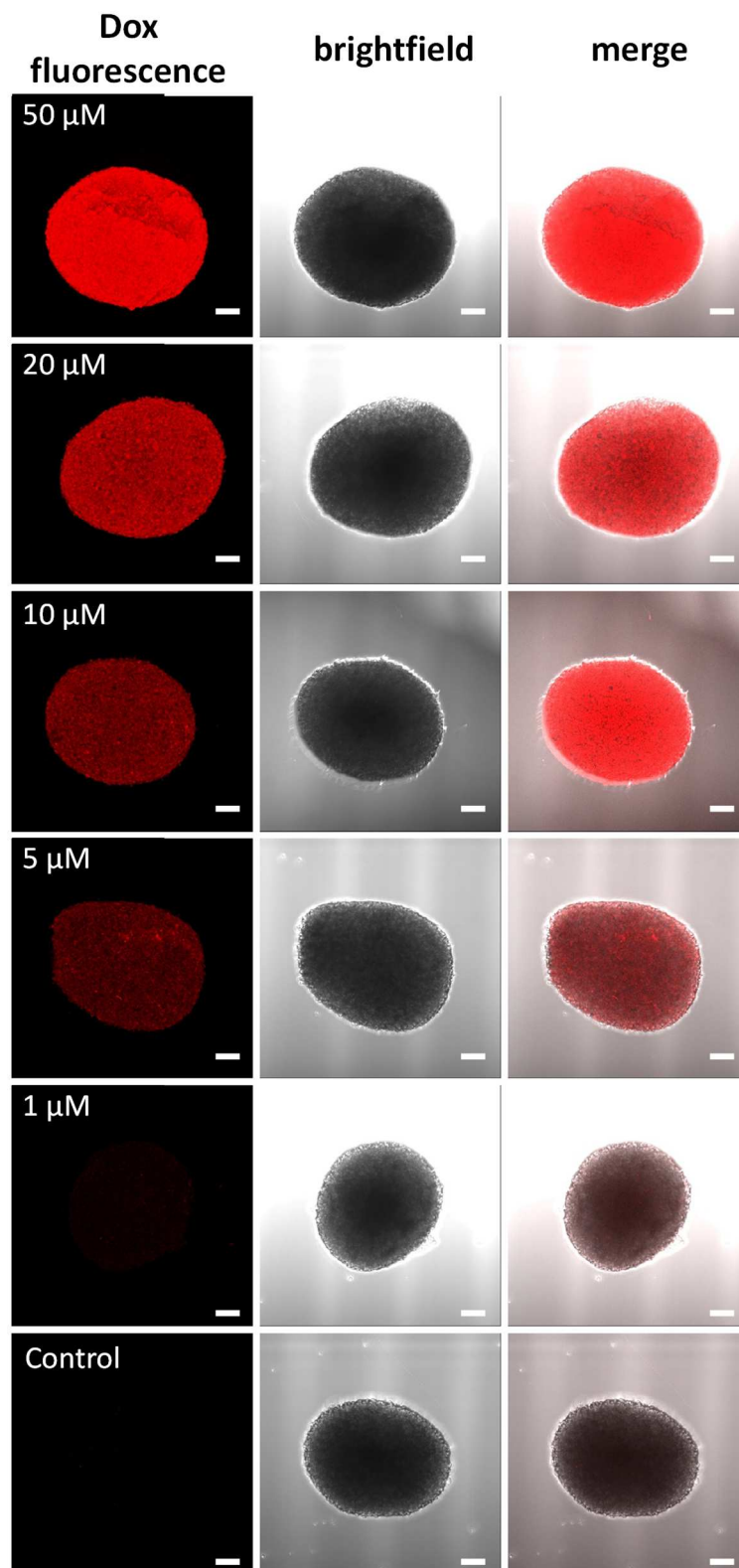


Figure A 8.39: HepG2 spheroids, DIV 7, 3 h incubation with **SSPC-3**. Scale bars are 100 μm .

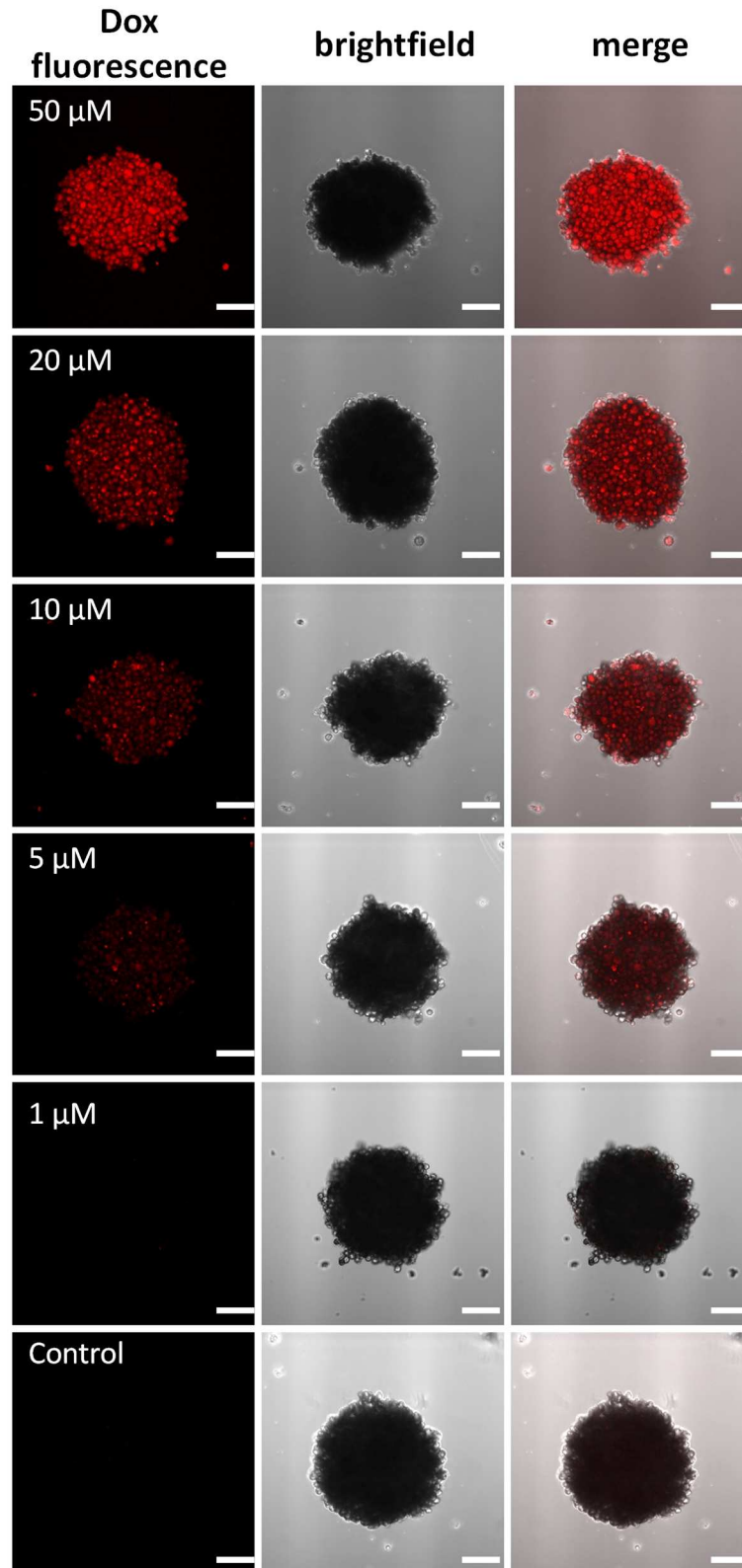


Figure A 8.40: SK-MEL-28 spheroids, DIV 7, 3 h incubation with Dox·HCl. Scale bars are 100 μm .

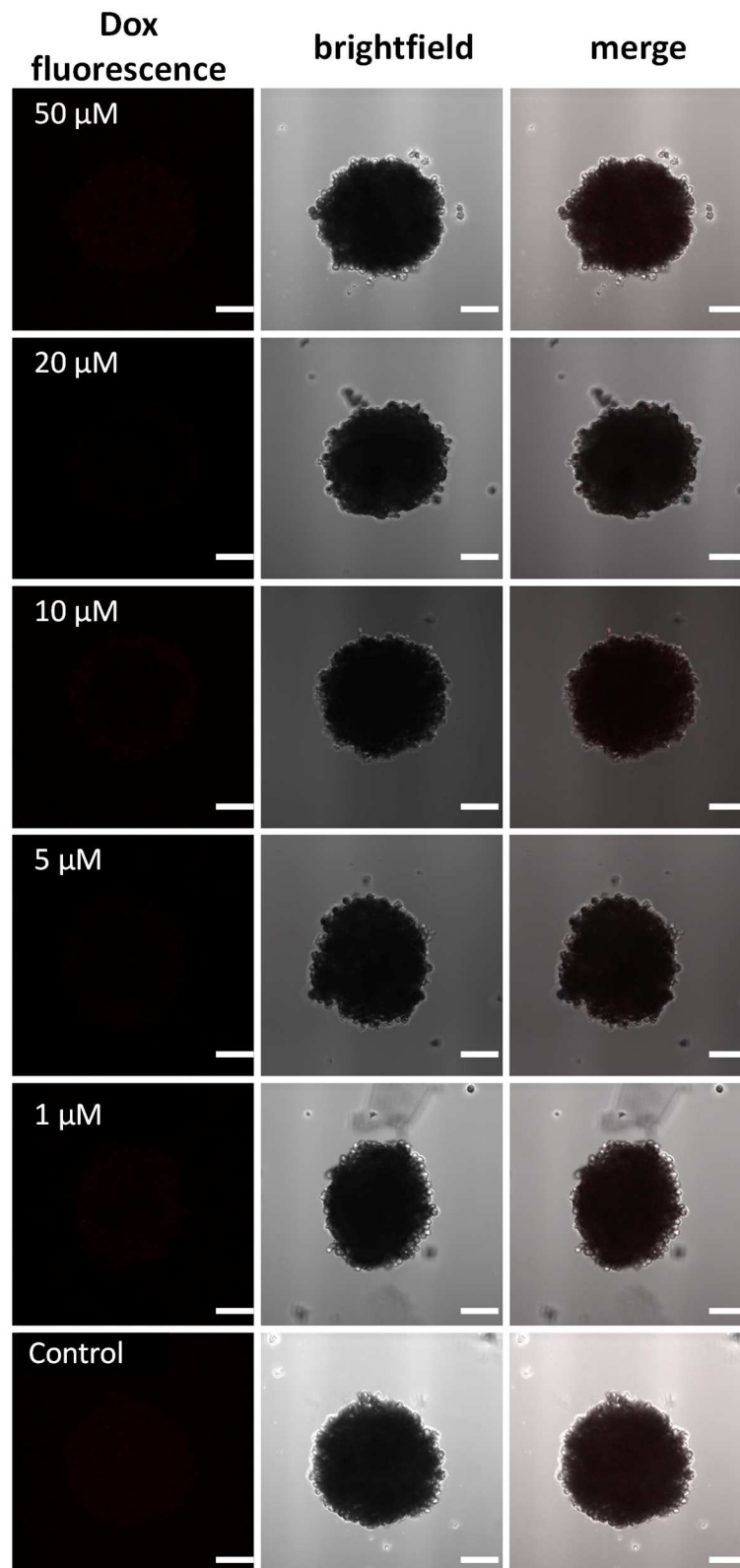


Figure A 8.41: SK-MEL-28 spheroids, DIV 7, 3 h incubation with **SSPC-2**. Scale bars are 100 μm .

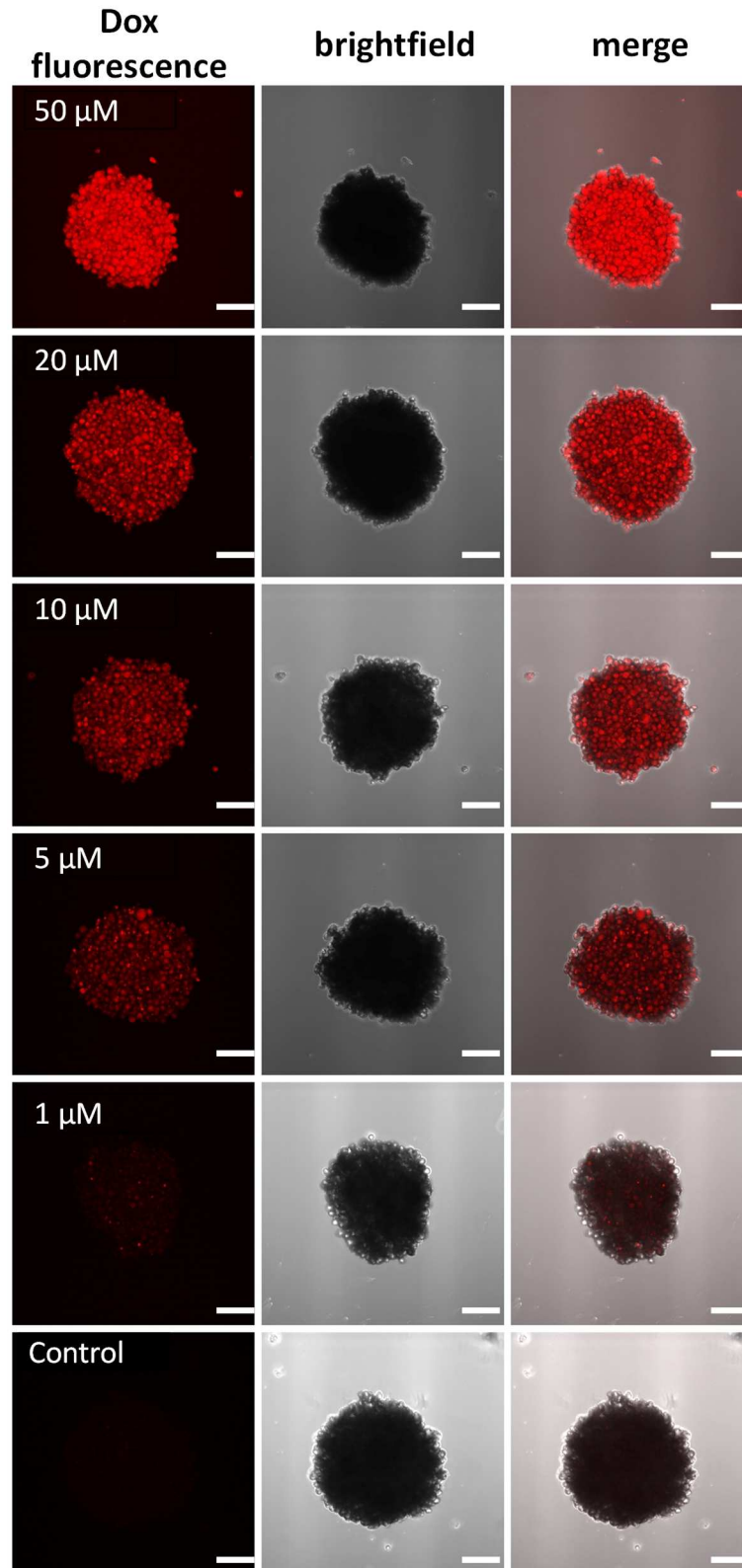


Figure A 8.42: SK-MEL-28 spheroids, DIV 7, 3 h incubation with **SSPC-3**. Scale bars are 100 μm .

8.1.10 Appendix Bio-Evaluation

Main Loop, setting persistent variables and determining input/output directories.

```

clear all
warning('off','images:initSize:adjustingMag');

inputFolder = [];
outputFolderParentPath = [];
outputFolderResultName = [];
outputFolderResultPath = [];

inputFileFluorpath = [];
inputfileFluor = [];
inputFileBrightfieldpath = [];
inputFileBrightfield = [];
outputFile = [];
listInputFluorFiles = [];
listInputBrightfieldFiles = [];

disp(['Please select Input Image folder']);
inputFolder = uigetdir();
listInputFluorFiles = ls([inputFolder '*ch00.tif']);
listInputBrightfieldFiles = ls([inputFolder '*ch01.tif']);

disp(['Please select Output Folder for all Evaluations']);
outputFolderParentPath = uigetdir();

disp(['You selected ' inputFolder ' as your Fluorescence Image
folder.']);
disp(['You selected ' inputFolder ' as your Brightfield Image
folder.']);
disp(['You selected ' outputFolderParentPath ' as your parent Output
folder.']);

disp(['Your input files are:']);
disp([listInputFluorFiles]);
disp('Hit Enter to continue, Ctrl+C to cancel!');
disp(['Your Brightfield files are:']);
disp([listInputBrightfieldFiles]);
disp('Hit enter to start, Ctrl+C to cancel!');
pause();

tic

for valEvalNum = 1 : size(listInputFluorFiles,1)
%     valEvalNum = valEvalNum +1;
    disp('#####');
    disp(['## Running evaluation #' num2str(valEvalNum) '...']);
    disp('#####');
%acquire input path, list input files, generate output directory
%provide feedback to operator and run mask generator
    inputFileFluorpath = fullfile(inputFolder, strtrim(listIn-
putFluorFiles(valEvalNum, :)));
    inputFileBrightfieldpath = fullfile(inputFolder, strtrim(listInput-
BrightfieldFiles(valEvalNum, :)));
    outputFolderResultName = strtrim(listInputFluorFiles(valEvalNum, :));
    outputFolderResultName = outputFolderResultName(1:end-4);

```

```

imshow(imread(inputFileFluorpath));
mkdir(outputFolderParentPath,[datestr(now,'yymmdd'),'\\',outputFolderResultName]);
outputFolderResultPath = [outputFolderParentPath, '\\',
datestr(now,'yymmdd'),'\\',outputFolderResultName '\\'];
saveas(gcf,[outputFolderResultPath 'EvalNum' num2str(valEvalNum)
'.png']);
close figure 1

%
run MaskCreator.m
% pause();
end

```

MaskCreator.m, called from main loop for mask generation,

```

valThresholdDefault = 0.5;
valThreshold = valThresholdDefault;
valThresholdChange = 0;%user input for threshold
valMeasurelength = 350;%default vector length for profiling
valWidthMicrons = [];%horizontal resolution in 10-6 meters
valWidthPx = [];%horizontal Resolution in pixels
valWidthMicronsDefault = 733;%1053 HepG2, 733 SKMEL28
valResPxPerMicron = 0;%resolution for x-axis generation
valProfileNum = 0;
imgFluor = [];%image for analysis
imgMask = [];%image for mask generation

%%%%%%%%%%%%load mask image%%%%%%%%
% disp('Hit Enter to select MASK file.')

% [maskfile,maskpath] = uigetfile('*.');
% if isequal(maskfile,0)
%     disp('User selected Cancel');
% else
imgMask = imread(inputFileBrightfieldpath);
disp(['Selected ', inputFileBrightfieldpath, ' as mask image']);
% end

imgFluor = imread(inputFileFluorpath);
disp(['Selected ', inputFileFluorpath, ' as fluorescence image']);

%determine image resolution
if isempty(valWidthMicrons)
valWidthMicrons = valWidthMicronsDefault;
end

valWidthPx = size(imgFluor,2);
valResPxPerMicron = valWidthPx/valWidthMicrons;

disp(['Image width: ', num2str(valWidthMicrons), ' μm, ',
num2str(size(imgFluor,1)), ' px = ', num2str(valResPxPerMicron), '
px/μm'])
% imshow(imfuse(imgMask,imgFluor,'montage'));

%pick green channel for mask generation
imgMaskMono = imgMask(:,:,1);
valProfileNum = 0;%number the evaluation, start from 0

```

```

while ne(valThresholdChange, valThreshold)
    %generate binary mask image via adaptive thresholding
    imgMaskBinary = imbinarize(imgMaskMono, 'adaptive', 'ForegroundPolarity', 'dark', 'Sensitivity', valThreshold);
    %invert binary mask to turn ROIs = 1
    imgMaskBinaryInv = imcomplement(imgMaskBinary);
    %Omit all minor objects from mask
    imgMaskMajor = bwareafilt(imgMaskBinaryInv, 1);
    %remove "holes" from mask
    imgMaskMajorClean = imcomplement(bwareafilt(imcomplement(imgMaskMajor), 1));
    %get the center off mass from mask and display
    ptCenter = regionprops(uint8(imgMaskMajorClean), "area", "centroid");
    centroids = cat(1, ptCenter.Centroid);
    %show the generated Image and plot Center off Mass
    imshow(imfuse(imfuse(imgMaskMajorClean, imgMaskBinary, 'montage'), imfuse(imgMask, imgFluor, 'montage'), 'montage'))
    hold on
    plot(centroids(:,1), centroids(:,2), 'b*')
    hold off
    disp('Please check the mask you just created.')

    valThresholdChange = input(['Change threshold for mask creation? Default = ' num2str(valThresholdDefault) ', last = ' num2str(valThreshold) ', hit enter to continue: ']);

    if valThresholdChange < 0
        disp('Only values 0 > x > 1 allowed, setting to 0.01')
        valThresholdChange = 0.01;
    end

    if valThresholdChange > 1
        disp('Only values 0 > x > 1 allowed, setting to 0.99.')
        valThresholdChange = 0.99;
    end

    if valThresholdChange == 0
        disp('Only values 0 > x > 1 allowed, setting to 0.01.')
        valThresholdChange = 0.01;
    end

    valThreshold = valThresholdChange;

    % force loop to preview picture
    if isempty(valThresholdChange)
        valThresholdChange = valThreshold;
    else
        valThresholdChange = 0;
    end

end
disp('Alright, saved your mask for reference in the Output folder, evaluating now!')
run VectorCycle.m

```

VectorCycle.m, called after mask creation for the creation of profiling vectors and feedback to the operator.

```

valMeasureAngle = 0;
valMeasureLengthDefault = 450;
valMeasureLengthChange = 0;
valMeasureRadius = valMeasureLengthDefault;
valMeasureVector = valMeasureRadius;%init variable to pass to Profiling
Script
valMeasureX = 100;
valMeasureY = 0;
vectorMeasure = [valMeasureX, valMeasureY];
daring = [vectorMeasure];
radiusBad = 1;
evalRingPlot = [];
while ne(valMeasureRadius, valMeasureLengthChange)

    valMeasureVector = valMeasureRadius;

    hold on%keep mask preview

    evalRing = [0,0];
    valMeasureAngle = 0;
    while valMeasureAngle < 2*pi
        valMeasureAngle = valMeasureAngle + (pi/360);
        [valMeasureX, valMeasureY] = pol2cart(valMeasureAngle, valMeas-
ureRadius);
        [valMeasureX, valMeasureY] + ptCenter.Centroid;
        vectorMeasure = [valMeasureX, valMeasureY]+ptCenter.Centroid;
        evalRing = [evalRing; vectorMeasure];
    end;
    delete(evalRingPlot)
    evalRingPlot = plot(evalRing(:,1), evalRing(:,2), 'b*');

    valMeasureLengthChange = input(['Please enter the radius for evalua-
tion in pixels (for default ', num2str(valMeasureLengthDefault), 'px hit
enter): ']);

    if valMeasureLengthChange < 0
        disp('Only values x > 0 allowed, setting to 1')
        valMeasureLengthChange = 1;
    end

    if valMeasureLengthChange == 0
        disp('Only values 0 > x > 1 allowed, setting to 1.')
        valMeasureLengthChange = 1;
    end

    valMeasureRadius = valMeasureLengthChange;
%    force loop to preview picture
    if isempty(valMeasureLengthChange)
        valMeasureLengthChange = valMeasureRadius;
    else
        valMeasureLengthChange = -1;
    end
end

```

```
    disp(['Evaluating with a radius of ', num2str(valMeasureRadius),  
'px.'])  
    disp('Please check the Output window for a preview and make sure  
your ROI is inside the circle!')  
%    radiusBad = input('Hit enter if this looks fine, otherwise type a  
number:');  
    %imshow(imgMaskMajorClean, [ptCenter.Centroid(:,1) vectorMeas-  
ure(:,1)], [ptCenter.Centroid(:,2) vectorMeasure(:,2)]), grid on  
    hold off  
end  
saveas(gcf, [outputFolderResultPath outputFolderResultName ' -  
Mask.png'])  
disp(['saved your evaluation Template as ' outputFolderResultPath out-  
putFolderResultName, ' - Mask.png'])  
disp('Profiling now!')  
run Profiler.m
```

Profiler.m, called from vector generation, performing profile creation and writing results to output directory.

```
valMeasureAngle = 0;%initialize measurement angle  
valProfilingIncsCount = 0;%initialise increment counter  
valProfilingIncsDefault = 720;%fix increment number  
valProfilingIncs = [];%initialise increment number for profiling  
valProfileResMult = 4;%initialise number of samples per pixel while pro-  
filing  
valNoiseFloorInc = [];%initialise storage for a profile's background av-  
erage  
valNoiseFloorStack = 0;%initialise noisefloor storage for averaging  
valNoiseFloorAvg = [];%initialise storage for total noisefloor average  
valBackgroundStart = 1;%set first measuring index as the start of back-  
ground area  
valBackgroundEnd = [];%initialise variable used for reordering profiles  
for averaging  
profileFluor = []; %init array to record incremental profile  
profileFluorShift = [];%init array to handle and process incremental  
profile  
profileFluorAvg = [];%init array to take averaged profiles  
profileFluorAvgCorr = [];%init array to take background corrected, aver-  
aged profile  
profileMask = [];%init array to record mask profile  
profileMaskInverse = [];%init inverse mask array for background determi-  
nation  
profileBackground = [];%init array for storing incremental Background  
%%Set the number of profiles obtained  
  
if isempty(valProfilingIncs)  
    valProfilingIncs = valProfilingIncsDefault;  
end  
disp(['Running evaluation in ', num2str(valProfilingIncs), ' steps, ',  
num2str(valMeasureVector), ' px depth @ ', num2str(valMeasureVec-  
tor*valProfileResMult), ' samples'])  
  
%%initialise arrays for archiving profiles  
profileFluorCorrCat = zeros(valMeasureVector*valProfileResMult, valPro-  
filingIncs+1);  
profileFluorRawCat = zeros(valMeasureVector*valProfileResMult, valPro-  
filingIncs+1);
```

```

profileMaskCat = zeros(valMeasureVector*valProfileResMult, valProfiling-
Incs+1);
profileBackgroundCat = zeros(valMeasureVector*valProfileResMult, valPro-
filingIncs+1);

%%initialise arrays for averaging profiles
profileFluorCorrStack = zeros(valMeasureVector*valProfileResMult,1);
profileFluorRawStack = zeros(valMeasureVector*valProfileResMult,1);
profileBackgroundStack = zeros(valMeasureVector*valProfileResMult,1);

%%Start profiling
tic
fprintf(['\nrecording ' num2str(valProfilingIncs), ' Profiles. Profiles
recorded: '])

while valMeasureAngle < 2*pi

    valMeasureAngle = valMeasureAngle + (pi/(valProfilingIncs/2));%step
up measuring angle by one increment
%    transform current profile endge to cartesian and generate pro-
filing vector
    [valMeasureX, valMeasureY] = pol2cart(valMeasureAn-
gle, valMeasureVector);
    vectorMeasure = [valMeasureX, valMeasureY]+ptCenter.Centroid;
%    record fluorescence and mask profiles from profiling edge to-
wards center of mass
    profileFluor = improfile(imgFluor(:, :, 1), [vectorMeasure(:, 1)
ptCenter.Centroid(:, 1)], [vectorMeasure(:, 2) ptCenter.Centroid(:, 2)],
valMeasureVector*valProfileResMult, 'bilinear');
    profileMask = improfile(imgMaskMajorClean, [vectorMeasure(:, 1)
ptCenter.Centroid(:, 1)], [vectorMeasure(:, 2) ptCenter.Centroid(:, 2)],
valMeasureVector*valProfileResMult, 'nearest');
    profileMaskInverse = (profileMask-1)*-1;
    profileBackground = profileFluor.*profileMaskInverse;
%    find last packground pixel from mask
    valBackgroundEnd = find(profileMask, 1)-1;
    valNoisefloorInc = mean(profileBackground(1:valBackgroundEnd));
%    cut background area for profile alignment outside
    profileFluorShift = profileFluor.*profileMask;
    profileFluorShift = circshift(profileFluorShift, -valBack-
groundEnd);
%    Stack profiles for averaging. +1 to leave first column for
%    distance axis without concatting two arrays later
    valProfilingIncsCount = valProfilingIncsCount + 1;
    valNoisefloorStack = valNoisefloorStack + valNoisefloorInc;
    profileFluorCorrStack = profileFluorCorrStack + profileFlu-
orShift;
    profileFluorRawStack = profileFluorRawStack + profileFluor;
    profileBackgroundStack = profileBackgroundStack + profileBack-
ground;

%    write the last increments to results table+1 to leave first
column for
%    distance axis without concatting two arrays later
    profileFluorRawCat(:, valProfilingIncsCount+1) = profileFluor;
    profileFluorCorrCat(:, valProfilingIncsCount+1) = profileFlu-
orShift;
    profileMaskCat(:, valProfilingIncsCount+1) = profileMask;
    profileBackgroundCat(:, valProfilingIncsCount+1) = profileBack-
ground;

```

```

%       Visual feedback about process
if valProfilingIncsCount > 1
    for j=0:log10(valProfilingIncsCount-1)
        fprintf('\b');% delete previous counter display
    end
end
fprintf('%d', valProfilingIncsCount);

end
clear j;
fprintf('\n')
%determine the average noisefloor
valNoisefloorAvg = valNoisefloorStack / valProfilingIncsCount;
%Fill result arrays column 1 with distance information in um
profileFluorRawCat(:,1) = [1:size(profileFluorRawCat,1)]/valPro-
fileResMult/valResPxPerMicron;
profileFluorCorrCat(:,1) = [1:size(profileFluorCorrCat,1)]/valPro-
fileResMult/valResPxPerMicron;
profileMaskCat(:,1) = [1:size(profileMaskCat,1)]/valProfileResMult/val-
ResPxPerMicron;
profileBackgroundCat(:,1) = [1:size(profileBackgroundCat,1)]/valPro-
fileResMult/valResPxPerMicron;
% create averaged profiles and subtract noise floor
profileFluorAvg = [profileFluorCorrCat(:,1), profileFluor-
CorrStack/valProfilingIncs];
profileBackgroundAvg = [profileFluorCorrCat(:,1), profileBackground-
Stack/valProfilingIncs];
profileFluorAvgCorr = profileFluorAvg - valNoisefloorAvg;%subtract noise
floor
profileFluorAvgCorr = profileFluorAvgCorr(:,2).*(profileFluo-
rAvgCorr(:,2)>0);%keep only values >= 0

%%write results to disk
disp('Saving raw profiles...');
tableProfileCatRaw = array2table(profileFluorRawCat);
writetable(tableProfileCatRaw, [outputFolderResultPath outputFolderRe-
sultName ' - RawProfiles.csv']);
disp('Done!');
disp('Saving processed profiles...');
tableProfileCatProcd = array2table(profileFluorCorrCat);
writetable(tableProfileCatProcd, [outputFolderResultPath outputFolderRe-
sultName ' - ProcessedProfiles.csv']);
disp('Done!');
disp('Saving mask profiles...');
tableMaskCat = array2table(profileMaskCat);
writetable(tableMaskCat, [outputFolderResultPath outputFolderResultName
' - MaskProfiles.csv']);
disp('Done!');
disp('saving averaged profile');
tableProfileAvgd = array2table([profileFluorAvg, profileFluorAvgCorr]);
writetable(tableProfileAvgd, [outputFolderResultPath outputFolderResult-
Name ' - AveragedProfiles.csv']);
disp('saving averaged Background');
tableProfileAvgd = array2table([profileFluorCorrCat(:,1), profileBack-
groundStack/valProfilingIncs]);
writetable(tableProfileAvgd, [outputFolderResultPath outputFolderResult-
Name ' - AveragedBackgrounds.csv']);
disp('Done!');
toc
% plot results for immediate feedback and save results as PNG
plot(profileFluorCorrCat(:,1),profileFluor);

```

```
hold on
plot(profileFluorCorrCat(:,1),profileMask);
plot(profileFluorCorrCat(:,1),profileFluorRawStack/valProfilingIncs)
hold off
saveas(gcf,[outputFolderResultPath outputFolderResultName ' - Pro-
filesUnprocessed.png']);
plot(profileFluorCorrCat(:,1),profileFluorCorrStack/valProfilingIncs)
hold on
plot(profileFluorCorrCat(:,1),profileFluorShift);
hold off
saveas(gcf,[outputFolderResultPath outputFolderResultName ' - Pro-
filesProcessed.png']);
plot(profileMaskCat(:,1),profileMaskCat(:,2:end));
saveas(gcf,[outputFolderResultPath outputFolderResultName ' - Pro-
filesMasks.png']);
disp('Done!');
plot(profileBackgroundCat(:,1),profileBackgroundCat(:,2:end));
saveas(gcf,[outputFolderResultPath outputFolderResultName ' - Pro-
filesBackgrounds.png']);
disp('Done!');
plot(profileBackgroundCat(:,1),profileBackgroundStack/valProfilingIncs)
saveas(gcf,[outputFolderResultPath outputFolderResultName ' - Averaged-
Backgrounds.png']);
disp('Profiling Complete!')
disp(['Total number of increments: ' num2str(valProfilingIncs)])
disp(['Profile Depth: ' num2str(valMeasureVector) 'px'])
disp(['Profile Resolution: ' num2str(valMeasureVector*valProfileResMult)
' samples'])
```

8.2 APPENDIX LIGHT RESPONSIVE RELEASE SYSTEM

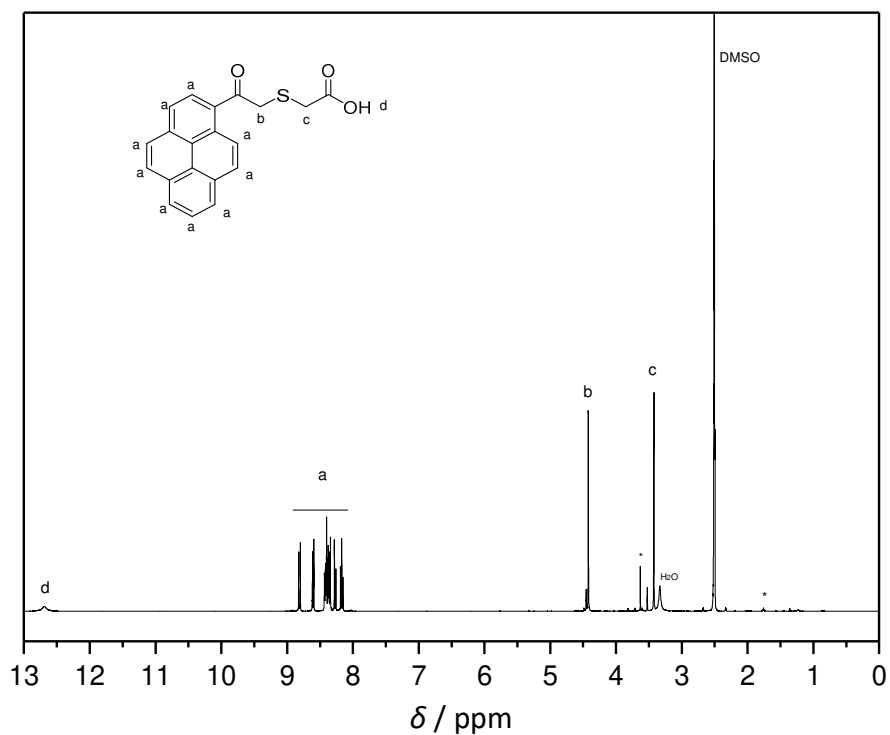


Figure A 8.43: $^1\text{H-NMR}$ (600 MHz, DMSO-d_6) spectrum of pyreneacyl sulfide acid. Residual DCM and THF impurities are marked with *.

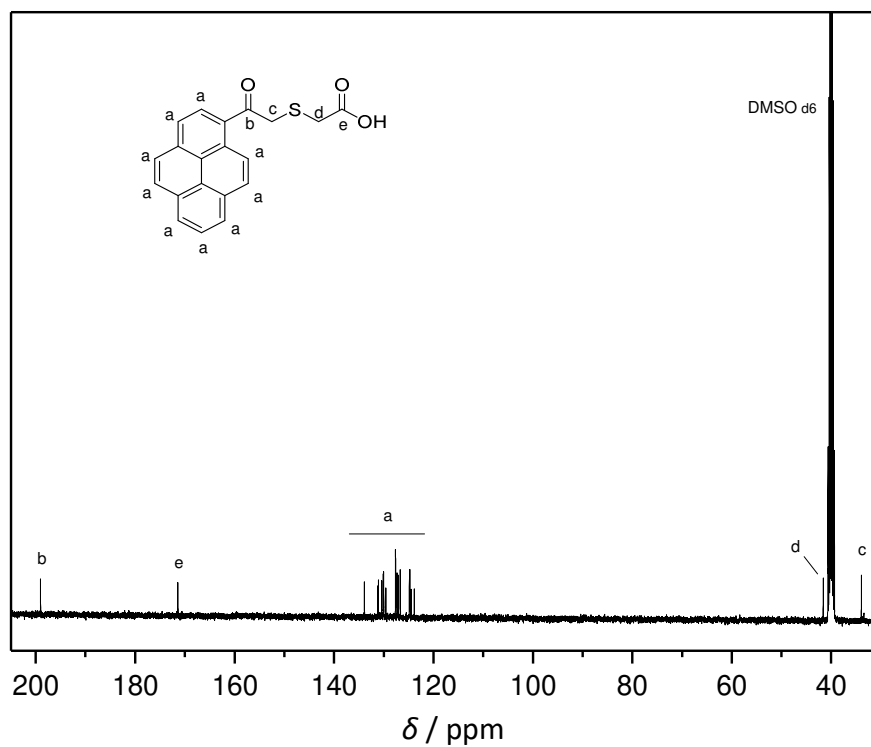
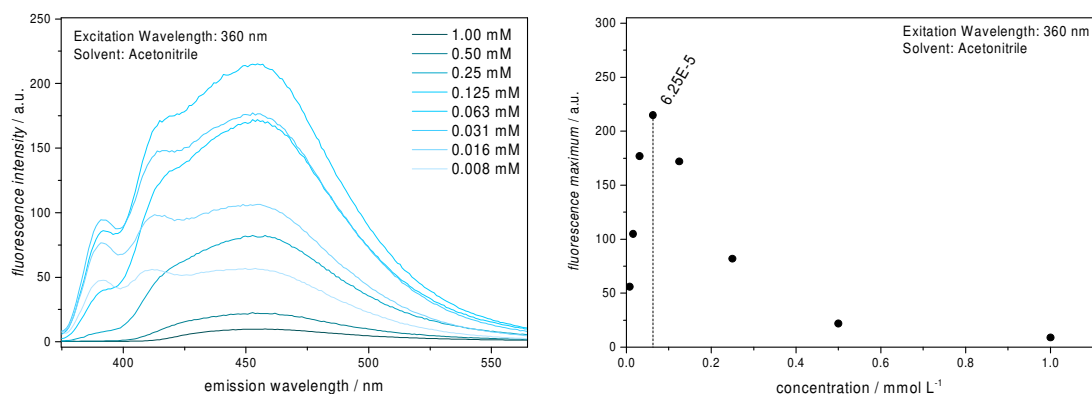


Figure A 8.44: $^{13}\text{C-NMR}$ (151 MHz, DMSO-d_6) of PAS.

Table A 8.14: Attempted coupling conditions for the generation of a small molecule system for light triggered release.

<i>coupling reagent</i>	<i>2. coupling agent</i>	<i>additives</i>	<i>reactive species</i>	<i>solvent</i>	<i>outcome</i>
EDC	HOBt	DMAP	act. ester	DCM	only traces of product formed
DCC	HOBt	DMAP	act. ester	DCM	unknown product formed
DCC	---	DMAP	---	DCM	amine did not react
DCC	NHS	DMAP	act. ester	DCM	amine did not react
DPPCI	---	ethyl-morpholine	diphenyl phosphinate	DCM	amine did not react
SOCL ₂	---	pyridine	acid chloride	Toluene	PAS regained
SOCL ₂	---	pyridine	acid chloride	THF/DCM	only traces of product formed
SOCL ₂	---	pyridine	acid chloride	DCM	PAS decomposed
SOCL ₂	---	DME	acid chloride	DCM	PAS decomposed
SOCL ₂	---	NEt ₃	acid chloride	THF	starting material recovered
SOCL ₂	---	---	acid chloride	neat	PAS decomposed

**Figure A 8.45:** Concentration dependence of PAS fluorescence. The spectra show a drastic drop in intensity at concentrations greater than approximately 62.5 μM .

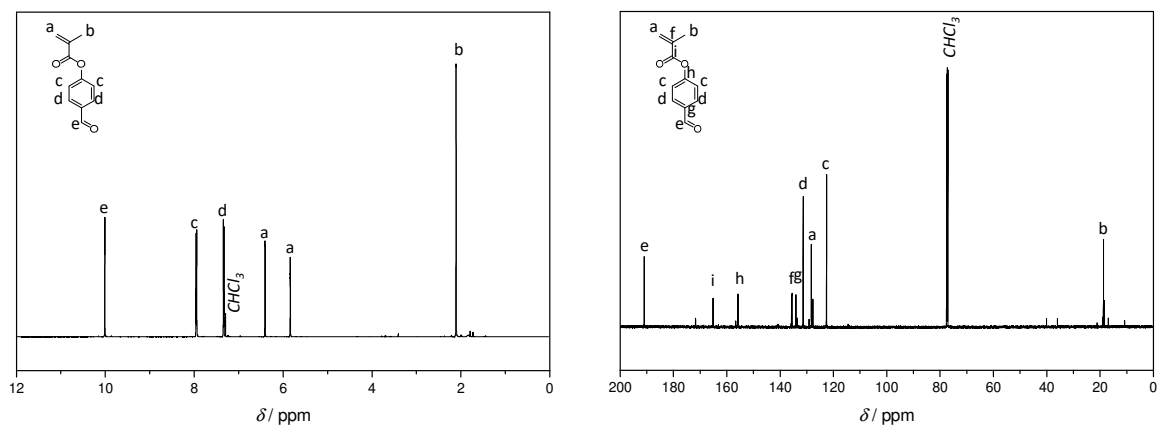


Figure A 8.46: ^1H -NMR of FPMA in CDCl_3 . Right: ^{13}C -NMR of FPMA in CDCl_3 .

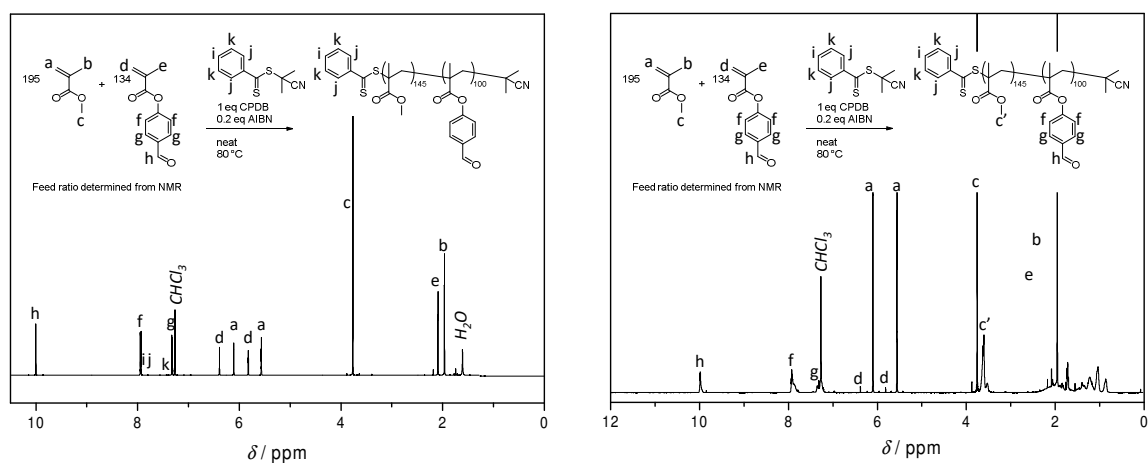


Figure A 8.47: ^1H -NMR-spectra used to calculate feed ratio and conversion for the polymerisation of **LRC-0**. Left: reaction mixture before polymerisation. Right: Spectrum after 4.5 hours. Integrals before and after 4.5 hours were used to calculate conversion. Feed ratio was determined from integrals d and a, ratio of incorporation was determined from c' and h'.

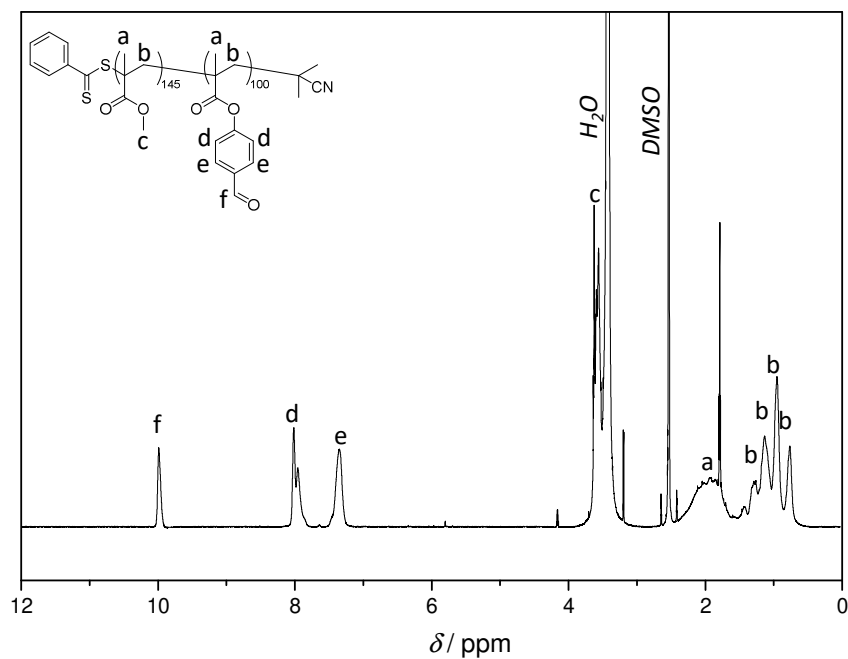


Figure A 8.48: $^1\text{H-NMR}$ of LRC-0 in DMSO-D_6 .

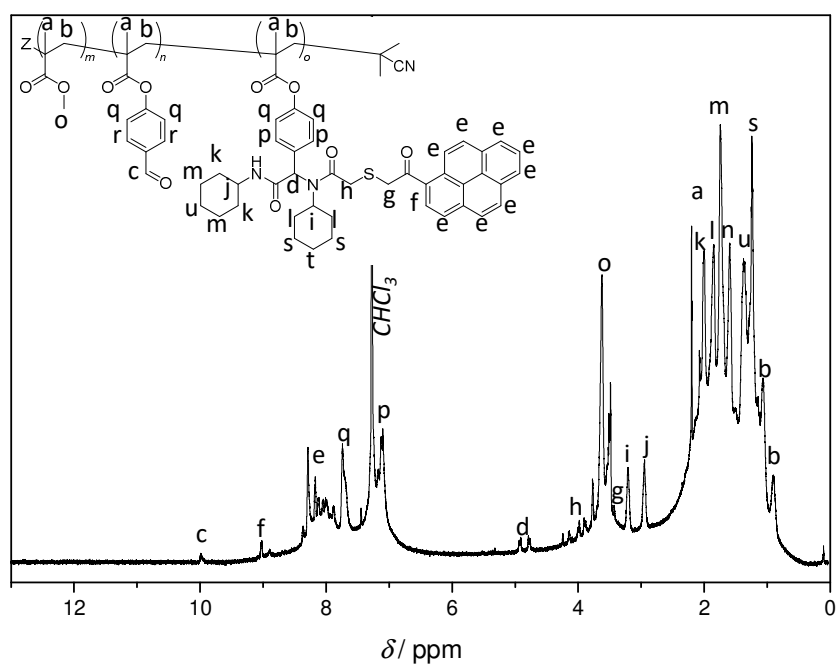


Figure A 8.49: $^1\text{H-NMR}$ of LRC-5 in CDCl_3 .

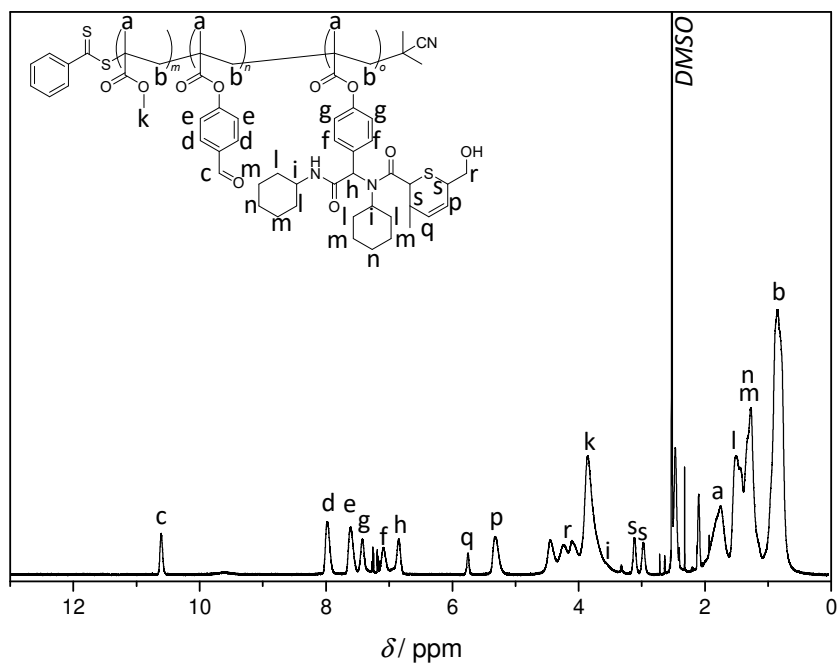
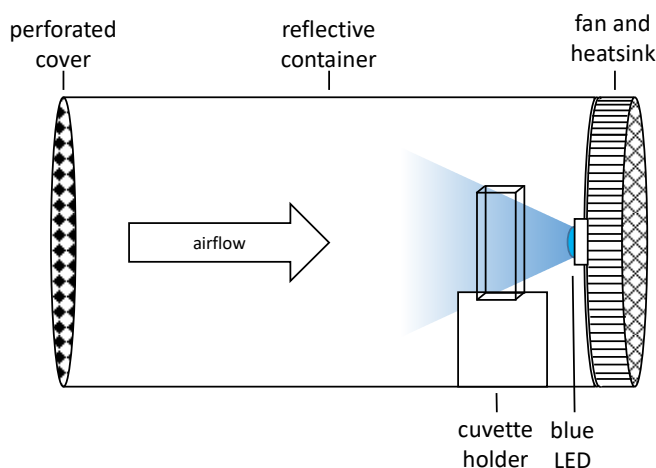


Figure A 8.50: ^1H -NMR of LRC-6 after irradiation in DMSO- D_6 .



Scheme A 8.1: Schematic of the photo reactor used in the release experiments. The cuvette holder was 3D-printed and fixed in order to not obstruct the light's pathway and keep a consistent distance to the LED when the cuvette is taken out for measurement. The container was made from a reflective material in order to achieve maximum illumination of the sample.

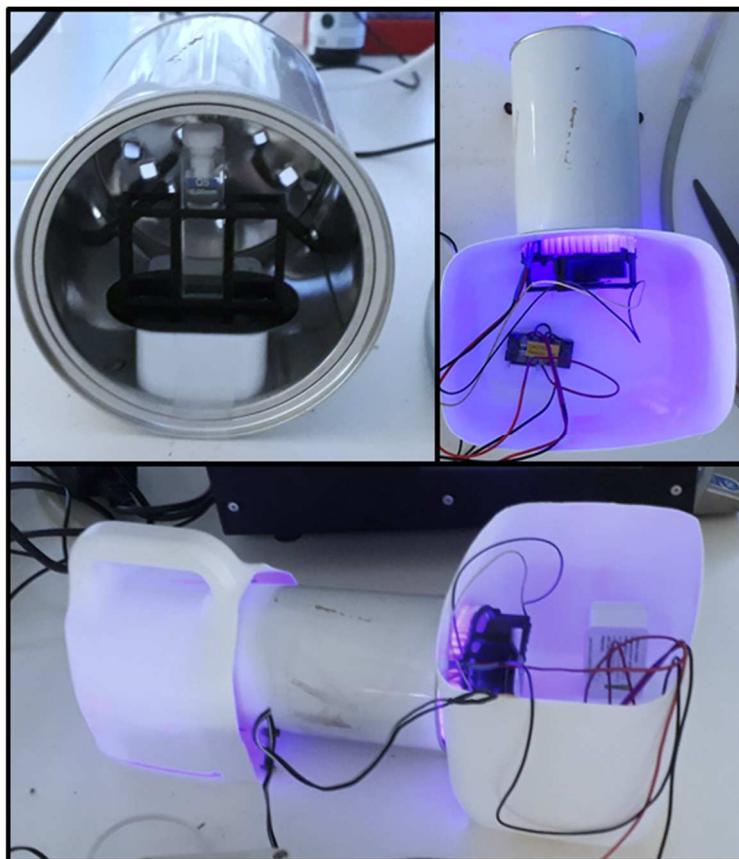


Figure A 8.51: Photograph of the custom reactor setup. The top left shows the custom cuvette holder with **LRC-2** for bulk-release in a quartz-cuvette.

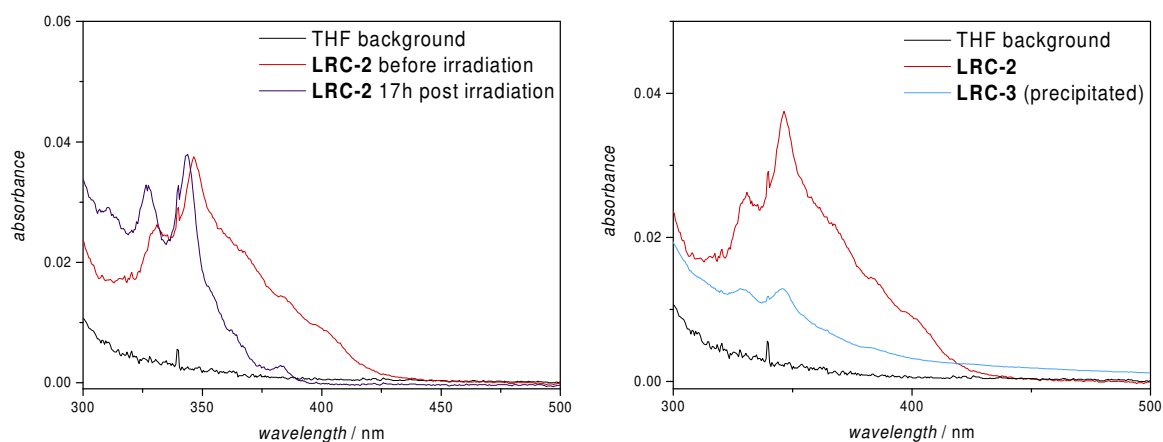


Figure A 8.52: UV/Vis spectra of **LRC-2** and **LRC-3** along the release process. The spectrum on the left shows the same solution of **LRC-2** before and after irradiation. Clearly visible is a shift in towards shorter wavelength due to spatial separation of the absorbing fluorophores, reducing excimer and stacking effects. The spectrum on the right additionally shows a clear decrease in absorption after precipitation of the polymer and removal of free, released acetylpyrene, confirming the release event.

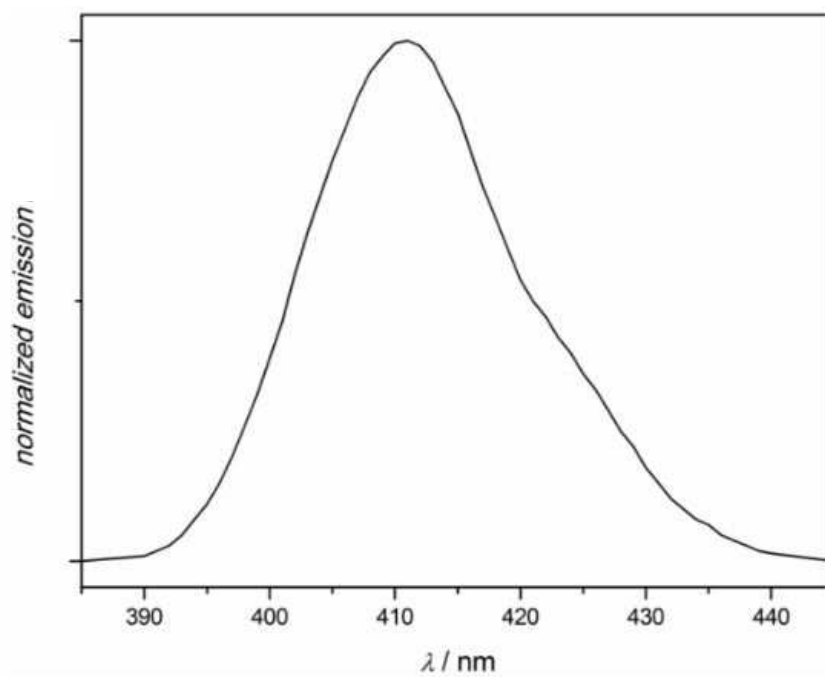


Figure A 8.53: Emission spectrum of the Avonec LED used for irradiation of **LRC-2** and **LRC-5**. Reproduced from [211] with permissions from RSC.

8.3 APPENDIX MSOT DYE

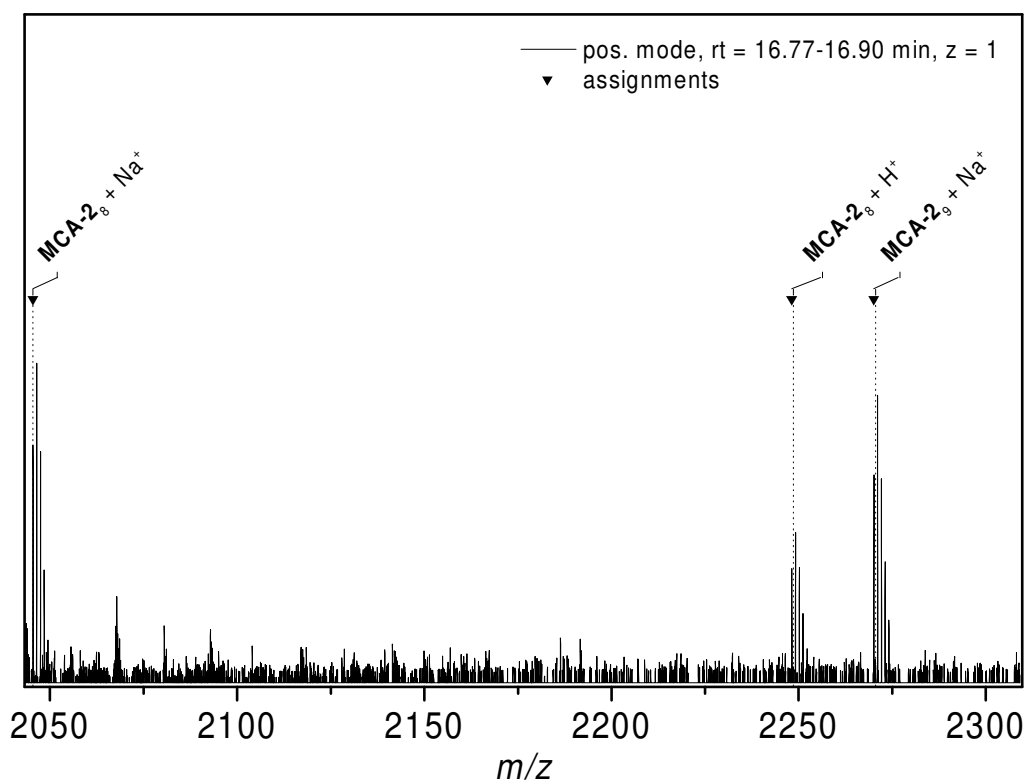


Figure A 8.54: SEC-MS spectrum of **MCA-0**. One repeating unit (length 8-9 monomers) is shown. High amine content led to high amount of proton-adducts for ionisation. Only RAFT-group terminated chains could be detected.

Table A 8.15: MS values obtained from SEC-MS of **MCA-0** and calculated values for comparison. Column “Label” denotes the chain composition and label in the spectrum. $\Delta\Delta m/z$ max. denotes the theoretical maximum deviation in m/z by instrument parameters.

Label	m/z exp.	m/z calcd.	$\Delta\Delta m/z$	$\Delta\Delta m/z$ max.
MCA-2₈ + Na	2045.4279	2045.40626	0.0216	0.0222
MCA-2₉ + Na	2270.6028	2270.57916	0.0236	0.0267
MCA-2₈ + H+	2248.6172	2248.5972	0.0200	0.0275

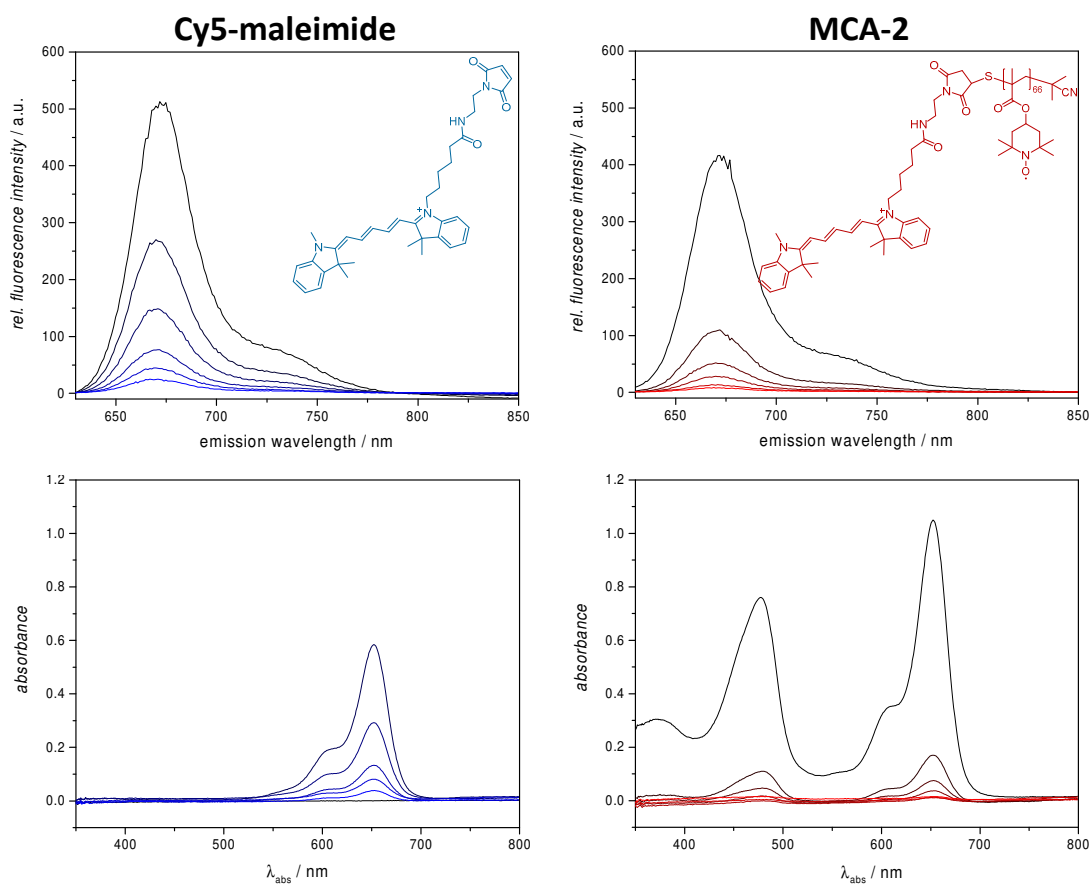


Figure A 8.55: Absorption and fluorescence emission spectra of free Cy5-maleimide and MCA-2 from which comparisons of spin silencing efficiency were drawn.

9

Lists

List of References

- [1] S. McGuire, *Adv. Nutr.* **2016**, 7, 418–9.
- [2] H. Maeda, J. Wu, T. Sawa, Y. Matsumura, K. Hori, *J. Control. Release* **2000**, 65, 271–284.
- [3] T. Förster, *Angew. Chem. Int. Ed.* **1969**, 8, 333–343.
- [4] E. M. Goldys, M. A. Sobhan, *Adv. Funct. Mater.* **2012**, 22, 1906–1913.
- [5] J. M. M. Martinez, *Mater. Today* **2006**, 9, 55.
- [6] G. A. Stahl, *A Short History of Polymer Science*, **1981**.
- [7] H. Staudinger, *Ber. Dtsch. Chem. Ges.* **1920**, 53, 1073–1085.
- [8] R. Braslau, *Handbook of Radical Polymerization*, John Wiley & Sons Inc., Hoboken, NJ, USA, **2002**.
- [9] P. Vana, T. P. Davis, C. Barner-Kowollik, *Aust. J. Chem.* **2002**, 55, 315–318.
- [10] H. Maeda, G. Y. Bharate, J. Daruwalla, *Eur. J. Pharm. Biopharm.* **2009**, 71, 409–419.
- [11] A. D. Jenkins, R. G. Jones, G. Moad, *Pure Appl. Chem.* **2009**, 82, 483–491.

- [12] K. Matyjaszewski, J. Spanswick, *Mater. Today* **2005**, 8, 26–33.
- [13] S. Kharasch, B. M. Kuderna, W. Urry, *J. Org. Chem.* **1948**, 13, 895–902.
- [14] J.-S. Wang, K. Matyjaszewski, *J. Am. Chem. Soc.* **1995**, 117, 5614–5615.
- [15] M. Kato, M. Kamigaito, M. Sawamoto, T. Higashimura, *Macromolecules* **1995**, 28, 1721–1723.
- [16] M. Destarac, D. Charmot, X. Franck, S. Z. Zard, *Macromol. Rapid Commun.* **2000**, 21, 1035–1039.
- [17] C. Barner-Kowollik, *Handbook of RAFT Polymerization*, Wiley-VCH Verlag GmbH & Co. KGaA, Weinheim, Germany, **2008**.
- [18] G. Moad, E. Rizzardo, S. H. Thang, *Polymer (Guildf)*. **2008**, 49, 1079–1131.
- [19] G. Moad, E. Rizzardo, S. H. Thang, *Polym. Int.* **2011**, 60, 9–25.
- [20] G. F. Meijs, E. Rizzardo, S. H. Thang, *Macromolecules* **1988**, 21, 3122–3124.
- [21] G. F. Meijs, E. Rizzardo, *Macromol. Rapid Commun.* **1988**, 9, 547–551.
- [22] D. Colombani, P. Chaumont, *Prog. Polym. Sci.* **1996**, 21, 439–503.
- [23] J. Chiefari, Y. K. Chong, F. Ercole, J. Krstina, J. Jeffery, T. P. T. Le, R. T. A. Mayadunne, G. F. Meijs, C. L. Moad, G. Moad, et al., *Macromolecules* **1998**, 31, 5559–5562.
- [24] D. Charmot, P. Corpart, H. Adam, S. Z. Zard, T. Biadatti, G. Bouhadir, *Macromol. Symp.* **2000**, 150, 23–32.
- [25] M. H. Stenzel, C. Barner-Kowollik, *Mater. Horizons* **2016**, 3, 471–477.
- [26] A. Goto, T. Fukuda, *Prog. Polym. Sci.* **2004**, 29, 329–385.
- [27] D. J. Keddie, G. Moad, E. Rizzardo, S. H. Thang, *Macromolecules* **2012**, 45, 5321–5342.
- [28] C. Barner-Kowollik, M. Buback, B. Charleux, M. L. Coote, M. Drache, T. Fukuda, A. Goto, B. Klumperman, A. B. Lowe, J. B. Mcleary, et al., *J. Polym. Sci. A* **2006**, 44, 5809–5831.
- [29] S. Perrier, *Macromolecules* **2017**, 50, 7433–7447.

- [30] L. Barner, S. Perrier, in *Handbook of RAFT Polymerization*, Wiley-VCH Verlag GmbH & Co. KGaA, Weinheim, Germany, **2008**, pp. 455–482.
- [31] T. Janoschka, A. Teichler, A. Krieg, M. D. Hager, U. S. Schubert, *J. Polym. Sci. A* **2012**, *50*, 1394–1407.
- [32] A. V. Fuchs, A. P. Bapat, G. J. Cowin, K. J. Thurecht, L. Zhao, G. Duan, Y. Cao, R. Zhou, P. Ni, K. J. Thurecht, *Polym. Chem.* **2017**, *7*, 4198–4212.
- [33] T. Gruending, M. Guilhaus, C. Barner-Kowollik, *Anal. Chem.* **2008**, *80*, 6915–6927.
- [34] W. Li, J. Zhang, F. L. S. Tse, *Handbook of LC-MS Bioanalysis*, John Wiley & Sons Inc., Hoboken, NJ, USA, **2013**.
- [35] B. Mertz, M. Lu, M. F. Brown, S. E. Feller, *Biophys. J.* **2011**, *101*, 17–19.
- [36] G. Bergamini, S. Silvi, Eds. , *Applied Photochemistry*, Springer International Publishing, Cham, **2016**.
- [37] W. Müller-Esterl, *Biochemie*, Springer Berlin Heidelberg, Berlin, Heidelberg, **2018**.
- [38] A. Jablonski, *Nature* **1933**, *131*, 839–840.
- [39] R. Rückamp, E. Benckiser, M. W. Haverkort, H. Roth, T. Lorenz, A. Freimuth, L. Jongen, A. Möller, G. Meyer, P. Reutler, et al., *New J. Phys.* **2005**, *7*, 144–144.
- [40] in *IUPAC Compendium of Chemical Terminology*, IUPAC, Research Triagle Park, NC, **n.d.**
- [41] J. Zhao, W. Wu, J. Sun, S. Guo, *Chem. Soc. Rev.* **2013**, *42*, 5323.
- [42] M. Pfeifle, Y. Georgievskii, A. W. Jasper, S. J. Klippenstein, *J. Chem. Phys.* **2017**, *147*, 084310.
- [43] K. Pettersson, K. Kilså, J. Mårtensson, B. Albinsson, *J. Am. Chem. Soc.* **2004**, *126*, 6710–6719.
- [44] S. Dufresne, L. Callaghan, W. G. Skene, *J. Phys. Chem. B* **2009**, *113*, 15541–15549.
- [45] *IUPAC Compendium of Chemical Terminology*, IUPAC, Research Triagle Park,

- NC
- [46] *IUPAC Compendium of Chemical Terminology*, IUPAC, Research Triangle Park, NC
- [47] R. B. Woodward, R. Hoffmann, *Angew. Chemie Int. Ed. English* **1969**, *8*, 781–853.
- [48] P. Mueller, M. M. Zieger, B. Richter, A. S. Quick, J. Fischer, J. B. Mueller, L. Zhou, G. U. Nienhaus, M. Bastmeyer, C. Barner-Kowollik, et al., *ACS Nano* **2017**, *11*, 6396–6403.
- [49] T. Gegenhuber, L. De Keer, A. S. Goldmann, P. H. M. Van Steenberge, J. O. Mueller, M.-F. Reyniers, J. P. Menzel, D. R. D’hooge, C. Barner-Kowollik, *Macromolecules* **2017**, *50*, 6451–6467.
- [50] N. Zydziak, F. Feist, B. Huber, J. O. Mueller, C. Barner-Kowollik, *Chem. Commun.* **2015**, *51*, 1799–1802.
- [51] K. K. Oehlenschlaeger, J. O. Mueller, N. B. Heine, M. Glassner, N. K. Guimard, G. Delaittre, F. G. Schmidt, C. Barner-Kowollik, *Angew. Chem. Int. Ed.* **2013**, *52*, 762–766.
- [52] F. Feist, J. P. Menzel, T. Weil, J. P. Blinco, C. Barner-Kowollik, *J. Am. Chem. Soc.* **2018**, *140*, 11848–11854.
- [53] B. T. Tuten, J. P. Menzel, K. Pahnke, J. P. Blinco, C. Barner-Kowollik, *Chem. Commun.* **2017**, *53*, 4501–4504.
- [54] G. Delaittre, A. S. Goldmann, J. O. Mueller, C. Barner-Kowollik, *Angew. Chem. Int. Ed.* **2015**, *54*, 11388–11403.
- [55] T. K. Claus, B. Richter, V. Hahn, A. Welle, S. Kayser, M. Wegener, M. Bastmeyer, G. Delaittre, C. Barner-Kowollik, *Angew. Chem. Int. Ed.* **2016**, *55*, 3817–3822.
- [56] O. Altintas, M. Glassner, C. Rodriguez-Emmenegger, A. Welle, V. Trouillet, C. Barner-Kowollik, *Angew. Chem. Int. Ed.* **2015**, *54*, 5777–5783.
- [57] C. Barner-Kowollik, M. Bastmeyer, E. Blasco, G. Delaittre, P. Müller, B. Richter, M. Wegener, *Angew. Chem. Int. Ed.* **2017**, *56*, 15828–15845.
- [58] P. Lederhose, N. L. Haworth, K. Thomas, S. E. Bottle, M. L. Coote, C. Barner-

- Kowollik, J. P. Blinco, *J. Org. Chem.* **2015**, *80*, 8009–8017.
- [59] J. Coffey, J. Wang, M. Smith, D. Bouchier-Hayes, T. Cotter, H. Redmond, *Lancet Oncol.* **2003**, *4*, 760–768.
- [60] L. Jiao, F. Song, J. Cui, X. Peng, *Chem. Commun.* **2018**, *54*, 9198–9201.
- [61] P. Agostinis, K. Berg, K. A. Cengel, T. H. Foster, A. W. Girotti, S. O. Gollnick, S. M. Hahn, M. R. Hamblin, A. Juzeniene, D. Kessel, et al., *CA. Cancer J. Clin.* **2011**, *61*, 250–281.
- [62] J. Ungelenk, C. Seidl, E. Zittel, S. Roming, U. Schepers, C. Feldmann, *Chem. Commun.* **2014**, *50*, 6600.
- [63] J. M. Metz, *Clin. Cancer Res.* **2004**, *10*, 6411–6417.
- [64] J. Czepas, A. Koceva-Chyła, K. Gwoździński, Z. Józwiak, *Cell Biol. Toxicol.* **2008**, *24*, 101–112.
- [65] C. S. Wilcox, *Pharmacol. Ther.* **2010**, *126*, 119–145.
- [66] G. P. Margison, M. F. Santibáñez Koref, A. C. Povey, *Mutagenesis* **2002**, *17*, 483–7.
- [67] M. C. Finniss, K. S. Chu, C. J. Bowerman, J. C. Luft, Z. a. Haroon, J. M. Desimone, *Med. Chem. Commun.* **2014**, *5*, 1355–1358.
- [68] R. E. Eliaz, J. Szoka, *Cancer Res.* **2001**, *61*, 2592–2601.
- [69] L. H. Lv, Y. Le Wan, Y. Lin, W. Zhang, M. Yang, G. N. Li, H. M. Lin, C. Z. Shang, Y. J. Chen, J. Min, *J. Biol. Chem.* **2012**, *287*, 15874–15885.
- [70] P. Kubes, M. Suzuki, D. N. Granger, *Proc. Natl. Acad. Sci. U. S. A.* **1991**, *88*, 4651–5.
- [71] Y. Zhao, Z. H. Houston, J. D. Simpson, L. Chen, N. L. Fletcher, A. V. Fuchs, I. Blakey, K. J. Thurecht, *Mol. Pharm.* **2017**, *10*, 3539–3549.
- [72] Y. Gilad, M. Firer, G. Gellerman, *Biomedicines* **2016**, *4*, 11.
- [73] S. Hirsjarvi, C. Passirani, J.-P. Benoit, *Curr. Drug Discov. Technol.* **2011**, *8*, 188–196.

- [74] J. Fang, H. Nakamura, H. Maeda, *Adv. Drug Deliv. Rev.* **2011**, *63*, 136–151.
- [75] J. C. Doloff, N. Khan, J. Ma, E. Demidenko, H. M. Swartz, Y. Jounaidi, *Curr. Cancer Drug Targets* **2009**, *9*, 777–88.
- [76] J. Folkman, *Nat. Med.* **1995**, *1*, 27–31.
- [77] L. M. Sherwood, E. E. Parris, J. Folkman, *N. Engl. J. Med.* **1971**, *285*, 1182–1186.
- [78] J. Fang, T. Sawa, H. Maeda, in *Polym. Drugs Clin. Stage*, Kluwer Academic Publishers, Boston, **2009**, pp. 29–49.
- [79] K. Greish, J. Fang, T. Inutsuka, A. Nagamitsu, H. Maeda, *Clin. Pharmacokinet.* **2003**, *42*, 1089–1105.
- [80] R. B. Greenwald, C. W. Gilbert, A. Pendri, C. D. Conover, J. Xia, A. Martinez, *J. Med. Chem.* **1996**, *39*, 424–431.
- [81] N. Ohtsuka, T. Konno, Y. Miyauchi, H. Maeda, *Cancer* **1987**, *59*, 1560–1565.
- [82] N. Gueven, J. Luff, C. Peng, K. Hosokawa, S. E. Bottle, M. F. Lavin, *Free Radic. Biol. Med.* **2006**, *41*, 992–1000.
- [83] Y. Nakamura, A. Mochida, P. L. Choyke, H. Kobayashi, *Bioconjug. Chem.* **2016**, *27*, 2225–2238.
- [84] K. Hori, S. Saito, H. Takahashi, H. Sato, H. Maeda, Y. Sato, *Japanese J. Cancer Res.* **2000**, *91*, 261–269.
- [85] Y. Matsumura, M. Kimura, T. Yamamoto, H. Maeda, *Japanese J. Cancer Res.* **1988**, *79*, 1327–1334.
- [86] R. K. Jain, *Cancer Res.* **1987**, *47*, 3039–51.
- [87] T. P. Padera, B. R. Stoll, J. B. Tooredman, D. Capen, E. di Tomaso, R. K. Jain, *Nature* **2004**, *427*, 695–695.
- [88] C. Frantz, K. M. Stewart, V. M. Weaver, *J. Cell Sci.* **2010**, *123*, 4195–4200.
- [89] M. Suzuki, K. Hori, I. Abe, S. Saito, H. Sato, *J. Natl. Cancer Inst.* **1981**, *67*, 663–9.
- [90] A. Nagamitsu, K. Greish, H. Maeda, *Jpn. J. Clin. Oncol.* **2009**, *39*, 756–766.

-
- [91] R. Ansiaux, *Clin. Cancer Res.* **2006**, *12*, 1276–1283.
- [92] C. S. Wilcox, A. Pearlman, *Pharmacol. Rev.* **2008**, *60*, 418–469.
- [93] T. Zong, L. Mei, H. Gao, W. Cai, P. Zhu, K. Shi, J. Chen, Y. Wang, F. Gao, Q. He, *Mol. Pharm.* **2014**, *11*, 2346–2357.
- [94] S. Zununi Vahed, R. Salehi, S. Davaran, S. Sharifi, *Mater. Sci. Eng. C* **2017**, *71*, 1327–1341.
- [95] N. S. Khelfallah, G. Decher, P. J. Mésini, *Biointerphases* **2007**, *2*, 131–135.
- [96] D. Steinhilber, T. Rossow, S. Wedepohl, F. Paulus, S. Seiffert, R. Haag, *Angew. Chem. Int. Ed.* **2013**, *52*, 13538–13543.
- [97] C. S. Ki, H. Shih, C.-C. Lin, *Polymer (Guildf)*. **2013**, *54*, 2115–2122.
- [98] J. Min, H. Moon, H. J. Yang, H.-H. Shin, S. Y. Hong, S. Kang, *Macromol. Biosci.* **2014**, *14*, 557–64.
- [99] P. B. Patil, V. C. Karade, P. P. Waifalkar, P. S. Patil, in *2017 IEEE Int. Magn. Conf.*, IEEE, **2017**, pp. 1–2.
- [100] Y. Zhang, L. Li, F. Tang, J. Ren, *J. Nanosci. Nanotechnol.* **2006**, *6*, 3210–3214.
- [101] J. Y. Jang, H. T. T. Duong, S. M. Lee, H. J. Kim, Y.-J. Ko, J. H. Jeong, D. S. Lee, T. Thambi, S. U. Son, *Chem. Commun.* **2018**, *54*, 3652–3655.
- [102] M. Xing, F. Yan, S. Yu, P. Shen, *PLoS One* **2015**, *10*, e0133569.
- [103] G. Batist, G. Ramakrishnan, C. S. Rao, A. Chandrasekharan, J. Gutheil, T. Guthrie, P. Shah, A. Khojasteh, M. K. Nair, K. Hoelzer, et al., *J. Clin. Oncol.* **2001**, *19*, 1444–1454.
- [104] Q.-D. Hu, H. Fan, Y. Ping, W.-Q. Liang, G.-P. Tang, J. Li, *Chem. Commun.* **2011**, *47*, 5572.
- [105] J. A. MacKay, M. Chen, J. R. McDaniel, W. Liu, A. J. Simnick, A. Chilkoti, *Nat. Mater.* **2009**, *8*, 993–9.
- [106] S. Ganta, H. Devalapally, A. Shahiwala, M. Amiji, *J. Control. Release* **2008**, *126*, 187–204.

- [107] C. R. Becer, S. Hahn, M. W. M. Fijten, H. M. L. Thijs, R. Hoogenboom, U. S. Schubert, *J. Polym. Sci. A* **2008**, *46*, 7138–7147.
- [108] G. Zhou, L. Li, J. Xing, S. Jalde, Y. Li, J. Cai, J. Chen, P. Liu, N. Gu, M. Ji, *Colloids Surfaces B Biointerfaces* **2016**, *148*, 518–525.
- [109] J. Yang, A. Bahreman, G. Daudey, J. Bussmann, R. C. L. Olsthoorn, A. Kros, *ACS Cent. Sci.* **2016**, *2*, 621–630.
- [110] H. Li, X. Yang, Z. Zhou, K. Wang, C. Li, H. Qiao, D. Oupicky, M. Sun, *J. Control. Release* **2017**, *261*, 126–137.
- [111] P. Saint-Cricq, S. Deshayes, J. I. Zink, A. M. Kasko, *Nanoscale* **2015**, *7*, 13168–13172.
- [112] S.-Y. Li, L.-H. Liu, H.-Z. Jia, W.-X. Qiu, L. Rong, H. Cheng, X.-Z. Zhang, *Chem. Commun.* **2014**, *50*, 11852–11855.
- [113] R. Patil, J. Portilla-Arias, H. Ding, B. Konda, A. Rekechenetskiy, S. Inoue, K. L. Black, E. Holler, J. Y. Ljubimova, *Int. J. Mol. Sci.* **2012**, *13*, 11681–11693.
- [114] M. A. Sowers, J. R. McCombs, Y. Wang, J. T. Paletta, S. W. Morton, E. C. Dreaden, M. D. Boska, M. F. Ottaviani, P. T. Hammond, A. Rajca, et al., *Nat. Commun.* **2014**, *5*, 5460.
- [115] T. Yoshitomi, Y. Ozaki, S. Thangavel, Y. Nagasaki, *J. Control. Release* **2013**, *172*, 137–143.
- [116] T. Yildirim, A. Traeger, E. Preussger, S. Stumpf, C. Fritzsche, S. Hoepfener, S. Schubert, U. S. Schubert, *Macromolecules* **2016**, *49*, 3856–3868.
- [117] S. J. Sonawane, R. S. Kalhapure, T. Govender, *Eur. J. Pharm. Sci.* **2017**, *99*, 45–65.
- [118] X. Su, I. Arahamian, *Chem. Soc. Rev.* **2014**, *43*, 1963.
- [119] C. Hatzis, P. L. Bedard, N. J. Birkbak, A. H. Beck, H. J. W. L. Aerts, D. F. Stern, L. Shi, R. Clarke, J. Quackenbush, B. Haibe-Kains, *Cancer Res.* **2014**, *74*, 4016–4023.
- [120] S. A. Langhans, *Front. Pharmacol.* **2018**, *9*, 6.

-
- [121] R. Edmondson, J. J. Broglie, A. F. Adcock, L. Yang, *Assay Drug Dev. Technol.* **2014**, *12*, 207–218.
- [122] H. D. H. Showalter, W. A. Denny, *Tuberculosis* **2008**, *88*, 3–17.
- [123] F. Barré-Sinoussi, X. Montagutelli, *Futur. Sci. OA* **2015**, *1*, 63.
- [124] T. Höfer, I. Gerner, U. Gundert-Remy, M. Liebsch, A. Schulte, H. Spielmann, R. Vogel, K. Wettig, *Arch. Toxicol.* **2004**, *78*, 549–564.
- [125] J. Tannenbaum, B. T. Bennett, *J. Am. Assoc. Lab. Anim. Sci.* **2015**, *54*, 120–32.
- [126] A. L. Rasmussen, A. Okumura, M. T. Ferris, R. Green, F. Feldmann, S. M. Kelly, D. P. Scott, D. Safronetz, E. Haddock, R. LaCasse, et al., *Science* **2014**, *346*, 987–991.
- [127] A.-S. Liovat, B. Jacquelin, M. J. Ploquin, F. Barré-Sinoussi, M. C. Müller-Trutwin, *Curr. HIV Res.* **2009**, *7*, 39–50.
- [128] M. A. Friese, *Brain* **2006**, *129*, 1940–1952.
- [129] C. Ergorul, L. A. Levin, *Curr. Opin. Pharmacol.* **2013**, *13*, 108–114.
- [130] X. Gong, C. Lin, J. Cheng, J. Su, H. Zhao, T. Liu, X. Wen, P. Zhao, *PLoS One* **2015**, *10*, 1–18.
- [131] Y. Fang, R. M. Eglen, *SLAS Discov. Adv. Life Sci. R&D* **2017**, *22*, 456–472.
- [132] F. Piccinini, *Comput. Methods Programs Biomed.* **2015**, *119*, 43–52.
- [133] M. Zanoni, F. Piccinini, C. Arienti, A. Zamagni, S. Santi, R. Polico, A. Bevilacqua, A. Tesei, *Sci. Rep.* **2016**, *6*, 19103.
- [134] F. Sambale, A. Lavrentieva, F. Stahl, C. Blume, M. Stiesch, C. Kasper, D. Bahnemann, T. Scheper, *J. Biotechnol.* **2015**, *205*, 120–129.
- [135] D. L. Priwitaningrum, J. B. G. Blondé, A. Sridhar, J. van Baarlen, W. E. Hennink, G. Storm, S. Le Gac, J. Prakash, *J. Control. Release* **2016**, *244*, 257–268.
- [136] S. M. Sagnella, H. Duong, A. MacMillan, C. Boyer, R. Whan, J. A. McCarroll, T. P. Davis, M. Kavallaris, *Biomacromolecules* **2014**, *15*, 262–275.
- [137] Y. A. Luqmani, *Med. Princ. Pract.* **2005**, *14*, 35–48.

- [138] K. Stock, M. F. Estrada, S. Vidic, K. Gjerde, A. Rudisch, V. E. Santo, M. Barbier, S. Blom, S. C. Arundkar, I. Selvam, et al., *Sci. Rep.* **2016**, *6*, 1–15.
- [139] V. Kappings, C. Grün, D. Ivannikov, I. Hebeiss, S. Kattge, I. Wendland, B. E. Rapp, M. Hettel, O. Deutschmann, U. Schepers, *Adv. Mater. Technol.* **2018**, *3*, 1700246.
- [140] K.-A. Hansen, J. Nerkar, K. Thomas, S. E. Bottle, A. P. O'Mullane, P. C. Talbot, J. P. Blinco, *ACS Appl. Mater. Interfaces* **2018**, *10*, 7982–7988.
- [141] H. V. T. Nguyen, Q. Chen, J. T. Paletta, P. Harvey, Y. Jiang, H. Zhang, M. D. Boska, M. F. Ottaviani, A. Jasanoff, A. Rajca, et al., *ACS Cent. Sci.* **2017**, *3*, 800–811.
- [142] P. Kuppusamy, M. Chzhan, K. Vij, M. Shteynbuk, D. J. Lefer, E. Giannella, J. L. Zweier, *Proc. Natl. Acad. Sci. U. S. A.* **1994**, *91*, 3388–92.
- [143] O. H. Griffith, A. S. Waggoner, *Acc. Chem. Res.* **1969**, *2*, 17–24.
- [144] D. A. Chernova, A. K. Vorobiev, *J. Polym. Sci. B* **2009**, *47*, 563–575.
- [145] M. E. Brik, H. Remita, M. O. Delcourt, *J. Chem. Soc. Chem. Commun.* **1991**, 24–25.
- [146] J. P. Blinco, K. E. Fairfull-Smith, B. J. Morrow, S. E. Bottle, *Aust. J. Chem.* **2011**, *64*, 373.
- [147] J. P. Allen, M. C. Pfrunder, J. C. McMurtrie, S. E. Bottle, J. P. Blinco, K. E. Fairfull-Smith, *European J. Org. Chem.* **2017**, 2017, 476–483.
- [148] Z. Jia, Q. Fu, J. Huang, *Macromolecules* **2006**, *39*, 5190–5193.
- [149] S. E. Bottle, U. Chand, A. S. Micallef, *Chem. Lett.* **1997**, *26*, 857–858.
- [150] J. T. Paletta, M. Pink, B. Foley, S. Rajca, A. Rajca, *Org. Lett.* **2012**, *14*, 5322–5325.
- [151] D. S. Weiss, *J. Photochem.* **1976**, *6*, 301–304.
- [152] A. R. Watkins, *Chem. Phys. Lett.* **1974**, *29*, 526–528.
- [153] O. L. J. Gijzeman, F. Kaufman, G. Porter, *J. Chem. Soc. Faraday Trans.* **1973**, *69*, 727.

-
- [154] S. a. Green, D. J. Simpson, G. Zhou, P. S. Ho, N. V. Blough, *J. Am. Chem. Soc.* **1990**, *112*, 7337–7346.
- [155] C. Aliaga, P. Fuentealba, M. C. Rezende, C. Cárdenas, *Chem. Phys. Lett.* **2014**, *593*, 89–92.
- [156] D. J. Keddie, *The Synthesis of Profluorescent Nitroxide Probes*, QUT ePrints **2008**.
- [157] B. K. Hughes, W. a Braunecker, A. J. Ferguson, T. W. Kemper, R. E. Larsen, T. Gennett, *J. Phys. Chem. B* **2014**, *118*, 12541–8.
- [158] E. M. Simpson, Z. D. Ristovski, S. E. Bottle, K. E. Fairfull-Smith, J. P. Blinco, *Polym. Chem.* **2015**, *6*, 2962–2969.
- [159] K. Hansen, K. E. Fairfull-smith, S. E. Bottle, J. P. Blinco, *Macromol. Chem. Phys.* **2016**, *217*, 2330–2340.
- [160] A. De Mel, F. Murad, A. M. Seifalian, *Chem. Rev.* **2011**, *111*, 5742–5767.
- [161] V. Liu, P. Huang, *Cardiovasc. Res.* **2007**, *109*, 4580–95.
- [162] J. E. Freedman, R. Sauter, E. M. Battinelli, K. Ault, C. Knowles, P. L. Huang, J. Loscalzo, *Circ. Res.* **1999**, *84*, 1416–21.
- [163] U. C. Garg, A. Hassid, *J. Clin. Invest.* **1989**, *83*, 1774–1777.
- [164] J. N. Sharma, A. Al-Omran, S. S. Parvathy, *Inflammopharmacology* **2007**, *15*, 252–259.
- [165] J. Aliancy, W. D. Stamer, B. Wirostko, *Ophthalmol. Ther.* **2017**, *6*, 221–232.
- [166] M. Lewandowski, K. Gwozdziński, *Int. J. Mol. Sci.* **2017**, *18*, DOI 10.3390/ijms18112490.
- [167] S. M. Hahn, A. M. Deluca, D. Coffin, C. M. Krishna, J. B. Mitchell, *Int. J. Radiat. Oncol. Biol. Phys.* **1998**, *42*, 839–842.
- [168] K. Matsumoto, M. C. Krishna, J. B. Mitchell, *J Pharmacol Exp Ther* **2004**, *310*, 1076–1083.
- [169] S. Reuters, S. C. Gupta, M. M. Charturvedi, B. B. Aggarwal, *Free Radic. Biol. Med.* **2010**, *49*, 1603–1616.

- [170] S. Tabaczar, A. Koceva-Chyla, J. Czepas, A. Pieniazek, J. Piasecka-Zelga, K. Gwozdziński, *J. Physiol. Pharmacol.* **2012**, *63*, 153–163.
- [171] J. S. Dickey, Y. Gonzalez, B. Aryal, S. Mog, A. J. Nakamura, C. E. Redon, U. Baxa, E. Rosen, G. Cheng, J. Zielonka, et al., *PLoS One* **2013**, *8*, e70575.
- [172] C. Ugi, I. Meyr, R.; Fetzer, U.; Steinbrückner, *Angew. Chemie* **1959**, *71*, 373–388.
- [173] M. A. Mironov, *Russ. J. Gen. Chem.* **2010**, *80*, 2628–2646.
- [174] A. Dömling, *Comb. Chem. High Throughput Screen.* **1998**, *1*, 1–22.
- [175] J. S. P. Schwarz, *J. Org. Chem.* **1972**, *37*, 2906–2908.
- [176] O. Mumm, *Ber. Dtsch. Chem. Ges.* **1910**, *43*, 886–893.
- [177] N. Chéron, R. Ramozzi, L. El Kaïm, L. Grimaud, P. Fleurat-Lessard, *J. Org. Chem.* **2012**, *77*, 1361–1366.
- [178] J.-C. Bradley, K. Baig Mirza, T. Osborne, A. Williams, K. Owens, *J. Vis. Exp.* **2008**, e942.
- [179] J. Lei, J.-P. Meng, D.-Y. Tang, B. Frett, Z.-Z. Chen, Z.-G. Xu, *Mol. Divers.* **2018**, *22*, 503–516.
- [180] A. Llevot, A. C. Boukis, S. Oelmann, K. Wetzels, M. A. R. Meier, *Top. Curr. Chem.* **2017**, *375*, 66.
- [181] A. C. Boukis, K. Reiter, M. Frölich, D. Hofheinz, M. A. R. Meier, *Nat. Commun.* **2018**, *9*, 1–10.
- [182] J. M. Saya, B. Oppelaar, R. C. Cioc, G. van der Heijden, C. M. L. Vande Velde, R. V. A. Orru, E. Ruijter, *Chem. Commun.* **2016**, *52*, 12482–12485.
- [183] T. Luo, C. Loira-Pastoriza, H. P. Patil, B. Ucakar, G. G. Muccioli, C. Bosquillon, R. Vanbever, *J. Control. Release* **2016**, *239*, 62–71.
- [184] A. K. Pearce, B. E. Rolfe, P. J. Russell, B. W.-C. Tse, A. K. Whittaker, A. V. Fuchs, K. J. Thurecht, *Polym. Chem.* **2014**, *5*, 6932–6942.
- [185] Y. Wu, S. Ihme, M. Feuring-Buske, S. L. Kuan, K. Eisele, M. Lamla, Y. Wang, C. Buske, T. Weil, *Adv. Healthc. Mater.* **2013**, *2*, 884–894.

- [186] S. L. Kuan, S. Fischer, S. Hafner, T. Wang, T. Syrovets, W. Liu, Y. Tokura, D. Y. W. Ng, A. Riegger, C. Förtsch, et al., *Adv. Sci.* **2018**, *5*, 1701036.
- [187] Y. Bae, N. Nishiyama, S. Fukushima, H. Koyama, M. Yasuhiro, K. Kataoka, *Bioconjug. Chem.* **2005**, *16*, 122–130.
- [188] P. Chytil, T. Etrych, Č. Koňák, M. Šírová, T. Mrkvan, B. Říhová, K. Ulbrich, *J. Control. Release* **2006**, *115*, 26–36.
- [189] J. M. Priegue, D. N. Crisan, J. Martínez-Costas, J. R. Granja, F. Fernandez-Trillo, J. Montenegro, *Angew. Chem. Int. Ed.* **2016**, *55*, 7492–7495.
- [190] L. Y. Qiu, Y. H. Bae, *Pharm. Res.* **2006**, *23*, 1–30.
- [191] H. R. Ihre, O. L. Padilla De Jesús, F. C. Szoka, J. M. J. Fréchet, *Bioconjug. Chem.* **2002**, *13*, 443–452.
- [192] Jitendra, P. K. Sharma, S. Bansal, A. Banik, *Indian J. Pharm. Sci.* **2011**, *73*, 367–75.
- [193] Q. Chen, D. A. Sowa, J. Cai, R. Gabathuler, *Synth. Commun.* **2003**, *33*, 2401–2421.
- [194] G. Moad, E. Rizzardo, S. H. Thang, *Aust. J. Chem.* **2009**, *62*, 1402.
- [195] G. Moad, E. Rizzardo, S. H. Thang, *Chem. Asian J.* **2013**, *8*, 1634–1644.
- [196] B. Zhang, X. Yan, P. Alcouffe, A. Charlot, E. Fleury, J. Bernard, *ACS Macro Lett.* **2015**, *4*, 1008–1011.
- [197] Y. Tian, K. C. Tam, T. A. Hatton, L. Bromberg, **n.d.**
- [198] Q. Zhang, M. Fu, C. Wang, J. Wang, S. Zhu, *Polym. Chem.* **2017**, *8*, 5469–5473.
- [199] M. M. Cecchini, J. Steinkoenig, S. Reale, L. Barner, J. Yuan, A. S. Goldmann, F. De Angelis, C. Barner-Kowollik, *Chem. Sci.* **2016**, *7*, 4912–4921.
- [200] J. Steinkoenig, M. M. Cecchini, A. S. Goldmann, S. Reale, F. De Angelis, C. Barner-Kowollik, *Macromol. Rapid Commun.* **2016**, *37*, 1662–1666.
- [201] H. He, M. Zhong, B. Adzima, D. Luebke, H. Nulwala, K. Matyjaszewski, *J. Am. Chem. Soc.* **2013**, *135*, 4227–4230.

- [202] S. Han, M. Hagiwara, T. Ishizone, *Macromolecules* **2003**, *36*, 8312–8319.
- [203] K. Ponnusamy, R. P. Babu, R. Dhamodharan, *J. Polym. Sci. A* **2013**, *51*, 1066–1078.
- [204] N. S. H. Motlagh, P. Parvin, F. Ghasemi, F. Atyabi, *Biomed. Opt. Express* **2016**, *7*, 2400.
- [205] T. Mrkvan, M. Sirova, T. Etrych, P. Chytil, J. Strohalm, D. Plocova, K. Ulbrich, B. Rihova, *J. Control. Release* **2005**, *110*, 119–129.
- [206] X. Zhang, Y. Lin, R. J. Gillies, *J. Nucl. Med.* **2010**, *51*, 1167–1170.
- [207] Z. Wang, G. Ma, J. Zhang, Z. Yuan, L. Wang, M. Bernards, S. Chen, *Biomaterials* **2015**, *62*, 116–127.
- [208] R. T. Cummings, G. A. Krafft, *Tetrahedron Lett.* **1988**, *29*, 65–68.
- [209] H. Nam, J. E. Kwon, M. W. Choi, J. Seo, S. Shin, S. Kim, S. Y. Park, *ACS Sensors* **2016**, *1*, 392–398.
- [210] S. K. Chattopadhyay, P. K. Das, G. L. Hug, *J. Am. Chem. Soc.* **1983**, *105*, 6205–6210.
- [211] M. Eing, B. Olshausen, K. E. Fairfull-Smith, U. Schepers, C. Barner-Kowollik, J. P. Blinco, *Polym. Chem.* **2018**, *9*, 499–505.
- [212] J. Hoche, H.-C. Schmitt, A. Humeniuk, I. Fischer, R. Mitrić, M. I. S. Röhr, *Phys. Chem. Chem. Phys.* **2017**, 25002–25015.
- [213] K. Schug, H. M. McNair, *J. Sep. Sci.* **2002**, *25*, 759–766.
- [214] K. Schug, H. M. McNair, *J. Chromatogr. A* **2003**, *985*, 531–9.
- [215] J. Hermans, S. Ongay, V. Markov, R. Bischoff, *Anal. Chem.* **2017**, *89*, 9159–9166.
- [216] P. Larkin, *Infrared and Raman Spectroscopy*, Elsevier, **2011**.
- [217] M. E. Jacox, *J. Phys. Chem. Ref. Data* **2003**, *32*, 1–441.
- [218] D. A. Reid, S. E. Bottle, *Chem. Commun.* **1998**, *4*, 1907–1908.
- [219] T. Hagendorn, S. Bräse, *European J. Org. Chem.* **2014**, *2014*, 1280–1286.
- [220] B. Olshausen, *Shining Bright: Fluorescent Tools for Drug Discovery, Development*

- and Delivery*, Cuvillier Verlag, Göttingen, **2018**.
- [221] G. Moad, E. Rizzardo, S. H. Thang, *Aust. J. Chem.* **2005**, *58*, 379.
- [222] C. Barner-Kowollik, S. Perrier, *J. Polym. Sci. A Polym. Chem.* **2008**, *46*, 5715–5723.
- [223] E. P. Maziarz, G. A. Baker, S. A. Lorenz, T. D. Wood, *J. Am. Soc. Mass Spectrom.* **1999**, *10*, 1298–1304.
- [224] Y. Shiraishi, Y. Tokitoh, T. Hirai, *Org. Lett.* **2006**, *8*, 3841–3844.
- [225] S. Rondinini, *Anal. Bioanal. Chem.* **2002**, *374*, 813–816.
- [226] A. Dembska, P. Rzepecka, B. Juskowiak, *Chemosensors* **2015**, *3*, 211–223.
- [227] D. C. Dong, M. A. Winnik, *Can. J. Chem.* **1984**, *62*, 2560–2565.
- [228] W. Yan, D. Ammon, J. Gardella, E. Maziarz, A. Hawkridge, G. Grobe, T. Wood, *Eur. J. Mass Spectrom.* **1998**, *4*, 467.
- [229] A. Savitzky, M. J. E. Golay, *Anal. Chem.* **1964**, *36*, 1627–1639.
- [230] J. Andrew MacKay, M. Chen, J. R. McDaniel, W. Liu, A. J. Simnick, A. Chilkoti, *Nat. Mater.* **2009**, *8*, 993–999.
- [231] E. C. Costa, A. F. Moreira, D. de Melo-Diogo, V. M. Gaspar, M. P. Carvalho, I. J. Correia, *Biotechnol. Adv.* **2016**, *34*, 1427–1441.
- [232] A. Knight, *Animals* **2012**, *2*, 85–92.
- [233] F. Netzlaff, C. M. Lehr, P. W. Wertz, U. F. Schaefer, *Eur. J. Pharm. Biopharm.* **2005**, *60*, 167–178.
- [234] C. F. M. Hendriksen, *ILAR J.* **2002**, *43 Suppl*, S43–8.
- [235] T. D. Pollard, J. A. Cooper, *Science.* **2009**, *326*, 1208–1212.
- [236] J. Huisken, J. Swoger, F. Del Bene, J. Wittbrodt, E. H. K. Stelzer, J. Huisken, J. Swoger, F. Del Bene, J. Wittbrodt, E. H. K. Stelzer, **2014**, *1007*, 13–16.
- [237] D. J. Kerr, T. E. Wheldon, S. Hydns, S. B. Kaye, *Xenobiotica* **1988**, *18*, 641–648.
- [238] S. Beigrezaei, H. Nasri, *Ann. Res. Antioxidants* **2017**, *2*, e1.

- [239] A. Schneider, M. Simons, *Cell Tissue Res.* **2013**, 352, 33–47.
- [240] Y. Iguchi, L. Eid, M. Parent, G. Soucy, C. Bareil, Y. Riku, K. Kawai, S. Takagi, M. Yoshida, M. Katsuno, et al., *Brain* **2016**, 139, 3187–3201.
- [241] L. Pascucci, V. Coccè, A. Bonomi, D. Ami, P. Ceccarelli, E. Ciusani, L. Viganò, A. Locatelli, F. Sisto, S. M. Doglia, et al., *J. Control. Release* **2014**, 192, 262–270.
- [242] A. S. Michaels, S. K. Chandrasekaran, J. E. Shaw, *AIChE J.* **1975**, 21, 985–996.
- [243] Y. Guo, L. Wang, P. Lv, P. Zhang, *Oncol. Lett.* **2015**, 9, 1065–1072.
- [244] X. Wang, H. Tang, C. Wang, J. Zhang, W. Wu, X. Jiang, *Theranostics* **2016**, 6, 1378–1392.
- [245] T. Seidal, A. J. Balaton, H. Battifora, *Am. J. Surg. Pathol.* **2001**, 25, 1204–1207.
- [246] A. Korzynska, L. Roszkowiak, C. Lopez, R. Bosch, L. Witkowski, M. Lejeune, *Diagn. Pathol.* **2013**, 8, 757.
- [247] M. K. Kim, *J. Opt. Soc. Korea* **2010**, 14, 368–375.
- [248] C. Ash, M. Dubec, K. Donne, T. Bashford, *Lasers Med. Sci.* **2017**, 32, 1909–1918.
- [249] M. Clement, G. Daniel, M. Trelles, *J. Cosmet. Laser Ther.* **2005**, 7, 177–189.
- [250] J. Frangioni, *Curr. Opin. Chem. Biol.* **2003**, 7, 626–634.
- [251] H. C. Shi, Y. Li, *J. Mol. Catal. A Chem.* **2007**, 271, 32–41.
- [252] V. C. Jayawardena, K. E. Fairfull-Smith, S. E. Bottle, *Aust. J. Chem.* **2013**, 66, 619–625.
- [253] G. B. Payne, P. H. Williams, *J. Org. Chem.* **1959**, 24, 54–55.
- [254] V. T. Huynh, J. Y. Quek, P. L. de Souza, M. H. Stenzel, *Biomacromolecules* **2012**, 13, 1010–1023.
- [255] P. Klan, T. Solomek, C. G. Bochet, R. Givens, M. Rubina, V. Popik, A. Kostikov, J. Wirz, *Chem. Rev.* **2012**, 113, 119–191.
- [256] F. B. Peters, A. Brock, J. Wang, P. G. Schultz, *Chem. Biol.* **2009**, 16, 148–152.
- [257] B. T. Tuten, J. P. Menzel, K. Pahnke, J. P. Blinco, C. Barner-Kowollik, *Chem. Commun.* **2017**, 53, 4501–4504.

- [258] E. Vedejs, T. H. Eberlein, R. G. Wilde, *J. Org. Chem.* **1988**, *53*, 2220–2226.
- [259] M. Eing, B. Tuten, J. P. Blinco, C. Barner-Kowollik, *Chem. Eur. J.* **2018**, 1–5.
- [260] T. S. Fischer, S. Spann, Q. An, B. Luy, M. Tsotsalas, J. P. Blinco, H. Mutlu, C. Barner-Kowollik, *Chem. Sci.* **2018**, *9*, 4696–4702.
- [261] V. Ntziachristos, D. Razansky, *Chem. Rev.* **2010**, *110*, 2783–2794.
- [262] S. Farhangi, H. Weiss, J. Duhamel, *Macromolecules* **2013**, *46*, 9738–9747.
- [263] C.-J. Carling, F. Nourmohammadian, J.-C. Boyer, N. R. Branda, *Angew. Chem. Int. Ed.* **2010**, *49*, 3782–3785.
- [264] G. R. Fulmer, A. J. M. Miller, N. H. Sherden, H. E. Gottlieb, A. Nudelman, B. M. Stoltz, J. E. Bercaw, K. I. Goldberg, *Organometallics* **2010**, *29*, 2176–2179.
- [265] K. G. Meyer, *Synlett* **2004**, 2355–2356.
- [266] A. J. Inglis, P. Pierrat, T. Muller, S. Bräse, C. Barner-Kowollik, *Soft Matter* **2010**, *6*, 82–84.
- [267] F. Hua, X. Jiang, D. Li, B. Zhao, *J. Polym. Sci. A* **2006**, *44*, 2454–2467.

List of Figures

- Figure 2.1:** Effect of SEC-MS hyphenation. Shown are the same RAFT poly-TEGMA samples in direct injection and SEC-ESI-MS. SEC-hyphenation effectively allows for the measurement of a near-monodisperse slice of the analyte. This enables the identification of singled out isotopic patterns for each species of macromolecule present in the mixture.....16
- Figure 2.2:** Example of a complicated copolymer SEC-ESI-MS spectrum. Overlapping signals from different chain compositions can inherently overcomplicate spectra.17
- Figure 2.3:** Schematic representation (top) and CLSM fluorescence images (bottom) obtained in confocal imaging of 3D cell culture. Single confocal images (Z-slices of 5-10 μm thickness) are recorded across the full depth of a sample. Slices can subsequently be concatenated into Z-stacks to yield either 2D or 3D representations of the imaged sample.....41
- Figure 3.1:** ESI-MS spectrum of **3-9**, showing almost solely product and coulomb dimers of **3-9**. Different reduction stages of **3-9** can be found as coulomb dimers, attributed to ionisation artefacts.....53
- Figure 3.2:** $^1\text{H-NMR}$ spectrum and low-molecular-weight SEC-MS slice of **SAP-0**. Polymer composition was determined by resonances c and h. The zoom shows the three resonances assigned to the phenyl moiety of the Z-group, used for determination of molecular weight. Right: The mass spectrum shows a zoom of one repeating unit at a chain-length of 26 to 27. Indices in the signal labels denominate the number of GMA units per total chain length. Smaller, unmarked signals could partially be assigned to salt/solvent adducts, yet overlays of patterns complicate unambiguous assignment (**Figure 2.2**). The inset shows the overlay of a comparatively undisturbed isotopic pattern and the simulation of the assigned chain composition, demonstrating the precision of the method.....56
- Figure 3.3:** Left: $^1\text{H-NMR}$ spectrum of **SAP-1** after photo protection. The zoom shows the shift of proton resonances i, j, and k towards the low-field as a result of the HDA-reaction with the photocaged diene. Right: Zoom into one repeating unit in the SEC-MS spectrum of **SAP-1**. No signals correlated to the unprotected form of **SAP-0** were found, indicating quantitative conversion. Indices in the signal labels indicate the count of GMA units per chain length. The inset shows the overlay of a comparatively undisturbed isotopic pattern and the simulation of the assigned chain composition.57
- Figure 3.4:** GPC-elugrams of **SAP-0** through **SAP-2**. No significant shift in molecular weight was observable. The decrease in dispersity upon photo protection (**SAP-1**) was attributed to repeated purification steps, the subsequent line-broadening of **SAP-2** most likely stems from the newly

- formed hydroxyl-groups, which slightly alter the both level of hydrophilicity and possible interaction with the column material.....58
- Figure 3.5:** Left: $^1\text{H-NMR}$ spectrum of **SAP-2** after GMA-opening by NaN_3 . The zoom shows the shift of the resonance of protons f, g, and h upfield, now coalescing with TEG signals. Right: Zoom into one repeating unit in the SEC-MS spectrum of **SAP-2**. The spectrum shows excellent levels of conversion with no detectable precursor polymer left. The signals were unambiguously assigned to chains bearing the HDA end group from the previous step. Indices indicate the count of GMA units per chain length. The inset shows the overlay of an undisturbed isotopic pattern and the simulation of the assigned chain composition.59
- Figure 3.6:** ATR- FTIR transmission spectrum of **SAP-1** and **SAP-2** to investigate the azidation reaction. A clear absorption band at 2110 cm^{-1} becomes visible upon ring-opening of GMA *via* sodium azide.^[216] The signal is characteristic for the stretching vibration of azides and was further used to monitor azide presence over the following steps.....59
- Figure 3.7:** $^1\text{H-NMR}$ spectrum of **SAP-3.1**. The incorporation of succinic acid was followed by the emerging resonances k and l.....61
- Figure 3.8:** IR spectra of transformations attempted on the **SAP-2** platform towards **SAP-3**. Upon coupling of succinic anhydride, the acid becomes visible as a very broad signal spanning $3500\text{-}2500\text{ cm}^{-1}$. Coupling of the acid leaves the azide signal at 2100 cm^{-1} unaffected. Clicking before coupling of the anhydride (**SAP-2** SPAAC) led to complete disappearance of the azide band. Clicking after coupling of succinic acid shows only slight reduction of the azide signal.62
- Figure 3.9:** ESI-MS spectrum of PEG- N_3 and CuAAC products from the control reaction. One repeating unit of the PEG chain is shown for clarity. No azide -terminated PEG can be detected in the product (top, red), suggesting full conversion.63
- Figure 3.10:** GPC of **SAP-2** click product with cyclooctyne-fluorescein. A clear alignment of RI and absorption detector signal at $\lambda_{\text{abs}} = 360\text{ nm}$ are clearly visible, indicating attachment of fluorescein to the polymer.....64
- Figure 3.11:** Left: $^1\text{H-NMR}$ -Spectrum of **PC-0**. Monomer incorporation was determined by resonances a, d and e. Right: SEC-MS spectrum, positive mode. The assigned peaks represent the exact structure on the left with numbers representing the measured TEGMA-bHMA-TMPMA ratio. Assignments mark the monoisotopic first peak of every isotopic pattern. Assignments are listed in the **Appendix, Table A 8.7**.....68
- Figure 3.12:** DOSY spectrum of **PC-0** in CDCl_3 . The spectrum shows all relevant polymer resonances correlated to the same diffusion coefficient close to $10^{-6}\text{ m}^2\cdot\text{s}^{-1}$. Resonances correlated with higher diffusion coefficients were assigned to water and CHCl_3 from the NMR solvent. The inset on top shows the spectrum at diffusion coefficient of $1.17 \cdot 10^6\text{ m}^2\cdot\text{s}^{-1}$, presenting all resonances found in the 1D-spectrum measured before (refer to **Figure 3.11**). The trace on the right shows a histogram across the full 2D matrix, clearly indicating a narrow distribution along the diffusion coefficients.....69

- Figure 3.13:** $^1\text{H-NMR}$ spectra of **PC-0** and **PC-2**, before and after boc-deprotection. The inset shows a zoom of the low-field area from 0.5-2.5 ppm. The disappearance of the highlighted resonance at 1.4 ppm indicates the complete removal of boc groups from the polymer backbone. All other resonances were unaffected, confirming the structural integrity of the polymer.71
- Figure 3.14:** ESR spectra of the same $1 \text{ mg}\cdot\text{mL}^{-1}$ solution of **PC-1** and **PC-2** in THF before and after boc-removal. The left spectrum shows the polymer directly after oxidation *via* *m*CPBA. On the right, a slight decrease in double-integral area is visible, yet only to a minor extent. Radical densities were determined to be 99% (**PC-1**) and 89% (**PC-2**) respectively.71
- Figure 3.15:** Comparison of RI and UV/-vis traces in GPC. Left: RI traces of polymers **PC-0** through **PC-3r**. Line shape and elution volumes are dominated by the chemical composition of the analytes rather than their actual molecular weight. RI traces thus predominantly served as a measure of orientation when evaluating fluorophore loading of the polymer. Right: UV/Vis-absorption of polymers **PC-0** through **PC-3r**. A strong increase of absorption is visible after loading with acetyl-pyrene (**PC-3**). Absorption visibly decreases after release (**PC-3r**), indicating removal of pyrene from the backbone.72
- Figure 3.16:** Pyrene release from a solution of **PC-3** in ACN, monitored by fluorescence spectroscopy. A strong increase in fluorescence can be observed upon acidification by the addition of $30 \mu\text{L}$ of TFA. Irradiation at $\lambda_{\text{ex}} = 360 \text{ nm}$. Increase in fluorescence slowed over time, with approximately 50% of all fluorescence recovery observed in the first 30 minutes.73
- Figure 3.17:** $^1\text{H-NMR}$ spectrum of **SSPC-0** in CDCl_3 , used for determination of composition. Resonances c, f, and g were utilised to calculate the ratio of incorporation for TEGMA, bHMA and TMPMA respectively. Reproduced from [211] with permission from the RSC.75
- Figure 3.18:** Direct comparison of **SSPC-0** and **SSPC-1** ESR spectra. A clear increase in ESR signal intensity, the triplet shape and the slight line-broadening, typical for polymer-bound nitroxides becomes visible upon oxidation. Double integration indicates quantitative conversion of TMPMA-sidechains. For numerical data refer to the **Appendix, Table A 8.8**. Reproduced from [211] with permission from the RSC.76
- Figure 3.19:** $^1\text{H-NMR}$ spectra comparison of **SSPC-0** and **SSPC-2** before and after boc-deprotection. The inset shows a zoom of the relevant chemical shift region from 2.5 - 0.5 ppm. The spectrum of **SSPC-2** clearly shows the disappearance of the highlighted boc-proton resonance at 1.4 ppm.77
- Figure 3.20:** Comparison of RI and UV/Vis absorption traces in the GPC. The left shows the RI traces of all synthetic intermediates leading to the release experiment of **SSPC-3**. Additionally, Dox·HCl was assessed as a reference to identify small molecular signals in the release experiment. The latter showcases released Dox present in the analyte. The right hand graph compares absorption at $\lambda = 500 \text{ nm}$ across all modification steps. A significant increase in absorption can be seen in **SSPC-3** upon drug-

- loading, confirming the molecular architecture of the nanodrug. A decrease in absorption becomes visible upon release, as well as a small-molecular signal, which coincides with the elution of Dox, confirming successful release. Reproduced from [211] with permission from the RSC.....78
- Figure 3.21:** $^1\text{H-NMR}$ spectra of **SSPC-0** as a reference and **SSPC-3** after drug loading. The presence of Dox can be monitored by its characteristic aromatic resonances j, k, and l. Absolute quantification from the NMR spectrum was not possible, as nitroxide-related line-broadening leads to issues with integration. The inset on the right shows a zoom to the utilised peaks. Reproduced from [211] with permission from the RSC.....79
- Figure 3.22:** Fluorescence spectra acquired over the course of seven days. Time increments were increased every 12 h in order to be able to capture the longest uninterrupted timeframe possible. Upon acidification, a strong increase in fluorescence is observed immediately, rapidly increasing 2-fold over the course of the first hours. Lighter reds indicate later time points. Adapted from [211] with permission from the RSC.80
- Figure 3.23:** Comparison of **SSPC-3** fluorescence before and after release, and free Dox in the same concentration. The graph on the right depicts the evolution of the total fluorescence integral over time in comparison to a solution at pH 7.4 (**Figure 3.22**). The inset shows a zoom of the first 8 h, indicating a strong burst release upon acidification. Reproduced from [211] with permission from the RSC.80
- Figure 3.24:** Left: UV/Vis absorption spectra employed quantify the release from 50 mg of **SSPC-3**. The spectra were smoothed in post-processing in order to obtain better resolution, as the low concentrations were just above the minimum level of detection. Right: Fluorescence measurements of the same solutions. A clearly stronger fluorescence signal can be detected for the acidic solution. Adapted from [211] with permission from the RSC.81
- Figure 3.25:** Cuvettes with **SSPC-3** before and after release. The visible orange fluorescence increases from barely visible to bright and easily detectable. Excitation was carried out with a green laser-pointer, visible on the right. Reproduced from [211] with permission from the RSC.....82
- Figure 3.26:** MTT viability assay results of HepG2 and SK-MEL-28 cells. A significantly elevated susceptibility of SK-MEL-28 to both free Dox and the **SSPC-3** assembly is evident in comparison to HepG2-cells. In both cell lines viability is decreased in the case of **SSPC-3** incubation. Up to the highest tested concentrations, no significant toxicity of the unloaded **SSPC-2** backbone can be detected.85
- Figure 3.27:** CLSM imaging of 2D HepG2 cell culture after 3h of incubation with **SSPC-3** or Dox·HCl. Arrows highlight sites of highly localised fluorescence outside the cell nuclei.85
- Figure 3.28:** CLSM imaging of 2D HepG2 cell culture after 24 h of incubation with **SSPC-3** or Dox·HCl. Arrows highlight sites of highly localised fluorescence outside the nuclei, indicating long-term storage of Dox in vesicles.....86

- Figure 3.29:** Bright-field confocal microscopy images of spheroids, grown for 7 d after 3 h of incubation with pure buffer. Differences in density and structure are clearly identifiable: HepG2 spheroids (left) form denser and more solid spheroids in direct comparison with identically treated SK-MEL-28 spheroids (right). Growth proceeds at a higher rate, yielding spheroids of 15-20% greater diameter on average. The darkened central area of both spheroids represent the necrotic core, where hypoxic conditions lead to a high prevalence of quiescent and necrotic cells.88
- Figure 3.30:** Results of MTT viability assays of HepG2 and SK-MEL-28 spheroids, used to investigate transferability of 2D-culture findings to 3D-culture experiments. Cells were incubated for 72 h in the shown concentrations (refer to **Section 7.3.6**) HepG2 spheroids (left) exhibit increased susceptibility to free Dox in comparison to **SSPC-3**. Viability appears uninfluenced by Dox concentration for both the free drug and **SSPC-3**. SK-MEL-28 spheroids exhibit overall higher susceptibility to both free Dox and **SSPC-3** in comparison to HepG2 spheroids, with increased susceptibility towards **SSPC-3**. Polymer backbone concentration does not appear to influence viability in any case.....89
- Figure 3.31:** Comparison of HepG2 spheroids, DIV 7, incubated with free Dox or **SSPC-3**. Scale bars are 100 μm . An increased level of Dox-fluorescence can be observed in the case of **SSPC-3** (right), indicating elevated uptake when the drug is conjugated to the nitroxide-bearing polymer.91
- Figure 3.32:** Penetration profiles of Dox·HCl and **SSPC-3** into HepG2 spheroids. The image on the right shows a spheroid incubated with 20 μM **SSPC-3** for size reference. Dashed grid lines in the graphs indicate cell layers. The profiles demonstrate strongly increased fluorescence in the case of **SSPC-3**. Fluorescence scales evenly with increasing concentration, indicating a predominantly diffusion-dependent uptake into both the spheroid and the cells.91
- Figure 3.33:** Comparison of SK-MEL-28 spheroids DIV 7, incubated with free Dox or **SSPC-3**. An increased level of Dox-fluorescence can be observed in the case of **SSPC-3** incubation, indicating elevated uptake when the drug is conjugated to the nitroxide-bearing polymer. Scale bars are 100 μm93
- Figure 3.34:** Penetration profiles of Dox·HCl and **SSPC-3** into SK-MEL-28 spheroids. The image on the right shows a spheroid incubated with 5 μM **SSPC-3** for reference. Dashed grid lines in the graphs indicate cell layers. The profiles exhibit strongly increased fluorescence in the case of **SSPC-3**. Additionally, penetration depth remains broader over a wider range of concentrations, as visible by a persistent, second mode in the distribution of ca. 20-40 μm penetration depth for the polymeric assembly. Fluorescence increase reaches a plateau at a concentration between 20-50 μM drug equivalent in the case of **SSPC-3**.93
- Figure 3.35:** Microscopy images of SK-MEL-28 spheroids in co-culture with NHDF cells in a GelMA matrix, DIV 7. Incubation with free Dox also yields fluorescent cells in the spheroid. Spheroids show a clear increase in fluorescence in comparison to NDHF cells when exposed to the **SSPC-3**

- carrier. Images of the buffer control and unloaded **SSPC-2** were used for background determination.95
- Figure 3.36:** Comparison between penetration-profiles obtained by averaging eight manually measured profiles across a single HepG2 spheroid (right) and the averaging of 720, distance-aligned profiles from the same image (left). As clearly visible, manual acquisition of such profiles retains a significant level of noise. Poor alignment of measurements before averaging leads to artefacts like multiple maxima and distribution broadening. Artefacts, measurement noise and measurement background can efficiently be eliminated by acquisition of a high number of profiles before averaging, as visible on the right. Original images are shown in the bottom row, with the left two pictures representing masking layers, utilised to obtain averaged profiles. Refer to **Section 7.3.7**, page 155 for a detailed description of the procedure.98
- Figure 3.37:** $^1\text{H-NMR}$ and fluorescence spectra of **DLPC-0**. As incorporation of Cy5 appeared to be too low to be visible in NMR, its incorporation was successfully confirmed by fluorescence measurement (right).....101
- Figure 3.38:** Example pictures of Cy5-degradation by the addition of *m*CPBA. Left: Photograph of **DLPC-0** solutions before and after oxidation *via m*CPBA. The solution exhibits the typical blue color of Cy5 before oxidation, which completely vanishes as soon as minute amounts of oxidizing agent are added. Right: The oxidised polyoymer after precipitation.102
- Figure 3.39:** $^1\text{H-NMR}$ spectra of Ugi-intermediate **ULC-0.1** and -product **ULC-0.2**. Imine formation is clearly visible, indicating quantitative loading by the boc-associated resonance h. Subsequent completion of the MCR reveals additional resonances, which could be attributed to g, yet the presence of nitroxides most likely hides most relevant signals.104
- Figure 3.40:** GPC elugrams of **ULC-0** – **ULC-0.2** before and after imine loading. A significant increase is visible upon imine loading. Molecular weights were determined from a PMMA calibration.....105
- Figure 4.1:** $^1\text{H-NMR}$ of **LRC-0** after precipitation. Peaks c and f were used for quantification of polymer incorporation ratios. Figure adapted from [259] with permission from Wiley VCH.....114
- Figure 4.2:** $^1\text{H-NMR}$ and ESR spectra of **LRC-1**. Almost complete disappearance of signal c indicates near-quantitative loading of available aldehydes with amino-TEMPO. Double integration of the ESR spectrum on the right indicated a total loading of 59%, yet the spectrum shows extensive broadening, stretching beyond the calibrated window. Figure adapted from [259] with permission from Wiley VCH.114
- Figure 4.3:** $^1\text{H-NMR}$ and ESR spectra of **LRC-2**. Successful coupling can be seen by the presence of signals e and f. The ESR spectrum on the right confirms nitroxide presence. Double integration of the ESR spectrum on the right indicated a total loading of 43%. Line broadening and crosstalk decreased compared to **LRC-1**, indicating stronger separation of the present nitroxides. Figure adapted from [259] with permission from Wiley VCH.115

- Figure 4.4:** Time-resolved fluorescence spectroscopy of **LRC-2** release experiment. Over a time of 8 h, a 10.5-fold increase in total fluorescence, determined by integration of the individual spectra, could be observed. Right: side-by-side comparison of both **LRC-2** and **LRC-5** cuvettes before and after release. The change in fluorescence is intense enough to be readily observable to the naked eye in both cases, with the nitroxide-containing polymer exhibiting vastly increased quenching efficiency. Figure adapted from [259] with permission from Wiley VCH.116
- Figure 4.5:** GPC elugrams of **LRC** before and after coupling as well as after photo release. A significant increase in molecular weight can be seen upon loading of the polymer, as well as a return to lower molecular weights upon cleavage of pyrene from the backbone. Figure adapted from [259] with permission from Wiley VCH.....117
- Figure 4.6:** Stacked $^1\text{H-NMR}$ spectra of **LRC-0-6**. Pyrene coupling was monitored *via* both disappearance of signal a and the surfacing of pyrene signals b. Release and thioaldehyde scavenging was followed by the disappearance of pyrene signals b and the surfacing of signals p and q. Spectral assignments have been heavily simplified for clarity. Fully assigned singled out spectra can be found in the **Appendix, Section 8.1.7**, pp. 205. Figure adapted from [259] with permission from Wiley VCH.119
- Figure 4.7:** GPC elugrams of **LRC-0** through **LRC-6** before and after coupling of PAS, as well as after photo-release. A significant increase in molecular weight can be observed upon loading of the polymer, as well as a return to lower molecular weights upon cleavage of pyrene from the backbone. Figure adapted from [259] with permission from Wiley VCH.120
- Figure 4.8:** Comparison of fluorescence spectra over time. While both nitroxide-bearing **LRC-2** (top left) and negative control **LRC-5** (top right) top out at similar rates of fluorescence, intensity of the polymer is vastly different. Reduction of the nitroxides in **LRC-2** (bottom left) leads to roughly half the fluorescence recovery observed in the actual release experiment. Relative rates of fluorescence recovery are visualised on the bottom right. Figure adapted from [259] with permission from Wiley VCH.121
- Figure 5.1:** $^1\text{H-NMR}$ spectrum of **MCA-0**. The inset shows a zoom of the RAFT end group protons f, g, and h, which were used with the TMP signal a to calculate the average chain length.125
- Figure 5.2:** GPC elugrams and ESR spectra of **MCA-0** through **MCA-2**. Left: Clear narrowing of the elugram and a shift to the expected molecular weight can be observed upon oxidation to **MCA-1**. No significant change can be observed upon end group modification. Right: A strong increase in ESR signal, completely broadened into one single signal can be observed upon oxidation. End group modification to **MCA-2** led to a slight change in signal shape- and intensity, yet retaining the same level of oxidation. ..125
- Figure 5.3:** Fluorescence yield comparison. Total fluorescence integrals were plotted against the absorption maxima of Cy5 at $\lambda = 650$ nm. Linear fitting allowed a comparison of relative fluorescence yields, returning a ratio of 1.00:0.68 Cy5-maleimide:**MCA-2**.126

Figure 7.1: Mask creation and evaluation process. Red arrows indicate the evaluation vector at the starting angle of 0°. Red lines indicate a stylised representation of the profile acquired from the evaluation.....	156
Figure A 8.1: ¹ H-NMR (600 MHz, chloroform-d) of bHMA.....	165
Figure A 8.2: ¹³ C-NMR (151 MHz, chloroform-d) of bHMA.....	166
Figure A 8.3: ESI-MS spectrum of bHMA (negative mode).....	166
Figure A 8.4: ¹ H-NMR (400 MHz, chloroform-d) of Cy5-MAA.....	167
Figure A 8.5: ESI-MS spectrum of Cy5-MAA.....	167
Figure A 8.6: ¹ H- and ¹³ C NMR spectra of 3-3	168
Figure A 8.7: ¹ H- and ¹³ C NMR spectra of 3-3	168
Figure A 8.8: ¹ H- and ¹³ C NMR spectra of 3-4	168
Figure A 8.9: ESI-MS spectrum of 3-6 . Molecule peaks are marked. Due to the acid-group, the molecule ionised poorly in positive mode, showing many background contaminations. Negative mode spectra could not be acquired at the time.	169
Figure A 8.10: ESI-MS spectrum of 3-7 . Molecule peaks are marked. The molecule did not ionise well in both positive and negative mode, showing strong background contamination signals.	169
Figure A 8.11: ESI-MS spectrum of 3-8	170
Figure A 8.12: Concentration dependence of Acetylpyrene fluorescence. Fluorescence shows a significant drop in intensity at concentrations greater than approximately 31.5 µM. additionally a distortion of the fluorescence spectrum is visible at higher concentrations, indicating molecular interactions of the fluorophore. Lighter colours indicate higher concentrations.	170
Figure A 8.13: ESR spectra of TEMPOL at gain 200.	171
Figure A 8.14: ESR spectra of TEMPOL at gain 200	171
Figure A 8.15: ESR spectra of TEMPOL at gain 80.	172
Figure A 8.16: ESR spectra of TEMPOL at gain 40.	172
Figure A 8.17: ESR spectra of TEMPOL at gain 20.	173
Figure A 8.18: ESR spectra of TEMPOL at gain 10.	173
Figure A 8.19: ESR spectra of TEMPOL at gain 8.	174
Figure A 8.20: ESR spectra of TEMPOL at gain 4.	174
Figure A 8.21: ESR spectra of TEMPOL at gain 2.	175
Figure A 8.22: ESR spectra of TEMPOL at gain 1.	175
Figure A 8.23: ESR calibration curves of TEMPOL, used to evaluate nitroxide content of polymers. Slopes are listed in . Modified from [259] with permission from Wiley VCH.....	176

- Figure A 8.24:** $^1\text{H-NMR}$ of **PC-3** in CDCl_3 . The inset shows a zoom of the aromatic area. Signals are heavily influenced by the presence of nitroxides, most likely losing a lot of signal intensity to line broadening and distortion 178
- Figure A 8.25:** SEC-ESI-MS Spectrum recorded of **SSPC-0**. Monomer incorporation into the same chain was confirmed by mass difference of peaks from base peak A. Values are listed below in **Table A 8.7**.
Reproduced from [211] with permission from the RSC.....179
- Figure A 8.26:** $^1\text{H-NMR}$ (600 MHz, CDCl_3) spectrum of **SSPC-0** reaction mixture used to determine conversion. Ratio was determined from integrals c/c' and g/g' . Reproduced from [211] with permission from the RSC.180
- Figure A 8.27:** $^1\text{H-NMR}$ (600 MHz, CDCl_3) spectrum of **SSPC-0**. Polymer composition was determined from the ratio of the signals g, c, and f. Reproduced from [211] with permission from the RSC.....180
- Figure A 8.28:** $^1\text{H-NMR}$ (600 MHz, CDCl_3) spectrum acquired from a crude sample of **SSPC-1**. The spectrum shows a clear increase in band broadening of signals g, h, and i, stemming from nitroxide presence. Reproduced from [211] with permission from the RSC.....181
- Figure A 8.29:** ESR spectrum recorded of **SSPC-2**. The line broadening clearly indicates polymer bound-nitroxides. Partial formation of the TFA-salt with the nitroxide was assumed as the signal had decreased to 7032, where a theoretical maximum of 27248 indicated only 25.2% of radicals left. Reproduced from [211] with permission from the RSC.....182
- Figure A 8.30:** ESR spectrum of **SSPC-3** recorded after Dox-loading clearly shows the preservation of polymer-bound nitroxides. Reproduced from [211] with permission from the RSC.....183
- Figure A 8.31:** UV-Vis-absorption spectrum of $0.4 \text{ mg} \cdot \text{mL}^{-1}$ **SSPC-3** in PBS. Loading was determined from the absorption at 495 nm at pH = 7.4. The second measurement after acidification was conducted as a reference measurement to obtain a reliable reference for possible changes in absorptive properties. A slight change towards shorter wavelengths and a minute decrease in absorption are visible as a result of the slight increase in volume. Reproduced from [211] with permission from the RSC.....184
- Figure A 8.32:** Time-resolved fluorescence spectra of **SSPC-3** in PBS at pH = 7.4. In comparison to the release experiment at pH = 5.0 only a small increase in fluorescence can be observed. Lighter reds indicate later time-points. Reproduced from [211] with permission from the RSC.....185
- Figure A 8.33:** $^1\text{H-NMR}$ (400 MHz, CDCl_3) and ESI-MS (positive mode) of alkyne-RAFT agent (**3-13**)185
- Figure A 8.34:** ESR spectrum of **ULC-0.2**. The spectrum exhibits very slight line broadening and asymmetry, indicating polymer bound nitroxides. A proper quantification could not be performed, yet a lot more signal would have been expected from the assembly at high levels of incorporation.....186
- Figure A 8.35:** MTT viability test in HeLa cells. As it is clearly visible, no impact on cell viability of the **SSPC-2** backbone is observed. The loaded **SSPC-3** carrier exhibits slightly increased efficacy over free Dox.187

- Figure A 8.36:** MTT viability test in HeLa cells. As it is clearly visible, no impact on cell viability of the pTEGMA is evident.187
- Figure A 8.37:** HepG2 spheroids, DIV 7, 3 h incubation with **SSPC-2**. Scale bars are 100 μm188
- Figure A 8.38:** HepG2 spheroids, DIV 7, 3 h incubation with Dox·HCl. Scale bars are 100 μm189
- Figure A 8.39:** HepG2 spheroids, DIV 7, 3 h incubation with **SSPC-3**. Scale bars are 100 μm190
- Figure A 8.40:** SK-MEL-28 spheroids, DIV 7, 3 h incubation with Dox·HCl. Scale bars are 100 μm191
- Figure A 8.41:** SK-MEL-28 spheroids, DIV 7, 3 h incubation with **SSPC-2**. Scale bars are 100 μm192
- Figure A 8.42:** SK-MEL-28 spheroids, DIV 7, 3 h incubation with **SSPC-3**. Scale bars are 100 μm193
- Figure A 8.43:** ^1H -NMR (600 MHz, DMSO- d_6) spectrum of pyreneacyl sulfide acid. Residual DCM and THF impurities are marked with *.202
- Figure A 8.44:** ^{13}C -NMR (151 MHz, DMSO- d_6) of PAS.202
- Figure A 8.45:** Concentration dependence of PAS fluorescence. The spectra show a drastic drop in intensity at concentrations greater than approximately 62.5 μM203
- Figure A 8.46:** ^1H -NMR of FPMA in CDCl_3 . Right: ^{13}C -NMR of FPMA in CDCl_3204
- Figure A 8.47:** ^1H -NMR-spectra used to calculate feed ratio and conversion for the polymerisation of **LRC-0**. Left: reaction mixture before polymerisation. Right: Spectrum after 4.5 hours. Integrals before and after 4.5 hours were used to calculate conversion. Feed ratio was determined from integrals d and a, ratio of incorporation was determined from c' and h'.204
- Figure A 8.48:** ^1H -NMR of **LRC-0** in DMSO- D_6205
- Figure A 8.49:** ^1H -NMR of **LRC-5** in CDCl_3205
- Figure A 8.50:** ^1H -NMR of **LRC-6** after irradiation in DMSO- D_6206
- Figure A 8.51:** Photograph of the custom reactor setup. The top left shows the custom cuvette holder with **LRC-2** for bulk-release in a quartz-cuvette.207
- Figure A 8.52:** UV/Vis spectra of **LRC-2** and **LRC-3** along the release process. The spectrum on the left shows the same solution of **LRC-2** before and after irradiation. Clearly visible is a shift in towards shorter wavelength due to spatial separation of the absorbing fluorophores, reducing excimer and stacking effects. The spectrum on the right additionally shows a clear decrease in absorption after precipitation of the polymer and removal of free, released acetylpyrene, confirming the release event.207
- Figure A 8.53:** Emission spectrum of the Avonec LED used for irradiation of **LRC-2** and **LRC-5**. Reproduced from [211] with permissions from RSC.208
- Figure A 8.54:** SEC-MS spectrum of **MCA-0**. One repeating unit (length 8-9 monomers) is shown. High amine content led to high amount of proton-

adducts for ionisation. Only RAFT-group terminated chains could be detected.	209
Figure A 8.55: Absorption and fluorescence emission spectra of free Cy5-maleimide and MCA-2 from which comparisons of spin silencing efficiency were drawn.....	210

List of Schemes

- Scheme 1.1:** Basic structure and mode of action of a model drug, capable of self reporting of targeted molecular release. The macromolecular nature allows exploitation of the EPR effect, wherein transporters can permeate defective blood vessels in a tumour. Decreased pH in the tumour tissue facilitates the hydrolytic cleavage of hydrazones, binding Doxorubicin, a common chemotherapeutic to a nitroxide bearing carrier polymer. Nitroxides enable fluorescent readout of release and potentially increase permeation and uptake.....2
- Scheme 2.1:** FRP initiation steps. First, a radical initiator undergoes homolysis, forming two radicals in the process. Addition of an initiator radical to a monomer starts a radical-bearing, growing polymer chain.7
- Scheme 2.2:** Propagation of a growing chain by the sequential addition of monomers. The rate of addition is determined by the propagation constant k_p :.....7
- Scheme 2.3:** Termination by either disproportionation, or recombination of two polymer chains. Abstraction of a hydrogen atom from one chain leaves a saturated chain and a macromonomer. The recombination of two growing chains yields a single chain of higher molecular weight.8
- Scheme 2.4:** Chain transfer in FRP. Propagation is terminated by chain transfer to a transfer agent, which in turn is capable of reinitiation a new growing chain. The rate of transfer is governed by the rate coefficient k_{tr} , the rate of reinitiation is expressed by k_{rei} :.....8
- Scheme 2.5:** Commonly used techniques for RDRP. (I) NMP employs nitroxides, which scavenge growing chain macro-radicals. Polymerisation is reactivated by thermal dissociation. (II) In ATRP a leaving group, typically a halogen is transferred from the dormant chain to a metal complex. (III) RAFT relies on an equilibrium of dormant chains, bound to the CTA. The radical concentration stays constant, yet termination events are suppressed by chain transfer to the CTA. Figure adapted from [19] with permission from ACS.....10
- Scheme 2.6:** General RAFT mechanism. (I) Initiator decomposition, generating two radicals and initiation by addition of the initiator radical to a monomer M to form a macro-radical $P_n\bullet$. (II) Pre-equilibrium, in which a) initiated macro-radical add to the RAFT agent's C=S bond, forming an intermediate species and b) the R-group is released to initiate another chain $P_m\bullet$. (III) Propagation occurs, while the unbound macro-radical is elongated by more monomer units, forming a growing chain. (IV) Core-equilibrium, the controlling step in RAFT polymerisation, where growing chains add to the RAFT agent and dormant chains are released to continue propagation. (V) Termination by general FRP mechanisms.^[19]12
- Scheme 2.7:** Overview of Z- and R-groups and their compatibility with various monomers. Plain lines indicate good control, dashed lines indicate limited

- control. Z-groups: Addition-and fragmentation rates decrease from left to right. R-groups: Transfer coefficients and fragmentation rates decrease from left to right. Monomers: methyl methacrylate (MMA), N-(2-hydroxypropyl)methacrylamides (HPMAM), vinyl acetate (VAc), N-vinylpyrrolidone (NVP), N-vinyl caprolactam (NVC), styrene (St), methyl acrylate (MA), acrylamide (AM), acrylonitrile (AN).....13
- Scheme 2.8:** Possible end group modifications on the Z side. Clockwise from top left: Block-copolymerisation *via* RAFT or ATRP, nucleophilic cleavage and subsequent conjugation with enes or thiols, Thermolysis to generate alkene-terminated polymers, radically induced reduction, addition-fragmentation with a nitroxide to generate an NMP macro-CTA, radical induced oxidation with either peroxides or a cobalt-catalyst, addition-fragmentation coupling, end group-capping *via* HDA. Figure adapted from [19] with permission from ACS.14
- Scheme 2.9:** SEC-ESI-MS setup for the analysis of THF-soluble polymers. The sample is separated by size on a GPC system. The resulting stream of size-resolved polymers is split into an RI- and MS detector. The RI detector enables monitoring of eluted polymer molecular weight. Prior to injection into the ESI source, the polymer flow is mixed with methanol to facilitate ionisation. Detection *via* Orbitrap detector yields highly resolved spectra.^[33].....16
- Scheme 2.10:** Jablonski diagram of single-photon processes in a single molecule. Upon absorption of a photon, the molecule is excited from its ground singlet state S_0 into a vibrational ($V = 1, 2, \dots$) state of a higher singlet state. As transitions from one state to another can only occur from the individual ground state $V = 0$, higher vibrational states relax under loss of vibrational energy. From the ground state, the excited system can undergo either internal conversion (non-radiative), fluorescence (radiative), or intersystem crossing into a triplet state, from where it will either deactivate radiatively in phosphorescence or non-radiatively in a chemical reaction or another ISC.^[38].....19
- Scheme 2.11:** General concept of the Franck-Condon principle. Each parabola corresponds to the Lennard-Jones potential of a ground state and an excited state. Transitions generally occur from the ground state. Probability of transition is determined by the overlap of the wave-functions of ground- and excited state. Width of the absorption bands in UV/Vis spectroscopy (indicated in blue) is determined by the probability of transitions to different states. Figure adapted from [39] with permission from the IOP....20
- Scheme 2.12:** Left: Schematic representation of the linear decrease in intensity of the incident light. Right: A solution of acetylpyrene in ACN, fluorescing in the light of a 385 nm laser beam, visualizing the decrease in intensity as light traverses the solution.21
- Scheme 2.13:** Mechanism of photoenolisation. Upon irradiation, the molecule gets excited into its S_1 from where it can cross into a triplet state. After a first rotation, a proton abstraction from the methyl group occurs, upon which the molecule can undergo either enolisation or another rotation, also

- followed by enolisation. The rotation step inherently leads to two different E/Z-isomers, out of which the E-isomer is longer-lived and DA-reactive...22
- Scheme 2.14:** Photoenol reaction employed for the protection of dithiobenzoate end groups. Stabilisation of the E-enol form *via* H-bonding to the methoxy-oxygen increases quantum yield of the reaction. The photo-activated diene readily reacts with thiocarbonyls in an HDA reaction.....23
- Scheme 2.15:** Norrish-II cleavage of phenacyl sulfide. Upon irradiation, a 1,4-biradical is formed *via* abstraction of the γ -hydrogen. Upon dissociation of the biradical, an enol and a thioaldehyde are formed. The enol rapidly tautomerises back to the keto-form.....24
- Scheme 2.16:** Mechanism of β -cleavage of phenacyl sulfide in cases where no γ – hydrogen is available for abstraction.24
- Scheme 2.17:** Pyreneacyl sulfide, employed for polymer modification and visualisation of release in this thesis.....25
- Scheme 2.18:** Different types of nitroxides, typically encountered in technical or biomedical applications.26
- Scheme 2.19:** Quenching mechanism *via* fluorophore-nitroxide-interaction. Nitroxide and fluorophore spins for a doublet state. After excitation spin, exchange between the now occupied fluorophore's HOMO and the nitroxide's SOMO can occur. Scheme adapted from [146,155].28
- Scheme 2.20:** Redox cycle of nitroxides in biological system. Reactive oxygen species are readily oxidised or reduced, giving nitroxides a superoxide dismutase (SOD)-like function.^[82]30
- Scheme 2.21:** Nitroxides and -precursors employed in combination with Dox. Compounds 2-1 - 2-5 have been shown to drastically decrease damage to healthy tissue, while 2-6 has been shown to increase oxidative damage as a pro-oxidant. 2-1 TEMPO, 2-2 TEMPOL, 2-3 Tempace, 2-4 dexrazoxane, 2-5 Mito-TEMPOL, 2-6 Tempamine.^[166]31
- Scheme 2.22:** Enhanced permeation and retention in a tumour is caused by physiological conditions in the tumour. Elevated proliferation rates of cancer cells elevate the demand for oxygen and nutrients. As a result, vascularisation with angiogenic blood vessels, bearing defective endothelia (fenestrations) is elevated, allowing extravasation of blood-borne macromolecular assemblies into the tissue. A lack of lymphatic drainage effects a decrease in clearance from the tissue, allowing longer dwell times of macromolecules in the tumour and thus effectively increasing the timeframe to either enter the cells or release cargo.33
- Scheme 2.23:** Mechanism of hydrazone cleavage. The bond is formed in an equilibrium reaction. If water is withdrawn from the reaction, stable hydrazone bonds are formed. In the presence of excess water, the bond is near-quantitatively cleaved.36
- Scheme 2.24:** : Schematic representations of 2D and 3D cell culture systems: a) 2D cell culture, a monolayer of cells grown on a flat surface, b) free floating spheroid of cells in solution, c) a co-culture of a spheroid (red) with

- fibroblasts (green), grown in a three-dimensional matrix of biocompatible hydrogel (violet).38
- Scheme 2.25:** Representation of the 3D-microflow reactor in which polymeric assemblies will be tested. A 3D co-culture of spheroids and fibroblasts is grown around a semi-tubular, porous polycarbonate channel. The channel is cultured with endothelial cells, effectively mimicking a fenestrated blood vessel passing through a tumour. Samples for bio-testing can be supplied *via* the vascular circuit, simulating *in vivo* application of therapeutics. Image modified from [139] with permission from WILEY-VCH.39
- Scheme 2.26:** General setup of a confocal laser-scanning microscope (CLSM). Exciting light is provided by a laser source in a monochromatic and directional manner. The sample is reflected on a movable dichroic mirror, scanning the sample as the image is acquired. Fluorescent light enters the detector through a pinhole, which emits out-of-focus light, allowing the imaging of depth-defined planes of the sample specimen.40
- Scheme 2.27:** Proposed mechanisms for the Ugi reaction. Path A was initially proposed by Ugi, based upon the observation that the reaction proceeds faster in polar solvents. Path B has recently been proposed, based upon molecular simulations.^[177]43
- Scheme 3.1:** General concept for a nanodrug, capable of reporting the release of Dox. A methacrylate based, water-soluble construct was proposed to carry nitroxides and hydrazone bound fluorescent drug moieties. Transfer of the polymeric assembly to an acidic environment would facilitate hydrolytic cleavage of the hydrazone, releasing Dox from the polymer. The inherent fluorescence of Dox, now no longer quenched by proximal nitroxides, can be used to quantify release efficiency. Reproduced from [211] with permission from the RSC.49
- Scheme 3.2:** Synthesis of the small molecule assembly to demonstrate quenching and release. Pyrene was used as a fluorescent model drug and TMIO was to be used as a quencher.52
- Scheme 3.3:** Synthesis route for a modified approach, employing boc-hydrazido-TMIO as a synthon towards a profluorescent model system for pyrene release.54
- Scheme 3.4:** Synthetic strategy for the water soluble, single anchor platform (SAP), based on which a system for the reporting of molecular release is established. TEGMA and GMA are copolymerised *via* RAFT with CPDB as transfer agent, yielding the water-soluble copolymer **SAP-0**. In order to retain a high end group fidelity through following steps, the end group is protected with photoenol in a photo-HDA reaction, yielding **SAP-1**. In order to generate orthogonally addressable groups on the polymer, GMA is ring-opened by sodium-azide, yielding **SAP-2** as a base polymer for further modification.55
- Scheme 3.5:** Functionalisation strategies. The left (**SAP-3**) pathway was designed to build the hydrazide linkage from a diacid and click the nitroxide. The right (**SAP-4**) pathway was designed to immobilise the nitroxide *via*

- esterification, clicking the hydrazine moiety in the form of a protected hydrazide.....60
- Scheme 3.6:** Synthetic approach used to construct the polymeric nanodrug with a spin silencing-based reporter system. Firstly, a polymer is synthesised *via* RAFT. The incorporated nitroxide-precursors are subsequently oxidised and hydrazide-bearing sidechains are deprotected, generating a nitroxide-bearing platform for immobilisation of Dox in a pH-labile hydrazone linkage.....66
- Scheme 3.7:** Chemical structure of **SSPC-3**. The **SSPC-2** backbone bears a hydrazide moiety, on which Dox is immobilised *via* hydrolytically cleavable hydrazone linkage.....83
- Scheme 3.8:** Synthetic strategy for the incorporation of targeting (green) and tracking (blue) moieties into an **SSPC**-type platform.100
- Scheme 3.9:** Synthetic approach towards an Ugi loaded carrier (**ULC**) for self-reporting molecular release. A block copolymer of poly-PFMA-*stat*-MMA-block-TEGMA is synthesised *via* RAFT and subsequent chain extension. In an Ugi reaction, the polymer is loaded with carboxy TEMPO, boc-protected hydrazine and cyclohexyl isocyanide. After deprotection of the hydrazine, the polymer is loaded with Dox, analogously to approaches shown above.103
- Scheme 4.1:** Illustration demonstrating the synthesis and subsequent release from a light-responsive release-reporter. First, the polymer is synthesised, bearing an anchor group (I) which allows the coupling of both fluorophore and nitroxide quencher in a single multicomponent reaction (II). While bound to the backbone, the fluorophore is silenced by the nitroxide (III). Upon irradiation, the fluorophore is cleaved from the polymer backbone, escaping the effective quenching radius to the nitroxide, enabling release quantification *via* fluorescence readout (IV).108
- Scheme 4.2:** Mechanism of pyreneacyl sulfide cleavage. Upon irradiation, the acetylpyrene portion of the molecule undergoes ISC, generating an oxygen-centred radical, which will subsequently abstract the alpha-hydrogen from the sulfide, initiating a cascade in which a thioaldehyde and enol are generated. The enol undergoes tautomerisation, back to the keto-form. The thioaldehyde can readily react with nucleophiles, thiols or dienes. Interesting for this chapter was predominantly the third pathway, where the thioaldehyde can be scavenged quantitatively in the presence of a diene forming an unreactive HDA adduct.109
- Scheme 4.3:** Synthesis and release of a small molecule reporter system for light triggered release. Thioacetic acid is reacted with bromo-acetylpyrene, yielding PAS-acid **4-1**. Coupling with modified TEMPO would yield the spin-silenced PAS-conjugate **4-2**, which then can undergo photolytic cleavage. Coupling follows established esterification or amidation protocols.110
- Scheme 4.4:** Synthetic approach towards a light responsive carrier (**LRC**) to demonstrate the possibilities of light-triggered release. A FPMA/MMA copolymer is synthesised *via* RAFT, yielding the aldehyde-bearing polymer platform **LRC-0**. The polymer is subsequently modified in an Ugi

- reaction with amino-TEMPO, cyclohexyl isocyanate, and PAS-acid. The resulting polymer **LRC-2** is then irradiated in the presence of sorbic alcohol as a thioaldehyde scavenger, to release acetypyrene as a fluorescent reporter.112
- Scheme 4.5:** Synthesis of a nitroxide free analogue to investigate self-quenching effects of the pyrene moiety while attached to the polymer backbone. Cyclohexylamine was employed to generate a structural surrogate to amino-TEMPO as a building block for the MCR coupling.....118
- Scheme 5.1:** Synthetic strategy for a novel MSOT contrast agent. First, a nitroxide precursor polymer is synthesised *via* RAFT and subsequently oxidised to a TEMPO bearing platform. The end group is removed *via* aminolysis and functionalised *via* thiol-ene click with Cy5-maleimide.....124
- Scheme A 8.1:** Schematic of the photo reactor used in the release experiments. The cuvette holder was 3D-printed and fixed in order to not obstruct the light's pathway and keep a consistent distance to the LED when the cuvette is taken out for measurement. The container was made from a reflective material in order to achieve maximum illumination of the sample.206

List of Tables

Table A 7.1: Oxidation conditions for the attempted synthesis of DLPC-1	158
Table A 8.1: Correlation of TEMPOL concentration and double integral area. Increasing receiver gain values led to a strong increase in ESR signal. A range of calibration coefficients for a selection of gain stages 1-200 was recorded, since gain and signal did not scale in a consistent fashion.	176
Table A 8.2: MS values obtained from SEC-MS of SAP-0 and calculated values for comparison. Column “Label” denotes the chain composition and label in the spectrum. $\Delta\Delta m/z$ max. denotes the theoretical maximum deviation in m/z by instrument parameters.	177
Table A 8.3: MS values obtained from SEC-MS of SAP-1 and calculated values for comparison. Column “Label” denotes the chain composition and label in the spectrum. $\Delta\Delta m/z$ max. denotes the theoretical maximum deviation in m/z by instrument parameters. Single values slightly exceeding deviation maximum were due to poorly resolved peaks.	177
Table A 8.4: MS values obtained from SEC-MS of SAP-2 and calculated values for comparison. Column “Label” denotes the chain composition and label in the spectrum. $\Delta\Delta m/z$ max. denotes the theoretical maximum deviation in m/z by instrument parameters. Single values slightly exceeding deviation maximum were due to poorly resolved peaks.	177
Table A 8.5: NMR and ESR numerical results of PC-1 oxidation. Measured at 2.4 mg·mL ⁻¹ in DCM at gain 2. Monomer integrals and ratios determined from PC-0 NMR.	178
Table A 8.6: ESR numerical results of PC-2 after TEA addition. Measured at 2.7 mg·mL ⁻¹ in DCM at gain 2. Monomer integrals and ratios determined from PC-0 NMR.	178
Table A 8.7: ESI-MS values obtained from SEC-MS of SSPC-0 and calculated values for comparison. Column “rep. unit” denotes the repeating unit responsible for the indicated mass difference from base-signal A. $\Delta\Delta m/z$ max. denotes the allowed maximum deviation in m/z by instrument parameters.	179
Table A 8.8: Calculated conversion from EPR. Monomer ratios were taken from SSPC-0 NMR spectra.	181
Table A 8.9: Nitroxide density after boc-deprotection of SSPC-2 . Spectrum was measured at a gain of 40.	182
Table A 8.10: ESR evaluation data after Dox-loading of SSPC-3 indicated a preservation of 52%.	183
Table A 8.11: Dox-loading density of SSPC-3 as determined <i>via</i> NMR. x represents the relative incorporation of TEGMA and either the boc- or Dox-bearing hydrazide in SSPC-0 and SSPC-3 . SSPC-0 shows a hydrazide density of 1 mol hydrazide per 6.25 mol TEGMA. SSPC-3	

shows a ratio of incorporation of 1 mol Dox per 27.78 mol of TEGMA.
This results in a loading density of 22.5% loaded hydrazide anchors.....183

Table A 8.12: Calculation of loading density. The molar hydrazide content X_{HMA} was obtained from boc-signals' integral based on the NMR spectra of **SSPC-0**.184

Table A 8.13: Spectrometric data used for calculation of release efficiency.184

Table A 8.14: Attempted coupling conditions for the generation of a small molecule system for light triggered release.203

Table A 8.15: MS values obtained from SEC-MS of **MCA-0** and calculated values for comparison. Column "Label" denotes the chain composition and label in the spectrum. $\Delta\Delta m/z$ max. denotes the theoretical maximum deviation in m/z by instrument parameters.209

Acknowledgements

A project like this always entails a journey of great scientific and personal ups and downs, achievements and challenges, gifts and lessons. It has been a long road with many people accompanying me along the way, who shall not go unmentioned:

First and foremost I would like to extend my sincere gratitude to my outstanding board of supervisors, Prof. Christopher Barner-Kowollik, Prof. Kathryn Fairful-Smith, and Dr. James Blinco, who not only offered me an interesting and challenging topic, provided me with an inexhaustible source of scientific input and support, but also always had an open door in all matters of a PhD between the two ends of the world.

I would like to thank Prof. Ute Schepers for the years of collaboration, bio-testing, and project design, always allowing me to keep one foot in the door of biological research. Big thanks to Prof. Stephen Blanksby, Dr. Berwyck Poad, and Dr. David Marshall for their support with the MS setup. I would also like to acknowledge Prof. Steven Bottle for accommodating me in his group at QUT.

Very special thanks to Dr. Bettina Olshausen and Dr. Vanessa Kappings, who spent countless hours keeping the cells alive. Your help and input with the cell-experiments is invaluable!

Ein großer Dank gebührt auch allen Mitgliedern unserer großartigen Arbeitsgruppe für eine einzigartige Atmosphäre. Insbesondere seien hier diejenigen genannt, die nicht nur Kollegen, sondern gute Freunde waren oder geworden sind: Michi, Thomas, Katrin, David, Waldemar, Jan, Johannes, der andere Jan, Caro, Andrea, Fede, Divya.

Unbedingt seien auch all diejenigen genannt, die hinter den Kulissen die Infrastruktur unserer Gruppe am KIT Tag für Tag aufrechterhalten: Dr. Anja Goldmann, Dr. Maria Schneider, Vincent Schüler, und Katharina Elies.

I would like to thank to everybody at QUT who kept the infrastructure running: Kaz, Aaron, Michael and Dr. Mark Wellard.

Ein großer Dank gebührt auch allen abseits des Campus, ohne die diese Promotion nicht möglich gewesen wäre: Philipp und die Bayers, Nachtschatten, Elzar, die Haustür/Neon

Jam, die ChemBios, LocustPCR, das HLSL am DKFZ, die DoKo-Runde, meine Mitbewohner, die Kletterer, die Powders und zwei Städte voll inspirierender Menschen, die ich hier unmöglich alle namentlich aufzählen könnte. Auf tausend neue Projekte mit euch!

Danke meinen beiden Co-Cotutellisten, Hendrik und Hannes, die zeitgleich mit mir um die Welt gereist sind und mit denen ich bald hoffentlich angemessen feiern werde.

Big thanks to everyone who made Brisbane my home away from home: Alana, Christiane, Nathan, Raf, Sean, Tobi, Kristina, Sam, Lukas, Kai, Tenille, Jack, Komba, the Kangaroo Point Crowd, and the Cliffhangers. It's been an unforgettable experience!

Und selbstverständlich, last but definitely not least: Meinen Eltern, meinen Geschwistern und meiner gesamten Familie danke ich für ihre Unterstützung und unerschöpfliche Geduld! Hals- und Beinbruch, auf euch kann man immer zählen.